On collective behaviour of coupled micro/nano electromechanical sensors



Guowei Tao

Pembroke College

University of Oxford

A thesis submitted for the degree of

Doctor of Philosophy

Hilary 2018

Abstract

With advances in nanotechnology, resonant sensors based on micro/nano electromechanical systems (M/NEMS) have been manufactured utilising a process similar to that of microelectronics. By providing a frequency shift proportional to the mass/stiffness change, these small resonators enable rapid detection of extremely minute changes in mass and force. For example, they can be used to trace the concentration of pathogens. M/NEMS resonators also demonstrate excellent compatibility with electronic circuits, hence offering multi-function and single-chip solutions for next-generation sensing applications. Resonators are coupled to provide extra degrees of freedom for multi-sensing, while reducing a majority of connections required. The collective behaviour of coupled systems gives rise to new sensing methods such as eigenvalue and eigenvector sensing, which exhibit enhanced sensitivity and linearity as opposed to the traditional frequency-shift approach.

However, the mechanisms of coupling have not yet been fully exploited. Coupled micro/nano systems are exposed to several challenges. First, process variability is known to degrade sensor performance. Moreover, the readout and signal processing issues in large arrays have not been addressed. Hence, actuating and testing coupled sensors are expensive and time-consuming. These hurdles can be circumvented using a novel inverse eigenvalue analysis (IEA) method proposed in this thesis, which is capable of characterising coupled systems based on inverse and forward analysis. The method extracts the system matrix, which carries deterministic information about process and sensitivity, by attaching a peripheral electrical resonator to the MEMS array, therefore providing the advantages of simplified actuation, accurate calibration and sensitivity trimming. To explore the ultimate limit of scaling, prototype sensors consisting of different numbers of coupled resonators have been designed, fabricated and tested for sensing. By investigating the unique behaviour of eigenvalues, various approaches have been proposed to enhance the accuracy of inverse eigenvalue sensing in large coupled systems.

Acknowledgements

First and foremost, I would like to express my deepest gratitude to my supervisor Professor Bhaskar Choubey for offering me the chance to work and learn from him. He is a creative scientist and great mentor. My research would become unimaginable without his constant guidance and encouragement.

Special thanks are due to my dear colleagues in the lab, including Dr Rhett Davis, Oscar Rahnama, Deyan Levski, Heather Nelson, Mus'ab Shaharom etc., for their friendship and support. I have definitely benefited from the illuminating conversations with them. In addition, I am fortunate enough to have met Professor Steve Collins, Professor Steve Elston, Dr Aleksej Makarov, Dr Ching-Mei Chen and Dr Madhav Kumar. Their valuable input has assisted me at different stages of my research. My confirmation of status and transfer report were examined by Professor Stephen Morris and Professor Steve Sheard. My viva was examined by Professor Harish Bhaskaran and Dr Barry Gallacher. I am very grateful for their expertise and insightful feedback to improve my work.

I would like to thank the wonderful people I met outside my university. Constructive discussions with Professor Honglong Chang and Dr Hemin Zhang from Northwestern Polytechnic University have broadened my understanding of coupled resonators. Vladimir Cizelj and Milan Petrovic from Vlatacom treated me like a family member during my secondment in Serbia. Dr Anoosh Lachin from London has suggested a series of interesting quotes for my thesis.

I am also thankful for all my Chinese friends, who have made my study abroad more joyful. I express my love and gratefulness to my girlfriend Yuxi Zhang. Thank you for your kind company. Last but not least, I would not have come to this level without the unconditional care from my family.

Publications

A portion of this thesis is either based on or partly related to the following publications in peer-reviewed journals and international conferences. The journal articles include:

- Guowei Tao, Hemin Zhang, Honglong Chang, and Bhaskar Choubey. "Inverse eigenvalue sensing in coupled micro/nano system". In: *Journal of Microelectromechanical Systems* 27.5 (2018), pp. 886–895
- Guowei Tao and Bhaskar Choubey. "Variability induced sensitivity degradation in coupled nano/micro resonant sensors". In: *IEEE Transactions on Nanotechnology* 17.4 (2018), pp. 709–713
- Guowei Tao and Bhaskar Choubey. "Inverse eigenvalue sensing with corner coupled square plate MEMS resonators array". In: *Analog Integrated Circuits and Signal Processing* 95.3 (2018), pp. 447–455
- Guowei Tao and Bhaskar Choubey. "A simple technique to readout and characterize coupled MEMS resonators". In: *Journal of Microelectromechanical Systems* 25.4 (2016), pp. 617–625

The conference proceedings include:

- Guowei Tao and Bhaskar Choubey. "IEA sensing for corner coupled square plate MEMS resonators arrays". In: *Oxford Circuits and Systems Conference (OXCAS)*. 2017
- Guowei Tao and Bhaskar Choubey. "On measuring variability and its effect on sensitivity of coupled nano/micro resonators". In: *Nano/Micro Engineered and Molecular Systems (NEMS), 2017 IEEE 12th International Conference on*. IEEE. 2017, pp. 657–660
- Guowei Tao and Bhaskar Choubey. "Inverse eigenvalue analysis techniques for coupled M/NEMS resonators". In: *Nano/Micro Engineered and Molecular Systems (NEMS), 2016 IEEE 11th Annual International Conference on*. IEEE. 2016, pp. 217–220

- Guowei Tao and Bhaskar Choubey. "Characterizing coupled MEMS resonators with an electrical resonator". In: *Journal of Physics: Conference Series*. Vol. 757. 1. IOP Publishing. 2016, p. 012017
- Vojislav Z Lukic, Aleksej Makarov, Guowei Tao, and Bhaskar Choubey. "Vehicle speed estimation from tracking license plates". In: *Telecommunications Forum Telfor (TELFOR), 2015 23rd*. IEEE. 2015, pp. 429–432
- Aleksej Makarov, Vojislav Lukic, Guowei Tao, and Bhaskar Choubey. "Vehicle speed estimation from partially calibrated monocular images". In: *International Conference on Sensors Engineering and Electronics Instrumental Advances (SEIA' 2015)*. 2015

This thesis is dedicated to my 96-year old grandfather

Daxuan Tao

Throughout the long past ages,

he fought against invasion, oppression and cancer

Contents

List of Figures **xi**

List of Tables **xvi**

1 Introduction **1**
1.1 Micro/Nano Electromechanical Systems 1
1.2 Micro/Nano Resonators 2
1.2.1 Background 3
1.2.2 Resonators as Sensors 4
1.2.3 Frequency Shift 6
1.2.4 Resonator Array 8
1.3 Challenges 9
1.3.1 Connectivity 9
1.3.2 Process Variability 10
1.4 Coupled Resonators 11
1.4.1 Coupling 11
1.4.2 Multiplexed Actuation 14
1.4.3 Device and Process Characterisation 15
1.4.4 Emerging Applications 15
1.5 Objectives and Thesis Outline 18
1.5.1 Objectives 19
1.5.2 Thesis Outline 19

2 Analysis of Coupled Systems **22**
2.1 Introduction 23
2.2 Eigen-problem in Coupled Systems 24
2.3 Perturbation Theory 27
2.3.1 Mass and Stiffness Change 27
2.3.2 Sensitivity Analysis 28
2.3.3 Differential and Common Mode Responses 31
2.4 Limitations 32
2.4.1 Practical Constraints 33

2.4.2 Resolution . . . 34
2.4.3 Dynamic Range . . . 35
2.5 Inverse Eigenvalue Analysis . . . 36
2.5.1 Known Techniques . . . 37
2.5.2 New Approach . . . 40
2.5.3 Comparison . . . 43
2.5.4 Discussion . . . 48
2.6 Summary . . . 49

3 Two Coupled Resonators **51**
3.1 Introduction . . . 51
3.2 Sensing Metrics . . . 52
3.2.1 Eigenvalues . . . 53
3.2.2 Eigenvectors . . . 57
3.3 Inverse Eigenvalue Sensing . . . 59
3.3.1 Full-parameter Extraction . . . 59
3.3.2 Eigenvector Error . . . 61
3.3.3 Stiffness Error . . . 63
3.4 Summary . . . 66

4 Sensor Characterisation **68**
4.1 Introduction . . . 69
4.2 Resonant Sensor . . . 70
4.2.1 Sensor Architecture . . . 70
4.2.2 Circuitry . . . 72
4.2.3 Electrostatic Stiffness . . . 75
4.2.4 Experimental Setup . . . 76
4.3 Tow Thomas Biquad Resonator . . . 78
4.3.1 Configuration . . . 79
4.3.2 Coupling Mechanism . . . 81
4.4 Experiment and Results . . . 84
4.4.1 Frequency Response and System Matrix . . . 84
4.4.2 Validation . . . 85
4.5 Sensitivity Determination . . . 86
4.5.1 Process Variability . . . 87
4.5.2 Characterisation Results . . . 89
4.5.3 Sensitivity Shift . . . 90
4.5.4 Sensitivity Tuning . . . 93
4.5.5 Scalability . . . 95
4.6 Summary . . . 96

5 Corner Coupled Square Plate Resonators **98**
5.1 Introduction . . . 99
5.2 Resonant Square Plate . . . 100
5.2.1 Resonance . . . 100
5.2.2 Direct Drive and Readout . . . 102
5.2.3 DC Bias . . . 104
5.3 Corner Coupling . . . 106
5.4 Design and Fabrication . . . 108
5.4.1 PolyMUMPs . . . 109
5.4.2 Parameters . . . 110
5.5 Performance . . . 111
5.5.1 Electromechanical Properties . . . 111
5.5.2 Over-sizing . . . 114
5.6 Array Perturbation . . . 115
5.6.1 Electrostatic Perturbation . . . 115
5.6.2 Terminal Decoupling . . . 117
5.7 Summary . . . 118

6 Inverse Eigenvalue Sensing in Large Coupled Systems **120**
6.1 Introduction . . . 120
6.2 Damping . . . 121
6.2.1 Error Analysis . . . 122
6.2.2 Maximum Number of Resonators . . . 124
6.3 Mode Attenuation . . . 125
6.3.1 Eigen-mode Analysis . . . 126
6.3.2 Multiple Actuation . . . 127
6.4 Eigenvalue Readout . . . 129
6.4.1 Interweaving Condition . . . 129
6.4.2 Eigenvalue Change . . . 130
6.4.3 Device Failure . . . 132
6.5 Sensing Complexity . . . 133
6.5.1 Linearisation . . . 134
6.5.2 Accuracy . . . 135
6.5.3 An Example of Twenty Coupled Resonators . . . 136
6.6 Summary . . . 137

7 Conclusions and Future Work **139**
7.1 Conclusions 139
7.2 Future Outlook 141
7.2.1 Sensor Design and Fabrication 141
7.2.2 Simultaneous Eigenvalue Readout 143
7.2.3 Damping and Non-linearity Compensation 145
7.2.4 System Integration 146

Appendices

A MATLAB Code **148**
A.1 Eigenvector Extraction 148
A.1.1 Traditional Method 148
A.1.2 Linearised Method 149
A.2 Inverse Lanczos' Algorithm 149
A.3 De Boor and Golub's Algorithm 150

B Mathematical Proof for Inverse Eigenvalue Analysis **153**
B.1 Inverse Lanczos' Algorithm 153
B.2 Gladwell's Inverse Problem 154

C Test Chips **156**
C.1 Layout and Packaging 156
C.2 Test Chip I 158
C.3 Test Chip II 158
C.4 Test Chip III 159
C.5 Test Chip IV 160

References **163**

List of Figures

1.1 2015-2021 MEMS and sensors market projection, image reproduced with permission of the rights holder, Yole Développement [20]. . . . 3

1.2 (a) The lumped-parameter model of one resonant structure, and (b) its frequency responses of displacement (magnitude and phase) in different damping conditions. 4

1.3 The spring-mass model of two coupled systems and their individual frequency responses of displacement. 12

1.4 Four commonly used coupling methods: (a) electrostatic coupling [60], (b) magnetic coupling [61], (c) mechanical coupling [62] and (d) parasitic coupling [58]. 13

1.5 An array of four coupled microcantilevers for single-input-single-output multi-sensing, image reproduced from [65], with the permission of AIP Publishing. 14

1.6 (a) The scanning electron microscope (SEM) image of two coupled gold-foil cantilevers fabricated by Spletzer *et al.* and (b) the measured sensitivities of eigenvalues and eigenvectors, images reproduced from [73], with the permission of AIP Publishing. 16

1.7 The relationship between sensitivity, characterisation and process variation. 18

2.1 An array of n nearest-neighbour coupled resonators. 24

2.2 The ratios of the average eigenvector sensitivity $|\partial\mathbf{x}/\mathbf{x}|$ to the average eigenvalue sensitivity $|\partial\lambda/\lambda|$ for different numbers of resonators, assuming $\kappa = 1\%$. 29

2.3 The ratios of the average eigenvector sensitivity $|\partial\mathbf{x}/\mathbf{x}|$ to the average eigenvalue sensitivity $|\partial\lambda/\lambda|$ for different coupling ratios, assuming $n = 10$. 30

2.4 Perturbation mechanisms of two IEA approaches: the old method changes the stiffness (or mass) of one resonator, while the new method couples a new element to the array. 40

2.5 Amplitude responses of the first resonator before perturbing the terminal element (solid line), after perturbing the terminal element (dashed line) and after coupling an additional resonator (dash-dot line). 42
2.6 Monte Carlo analysis of the spread in the extracted terminal element when a 1Hz standard deviation Gaussian noise is added to the measurement. 44
2.7 Percentage errors of the derived system matrix for different noise levels and different numbers of resonators (before correction). 45
2.8 Percentage errors of the derived system matrix for different noise levels and different numbers of resonators (after correction). 46
2.9 Percentage errors of the old method for different perturbation values, assuming 1Hz standard deviation noise. 47
2.10 Percentage errors of the new method for different resonant frequencies of the additional resonator, assuming 1Hz standard deviation noise. 47

3.1 Simulated frequency responses from (a) resonator 1 and (b) resonator 2 under different stiffness perturbations. (c) Sensitivity analysis of eigenvalues at both modes. 54
3.2 The sensitivity of using the mean of two eigenvalues as a sensing metric. 55
3.3 Relative changes of 4 eigenvalue sensing metrics under different stiffness perturbations for (a) 1% coupling and (b) 10% coupling. . 56
3.4 Eigenvector changes under different stiffness perturbations for (a) 10% coupling and (b) 5% coupling. 58
3.5 Using Monte Carlo analysis and analytical expressions to determine the relative errors of the first eigenvector ($v_1 = x_{1,1}/x_{2,1}$) under different perturbations and coupling ratios. 63
3.6 The relative errors of extracted (a) stiffness k and (b) stiffness change Δk under different perturbations and coupling ratios. 65
3.7 Monte Carlo analysis for the relative errors of k_1, k_2 and k_c under different eigenfrequency errors ($\kappa = 0.25\%$, $\Delta k/k = 1\%$). 66

4.1 (a) A comb structure MEMS resonator and (b) the geometry of opposing fingers. 70
4.2 SEM images of the comb structure sensor: (a) single resonator, (b) two rows of opposing comb fingers and (c) an array of two coupled resonators. 71
4.3 The circuit for generating a differential pair of driving signals. . . . 73
4.4 A constant voltage readout circuit using a transimpedance amplifier. 74

4.5 The full readout circuit using two transimpedance amplifiers and one instrumentation amplifier. 74
4.6 Test environment using a vacuum pump. 77
4.7 Schematic of the Tow-Thomas biquad filter used as an electrical resonator. 79
4.8 (a) SEM of two mechanically coupled MEMS resonators and (b) typical frequency responses of both resonators. E1 and E2 denote the first and second eigen-mode. 80
4.9 The effect of quality factor mismatch between the electrical and mechanical resonators. 81
4.10 Coupling and actuation circuits for the new coupled systems: (a) schematic diagram and (b) electrical circuit board. 82
4.11 Total frequency shift after coupling an additional electrical resonator with different resonant frequencies to an array of two MEMS resonators. 83
4.12 Simulated responses from electrical and mechanical resonators before and after coupling. 84
4.13 Experimentally measured responses from electrical and mechanical resonators after coupling. 85
4.14 Measured responses of the electrical resonator and the mechanical resonator before and after a perturbation upon the centre frequency of the electrical resonator. 87
4.15 The effect of device mismatch on eigenfrequency and eigenvector sensitivities, assuming under 1% perturbation. 88
4.16 Designed and characterised sensitivities of (a) eigenfrequencies and (b) eigenvectors under different perturbations. 90
4.17 SEM images of (a) resonator comb structure and (b) coupling string. (c) Sensitivity errors of eigenfrequency and eigenvector methods caused by spring constant variations. 91
4.18 Sensitivity tuning by changing the centre frequency of the electrical resonator. 94

5.1 The three lowest modes of a resonant plate under free flexural vibration. 100
5.2 Electrical connections for one centre-stemmed plate resonator. . . . 102
5.3 Actuating the capacitive resonator with a transimpedance amplifier. 103
5.4 A simplified pull-in model using two parallel plates. 104
5.5 In-phase and anti-phase resonant modes of two coupled square plate resonators. 107
5.6 (a) The geometry of coupled square plate resonators and (b) simulated coupling ratios for different beam lengths and widths. 108

5.7 (a) Cross-sectional view of all layers of PolyMUMPs (courtesy of MEMSCAP). (b) Layers used for the proposed design and their dimensions. 108
5.8 Layout of an example of two corner coupled square plate resonators. 109
5.9 FEM simulation of the static displacement under various DC voltages. 112
5.10 Experimental setup: (a) drive and readout PCB with rubber ring to seal the device under a vacuum pump; (b) SEM image of a single square plate resonator and test arrangement for the impedance analyser. 112
5.11 Experimental characterisation of a single resonator: (a) conductance and phase responses of a single resonator, (b) quality factor under different pressures and (c) square root of the electrostatic stiffness as a linear function of DC bias voltage. The inset shows the breakdown of a resonator due to pull-in. 113
5.12 Over-sizing effect of the plate side length. 114
5.13 Two coupled micro mechanical systems based on different perturbation channels: design (a) has full DC voltage control and readout for all elements, while (b) connects the first four resonators and perturbs the terminal element only. Each five-element array takes up a total size of approximately 920μm $\times$ 330 μm excluding the bond pads. . 116
5.14 Frequency responses of the shunt conductance measured from the first four elements using the second design before and after terminal perturbation. 117
5.15 Decoupling the terminal resonator by applying a pull-in voltage to the terminal unit. 118

6.1 Amplitude responses of an array of three coupled resonators under different damping ratios and coupling strengths. 122
6.2 Percentage errors of the diagonal elements in the system matrix under different damping ratios for coupled arrays of three, five and ten resonators ($\kappa = 5\%$). 123
6.3 Percentage errors of the diagonal elements in the system matrix under different effective quality factors for coupled arrays of three, five and ten resonators ($\kappa = 5\%$). 124
6.4 Eigen-modes of five corner coupled square plate resonators and the spring-mass model. 126
6.5 Simulated frequency responses of five coupled resonators when there is (a) no mismatch and (b) 1% frequency variation, under both the single and multiple actuation schemes. 127
6.6 Measured frequency responses of a fabricated array of five corner coupled square plate MEMS resonators using both actuation schemes. 129

6.7 The interweaving condition for de Boor and Golub's algorithm, observed from the frequency responses of seven coupled resonators before and after pull-in of the terminal element. 130
6.8 The shifts of eigenvalues after changing the perturbation voltage of the terminal resonator. 131
6.9 Failure of an array of fifty coupled square plate MEMS resonators caused by fabrication error in one resonant unit. 133
6.10 Complexity of the previous eigenvector extraction algorithm and the new linearised algorithm for different numbers of coupled resonators. 134
6.11 Sensing errors of the linearised algorithm for extracting (a) diagonal elements and (b) off-diagonal elements. 135
6.12 The frequency response of twenty corner coupled square plate MEMS resonators. 136
6.13 Extracted *uncoupled* natural frequency, stiffness and mass of all twenty resonators using the linearised eigen-sensing method and the previous algorithm. 137

7.1 Contaminations of fabricated chips resulting from photoresist residue. 142
7.2 Schematic of a Tow Thomas oscillator. 143
7.3 (a) Output from the oscillator in the time domain and (b) FFT analysis of the time domain signal. 144

C.1 Full layout for the square plate MEMS resonators. 157
C.2 Bonding diagrams for the four test chips. 158

List of Tables

2.1 Different algorithms to extract the system matrix. 48

4.1 Typical parameters for the drive and readout circuits. 77
4.2 Designed and characterised performance of the device. 91
4.3 Eigenvector and eigenvalue changes after 0.1% perturbation on the first MEMS resonator. 93
4.4 Eigenvector and eigenvalue changes after 0.1% perturbation on the second MEMS resonator. 93

5.1 Designed parameters of the proposed corner coupled square plate MEMS resonator array. 110

6.1 Normalised resonant magnitudes of five coupled resonators at five modes. 127

C.1 Electrical connections for test chip I. 159
C.2 Electrical connections for test chip II. 160
C.3 Electrical connections for test chip III. 161
C.4 Electrical connections for test chip IV. 162

I feel a little bit like the Wright brothers, who were flying 100 years ago for the first time and then people were saying "why do we need a flying machine?" And now we have a Boeing 747 and an Airbus.

— Bernard L. Feringa

1 Introduction

Contents

1.1 Micro/Nano Electromechanical Systems 1
1.2 Micro/Nano Resonators 2
1.2.1 Background 3
1.2.2 Resonators as Sensors 4
1.2.3 Frequency Shift 6
1.2.4 Resonator Array 8
1.3 Challenges 9
1.3.1 Connectivity 9
1.3.2 Process Variability 10
1.4 Coupled Resonators 11
1.4.1 Coupling 11
1.4.2 Multiplexed Actuation 14
1.4.3 Device and Process Characterisation 15
1.4.4 Emerging Applications 15
1.5 Objectives and Thesis Outline 18
1.5.1 Objectives 19
1.5.2 Thesis Outline 19

1.1 Micro/Nano Electromechanical Systems

In 1959, the famous talk "There's Plenty of Room at the Bottom" delivered by physicist Richard Feynman addressed the potential of manipulating atoms to establish nanoscale machines and hence blazed the trail for top-down nanotechnology

[11]. Since then a myriad of researchers have been diverted to this new and exciting field, including the 2016 Nobel Prize winners Jean-Pierre Sauvage, Sir J. Fraser Stoddart and Bernard L. Feringa, who have been recognised for the design and synthesis of molecular machines [12–14].

From ink-jet printers to smart phone sensors, the ubiquitous presence of these very small machines stems from the rise of micro/nano electromechanical systems (M/NEMS). M/NEMS is the technology that utilises the electrical and mechanical properties of miniaturised machines or systems. Based on the similar semiconductor processes such as deposition, lithography and etching, M/NEMS devices can be fabricated with a feature size ranging from millimetre towards nanometre. In the past few decades, the rapid development of micro/nano fabrication techniques, including bulk micromachining, surface micromachining and high aspect ratio silicon micromachining, has paved the way for the shrinking of M/NEMS sensors, actuators, motors and microfluidic systems [15–17]. A vast variety of these devices, such as pressure sensors, microphones and radio frequency (RF) filters, are now commercially available and transforming our daily life in medical, industrial and automotive applications [9, 18, 19]. A recent report released by Yole Développement, a "More than Moore" market research and strategy consulting company, projects that the market revenue of MEMS would reach $20 billion by the year 2021, with a trend shown in Figure 1.1 [20]. M/NEMS is an interdisciplinary subject straddling assorted research fields, including microelectronics, mechanical engineering, nanotechnology and biomedical engineering, therefore spurring more groundbreaking innovations yet to be unveiled.

1.2 Micro/Nano Resonators

There are an assortment of micro/nano electromechanical systems available, such as inertial, electrostatic and magnetic structures with dimensions from nanometre to micrometre. Of these, the majority operate as resonators. M/NEMS resonators are small electromechanical structures that vibrate at high frequencies. Micro/Nano resonators have been widely applied as inertial sensors, ultrasound transducers

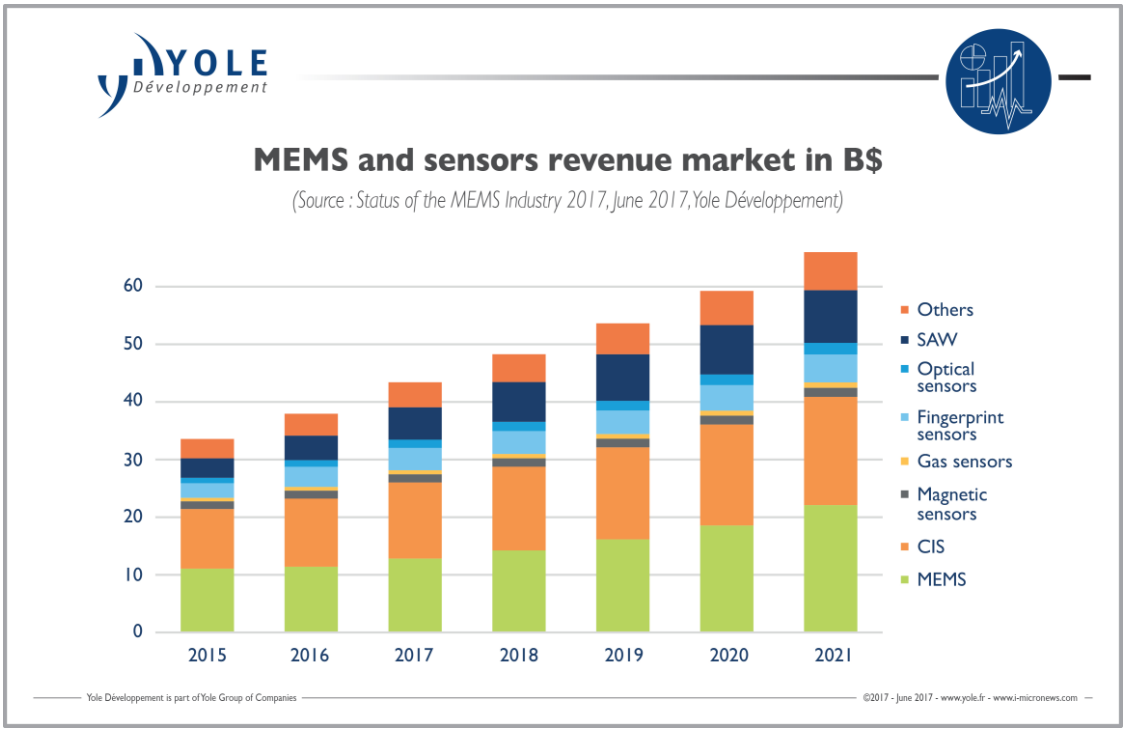


Figure 1.1: 2015-2021 MEMS and sensors market projection, image reproduced with permission of the rights holder, Yole Développement [20].

and RF filters. These resonators can also be used to build MEMS oscillators by integrating them with electronic circuits (e.g. sustaining amplifiers), hence providing stable and adjustable output frequencies. The understanding of a resonating system is critical for MEMS design. Therefore, resonators will be further explored in this section.

1.2.1 Background

The micro/nano resonator has played an indispensable role throughout the development of MEMS. The resonant gate transistor, which was fabricated by Nathanson *et al.* in the 1960s, was one of the earliest attempts [21]. Nathanson *et al.* incorporated vibrating beams into integrated circuits (ICs) to enhance the frequency selection, hence breaking the barrier between electrical and mechanical components. Inspired by the work, scientists later developed new applications, including pressure transducers and frequency synthesisers, which turned out to be commercially successful in the 1970s and 1980s [22]. From the 1990s, advancing fabrication

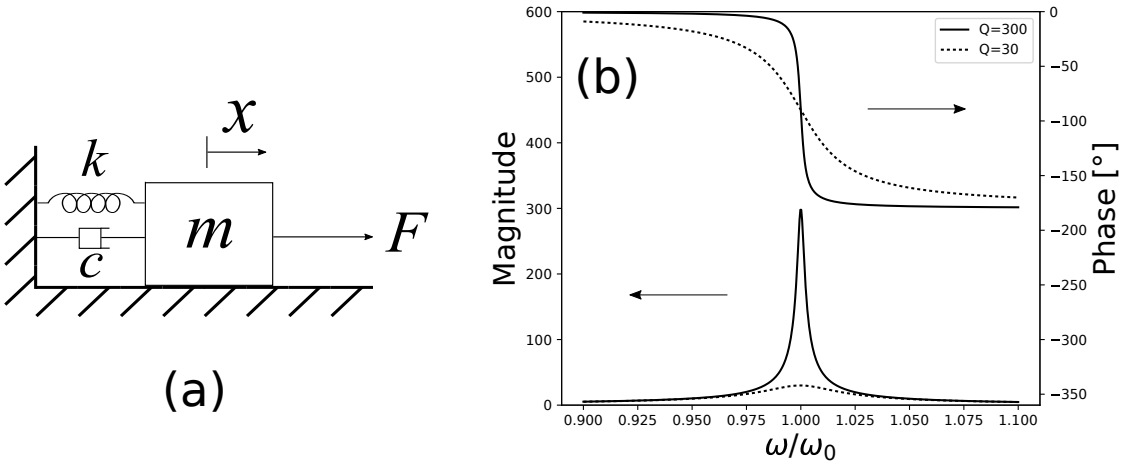


Figure 1.2: (a) The lumped-parameter model of one resonant structure, and (b) its frequency responses of displacement (magnitude and phase) in different damping conditions.

technologies enabled the batch production of MEMS products at lower cost. These included accelerometers, micromirrors and microphones. Nowadays, the family of MEMS has become more diversified. Micro/Nano resonators are being constantly used in optical [23], RF [24], and lab-on-a-chip [25] applications.

1.2.2 Resonators as Sensors

There are different types of resonator structures, including cantilever, fixed-fixed beam, double-ended-tuning-fork (DETF), diaphragm, ring shape disk resonator and interdigitated comb structures [26]. These resonators can be driven by electrostatic force, magnetic field, inverse piezoelectric effect, resistive heating or laser thermal stress. Their motion can be monitored either directly or indirectly, using capacitive, optical, piezoelectric or magnetic readout schemes [27].

One important characteristic of a mechanical resonator is its resonance. Mechanical resonance is the phenomenon of a mechanical system to respond at larger magnitude when the frequency of its vibration is equal or very close to the system's natural frequency. The frequency at which the magnitude is a relative maximum is defined as the resonance or resonant frequency.

Figure 1.2(a) shows the lumped-parameter model of a M/NEMS resonator represented by a mass-spring mechanical system, where k is the stiffness, m is the

effective mass and c is the damping. An external driving force F is applied to the mass. The mechanical displacement x has a maximum magnitude at the resonant frequency. Figure 1.2(b) shows the typical magnitude and phase responses of the system under various driving frequencies. Notably, it is also possible to find the resonance through phase tracking, which declines by 90° at ω_0, and eventually flips by 180° when increasing the frequency further. For an undamped system, the resonant frequency matches the system's natural frequency ω_0, which is given by

$$\omega_0 = \frac{k}{m} \tag{1.1}$$

To understand the resonator's motion when there is damping, one can apply Newton's second law. In Figure 1.2(a), the mechanical displacement x as a function of the time t can be modelled by a second order differential equation:

$$F - kx - c\dot{x} = m\ddot{x} \tag{1.2}$$

which leads to the following equation:

$$\ddot{x} + \frac{c}{m}\dot{x} + \frac{k}{m}x = \frac{F}{m} \tag{1.3}$$

The quality factor Q is associated with the damping c as

$$Q = \frac{m\omega_0}{c} \tag{1.4}$$

The quality factor represents the extent of the under-damp. As can be seen in Figure 1.2(b), a higher Q tends to sharpen the magnitude peak and steepen the fall of the phase response.

The precise definition of the quality factor Q is the ratio of the energy stored to the energy dissipated over one radian of the oscillation [28]. In practice, it can be determined using the frequency-to-bandwidth ratio:

$$Q = \frac{\omega_0}{\omega_H - \omega_L} \tag{1.5}$$

where ω_H and ω_L are the high and low cut-off frequencies where the power is half the maximum value. Alternatively, Q can be measured in the time domain

using a ring-down approach that calculates how many cycles it takes for an initial oscillation to die down [29].

In the frequency domain, the transfer function is defined as the ratio between the frequency-dependent amplitude $X(j\omega)$ and mass-normalised driving force:

$$H(j\omega) = \frac{X(j\omega)}{F(j\omega)/m} = \frac{1}{\omega_0^2 - \omega^2 + j\omega\omega_0/Q} \tag{1.6}$$

The magnitude $|H(j\omega)|$ and phase φ of the transfer function are given by

$$|H(j\omega)| = \frac{1}{\sqrt{(\omega_0^2 - \omega^2)^2 + (\omega\omega_0/Q)^2}} \tag{1.7}$$

$$\varphi = -\arctan\left(\frac{1}{Q} \cdot \frac{\omega/\omega_0}{1 - (\omega/\omega_0)^2}\right) \tag{1.8}$$

It can be seen that the quality factor is a key metric for resonator performance and disparate values are required for certain applications. According to the magnitude transfer function, the actual resonance frequency is always smaller than the natural frequency ω_0 due to damping:

$$\omega_0' = \sqrt{1 - \frac{1}{2Q}}\omega_0 \tag{1.9}$$

where ω_0' is the damped resonance frequency. It is worth noting that the above analysis is based on an ideal linear time-invariant (LTI) system with single degree-of-freedom (DOF).

1.2.3 Frequency Shift

As the natural frequency is dependent on the mass and stiffness, one can potentially use the frequency shift for sensing. When there is a shift in mass (Δm) or stiffness (Δk), the natural frequency changes proportionally:

$$\frac{\Delta\omega_0}{\omega_0} = \frac{\Delta k}{2k} \tag{1.10}$$

$$\frac{\Delta\omega_0}{\omega_0} = -\frac{\Delta m}{2m} \tag{1.11}$$

A mass change caused by adsorbed analytes such as viruses or molecules can therefore be measured. Force, acceleration or pressure sensing would follow a similar

fashion: the bending of the resonator results in a stiffness perturbation, which is subsequently translated into a frequency shift. By manufacturing smaller sensors at higher frequencies, their responsivity can be improved. For example, Chaste *et al.* have pushed down the minimum resolvable mass towards the range of yoctogram (10^{-24}g) using a 150nm long carbon nanotube that resonates at 2GHz [30].

In addition, the sensitivity can be improved by enabling a higher quality factor Q. This increases the gradient of the amplitude change around the resonance. Sensors with a Q ranging from 10^3 up to 10^6 have been extensively reported [31]. Besides sensing, a high Q is desired for various applications. For energy harvesting, it enhances the efficiency of the generator by reducing the mechanical loss [32]. Funasaka *et al.* reported a high-Q $LiNbO_3$ piezoelectric plate with 78% generation efficiency [33]. In communication applications, RF MEMS devices with high-Q and tunable properties are needed to fit in with multi-band systems and suppress undesired signals [34]. Micromachined ultrasound transducers, however, provide a different scenario. On the one hand, a lower Q means a higher bandwidth and hence expands the detection range for different ultrasonic wavelengths. On the other hand, it diminishes the conversion rate between electrical power to mechanical motion, and eventually results in acoustic energy loss [35]. Moreover, it impedes the detection sensitivity of the receiver.

There are several ways of tuning the quality factor. Intuitively, one can minimise the influence of surrounding air and liquid by changing the pressure level. Additionally, by understanding the damping mechanisms such as structure imbalance, internal material loss and thermal-elastic loss, appropriate MEMS designs and alternative materials can be employed to avert these damping losses. Chandorkar *et al.* proposed an improved anchor design and the use of silicon carbide for bulk MEMS resonators, resulting in one order of magnitude higher Q when compared with quartz [36]. The effective quality factor can also be adjusted electronically by implementing a feedback control signal added to the driving force in Equation 1.3 to counteract the damping term $\dot{x}$ on the left hand side of the equation. Such a feedback control mechanism has been developed by several researchers

to alter the effective quality factor of cantilever structures used for atomic force microscopy (AFM) [37] and to tweak the performance of biological detectors [38].

1.2.4 Resonator Array

Thus far, a single resonating system has been explored. In addition to a single resonator, arrays of micro/nano resonators have been investigated in exploding literature to unlock the full potential of individual MEMS sensors and build a real-world micro-analytical tool [39]. Fabricating more than one sensor on the same substrate has been made possible by the rapid progression of micro/nano fabrication technologies. Integrating a mass of micro/nano resonators on the same chip not only lessens the cost per unit, but also upgrades the performance. They provide a whole new universe of sensing, giving the green light to ultra-sensitive and multi-target detection of various biomarkers [40]. Additionally, resonator arrays provide timely and label-free identification of chemical substances using a direct sample (e.g. blood serum), hence avoiding the need for preconditioning [41]. Large-scale micro/nano resonators with a density of up to 10^5 nanostructures/cm^2 have been reported for multi-function or multi degree-of-freedom applications [42, 43]. Bargatin *et al.* fabricated thousands of resonators on the same die to withstand >1W input power while maintaining a detection capability of parts per billion (ppb) within a short time period of 2s [44].

Aside from sensing, arrays of resonators are widely seen in other fields. For ultrasonic applications, transducers are arranged in a particular pattern to allow flexible beam forming or steering [45]. For energy harvesting, they provide enhanced efficiency and power handling strength [46]. It is beyond doubt that the array configuration has significantly enhanced the performance of M/NEMS resonators. However, compared with a single resonator, resonator arrays are confronted with new challenges, which will be studied next.

1.3 Challenges

Like the scaling of microelectronics, miniature resonator arrays are faced with a similar connectivity issue and process variation. Accessing individual sensors and monitoring their behaviour are becoming increasingly challenging. With more uncertainty in process variability, such as device mismatch, the sensitivity of these micro/nano arrays has to be characterised and calibrated, thereby introducing extra cost and efforts. Hence, it is crucial to find a simple way of actuating and characterising these massive resonator arrays.

1.3.1 Connectivity

For an array of $n \times n$ resonating sensors, one needs n^2 sets of drive/readout bond pads to interface to the device. However, the size of a pad is subject to wire bonding, and is typically greater than 100μm $\times$ 100μm [47]. Given that the dimensions of a resonator are scalable to below a few microns, a substantial amount of the precious fabrication space is allocated to these bond pads [48]. In addition, wire bonding and routing can become complicated as there are an increasing number of interconnections. There is also a need for additional hardware to separate different channels and process readout signals.

To enhance the connectivity in a resonator array, Chee *et al.* proposed a top orthogonal to bottom electrode transducer architecture to actuate a single element in an $n \times n$ array, which biases one column at a time and transmits/receives signals from rows [49]. This column-by-column addressing technique has reduced the contact count from n^2 to $2n$, albeit at a slower speed. Other interfacing techniques, including optical/magnetomotive approaches, have been reported to readout resonator arrays [50–52]. These methods require extreme conditions such as a strong magnetic field and are hence impractical to implement. Furthermore, the optical/magnetic modules are incompatible with standardised MEMS fabrication.

1.3.2 Process Variability

Micro/Nano mechanical arrays often require a chain of identical resonators that are prudently designed. However, any nano/micro manufacturing has process variations across a die and over time. Hence, it is almost impossible to obtain two or more identical resonators on a die. In addition, it is also very difficult, if not impossible, to fabricate resonators with parameters identical to the designed values due to variations in the fabrication processes. Process-induced variability, which could arise from environmental factors and lithography/etching errors, is known to deteriorate sensor performance, reduce yield, and add extra testing cost [53]. With one resonator per chip, one would only expect an absolute error between the designed and fabricated values of parameters, thereby typically leading to a shift of the resultant sensitivity as well as operating frequency. Such shifts can be measured and the sensors can be calibrated for them. However, in case of more than one resonator per die, relative variations between individual resonators also become vital and will affect the sensitivity. Furthermore, it may be possible to minimise the absolute error by considering process errors while designing a resonator. However, process variability data are rarely available from current micro/nano electromechanical processes. This is unlike the classical microelectronic processes, wherein transistor variations are well studied and recorded for individual processes. Therefore, process variation and its effects on sensor performance have received limited attention in the community, particularly for nanoelectronic devices. However, these devices share a similar process flow to that of microelectronic devices and therefore, should suffer from similar manufacturing variations.

One way of enhancing testability is to optimise MEMS by taking into account the presence of variability early in the design process. As an example, Xu and Tsai fabricated a 32kHz frequency-drift resilient micro resonator by balancing the ratio between the spring constant and effective mass through proper design of the supported springs and release holes [54]. This method, however, does not eliminate device mismatch, even if two resonators are fabricated on the same wafer with the identical shape and geometry. An alternative method is to test MEMS

devices at the wafer level and predict their performance at the package level [53]. Therefore, it is important to regularly monitor these fabricated devices or test structures included on the wafer.

1.4 Coupled Resonators

Coupled micro/nano mechanical resonators have been suggested to tackle both the connectivity and process variation problems by enabling multiplexed actuation and characterisation capabilities. In addition, the collective behaviour of coupled systems has been explored by expanding research efforts to further enhance their sensitivity and functionality [55–57]. These coupled systems can be modelled as an eigenvalue problem, which reveals new sensing opportunities using their eigen-information or mode-localisation.

1.4.1 Coupling

Coupling is typically an unwanted phenomenon first seen in micro/nano cantilever arrays, which interferes and corrupts the output signal. This is caused by the natural overhang structure that introduces parasitic crosstalk between neighbouring elements [58]. Recently, researchers started to realise that coupling could provide additional information about the array as well as novel sensing methods [59].

Coupled systems can exhibit a collective behaviour distinct from that of a classic single resonator. To appreciate this, one may consider a simple case of two coupled elements, which can be modelled by the spring-mass model in Figure 1.3. k_1 and k_2 are the stiffness of the two resonators, whereas m_1 and m_2 are their respective masses. k_c is the spring constant of the coupling string connecting two resonators. x_1 and x_2 are the displacement of each resonator and F is the driving force applied to one resonator. The force and displacement are restricted to the horizontal direction. One can see the frequency responses of both resonators are different from what is depicted in Figure 1.3 for a single uncoupled resonator. Coupling enables collective resonances at two frequencies f_1 and f_2. For undamped systems, these resonant frequencies correspond to the first and second eigen-mode

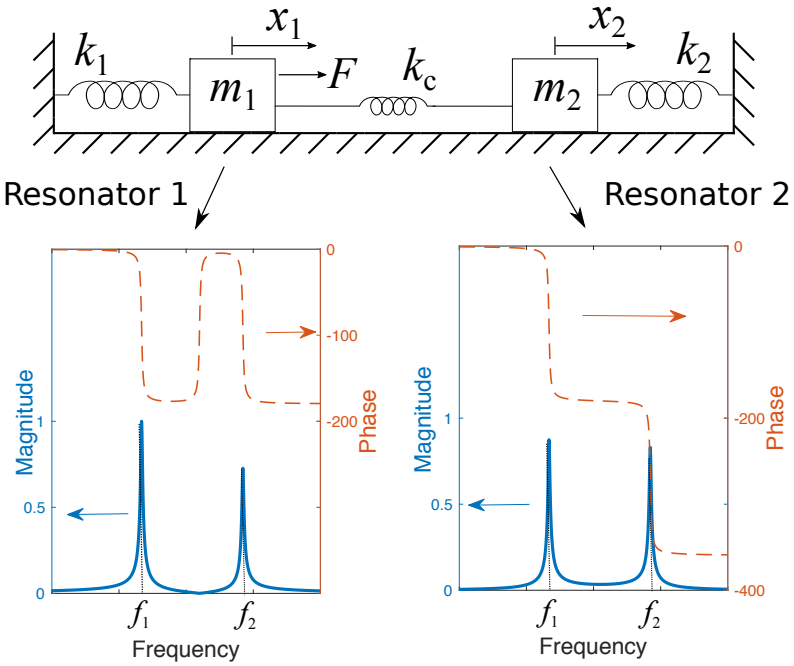


Figure 1.3: The spring-mass model of two coupled systems and their individual frequency responses of displacement.

respectively. Their values are shifted from the uncoupled natural frequency of any one resonator due to the coupling effect. The collective resonance is in-phase at the first mode, whereas there is a 180° phase difference at the second mode. This means both resonators vibrate towards the same direction at the first resonance, but against each other at the second mode.

There are various coupling mechanisms to provide either weak ($k_c \ll k$) or strong ($k_c \gg k$) coupling depending on the application. The coupling ratio κ is defined as the ratio between the coupling strength and the stiffness:

$$\kappa = \frac{k_c}{k} \tag{1.12}$$

There is no strict boundary for κ to distinguish between a weak and strong coupling, although some researchers suggest 10% as a threshold based on the interaction and separation between different modes [63]. Weak coupling is typically used for amplitude-based sensing. However, Hajhashemi and Bahreyni showed the feasibility of strong coupling ($\kappa \gg 10\%$) for the frequency-shift approach [64]. Hence, proper selection of the coupling ratio is a primary concern when building the coupled devices.

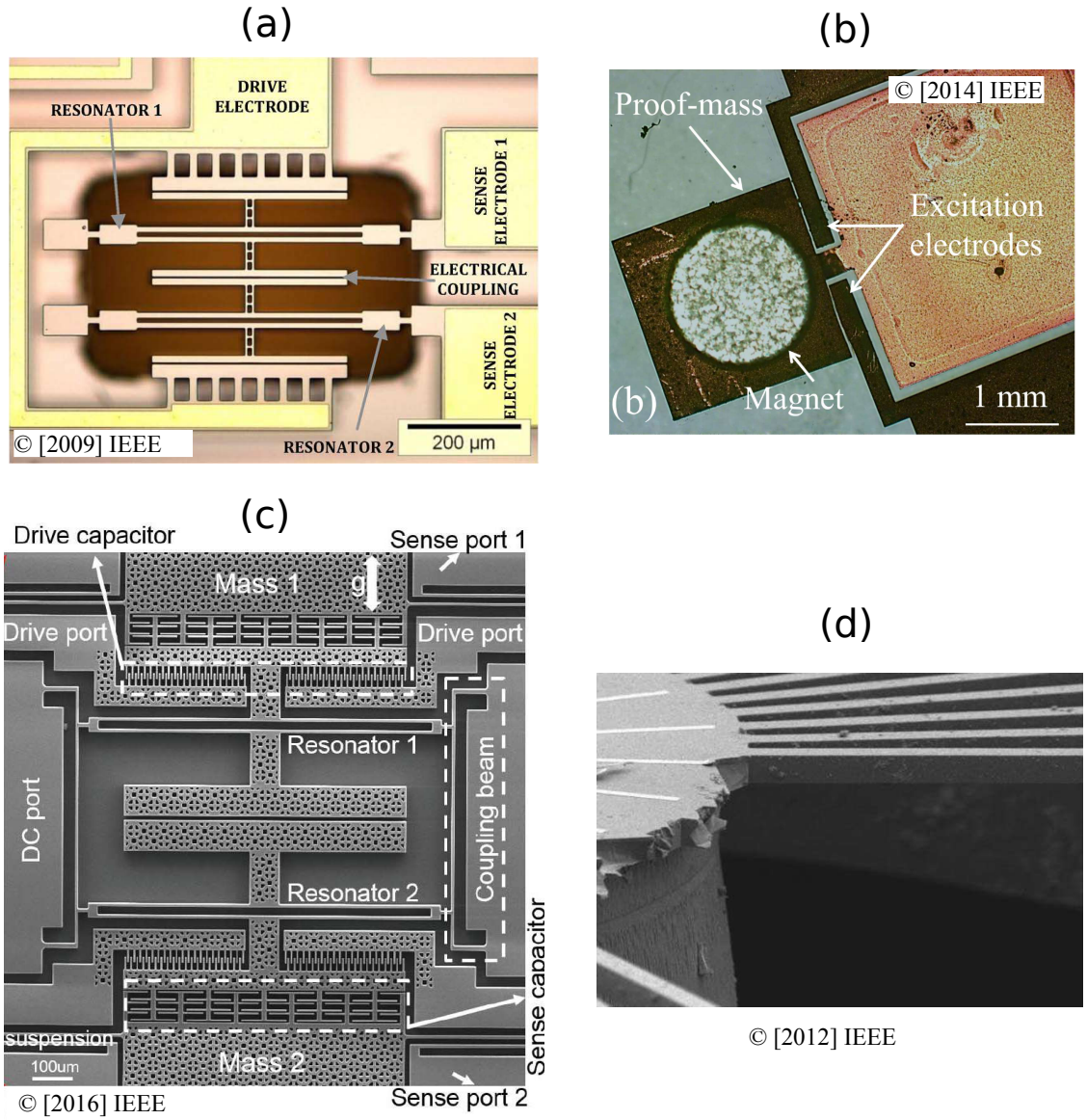


Figure 1.4: Four commonly used coupling methods: (a) electrostatic coupling [60], (b) magnetic coupling [61], (c) mechanical coupling [62] and (d) parasitic coupling [58].

Micro/Nano mechanical resonators can be coupled through different mechanisms. Commonly used methods include electrostatic coupling [60], magnetic coupling [61], mechanical coupling [62] and electromechanical coupling [4]. The images in Figure 1.4 depict four state-of-the-art examples of coupled systems using some of these approaches. Generally speaking, a coupling string is very small in size compared with the sensor itself, but has profound implications for sensitivity [60]. It is more vulnerable to process error, hence the design needs to be optimised. Coupling offers several advantages, which will be examined next.

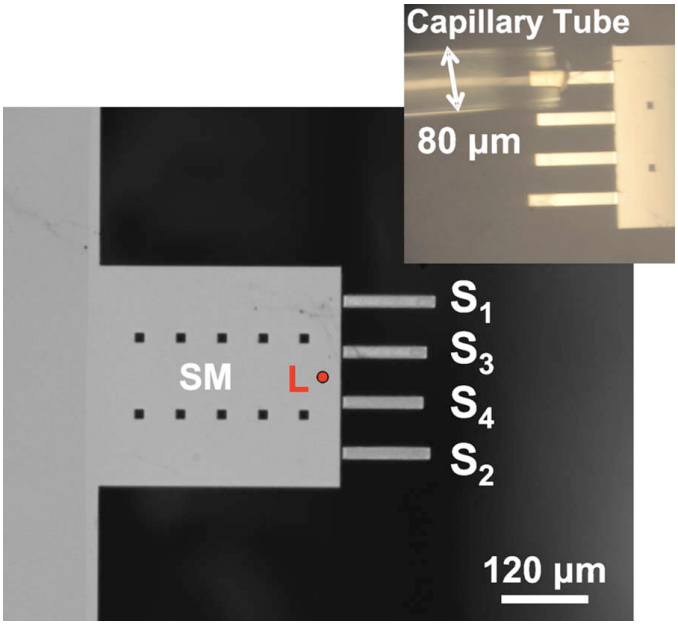


Figure 1.5: An array of four coupled microcantilevers for single-input-single-output multi-sensing, image reproduced from [65], with the permission of AIP Publishing.

1.4.2 Multiplexed Actuation

One advantage of coupling lies in the single-input-single-output (SISO) actuation scheme to perform multi-sensing. The SISO scheme uses a single sensor input and a single measurement readout to detect all the shifted modes in a coupled array of resonators. DeMartini *et al.* adopted an array of four coupled cantilevers to sense different chemicals at the same time with high selectivity [65]. These microcantilevers permit multi-analyte detection and identification by recording the frequencies at four resonances. A prototype sensor is shown in Figure 1.5. The novelty of this work lies in the functionalisation of the microbeams using different polymers and solvents, which distinguish toluene and methanol solvents based on the unique behaviour of four eigen-modes. These coupled resonators can potentially turn into a SISO multiplexed array of sensors, hence saving the space normally used for connection wires, bond pads, and readout channels, and reducing the bandwidth required for signal processing. This can be lucrative as these bond pads can take up the highest percentage of the fabrication areas. Ideally, for any number of coupled resonators, only one set of drive and readout connections are needed, which allows the sensor fill factor to substantially increase.

Another advantage of coupled resonators is their enhanced power handling and band tuning capabilities. Demirci and Nguyen coupled seven polysilicon square plate resonators and decreased their series motion resistance by 5.9× [66]. Coupled resonators have also been applied to boost the efficiency of energy scavenging at various frequencies, thereby making the device usable in different situations [67]. In the MEMS industry, SiTime developed an oscillator based on coupled DualMEMS Architecture on the same die to compensate for temperature [68], offering frequencies from 1MHz up to 700MHz with a stability of 100ppb.

1.4.3 Device and Process Characterisation

The SISO actuation scheme also facilitates sensor testing using inverse eigenvalue analysis (IEA), a deterministic approach for device/process characterisation suggested by Choubey *et al.* [69]. The method combines inverse problem theory and perturbation analysis to investigate the collective behaviour of coupled resonator arrays, and hence extracts the system matrix. The technique was successfully employed to sense the mass normalised stiffness and coupling ratio of an array of five coupled resonators by recording all the collective resonant frequencies [70]. Beyond that, IEA has found broad applications in the fields of process monitoring, sensitivity analysis and material characterisation [6, 8, 71]. Choubey *et al.* determined the Young's modulus of single-crystal silicon in different orientations within 1% accuracy using an array of seven coupled micro cantilevers [58]. Nevertheless, existing IEA methods are of limited practical benefit since they entail non-linear or destructive perturbation. The array size is also limited to several resonators due to the single actuation readout scheme. Furthermore, the multi-dimensional eigen-information extracted by the IEA has not been fully utilised to address the current sensing limits of coupled micro/nano resonators.

1.4.4 Emerging Applications

Another breakthrough of coupled sensing is its significantly enhanced sensitivity. As opposed to the traditional frequency-shift single resonator, coupled systems offer

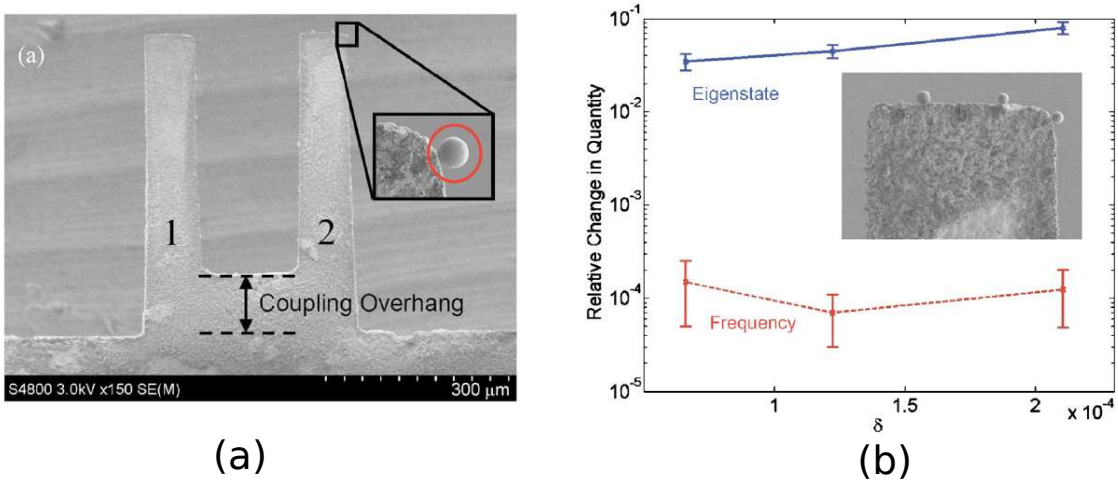


Figure 1.6: (a) The scanning electron microscope (SEM) image of two coupled gold-foil cantilevers fabricated by Spletzer *et al.* and (b) the measured sensitivities of eigenvalues and eigenvectors, images reproduced from [73], with the permission of AIP Publishing.

new eigen-sensing metrics such as eigenvalues, eigenvectors or a combination of both. The eigenvalues are associated with the natural frequencies, or eigenfrequencies, at multiple eigen-modes, while the eigenvectors correspond to the vibration amplitudes of all resonators.

With more than one eigenvalue available in the frequency spectrum, one would expect a most effective mode for sensing. Jin *et al.* improved the mass resolution from 0.17pg to 0.06pg by using a second mode resonant cantilever sensor, which demonstrated a higher quality factor than the first mode [72]. Another sensitivity enhancement approach was proposed by Hajhashemi and Bahreyni, who utilised the relative differences of eigenvalues to achieve a five-fold sensitivity increase in contrast to the single-resonance sensing method [64]. This method is immune to the process variation and device mismatch. It also reduces common mode noises, such as pressure or temperature drift, since the frequency fluctuations cancel each other out in the subtraction.

The amplitude-based eigenvector (or eigenstate) approach was inspired by the famous Anderson mode localisation effect seen in quantum mechanical systems. The approach was first proposed by Spletzer *et al.*, who observed the vibrations of two alike micro cantilevers and compared the amplitude ratio changes with frequency shifts under mass perturbations [73]. Their device is shown in Figure

1.6(a) and their experimental results are recorded in Figure 1.6(b). By comparing the relative changes of the eigenvector and eigenfrequency, it is evident that amplitude-based eigenvector sensing can boost the sensitivity by more than two orders of magnitude. In addition, the eigenvector method is exempted from common mode interference. Thiruvenkatanathan *et al.* confirmed this feature by performing both temperature and pressure tests on coupled resonators. Their results indicate that the environmental drift resilience of the eigenvector is one order of magnitude higher than that of the eigenvalue [74]. The reasons for the sensitivity enhancement and common mode noise rejection capabilities of the eigenvector approach will be further examined in Chapter 2 using mathematical analysis.

The eigenvector method has opened a new door for a broad range of sensing applications including mass sensor, accelerometer, electrometer and force sensor. Femtogram resolution has been reached by an eigenvector-based mass sensor using coupled twin cantilevers, as reported by Gil-Santos *et al.* [75]. Beyond that, Zhang *et al.* utilised two DETF resonators as an accelerometer, reaching a sensitivity (312162ppm/g) that is 302 times higher than the eigenfrequency method [62]. Recently, the eigenvector method has also been used for electrometers, and has advanced the sensing limit to $1.269fC$ [76].

The latest research shows that greater performance is attainable using more than two coupled resonators. Zhao *et al.* have demonstrated that three degree-of-freedom (DOF) coupled systems bring another two orders of magnitude increment in sensitivity compared with the conventional two coupled ones, thus providing a force sensitivity at 4.9×10^6/N [77]. Spletzer *et al.* adopted an array of fifteen coupled cantilevers with one order of magnitude higher sensitivity than the previously reported two coupled cantilevers [51]. Sensor records are being constantly refreshed by this new sensing paradigm.

Both the eigenvalue and eigenvector methods partially exploit the eigen-information available in the frequency domain of coupled systems. Recent efforts have also been geared towards the combination of both methods to provide more effective sensing metrics. For instance, the differential sensing attribute of the eigenvector approach

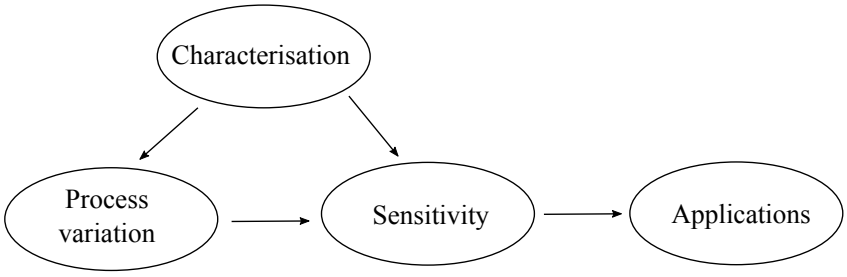


Figure 1.7: The relationship between sensitivity, characterisation and process variation.

can be merged with the common mode sensing capability of the eigenvalue method to accommodate different scenarios. As an example, de Lépinay *et al.* observed the orientation changes of both eigenvalues and eigenvectors to determine the local external force gradient of coupled nanomechanical resonators in two dimensions [78].

In addition to eigenvalue and eigenvector methods, new eigen-sensing approaches are being continuously explored. For instance, a non-linear sensing method using the amplitude difference has been reported to achieve even higher normalised sensitivity than eigenvectors under small perturbations [79, 80]. Zhang *et al.* adopted the algebraic summation of the amplitude ratios at two vibration modes, and therefore enhanced the linear sensing range to full scale [81]. Besides amplitude measurement, the phase difference between mutually injection-locked resonators was monitored by Prache *et al.* to suppress the temperature drift [82]. Furthermore, the anti-resonance Fano peaks of coupled cantilevers were suggested by Stassi *et al.* to increase the quality factor by ten-fold [83]. Without a doubt, these impressive eigen-sensing methods have enriched the applications of coupled mico/nano resonators.

1.5 Objectives and Thesis Outline

Despite the advancements over the past decade, coupled systems remain a field which is still not totally understood. This work aims to study the multi-dimensional eigen-information of coupled micro/nano resonators and exploit their sensing capabilities.

1.5.1 Objectives

The previous sections have devoted to three important aspects of coupled micro/nano electromechanical sensors: sensitivity, characterisation and process variation. Of these, sensitivity attracts most of the research attention, perhaps because it is directly linked to applications [84]. Nevertheless, process variation, which is having an increasing impact on sensitivity, remains relatively unknown to the research community. The flow diagram in Figure 1.7 shows the relationship between these three factors and how they make a joint contribution to eventual applications. Hence, there is a need for a deterministic approach to characterise coupled resonators and the associated fabrication processes, before converting the resonator arrays into chemical or biochemical sensors. The primary objective of this thesis is to develop and implement such a deterministic approach. Another aim is to address the non-linearity and impracticality of the previous IEA techniques by proposing a simple and effective characterisation method with improved accuracy. The analysis will shed light on process-induced sensitivity drift in coupled micro/nano resonators, and how such drift can be compensated for with an electronic trimming circuit. Through theoretical foundations and experimental results, a scalable actuation scheme with enhanced eigenvalue readout will be achieved for scores of coupled MEMS resonators.

1.5.2 Thesis Outline

This work evaluates the collective behaviour of coupled MEMS resonators and their sensing prospects. The thesis starts by introducing resonator-based micro/nano systems and their fundamental theories. A literature review on resonators and the advantages of coupling them are presented, hence revealing the important interactions between sensitivity, sensor characterisation and process variation.

Chapter 2 studies the underlying mathematical models for nearest-neighbour coupled resonators. Physical properties attached to the system matrix, including eigenvalues and eigenvectors, are explained. Stiffness and mass sensitivities of different eigen-sensing metrics are assessed with the forward perturbation theory. The sensing limits, including practical constraints, resolution and dynamic range

of coupled sensors are then investigated. In addition to the forward analysis, the backward problem in such coupled systems is studied using the proposed IEA methods. After explaining inverse Lanczos' algorithm and Gladwell's algorithm, a new IEA technique based on de Boor and Golub's algorithm is devised with an enhanced perturbation mechanism and improved robustness. Finally, Monte Carlo procedures are conducted for the purpose of error analysis.

In Chapter 3, the dynamics of two coupled resonators are modelled. The unique changes of eigenvalues and eigenvectors at two resonant modes are illustrated and dissected. Using IEA algorithms, analytical expressions are derived to showcase the full-parameter extraction capabilities of inverse eigenvalue sensing and are verified by Monte Carlo simulations.

After modelling dual coupled systems, two fabricated comb structure MEMS resonators are characterised in Chapter 4 to implement the old and new IEA methods. By connecting an electrical resonator to the MEMS array, an innovative perturbation approach was proposed in order to find out the sensor's system matrix, which provides vital sensitivity and process information. The chapter also gives insightful remarks on the process-induced sensitivity degradation widely seen in coupled micro/nano resonators.

With the aim of expanding coupled sensing to large systems and enhancing their sensitivity, large arrays of corner coupled square plate micro resonators have been designed and fabricated in Chapter 5. The sensor architecture, electrical connections, manufacturing procedures, electromechanical performance and perturbation mechanisms are described.

Chapter 6 extends inverse eigenvalue sensing to larger arrays using the fabricated square plate MEMS resonators. By bridging the gap between theoretical analysis and empirical research, the potential challenges of scaling are addressed, including damping, mode attenuation, eigenvalue readout and sensing complexity.

Chapter 7 provides the conclusions and future outlook.

There are three appendices: Appendix A and B present the MATLAB code and mathematical proof for the inverse eigenvalue techniques respectively, and Appendix C describes the four test chips used for various experiments.

It has long been an axiom of mine that the little things are infinitely the most important.

— Arthur Conan Doyle

2 Analysis of Coupled Systems

Contents

2.1 Introduction 23
2.2 Eigen-problem in Coupled Systems 24
2.3 Perturbation Theory 27
2.3.1 Mass and Stiffness Change 27
2.3.2 Sensitivity Analysis 28
2.3.3 Differential and Common Mode Responses 31
2.4 Limitations 32
2.4.1 Practical Constraints 33
2.4.2 Resolution 34
2.4.3 Dynamic Range 35
2.5 Inverse Eigenvalue Analysis 36
2.5.1 Known Techniques 37
2.5.2 New Approach 40
2.5.3 Comparison 43
2.5.4 Discussion 48
2.6 Summary 49

A part of this chapter has been published as:

- Guowei Tao and Bhaskar Choubey. "Inverse eigenvalue analysis techniques for coupled M/NEMS resonators". In: *Nano/Micro Engineered and Molecular Systems (NEMS), 2016 IEEE 11th Annual International Conference on.* IEEE. 2016, pp. 217–220

- Guowei Tao and Bhaskar Choubey. "Characterizing coupled MEMS resonators with an electrical resonator". In: *Journal of Physics: Conference Series*. Vol. 757. 1. IOP Publishing. 2016, p. 012017

2.1 Introduction

In the previous chapter, a simple array of two coupled resonators has been presented. In practice, coupled systems often involve large arrays to enable simultaneous detection of various physical quantities. As the array size increases, the systems render new eigen-modes that are mathematically more complicated. However, coupled MEMS resonators bear an analogy to the classic coupled pendulum structure [85], which can be modelled using a tridiagonal system matrix, with the off-diagonal elements being the interaction terms. The coupled systems then turn into an eigenvalue problem. This chapter provides eigenvalue modelling of such systems through forward perturbation analysis and inverse problem theory. The former interprets the physical meanings of the eigen-information available and shows how eigenvalues or eigenvectors could be used as sensing metrics. Key considerations such as sensitivity, resolution and dynamic range will hence be investigated. The backward problem, on the other hand, reveals how the system matrix can be reconstructed using physical observations. The system matrix is important because it carries details about device properties and manufacturing variabilities.

The chapter is organised as follows: first, it states the eigen-problem in coupled systems by modelling an array of nearest-neighbour coupled resonators. Second, forward perturbation is performed to understand the sensitivity. Limitations of practical sensing are then considered. In addition to forward analysis, backward methods based on inverse eigenvalue analysis (IEA) are studied to provide deterministic information about fabricated sensors. A new IEA algorithm is proposed to address the challenges faced by existing techniques.

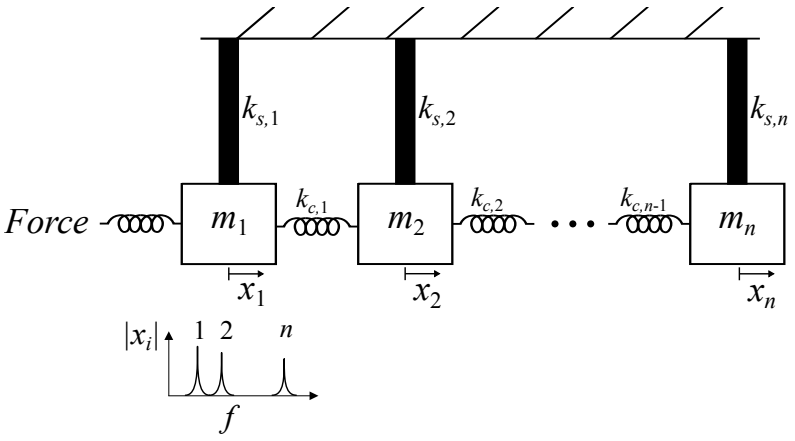


Figure 2.1: An array of n nearest-neighbour coupled resonators.

2.2 Eigen-problem in Coupled Systems

Figure 2.1 shows the mass-spring model of an array of n nearest-neighbour coupled resonators. The motion of such an array can be modelled by an array of n second order differential equations:

$$\begin{aligned}
m_1\ddot{x}_1 + c_1\dot{x}_1 + k_{s,1}x_1 + k_{c,1}(x_1 - x_2) &= F \\
m_2\ddot{x}_2 + c_2\dot{x}_2 + k_{s,2}x_2 + k_{c,1}(x_2 - x_1) + k_{c,2}(x_2 - x_3) &= 0 \\
m_3\ddot{x}_3 + c_3\dot{x}_3 + k_{s,3}x_3 + k_{c,2}(x_3 - x_2) + k_{c,3}(x_3 - x_4) &= 0 \\
&\cdots \\
m_i\ddot{x}_i + c_i\dot{x}_i + k_{s,i}x_i + k_{c,i-1}(x_i - x_{i-1}) + k_{c,i}(x_i - x_{i+1}) &= 0 \\
&\cdots \\
m_n\ddot{x}_n + c_n\dot{x}_n + k_{s,n}x_n + k_{c,n-1}(x_n - x_{n-1}) &= 0
\end{aligned} \tag{2.1}$$

x_i, m_i, $k_{s,i}$ and c_i denote the displacement, mass, stiffness and damping of the ith element. F is the driving force applied to the first element. $k_{c,i}$ is the coupling strength between the ith and $(i+1)$th resonator, which depends on the coupling mechanism.

Equation 2.1 can be rewritten in a matrix form

$$\mathbf{M}\ddot{\mathbf{x}} + \mathbf{C}\dot{\mathbf{x}} + \mathbf{K}\mathbf{x} = \mathbf{F} \tag{2.2}$$

where $\mathbf{x}$ is a column vector containing all x_i, $\mathbf{F}$ is the force vector. $\mathbf{C}$ is the damping matrix. Depending on the coupling method, damping mechanism and

operating environment, the damping matrix can be diagonal [86], tridiagonal [87] or have more complex forms [88, 89].

The mass matrix $\mathbf{M}$ and stiffness matrix $\mathbf{K}$ are

$$\mathbf{M} = \begin{bmatrix} m_1 & 0 & \cdots & 0 \\ 0 & m_2 & \cdots & 0 \\ \vdots & \vdots & \ddots & \vdots \\ 0 & 0 & \cdots & m_n \end{bmatrix} \tag{2.3}$$

$$\mathbf{K} = \begin{bmatrix} k_{s,1} + k_{c,1} & -k_{c,1} & \cdots & 0 \\ -k_{c,1} & k_{s,2} + k_{c,1} + k_{c,2} & \cdots & 0 \\ \vdots & \vdots & \ddots & \vdots \\ 0 & 0 & -k_{c,n-1} & k_{s,n} + k_{c,n-1} \end{bmatrix} \tag{2.4}$$

With the mass and stiffness matrices known, eigenvalue analysis can be performed using the array of differential equations. As micro/nano resonators normally operate under a high quality factor $Q \gg 1$, the damping matrix $\mathbf{C}$ can be ignored to facilitate the eigenvalue problem. There are n eigenfrequencies (natural frequencies) present in the coupled array. With negligible damping, these eigenfrequencies can be represented by the measured resonant frequencies. At the jth mode, the eigenfrequency is ω_j. Then, for each mode, Equation 2.2 is written as

$$-\omega_j^2 \mathbf{M}\mathbf{x_j} + \mathbf{K}\mathbf{x_j} = 0 \tag{2.5}$$

which is equivalent to the form

$$-\omega_j^2 \mathbf{x_j} + \mathbf{M}^{-1/2}\mathbf{K}\mathbf{M}^{1/2}\mathbf{x_j} = 0 \tag{2.6}$$

Herein, $\mathbf{M}^{-1/2}\mathbf{K}\mathbf{M}^{1/2}$ is defined as the system matrix $\mathbf{S_n}$. This form is used because it guarantees a symmetric tridiagonal (Jacobian) matrix [90]. Therefore, the system matrix

$$\mathbf{S_n} = \begin{bmatrix} \frac{k_{s,1}+k_{c,1}}{m_1} & \frac{-k_{c,1}}{\sqrt{m_1 m_2}} & \cdots & 0 \\ \frac{-k_{c,1}}{\sqrt{m_1 m_2}} & \frac{k_{s,2}+k_{c,1}+k_{c,2}}{m_2} & \cdots & 0 \\ \vdots & \vdots & \ddots & \vdots \\ 0 & 0 & \frac{-k_{c,n-1}}{\sqrt{m_{n-1} m_n}} & \frac{k_{s,n}+k_{c,n-1}}{m_n} \end{bmatrix} \tag{2.7}$$

leads to a simplified eigenvalue problem:

$$-\omega_j^2 \mathbf{x_j} + \mathbf{S_n} \mathbf{x_j} = 0 \tag{2.8}$$

which will facilitate the inverse problem in Section 2.5. Each entry of the system matrix $S_n(p,q)$ for $p,q = 1,\cdots,n$ is given by

$$S_n(p,q) = \begin{cases} \frac{k_{s,p}+k_{c,p}}{m_p} & \forall p = q = 1 \\ \frac{k_{s,p}+k_{c,p-1}}{m_p} & \forall p = q = n \\ \frac{k_{s,p}+k_{c,p-1}+k_{c,p}}{m_p} & \forall p = q \neq 1|n \\ \frac{-k_{c,p}}{\sqrt{m_p m_q}} & \forall p = q-1 \\ \frac{-k_{c,p-1}}{\sqrt{m_p m_q}} & \forall p = q+1 \\ 0 & \forall \text{others} \end{cases} \tag{2.9}$$

According to the definition of an eigenvalue,

$$\lambda_j = \omega_j^2 \tag{2.10}$$

is the jth eigenvalue of the system matrix $\mathbf{S_n}$. The scaled displacement vector, $\mathbf{x_j}$, is the corresponding eigenvector at jth mode. Let Λ be a diagonal matrix containing all the eigenvalues

$$\Lambda = \begin{bmatrix} \lambda_1 & & & \\ & \lambda_2 & & \\ & & \ddots & \\ & & & \lambda_n \end{bmatrix} \tag{2.11}$$

and $\mathbf{X}$ be the displacement matrix that includes all the eigenvectors as

$$\mathbf{X} = [\mathbf{x_1}, \mathbf{x_2}, \cdots, \mathbf{x_n}] \tag{2.12}$$

Each element $x_{i,j}$ represents the displacement of the ith resonator at the jth eigen-mode. Equation 2.8 can be generalised as

$$\mathbf{X}\Lambda = \mathbf{S_n}\mathbf{X} \tag{2.13}$$

It should be noted that the above analysis is based on the assumption of low damping. In practice, damping leads to a smaller measured ω_j^2 than the actual eigenvalue λ_j.

The collective behaviour provided by coupling makes it possible to observe all eigenvalues from any resonator since n resonant peaks are present in any element of the array. This lays the foundation for the SISO actuation scheme. As long as each resonance can be observed, eigenvalues are obtainable no matter where the force is applied and how many resonators are being driven.

In summary, the eigenvalue can be captured from the frequency response of any one resonator thanks to the collective behaviour, whereas eigenvector measurement requires access to all resonators. Both eigenvalues and eigenvectors are related to the system matrix, and have been extensively used as sensing metrics for resonant sensors [79]. However, they bear divergent characteristics in terms of sensing, which will be investigated in the following section with the help of forward perturbation analysis.

2.3 Perturbation Theory

For any sensing application, a change in either mass or stiffness can be regarded as a perturbation that modifies the system matrix and therefore the eigenvalues and eigenvectors, which can be modelled using Lord Rayleigh's perturbation analysis [91]. This section performs forward perturbation analysis on coupled systems and derive their mass or stiffness sensitivity.

2.3.1 Mass and Stiffness Change

To differentiate mass and stiffness sensing, one can rewrite Equation 2.8 as

$$\mathbf{K}\mathbf{x_i} = \lambda_i \mathbf{M}\mathbf{x_i} \tag{2.14}$$

Let $\Delta\mathbf{K}$ and $\Delta\mathbf{M}$ be the stiffness and mass change in matrix format, the eigenvalue problem after perturbation is

$$(\mathbf{K} + \Delta\mathbf{K})(\mathbf{x_i} + \boldsymbol{\Delta}\mathbf{x_i}) = (\lambda_i + \Delta\lambda_i)(\mathbf{M} + \Delta\mathbf{M})(\mathbf{x_i} + \Delta\mathbf{x_i}) \tag{2.15}$$

By expanding and simplifying the equation, the second and third order terms can be ignored:

$$\mathbf{K}\Delta\mathbf{x_i} + \Delta\mathbf{K}\mathbf{x_i} = \lambda_i\mathbf{M}\Delta\mathbf{x_i} + \lambda_i\Delta\mathbf{M}\mathbf{x_i} + \Delta\lambda_i\mathbf{M}\mathbf{x_i} \tag{2.16}$$

The eigenvalue or eigenvector shift can be solved by using the symmetry of the matrices as well as the orthogonality of the eigenvectors [92]. The eigenvector change is given by a linear combination of the orthogonal eigenvectors:

$$\Delta \mathbf{x_i} = \sum_{j=1}^{n} \varepsilon_{i,j} \mathbf{x_j} \tag{2.17}$$

where $\varepsilon_{i,j}$ is the coefficient that can be derived as [93]

$$\varepsilon_{i,j} = \frac{\mathbf{x_j^T}(\Delta \mathbf{K} - \lambda_i \Delta \mathbf{M})\mathbf{x_i}}{\lambda_i - \lambda_j} \qquad i \neq j \tag{2.18}$$

or

$$\varepsilon_{i,i} = -\frac{1}{2}\mathbf{x_i^T} \Delta \mathbf{M} \mathbf{x_i} \tag{2.19}$$

These coefficients relate any stiffness/mass change to the unperturbed eigenvectors and eigenvalues, which facilitate subsequent perturbation analysis to determine the sensitivity. In addition, the eigenvalue shift has a simple form

$$\Delta \lambda_i = \mathbf{x_i^T}(\Delta \mathbf{K} - \lambda_i \Delta \mathbf{M})\mathbf{x_i} \tag{2.20}$$

2.3.2 Sensitivity Analysis

With the knowledge of eigenvalue and eigenvector changes, the new set of eigenvalues λ_i^* and eigenvectors $\mathbf{x_i^*}$, after very small stiffness/mass perturbations, can be calculated as

$$\lambda_i^* = \lambda_i + \mathbf{x_i^T}(\Delta \mathbf{K} - \lambda_i \Delta \mathbf{M})\mathbf{x_i} \tag{2.21}$$

$$\mathbf{x_i^*} = \mathbf{x_i}(1 - \frac{1}{2}\mathbf{x_i^T} \Delta \mathbf{M} \mathbf{x_i}) + \sum_{j=1, j\neq i}^{n} \frac{\mathbf{x_j^T}(\Delta \mathbf{K} - \lambda_i \Delta \mathbf{M})\mathbf{x_i}}{\lambda_i - \lambda_j} \mathbf{x_j} \tag{2.22}$$

It is now possible to determine the stiffness or mass sensitivity for both eigenvalues and eigenvectors. Assuming there is a perturbation happening on the (p, q) element of the stiffness or mass matrix, for $p = q$ only one diagonal element changes, whereas for $p \neq q$ two off-diagonal elements change at the same time since the matrix is symmetric. Therefore, the eigenvalue sensitivities for stiffness and mass depend on the sensing location:

$$\frac{\partial \lambda_i}{\partial \mathbf{K}} = \frac{\partial}{\partial \mathbf{K}}(\lambda_i + \mathbf{x_i^T}(\Delta \mathbf{K} - \lambda_i \Delta \mathbf{M})\mathbf{x_i}) = x_{p,i} x_{q,i}(2 - \delta_{p,q}) \tag{2.23}$$

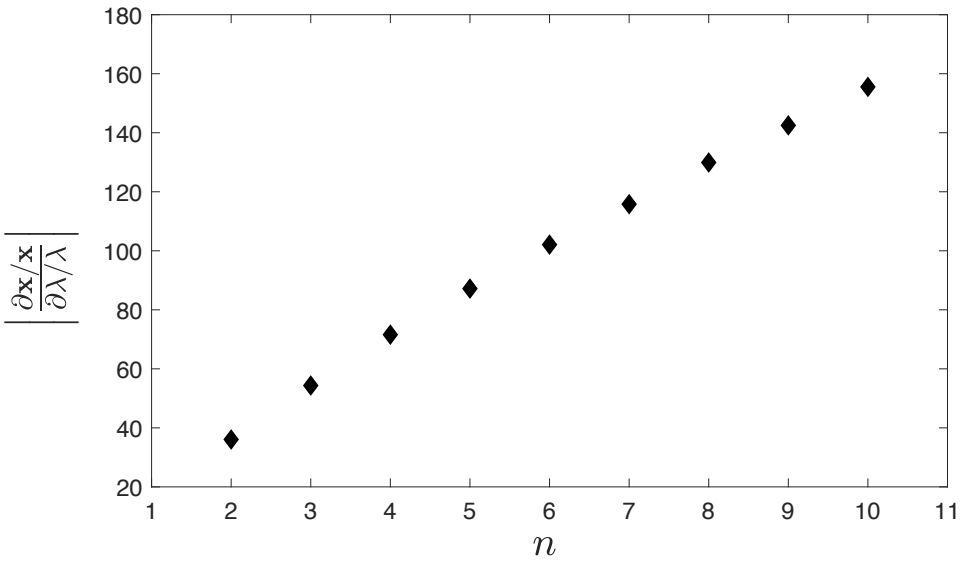


Figure 2.2: The ratios of the average eigenvector sensitivity $|\partial \mathbf{x}/\mathbf{x}|$ to the average eigenvalue sensitivity $|\partial\lambda/\lambda|$ for different numbers of resonators, assuming $\kappa = 1\%$.

$$\frac{\partial \lambda_i}{\partial \mathbf{M}} = \frac{\partial}{\partial \mathbf{M}}(\lambda_i + \mathbf{x_i^T}(\Delta\mathbf{K} - \lambda_i \Delta\mathbf{M})\mathbf{x_i}) = \lambda_i x_{p,i} x_{q,i}(2 - \delta_{p,q}) \tag{2.24}$$

where $\delta_{p,q}$ is the Kronecker delta given by

$$\delta_{p,q} = \begin{cases} 1 & \text{if } p = q \\ 0 & \text{else} \end{cases} \tag{2.25}$$

Similarly, the eigenvector sensing approach is also location-dependent, with stiffness and mass sensitivities being

$$\frac{\partial \mathbf{x_i}}{\partial \mathbf{K}} = \sum_{j=1, j\neq i}^{n} \frac{x_{p,j} x_{q,i}(2 - \delta_{p,q})}{\lambda_i - \lambda_j} \mathbf{x_j} \tag{2.26}$$

$$\frac{\partial \mathbf{x_i}}{\partial \mathbf{M}} = -\frac{1}{2} x_{p,i} x_{q,i}(2 - \delta_{p,q})\mathbf{x_i} - \sum_{j=1, j\neq i}^{n} \frac{\lambda_i x_{p,j} x_{q,i}(2 - \delta_{p,q})}{\lambda_i - \lambda_j} \mathbf{x_j} \tag{2.27}$$

This shows either the eigenvalue or the eigenvector can be pursued as a metric to convey a projective measurement of mass/stiffness change. To compare their sensitivities, one can consider an array of n identical resonators with 1% weak coupling and assume a stiffness change happening on the first element, i.e.

$$\Delta\mathbf{K} = \Delta k \mathbf{E_{1,1}} \tag{2.28}$$

Then, the relative magnitude changes of the eigenvalue and eigenvector can be derived. Figure 2.2 shows the ratios of the average eigenvector sensitivity $|\partial \mathbf{x}/\mathbf{x}|$

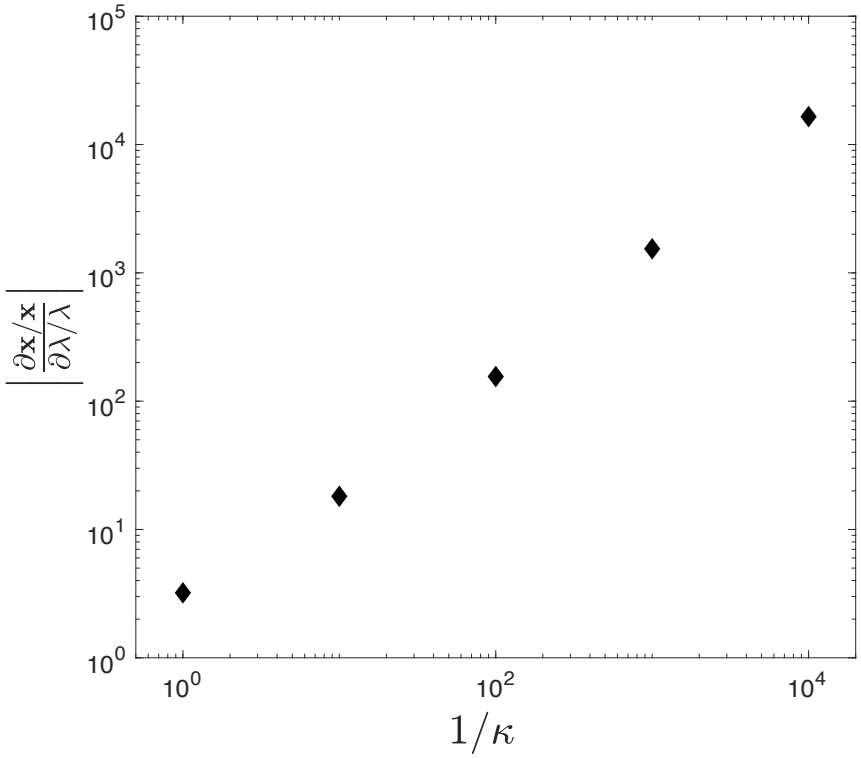


Figure 2.3: The ratios of the average eigenvector sensitivity $|\partial \mathbf{x}/\mathbf{x}|$ to the average eigenvalue sensitivity $|\partial \lambda/\lambda|$ for different coupling ratios, assuming $n = 10$.

to the average eigenvalue sensitivity $|\partial \lambda/\lambda|$ for different numbers of resonators. The impact of the coupling ratio has also been studied in Figure 2.3 by fixing the number of resonators to ten and sweeping the coupling ratios. These results are consistent with Spletzer's theory [73], showing that the sensitivity enhancement ratio of eigenvector is linearly proportional to the number of resonators and is inversely proportional to the coupling ratio:

$$\left|\frac{\partial \mathbf{x}/\mathbf{x}}{\partial \lambda/\lambda}\right| \propto \frac{n}{\kappa} \tag{2.29}$$

Hence, by increasing the number of resonators and weakening the coupling ratio, the sensitivity can be further enhanced. However, there is an ultimate limit to these two factors, which will be discussed later in Section 2.4.

The above analysis has provided mathematical foundations for using eigenvalues and eigenvectors as sensing metrics. Their sensitivity for stiffness or mass change can be determined using forward perturbation analysis once the system matrix is known. Apart from determining sensor performance, one can also perform error

analysis based on the same principle [94]. In error analysis, a perturbation is regarded as a noise, rather than a sensing-related mass or stiffness change. It is noteworthy that the presented theory ignores higher order terms, hence the results are only valid for very small stiffness or mass changes. To enable wide range sensing, a deterministic approach is required.

2.3.3 Differential and Common Mode Responses

Previous analysis suggests that the eigenvalue or eigenvector sensitivity depends on the perturbation location. This means the perturbations acted on an array of n resonators can be either common-mode or differential. Hence, by shifting the mass or stiffness of each resonator differently, the sensor can produce a distinct response.

For example, one advantage of the eigenvector method is the common mode noise rejection capability. Common mode noises can be modelled by adding the same amount of perturbation δk to each resonator. In this circumstance, the stiffness perturbation matrix $\mathbf{\Delta K}$ is written as

$$\mathbf{\Delta K} = \delta k \mathbf{I_n} \tag{2.30}$$

where $\mathbf{I_n}$ is the n by n unit matrix. Using Equation 2.22, for $\mathbf{\Delta M} = \mathbf{0}$, the perturbed eigenvector

$$\mathbf{x_i^*} = \mathbf{x_i} + \sum_{j=1, j\neq i}^{n} \delta k \frac{\mathbf{x_j^T I_n x_i}}{\lambda_i - \lambda_j} \mathbf{x_j} = \mathbf{x_i} \tag{2.31}$$

remains unchanged. For the eigenvalue method, however, the perturbed λ_i^*, as calculated by Equation 2.21, would lead to a drifted value

$$\lambda_i^* = \lambda_i + \delta k \mathbf{x_i^T I_n x_i} = \lambda_i + \delta k \parallel \mathbf{x_i} \parallel \tag{2.32}$$

Equation 2.31 and 2.32 show that the eigenvector is immune to common mode perturbations, whereas the eigenvalue shift is proportional to the stiffness change. These two equations provide the mathematical foundation for the different sensing behaviours and noise characteristics of the eigenvector and eigenvalue methods.

In view of the above, the eigenvector is favoured for differential sensing, which ignores unexpected temperature or pressure changes that happen simultaneously

on all sensing units. Eigenvalues, on the other hand, can be used for common mode sensing. Prior to a perturbation, the sum of all the recorded n eigenvalues λ_i is equal to the trace of the system matrix:

$$\sum_{i=1}^{n} \lambda_i = \sum_{i=1}^{n} S_{i,i} \tag{2.33}$$

Considering a total stiffness change Δk distributed across all resonators, the new set of eigenvalues λ_i^* have a different summation

$$\sum_{i=1}^{n} \lambda_i^* = \sum_{i=1}^{n} S_{i,i} + \frac{\Delta k}{m} \tag{2.34}$$

Subtracting Equation 2.34 by 2.33 yields

$$\sum_{i=1}^{n} \Delta\lambda_i = \frac{\Delta k}{m} \tag{2.35}$$

where $\Delta\lambda_i$ is the change of each eigenvalue after the perturbation. This shows that by monitoring all the eigenvalues one can easily calculate the total stiffness or mass change. However, the eigenvalue resolution for any mode is lower than a traditional single resonator, which has only one eigenvalue

$$\lambda = \omega^2 = \frac{k}{m} \tag{2.36}$$

Under the same perturbation Δk, it changes by

$$\Delta\lambda = \frac{\Delta k}{m} \tag{2.37}$$

which is always larger than any eigenvalue shift $\Delta\lambda_i$ observed in coupled systems. This can be justified by the fact that the same amount of perturbation is shared by all the eigen-modes, making it more difficult to distinguish individual frequency shifts. As n increases, the average eigenvalue change $\Delta k/n$ would become smaller. The next section will provide further insight into the limits of coupled sensing in an array of n resonators.

2.4 Limitations

The eigenvalue problem in itself is not difficult to understand and fairly easy to implement. Nonetheless, successful implementation of eigen-sensing methods is conditional upon physical and experimental constraints.

2.4.1 Practical Constraints

Eigen-sensing approaches often involve switching between different modes and reading out from distinct resonators, hence the following practical issues need to be considered for both eigenvalue and eigenvector approaches.

The first challenge lies in the misalignment of resonant peaks at one single mode caused by damping. The eigenvector method relies on the amplitude ratio of different resonators, which need to be measured individually at the same resonance frequency. These amplitudes, however, can vary substantially when there is a slight frequency mismatch or drift. For the eigenvalue method, it only causes a slight error; but for eigenvectors it can be challenging since a small error or limited frequency shift would cause significant variations in the derived amplitude ratio, particularly when the damping is low.

The second difficulty is tracking multiple resonances. Multi-resonance sensing, which helps increase the sensing range for both eigenvalue and eigenvector methods, requires a phase lock loop (PLL) to perform complicated frequency scan and to keep track of more than one eigen-mode. Although a multi-frequency PLL and voltage-controlled oscillator (VCO) can be implemented [95], they add to the cost and complexity.

Thirdly, access to all resonators is needed for the eigenvector method. Although the eigenvector method can rely on one resonant mode to calculate the amplitude ratios, it necessitates amplitude information from all resonant members. This would increase the number of bond pads and hence the costly fabrication area [71]. The eigenvalue method is immune to this as it requires only one resonator to readout all eigenfrequencies. Calculating the amplitude ratios also increases the computational load and signal processing bandwidth, which should be considered by the researcher. For eigenvector sensing, there is a clear distinction between functionalised and reference resonators. The common mode suppression makes it impossible to sense correlated changes that happen on all resonators at the same time. Hence, a separate resonator is used as a reference, which can enlarge the sensor space. The eigenvalue method, however, is not bothered by such a problem.

2.4.2 Resolution

The sensing resolution, i.e. the smallest change the sensor can detect in the quantity that it is measuring, is a key parameter for practical measurement. Despite new eigen-sensing approaches having greatly enhanced sensitivity, none of these methods demonstrate substantial progress in resolution [75]. A low resolution is critical for ultra-sensitive applications as it relates to the minimum change of mass δm or stiffness δk that can be resolved in presence of noise.

For a single resonator, Ekinci *et al.* studied the ultimate limit of inertial mass sensing by considering the minimum measurable frequency shift $\delta\omega$ that is bounded by the thermomechanical noise of a voltage-controlled oscillator driven PLL [96]. The minimum resolvable frequency $\delta\omega$ can be derived as

$$\delta\omega \approx \left(\frac{k_B T}{E_c}\frac{\omega\Delta f}{Q}\right)^{1/2} \tag{2.38}$$

where k_B is the Boltzmann's constant, T is the temperature, and Δf represents the measurement bandwidth. E_c is the carrier energy given by

$$E_c = m\omega^2 \tag{2.39}$$

Taking mass sensing as an example, the resolution can be calculated by Equation 2.38:

$$\delta m \approx 2m\left(\frac{\Delta f}{Q\omega}\right)^{1/2}\left(\frac{E_{th}}{E_c}\right)^{1/2} = 2m\left(\frac{\Delta f}{Q\omega}\right)^{1/2} 10^{-SNR_{\max}/20} \tag{2.40}$$

where E_{th} is the thermal energy

$$E_{th} = k_B T \tag{2.41}$$

$SNR_{\max}$ (in dB) is the maximum signal-to-noise ratio (SNR) in terms of power that distinguishes coherent oscillation over thermal noise, i.e.

$$SNR_{\max} = 10\log_{10}\left(\frac{E_c}{E_{th}}\right) \tag{2.42}$$

For amplitude measurement, Thiruvenkatanatha *et al.* analysed the limits to mode-localised sensing of coupled resonators by taking into account of the noise

effect, coupling ratio and quality factor [97]. The sensing limit is given by

$$\frac{\delta k}{k} = \frac{\delta m}{m} = 8\kappa \sum_{i=1}^{n} \sqrt{\frac{E_{th}\Delta f}{2E_c Q\omega_i}} \tag{2.43}$$

where ω_i is the ith natural frequency. This shows a weak coupling ratio κ is desired to push down the resolution. However, to avoid mode liaison effect (the overlap of adjacent resonant peaks), the frequency separation between two resonances, which is proportional to the coupling ratio [75], should be broader than half the bandwidth ω/Q. This places a lower limit to the coupling ratio and hence determines the ultimate resolution. For real-world sensing, additional sources of noise, such as electronic noise, parasitic feedthrough and environmental interference need to be addressed. Various noise suppression techniques have been developed, including signal averaging [76] and the use of compensation circuit [98] and high order filters [86].

In practice, the eigenvector resolution $\delta\mathbf{x_i}$ can be experimentally determined using the amplitude noise of each resonator:

$$\left|\frac{\delta\mathbf{x_i}}{\mathbf{x_i}}\right| \approx \frac{\delta x_{1,i}}{x_{1,i}} + \frac{\delta x_{2,i}}{x_{2,i}} + \cdots + \frac{\delta x_{n,i}}{x_{n,i}} \tag{2.44}$$

which can then be used along with the sensitivity to determine the minimum resolvable stiffness or mass.

2.4.3 Dynamic Range

Dynamic range (DR) is another important parameter for sensor performance, which is defined as the logarithmic value of the difference between the largest and smallest signal values:

$$\mathrm{DR} = 20\log_{10}\left(\frac{\Delta k_{\max}/k}{\delta k/k}\right) \tag{2.45}$$

for stiffness sensing or

$$\mathrm{DR} = 20\log_{10}\left(\frac{\Delta m_{\max}/m}{\delta m/m}\right) \tag{2.46}$$

for mass sensing. $\Delta k_{\max}$ or $\Delta m_{\max}$ is the largest stiffness or mass change tolerable. A higher dynamic range is desired as it quantifies the flexibility of the sensor

to generate a wide range unsaturated sensing signal while maintaining adequate resolution. In terms of the eigenvalue method, the dynamic range of stiffness sensing can be calculated using Equation 2.45 and 2.40:

$$\mathrm{DR} \approx 20 \log_{10} \left(Q \frac{\Delta k_{\max}}{k} \right) + SNR_{\max} \tag{2.47}$$

Similarly, the DR for mass sensing is derived as

$$\mathrm{DR} \approx 20 \log_{10} \left(Q \frac{\Delta m_{\max}}{m} \right) + SNR_{\max} \tag{2.48}$$

Therefore, the DR of the eigenvalue method is reliant upon the maximum allowed stiffness or mass perturbation, quality factor as well as background noise. For the eigenvector method, however, it also depends on the maximum amplitude ratio $\mathbf{x}_{\max}$, which is restricted by the saturation voltage of test circuit. The very high sensitivity of the eigenvector, however, also imposes a limit to its dynamic range. As suggested by Zhao *et al.*, [77] the sensing boundaries for mass and stiffness are

$$\frac{\Delta k_{\max}}{k} < \left| \frac{\mathbf{x}_{\max}}{\gamma} \right| \tag{2.49}$$

$$\frac{\Delta m_{\max}}{m} < \left| \frac{\mathbf{x}_{\max}}{\gamma} \right| \tag{2.50}$$

γ is the eigenvector sensitivity, which is inversely proportional to the coupling ratio. Hence, if the coupling ratio is too small, the dynamic range would decrease. In conclusion, when designing the coupling ratio, one has to find a balance between sensitivity, mode liaison and dynamic range.

2.5 Inverse Eigenvalue Analysis

Previous analysis based on forward perturbation has shown that the system matrix of coupled systems, which is comprised of mass and spring constant for each element, provides multi-dimensional sensing properties. However, for most MEMS devices, it is the backward problem that draws more interest in the sensor community, since manufactured systems are rarely the same as the design. Furthermore, the system matrix enables real time monitoring of device parameters and enhances

collective sensing capacity. It also provides information on how the resonators are connected and arranged, and identifies the location and quantity of mass or stiffness change. Hence, it is desirable to attain the system matrix. To achieve this, an inverse eigenvalue analysis technique has been reported for multi-sensors [70]. The technique utilises perturbation analysis and robust inverse problem theory to explore the full potential of eigen-information. Other applications of IEA include process monitoring [8], sensitivity analysis [6], sensor actuation [4], material characterisation [58] and device testing [69].

This section gives a systematic review of the theoretical and empirical considerations of the existing IEA methods for coupled micro/nano resonators, then proposes a new IEA characterisation technique to overcome their limitations. MATLAB code for the algorithms in this section is presented in Appendix A.

2.5.1 Known Techniques

There are several existing techniques to extract the system matrix, including the eigendecomposition approach, inverse Lanczos' algorithm and Gladwell's algorithm. These techniques are based on different measurements and may require an external perturbation.

Eigendecomposition Algorithm

One straightforward way of constructing the system matrix is to use all the eigenvalues and eigenvectors based on the eigendecomposition algorithm:

$$\mathbf{S_n} = \mathbf{X}\Lambda\mathbf{X^T} \tag{2.51}$$

In practice, for an array of n coupled micro/nano resonators, one needs to record n eigenfrequencies as well as the amplitudes of n resonators at n modes. Hence, in total it requires contact with n resonators and records $n^2 + n$ measurements. For large arrays, this is complicated because it raises connectivity and bandwidth issues. Not only are these eigenvectors hard to measure, they are also unstable in nature. Experiments conducted by Saad *et al.* demonstrated up to 30% error of such an approach in extracting the system matrix [99].

Inverse Lanczos' Algorithm

To alleviate the readout problems, the inverse Lanczos' algorithm [100] can be implemented, which only requires n eigenvalues and n amplitudes of the first (or last) resonator. In total $2n$ measurements are needed, which can be captured from the terminal resonator only. Let

$$\mathbf{U} = [\mathbf{u_1}, \mathbf{u_2}, \cdots, \mathbf{u_n}] \tag{2.52}$$

be the transpose of $\mathbf{X}$. The ith diagonal element d_i and off-diagonal element o_i of the system matrix can be calculated using Lanczos' iterative approach described in [100]. To begin with, the first diagonal and off-diagonal elements are calculated to be

$$d_1 = \mathbf{u_1}^{\mathbf{T}} \Lambda \mathbf{u_1} \tag{2.53}$$

$$o_1 = - \parallel d_1 \mathbf{u_1} - \Lambda \mathbf{u_1} \parallel \tag{2.54}$$

The second row of $\mathbf{X}$ is then calculated by

$$\mathbf{u_2} = \frac{d_1 \mathbf{u_1} - \Lambda \mathbf{u_1}}{o_1} \tag{2.55}$$

The remaining d_i and o_i, as well as the rows of $\mathbf{X}$ can be determined iteratively using the following equations:

$$\begin{aligned} d_i &= \mathbf{u_i}^{\mathbf{T}} \Lambda \mathbf{u_i} \\ o_i &= - \parallel d_i \mathbf{u_i} - o_{i-1} \mathbf{u_{i-1}} - \Lambda \mathbf{u_i} \parallel \\ \mathbf{u_{i+1}} &= \frac{d_i \mathbf{u_i} - o_{i-1} \mathbf{u_{i-1}} - \Lambda \mathbf{u_i}}{o_i} \end{aligned} \tag{2.56}$$

Till now, all the elements in the system matrix have been extracted. The mathematical proof for this method is presented in Appendix B.1. It is worth noting that the inverse Lanczos' algorithm is based on the premise that the amplitudes of the terminal (first or last) element are known.

Gladwell's Algorithm

Gladwell's inverse problem theory offers another solution to system matrix extraction without the need for recording eigenvectors [101]. It is a robust way of reconstructing the system matrix based on eigenvalues and perturbation analysis. The system matrix in Equation 2.7 has n diagonal elements and $n-1$ off-diagonal elements, hence there are $2n-1$ unknown variables in total. Therefore, theoretically, one only needs $2n-1$ measurements. With n eigenvalues already available from the frequency spectrum of any one resonator, one can perturb the system slightly to derive a second set of n eigenvalues. In total, $2n$ eigenvalues are measured to derive the $2n-1$ terms in the system matrix plus the perturbation amount. Unlike the terminal readout requirement of Lanczos' algorithm, these eigenvalues are readable from any resonator.

To appreciate Gladwell's algorithm, one can consider perturbing the mass or stiffness of the pth element in the array. This generates a perturbed system matrix that only differs from $\mathbf{S_n}$ in the pth diagonal element:

$$\mathbf{S_n^*} = \mathbf{S_n} + (d_p^* - d_p)\mathbf{E_{p,p}} \tag{2.57}$$

which has a set of updated eigenvalues λ_i^*. λ_i and λ_i^* should fulfill the following interweaving condition:

$$\lambda_1 < \lambda_1^* < \lambda_2 < \lambda_2^* < \cdots < \lambda_n < \lambda_n^* \tag{2.58}$$

for $d_p^* > d_p$, or

$$\lambda_1^* < \lambda_1 < \lambda_2^* < \lambda_2 < \cdots < \lambda_n^* < \lambda_n \tag{2.59}$$

for $d_p^* < d_p$. Using the two sequences of eigenvalues λ_i and λ_i^*, the amplitudes of the pth resonator at all resonant modes are determined by (see proof in Appendix B.2):

$$x_{p,i}^2 = \frac{\lambda_i^* - \lambda_i}{\sum_{i=1}^{n}(\lambda_i^* - \lambda_i)} \prod_{j=1, j\neq i}^{n} \frac{\lambda_i - \lambda_j^*}{\lambda_i - \lambda_j} \tag{2.60}$$

When the perturbation happens on the terminal element ($p = 1|n$), the inverse Lanczos' algorithm can be applied subsequently to extract the system matrix.

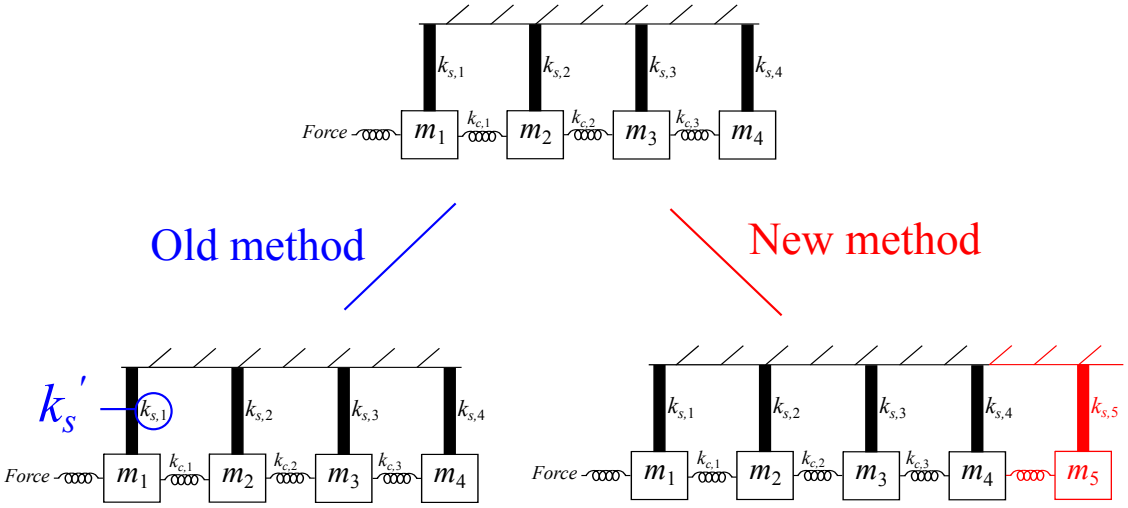


Figure 2.4: Perturbation mechanisms of two IEA approaches: the old method changes the stiffness (or mass) of one resonator, while the new method couples a new element to the array.

For non-terminal element perturbations ($1 < p < n$), one can only calculate the corresponding diagonal elements in the system matrix before and after perturbation:

$$d_p = [x_{p,1}, \cdots x_{p,n}]\Lambda[x_{p,1}, \cdots x_{p,n}]^{\mathbf{T}} \tag{2.61}$$

$$d_p^* = d_p + \sum_{i=1}^{n} (\lambda_i^* - \lambda_i) \tag{2.62}$$

One important feature of this method is that it entails perturbation to the array. In practical sensing, the mass or stiffness shift itself provides such a change. For the sake of calibration, the terminal element can be perturbed deliberately. To deliberately perturb the terminal resonator, researchers have proposed different methods. For cantilevers, focused ion beam (FIB) milling was suggested to cut off one section of the resonant beam [58]. For capacitive-type resonators, the stiffness can be perturbed electrostatically [7]. These approaches, however, are normally destructive or non-linear, and have a limited perturbation range.

2.5.2 New Approach

The old method using Gladwell's algorithm requires perturbations upon one resonant element. As mentioned before, typical perturbation methods, including electrostatic stiffness tuning and FIB milling, would introduce non-linearity or even damage to

the device. Hence, a new characterisation method based on de Boor and Golub's algorithm can be used [4]. This method couples or decouples the terminal element to derive a second set of eigenvalues without altering the spring constant.

The old method and the new method can be illustrated in Figure 2.4 using an array of four coupled resonators represented by mass-spring models. Each method has a unique perturbation mechanism that leads to distinct shifted eigenvalues, which can be used for their respective IEA algorithms. More specifically, the old method strikes the spring constant of the first element, whereas the new method attaches an external element to the established array. Once the device is fabricated and packaged, it can be difficult to mechanically couple to another resonator. However, the additional resonator can be an electrical one and coupled electrically, which will be discussed in Chapter 4.

The simulated amplitude responses of the first resonator are depicted in Figure 2.5 to showcase the eigenvalue behaviour using both perturbation mechanisms, assuming around 15kHz resonance and 5% coupling. For the previous perturbation mechanism, the four peaks shift towards the same left direction after terminal perturbation, and satisfy the interweaving condition set by Equation 2.59. For the new method, however, a new resonant peak has emerged and all the amplitudes have changed substantially.

The interesting behaviour in Figure 2.5 is understandable since attaching a new resonator with a similar resonant frequency to an array of n MEMS resonators would form a new array of $n+1$ members. This leads to an updated system matrix $\mathbf{S_{n+1}}$ with $n+1$ different eigenvalues μ_i, which can be recorded from the response of any one of the MEMS resonators, or even from the additional element. $\mathbf{S_n}$ is the left principal submatrix of the Jacobian matrix $\mathbf{S_{n+1}}$, hence de Boor and Golub's algorithm based on orthogonal polynomials can be applied to extract the system matrix [102] . The algorithm combines the n unperturbed eigenvalues (λ_i) and the new eigenvalues (μ_i) to reconstruct either $\mathbf{S_n}$ or $\mathbf{S_{n+1}}$ without extracting eigenvectors. It should be noted that de Boor and Golub's algorithm requires a

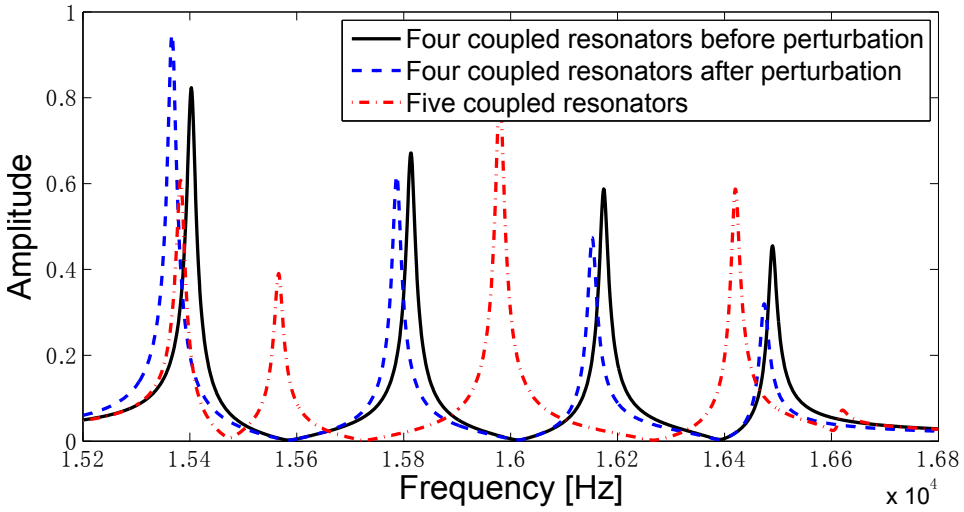


Figure 2.5: Amplitude responses of the first resonator before perturbing the terminal element (solid line), after perturbing the terminal element (dashed line) and after coupling an additional resonator (dash-dot line).

similar interweaving condition for μ_i and λ_i:

$$\lambda_1 < \mu_1 < \lambda_2 < \mu_2 < \cdots < \lambda_n < \mu_n < \lambda_{n+1} \tag{2.63}$$

De Boor and Golub's algorithm first calculates a set of weights w_i based on all measured eigenvalues, then a three-term recurrence relationship is used to derive a series of orthogonal polynomials p_k, which are functions of w_i. With w_i and p_k known, the diagonal and off-diagonal elements of the new system matrix can be extracted iteratively.

Mathematically, the weights w_i are calculated by the measured eigenvalues μ_i and λ_i using

$$w_i = \prod_{j=1}^{n} \frac{\mu_i - \lambda_j}{\mu_i - \mu_{j+1}} \qquad i = 1, \cdots, n+1 \tag{2.64}$$

Having derived these weights, a sequence of orthogonal polynomials related to a reflected version of $\mathbf{S_{n+1}}$ can be evaluated, of which the first two are

$$p_0(\mu_i) = 1 \qquad i = 1, \cdots, n+1 \tag{2.65}$$

$$p_1(\mu_i) = \mu_i - \frac{\sum_{j=1}^{n+1} w_j \mu_j}{\sum_{j=1}^{n+1} w_j} \qquad i = 1, \cdots, n+1 \tag{2.66}$$

Since the values of $p_0(\mu_i)$ and $p_1(\mu_i)$ are known, three-term recurrence relationships can be written to compute the elements of the system matrix as well as the

subsequent orthogonal polynomials $p_{k+1}(\mu_i)$ iteratively. If the diagonal elements $S_{n+1}(i,i)$ are d_i, and off-diagonal elements $S_{n+1}(i,i+1) = S_{n+1}(i+1,i)$ are o_i, then

$$d_{n+2-k} = \frac{\sum_{i=1}^{n+1} \lambda_i w_i p_{k-1}^2(\mu_i)}{\sum_{i=1}^{n+1} w_i p_{k-1}^2(\mu_i)} \qquad k = 1, \cdots, n+1 \tag{2.67}$$

$$o_{n+1-k}^2 = \frac{\sum_{i=1}^{n+1} w_i p_k^2(\mu_i)}{\sum_{i=1}^{n+1} w_i p_{k-1}^2(\mu_i)} \qquad k = 1, \cdots, n \tag{2.68}$$

In the meantime, the orthogonal polynomials are iteratively updated for $k = 2, \cdots, n-1$ by using

$$p_k(\mu_i) = (\mu_i - d_{n+2-k}) p_k(\mu_i) - o_{n+2-k}^2 p_{k-2}(\mu_i) \tag{2.69}$$

It is worth noting that the algorithm starts filling the matrix from $S_{n+1}(n+1, n+1)$ towards $S_{n+1}(1,1)$. Hence, both diagonal and off-diagonal elements of $\mathbf{S_{n+1}}$ are derived. Since $\mathbf{S_n}$ is the left principal submatrix of $\mathbf{S_{n+1}}$, all of the n MEMS resonators can be characterised. One appealing feature of this algorithm is that the weights can be calculated accurately due to a large separation between μ_i and λ_j. The old method based on Equation 2.60, however, involves subtraction between λ_i^* and λ_i, which can be very small and lead to unstable eigenvectors.

2.5.3 Comparison

Both the previous and the new methods provide deterministic solutions, but have different tolerances for measurement errors, which are inevitable in actual sensing. Arising from random temporal noise or environmental factors, these errors can adversely affect the accuracy of the inverse eigenvalue algorithms. Hence, it is important to determine the effect of noise for the two IEA approaches with numerical experiments.

Monte Carlo (MC) analysis is a method that relies on numerous repeated random samplings to obtain numerical results [103]. It is a simple and effective way of understanding complex systems when it is difficult to use analytical tools. For a given system matrix, the noise effect is represented by superimposing Gaussian distributed random variables to the set of eigenfrequencies $(f_1, f_2, \cdots, f_n)$ in each Monte Carlo run. By the same principle, similar Gaussian distributed noises

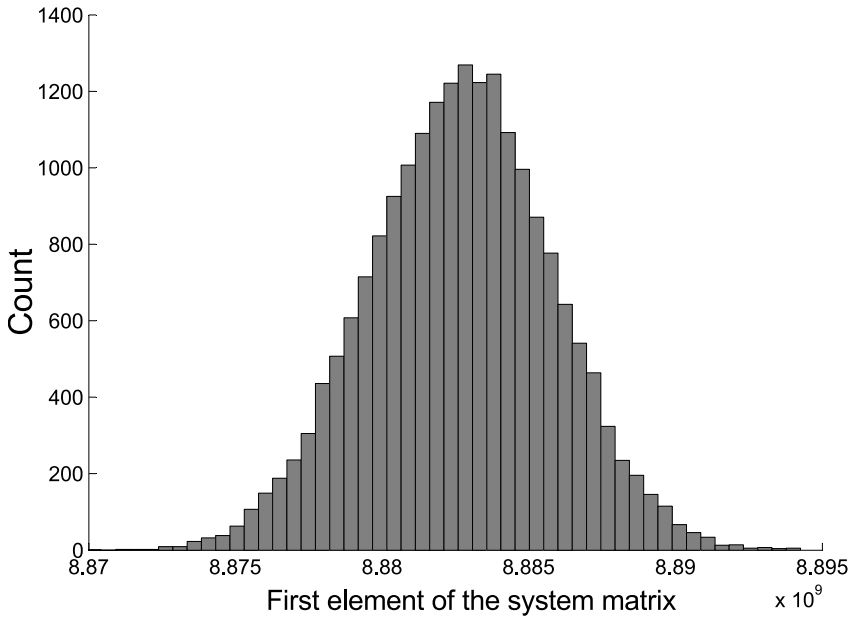


Figure 2.6: Monte Carlo analysis of the spread in the extracted terminal element when a 1Hz standard deviation Gaussian noise is added to the measurement.

can be added to the new eigenfrequencies of the perturbed array. Then, inverse eigenvalue analysis is performed to extract the stiffness or coupling strength using the two sets of eigenvalues before and after perturbation. These results are finally compared with actual values.

Figure 2.6 shows the spread in one extracted terminal element after 20000 Monte Carlo runs, using de Boor and Golub's algorithm. Herein, an example of two coupled resonators was simulated, assuming 15kHz resonance and 5% coupling. 1Hz Gaussian noises were added to the measurement before and after coupling an additional 15kHz resonator. The extracted terminal element also shows a bell-shaped Gaussian profile. The percentage spread of any matrix element $S_n(i,j)$ can be represented by the ratio of its standard deviation to the mean value in k Monte Carlo runs:

$$E_r(i,j) = \frac{\text{std}[S_{n,1}(i,j), \cdots, S_{n,k}(i,j)]}{\text{mean}[S_{n,1}(i,j), \cdots, S_{n,k}(i,j)]} \times 100\% \tag{2.70}$$

As only the diagonal elements of the system matrix are related to the characteristic of each resonator, a simple metric defined by the root mean square deviation of the diagonal elements can be used as an error metric:

$$D_r = \frac{\sqrt{\sum_{i=1}^{n} E_r^2(i,i)}}{n} \tag{2.71}$$

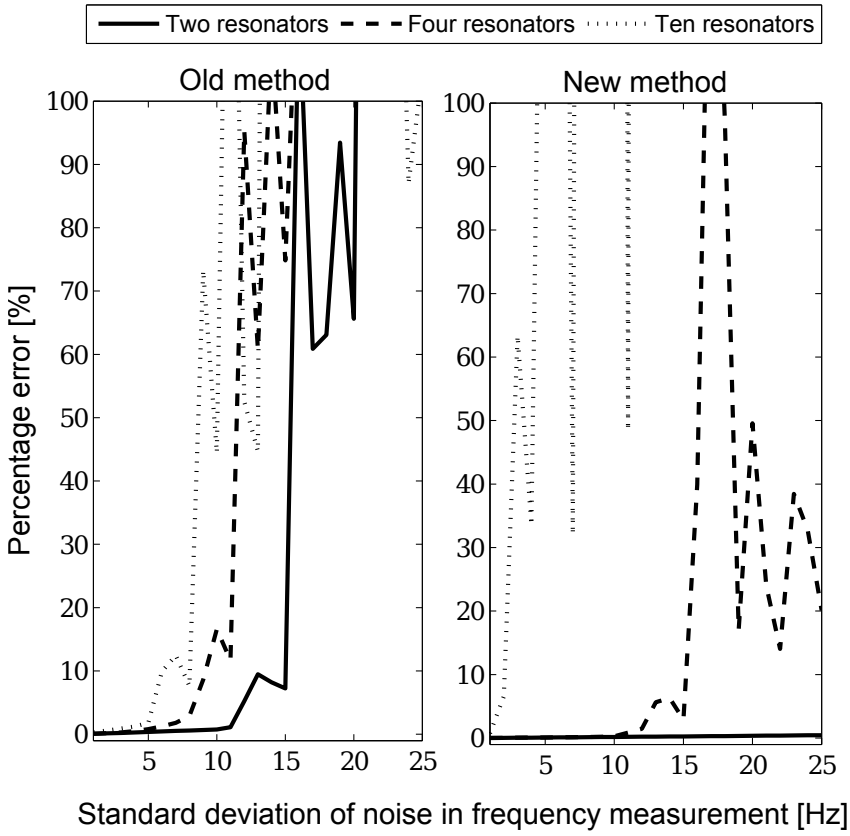


Figure 2.7: Percentage errors of the derived system matrix for different noise levels and different numbers of resonators (before correction).

With the error metric clearly defined, different frequency noises were simulated to understand the robustness of both the old and new methods. For the previous approach, a 1% perturbation was applied to the terminal element. For the new method, an identical resonator with 15kHz resonance was coupled externally. Figure 2.7 shows the percentage errors of the derived system matrix under different noise levels for two, four and ten coupled resonators. Surprisingly, for either approach, after the noise reaches a high level, the error would increase drastically with unpredictable fluctuations. These large errors could be justified by a few outliers where the frequency noises prevailed over the eigenfrequency shifts, hence the interweaving conditions in Equation 2.58, 2.59 and 2.63 were violated.

After applying the interweaving conditions to the numerical experiment and discarding outliers, the corrected percentage errors for both techniques were evaluated again, see Figure 2.8. As a result, the phenomena of sharp increase and

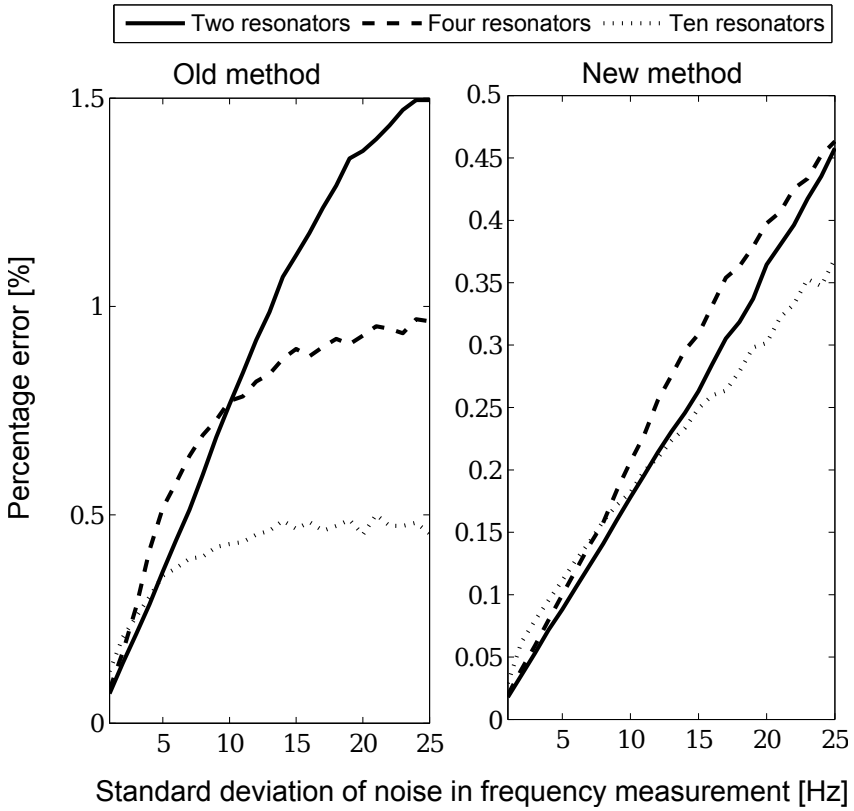


Figure 2.8: Percentage errors of the derived system matrix for different noise levels and different numbers of resonators (after correction).

unstable fluctuation have disappeared. The simulation results suggest that the new method is less noisy than the previous one, reducing the error by more than 50%. Nevertheless, once the interweaving conditions of inverse eigenvalue analysis are not satisfied, both techniques would fail completely. In practice, it is very important to control the readout noise level by discarding outliers that contravene the important interweaving conditions.

Different perturbation values required by the old method have also been studied using a similar four-element coupled array. The results in Figure 2.9 suggest that a larger frequency change of one resonator can reduce the percentage error to some extent: the larger the perturbation, the lower the error, with diminishing marginal increases. This is attributed to greater frequency shifts between perturbed and unperturbed eigenvalues which enhance the robustness of the extracted eigenvectors. However, it is very difficult to change the uncoupled natural frequency of a M/NEMS resonator by a large value and to precisely control the amount of

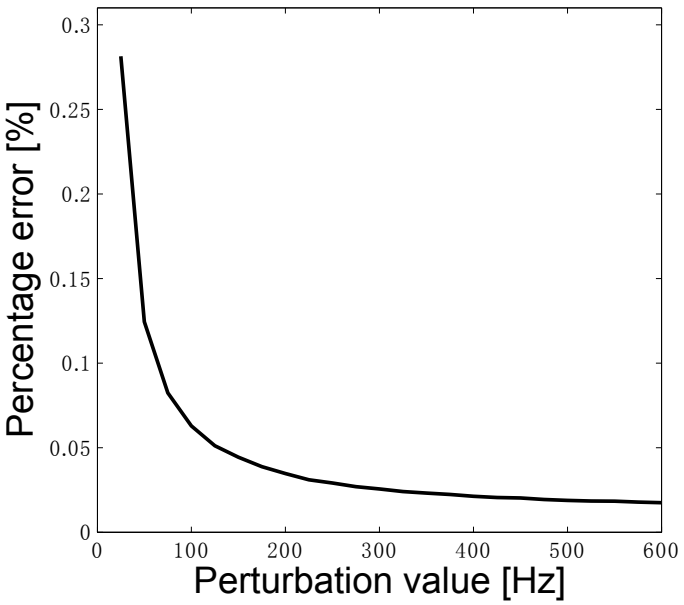


Figure 2.9: Percentage errors of the old method for different perturbation values, assuming 1Hz standard deviation noise.

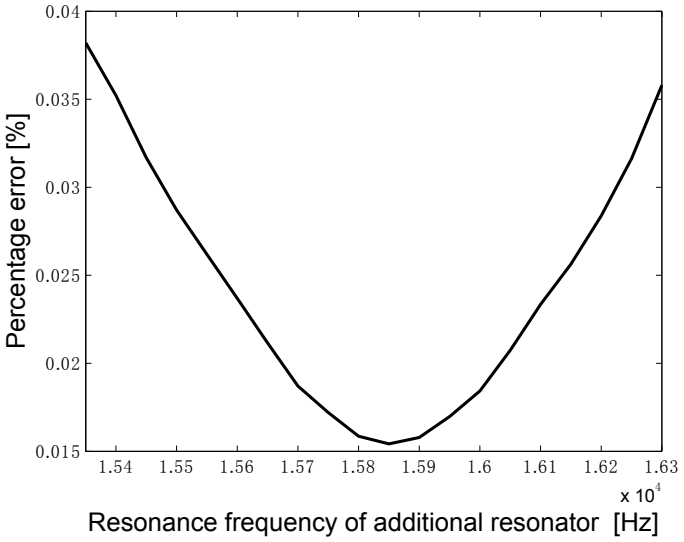


Figure 2.10: Percentage errors of the new method for different resonant frequencies of the additional resonator, assuming 1Hz standard deviation noise.

change. In comparison, the new method using an additional resonator is easier to implement. As demonstrated by the simulation results in Figure 2.10, there exists an optimal resonant frequency for the additional resonator to minimise the error of the new method.

In conclusion, both methods exert changes to the systems and provide a new set of eigenvalues that could be used together with the readily available ones to extract

Table 2.1: Different algorithms to extract the system matrix.

Algorithm	**Min. readout**	**Min. contact**	**Summary**
Eigendecomposition	$n^2 + n$	n	$\mathbf{S_n = X\Lambda X^T}$
Inverse Lanczos	$2n$	1 (terminal only)	Requires n terminal amplitudes and n eigenvalues
Gladwell	$2n$	1 (any resonator)	Requires two sets of n eigenvalues before and after terminal perturbation
De Boor and Golub	$2n + 1$	1 (any resonator)	Requires n eigenvalues before additional coupling and $n + 1$ eigenvalues afterwards

the system matrix. For the former method, two sets of eigenvalues before and after a change in the uncoupled natural frequency of the terminal element are used. The new method requires an additional resonator to be coupled to the existing array, in order to provide another set of eigenvalues. The major source of error for both techniques arises from the failure of the algorithms when the frequency noise goes beyond the normal frequency shift. However, this can be corrected by eliminating outliers which do not agree with the interweaving conditions. With regard to accuracy, the new method shows lower percentage error and is more practical to implement. The accuracy of the previous technique may be improved by increasing the perturbation value. The error of the new method may be reduced by tuning the frequency of the additional resonator.

2.5.4 Discussion

Till now, this section has fully described the theoretical foundations of inverse eigenvalue analysis. In order to determine the system matrix with minimal measurements, the inverse Lanczos' algorithm using the eigenvalues and terminal amplitudes has been introduced to replace the complicated eigendecomposition approach. However, it still involves amplitude measurement, which can be avoided

by Gladwell's inverse problem theory that takes advantage of the two sets of eigenvalues before and after perturbation to extract all eigenvectors. The previous generation of IEA employs Gladwell's algorithm by changing the spring constant of the terminal element. As such a perturbation mechanism is non-ideal, a new method has been proposed using de Boor and Golub's algorithm, which couples/decouples one resonator to/from the terminal, thereby improving the linearity and sensing accuracy. Table 2.1 summaries the ideas behind all these algorithms as well as their minimum requirements for readout and contact.

Monte Carlo analysis has also been performed to compare the two methods and identify sources of error as well as means of compensation. In summary, inverse eigenvalue techniques are easy to operate and significantly reduce the number of contacts and pads required, since readout from only one resonator is needed. It shows huge promise for future applications including M/NEMS device characterisation and process variability monitoring.

2.6 Summary

This chapter renders mathematical analysis of coupled resonator arrays, which can be modelled as an eigenvalue problem. With damping ignored, eigenvalues and eigenvectors are derived by measuring resonant frequencies and amplitudes respectively. Perturbation theory is used to determine and compare eigenvalues and eigenvectors when used as sensing metrics for mass or stiffness changes. The sensitivities of both under differential and common mode perturbations have been discussed. The analysis suggests that the amplitude-based eigenvector approach using weakly coupled resonators can enhance the sensitivity by several orders compared with the eigenvalue shift, and is favoured for differential sensing. The eigenvalue method, on the other hand, is capable of performing common mode sensing by determining the total change of mass or stiffness. Practical considerations and potential challenges associated with these eigen-sensing methods have also been studied. By considering noise, damping and coupling ratio, the theoretical limits of resolution and dynamic range have been analysed.

Apart from the forward perturbation theory, inverse problems in coupled sensing have been examined to determine the system matrix, which can be used for subsequent analysis of device sensitivity and process variations. To enhance the accuracy and linearity of known IEA techniques, a new approach based on de Boor and Golub's algorithm has therefore been proposed. In the next chapter, the eigen-problem theories will be further implemented in a simple two-element coupled array.

Few will have the greatness to bend history itself; but each of us can work to change a small portion of events, and in the total; of all those acts will be written the history of this generation.

— Robert Kennedy

3 Two Coupled Resonators

Contents

3.1 Introduction 51
3.2 Sensing Metrics 52
3.2.1 Eigenvalues 53
3.2.2 Eigenvectors 57
3.3 Inverse Eigenvalue Sensing 59
3.3.1 Full-parameter Extraction 59
3.3.2 Eigenvector Error 61
3.3.3 Stiffness Error 63
3.4 Summary 66

A part of this chapter has been published as

- Guowei Tao, Hemin Zhang, Honglong Chang, and Bhaskar Choubey. "Inverse eigenvalue sensing in coupled micro/nano system". In: *Journal of Microelectromechanical Systems* 27.5 (2018), pp. 886–895

3.1 Introduction

To better appreciate the unique behaviour of coupled micro/nano electromechanical resonators, one may start by examining two coupled systems. Not only are two coupled resonators easy to fabricate, their dynamics have already been widely

explored. Hence, they have gained tremendous popularity in coupled sensing applications such as mass, force and acceleration sensors [62, 73, 104] using either differential sensing or common mode detection. In addition, they only require few connections and provide great flexibility in post-fabrication tuning. This chapter implements the previously described theories of coupled systems in this type of simple array. First, different readout metrics of two-element coupled systems are inspected by performing forward perturbation analysis. Second, their potential of inverse eigenvalue sensing is explored using IEA algorithms.

3.2 Sensing Metrics

Two coupled systems provide various readout metrics like eigenvalues and eigenvectors that can be used for sensing. To understand them mathematically, one can consider two identical resonators with stiffness $k_1 = k_2 = k$, mass $m_1 = m_2 = m$ and a coupling ratio κ. The system matrix is expressed as

$$\mathbf{S} = \frac{k}{m}\begin{bmatrix} 1+\kappa & -\kappa \\ -\kappa & 1+\kappa \end{bmatrix} \tag{3.1}$$

Any stiffness perturbation Δk on the first element gives a new system matrix

$$\mathbf{S}^* = \frac{k}{m}\begin{bmatrix} 1+\kappa+\Delta k/k & -\kappa \\ -\kappa & 1+\kappa \end{bmatrix} \tag{3.2}$$

The eigenvalue and eigenvector sensitivities under different Δk can be determined numerically. The following analysis will be focused on stiffness change, but is also transferrable to mass sensing. It is noteworthy that a change in one resonator's mass would also modify the off-diagonal elements in the system matrix slightly and introduce higher order terms. However, as suggested by Chatterjee, these unwanted terms can be ignored when the change in mass is small enough ($\Delta m/m < 1\%$) [105]. Analysis in this chapter also assumes negligible damping. For resonators designed with a high Q or operated under a low pressure, the error caused by damping can often be ignored [106]. In damped systems, however, additional diagonal and coupling terms can be introduced by the damping matrix, hence causing errors such as modal mistuning, as suggested by Gallacher [107].

3.2.1 Eigenvalues

Eigenvalue sensing falls into two categories: single-resonance and multi-resonance. The former reads out one eigenvalue only, while the latter accesses more than one eigenvalue by capturing multiple eigen-modes.

Single-resonance

Figure 3.1(a)(b) simulate the responses of two weakly coupled systems ($k_1 = k_2$) when a driving force is applied to one resonator. The easiest sensing method for coupled resonators is to detect one eigenvalue at a particular resonance. This method requires only one frequency readout and operates at a single mode. Assuming a weak coupling ($\kappa = 10\%$) and a stiffness perturbation between -20% and +20%, the changes of two eigenvalues λ_1 and λ_2 are plotted in Figure 3.1(c). When increasing the perturbation, the first mode rises, but eventually converges to a flat value which is always smaller than the second mode. When reducing the perturbation, a similar rule applies to the eigenvalue of the second mode. It converges to a lower boundary that is constantly greater than the maximum value of the first mode. These can be explained by the interweaving conditions.

Furthermore, at the symmetric point (or zero perturbation point), there is a non-linear region for both modes hence none of the two eigenvalues are desirable for sensing. This region is associated with the mode veering phenomenon in weakly coupled systems [108]. It is beneficial to keep away from this region by choosing an operating point where $k1 \neq k2$. This can be achieved by designing them differently or through additional perturbations such as providing a bias voltage. In this framework, device mismatch caused by process variability can be an advantage. For $k_1 > k_2$, λ_2 is more linear and has a higher sensitivity while the gradient of λ_1 approaches zero. For $k_1 < k_2$, however, the first eigenvalue is preferred for sensing. In practice, other factors such as damping should be taken into consideration to determine which mode to use [72]. In short, it is impossible to find a single eigenvalue to cover a full sensing range. Hence, the single-resonance approach has limited applications.

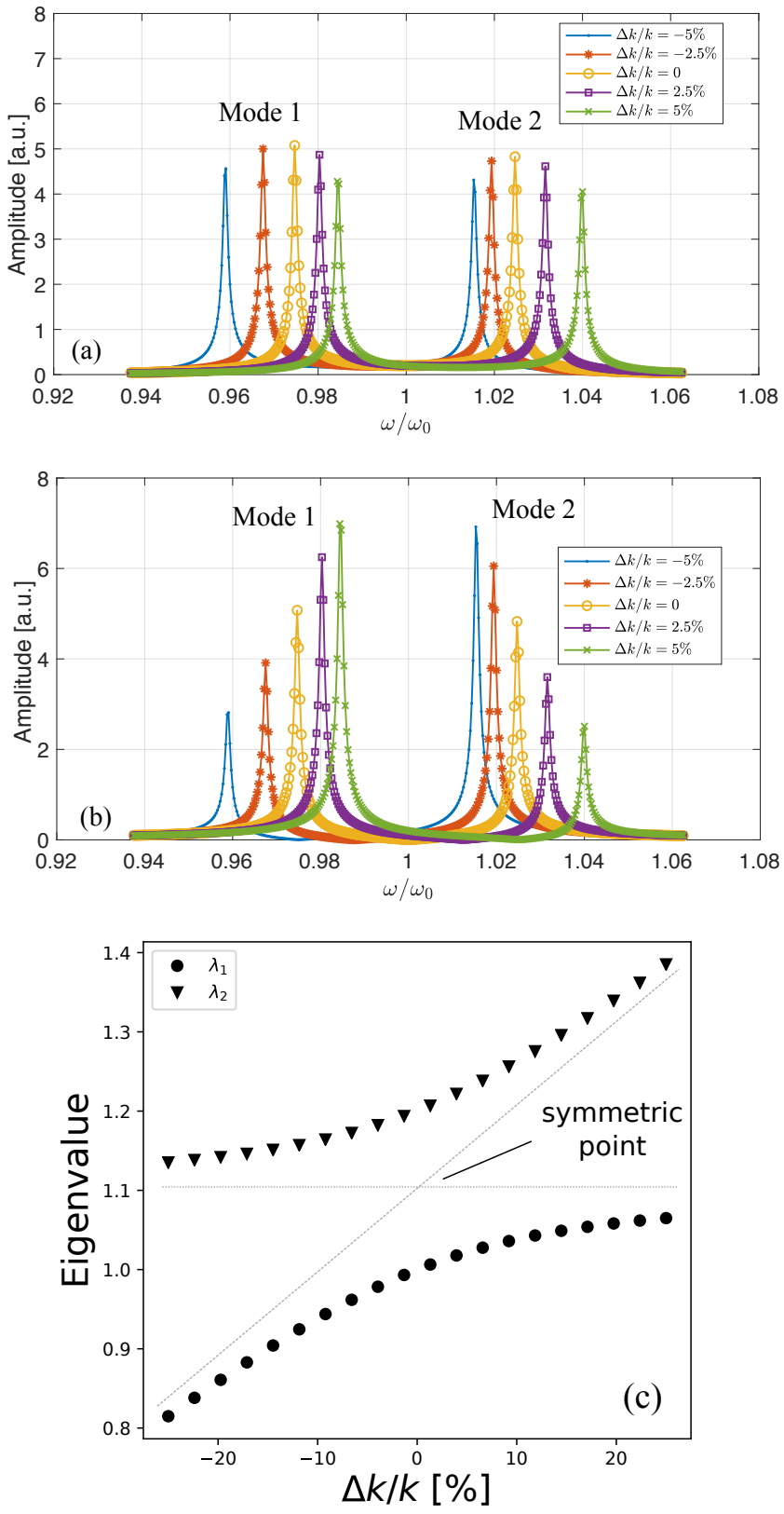


Figure 3.1: Simulated frequency responses from (a) resonator 1 and (b) resonator 2 under different stiffness perturbations. (c) Sensitivity analysis of eigenvalues at both modes.

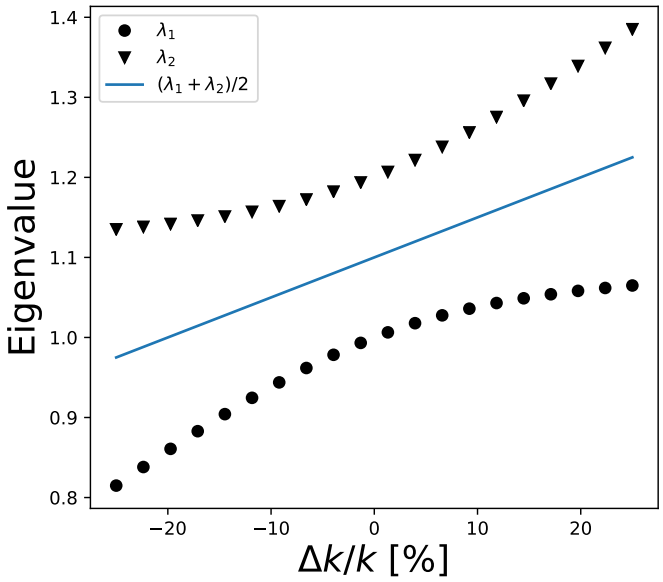


Figure 3.2: The sensitivity of using the mean of two eigenvalues as a sensing metric.

Multi-resonance

One way of overcoming the weakness of single resonance sensing is to explore the capabilities of multiple resonant modes [109]. If the mean (or sum) of two eigenvalues is used as a sensing metric for mass/stiffness change, the sensitivity curve would look like Figure 3.2. Compared with single-resonance, multi-resonance sensing enhances both the linearity and sensing range.

Another multi-resonance approach, as suggested by Hajhashemi and Bahreyni, is to utilise the difference of λ_2 and λ_1 [64]. This has the advantages of sensitivity enhancement and common mode noise suppression. Figure 3.3 compares the sensitivities of 4 different eigenvalue sensing methods, including the use of λ_1, λ_2, $\lambda_2 + \lambda_1$ and $\lambda_2 - \lambda_1$ as sensing metrics. Their relative changes as opposed to the zero point have been recorded for a perturbation range between 0% and +20%. The $\lambda_2 - \lambda_1$ metric has a significantly higher sensitivity than any other metric, while λ_1 is the least effective approach. However, if the coupling ratio increases from 1% to 10%, the sensitivity of λ_2 improves drastically by 4.7×, almost achieving the same sensitivity as λ_1. Conversely, the sensitivity of $\lambda_2 - \lambda_1$ deteriorates by more than one order of magnitude. To understand such shifts, one can first calculate

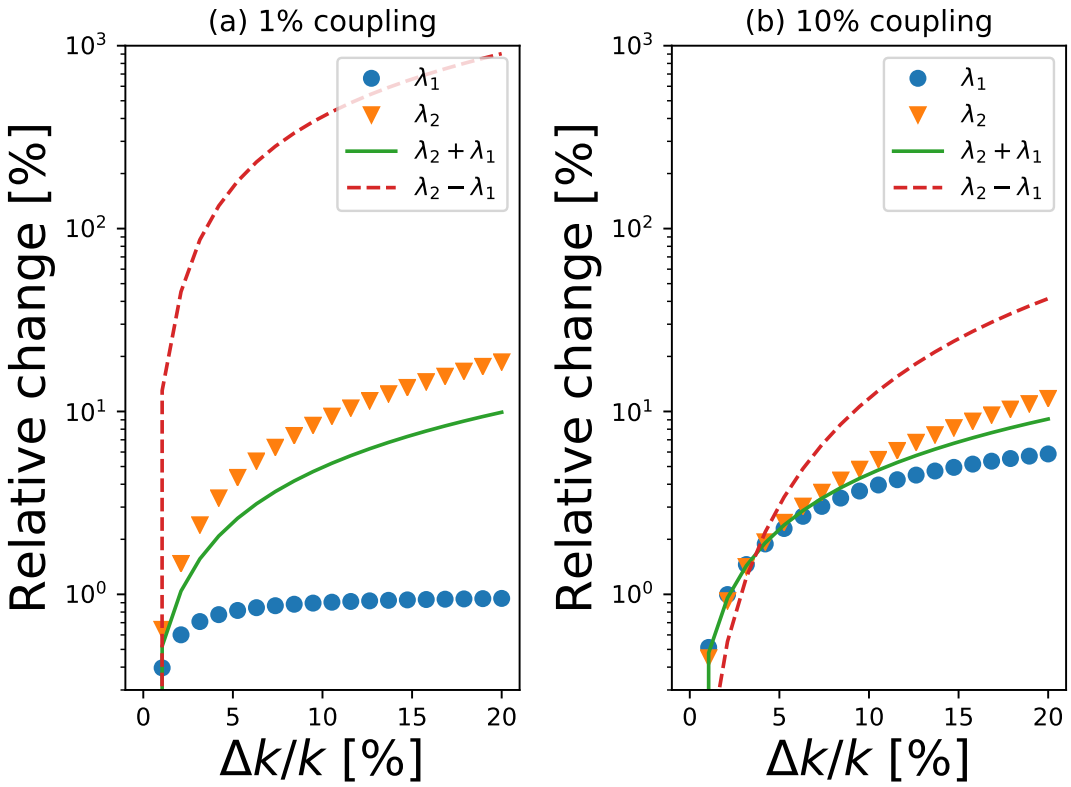


Figure 3.3: Relative changes of 4 eigenvalue sensing metrics under different stiffness perturbations for (a) 1% coupling and (b) 10% coupling.

the two eigenvalues at the zero perturbation point:

$$\lambda_1 = \frac{k}{m} \tag{3.3}$$

$$\lambda_2 = \frac{k + 2k_c}{m} \tag{3.4}$$

Thus, their difference is derived as

$$\lambda_2 - \lambda_1 = \frac{2k_c}{m} \tag{3.5}$$

As the coupling ratio increases, the two resonant peaks stretch further apart, leading to a larger zero point value for $\lambda_2 - \lambda_1$. Its relative change hence decreases.

In practice, the resonance frequency, rather than the eigenvalue, is typically used for sensing as it can be directly captured from the resonance. Frequency is also the most prevailing sensing method due to its high stability, robustness and quasi-digital readout scheme. To calculate an eigenvalue, the eigenfrequency needs

to be squared, which adds complexity to the signal processing. For actual sensing under a small perturbation, however, the eigenvalue change

$$\Delta\lambda_i = \Delta\omega_i^2 = 2\omega_i\Delta\omega_i \tag{3.6}$$

is linearly proportional to the frequency shift. In this situation, eigenfrequencies can be used without compromising the linearity.

3.2.2 Eigenvectors

As proposed by Spletzer *et al.*, the eigenvector (eigenstate) can be used as a sensing metric to boost the mass/stiffness sensitivity by more than two orders of magnitude [73]. An eigenvector is typically represented by the amplitude ratio of all the resonators at a single mode. To understand how the eigenvector method works in a dual-element coupled array, one can begin with the two scaled eigenvectors of the system matrix derived at the zero perturbation point:

$$\mathbf{x_1} = \frac{1}{\sqrt{2}}\begin{bmatrix} 1 \\ 1 \end{bmatrix} \tag{3.7}$$

$$\mathbf{x_2} = \frac{1}{\sqrt{2}}\begin{bmatrix} 1 \\ -1 \end{bmatrix} \tag{3.8}$$

The sensitivity represented by the relative change of eigenvectors can be calculated using Equation 2.26 and 3.5:

$$\left|\frac{\partial \mathbf{x_i}}{\mathbf{x_i}}\right| = \left|\frac{\Delta k}{4k_c}\right| \tag{3.9}$$

In contrast, the relative sensitivity for λ_i, as calculated by Equation 2.23, provides a value

$$\left|\frac{\partial \lambda_i}{\lambda_i}\right| = \left|\frac{\Delta k}{2\lambda_i}\right| \approx \left|\frac{\Delta k}{2k}\right| \tag{3.10}$$

Therefore, the sensitivity of the eigenvector is amplified by

$$\left|\frac{\partial \mathbf{x}}{\mathbf{x}}\right| \Big/ \left|\frac{\partial \lambda}{\lambda}\right| = \frac{1}{2\kappa} \tag{3.11}$$

times, compared with the eigenvalue method. This can be tempting when the coupling ratio is very weak. A κ ranging between 0.1% and 1% would lead to two or three orders of magnitude higher sensitivity.

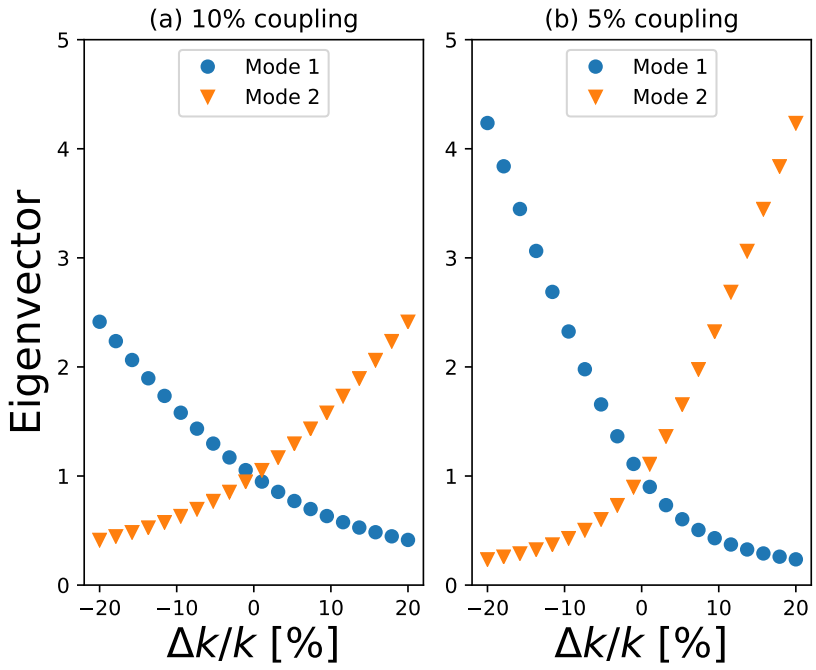


Figure 3.4: Eigenvector changes under different stiffness perturbations for (a) 10% coupling and (b) 5% coupling.

The amplitude behaviour of two coupled systems ($k_1 = k_2$) can also be observed in Figure 3.1. When perturbation upon the first element rises from -5% to 0%, the amplitude of the first resonator increases at both modes. Nevertheless, after increasing the perturbation further, it would start decreasing. Meanwhile, the amplitude of the second resonator exhibits a monotone increase (decrease) for the first (second) mode. For zero perturbation, the amplitudes of the two resonators at either mode are identical.

Figure 3.4 shows the eigenvector changes under different perturbations for 10% and 5% coupling respectively. The eigenvector here is defined by the absolute value of the amplitude ratio

$$v_i = \left| \frac{x_{1,i}}{x_{2,i}} \right| \qquad i = 1, 2 \tag{3.12}$$

where i is the resonant mode. Compared with the performance of eigenvalue sensing in Figure 3.1, eigenvectors have demonstrated enhanced sensitivity and linearity. However, the performance of the eigenvector is highly dependent on the coupling ratio, which is prone to process variabilities. Hence, for mechanical coupling, the

geometry and location of the coupling beam need to be judiciously considered. To get around this issue, electrostatic coupling has been proposed and implemented by Thiruvenkatanathan *et al.* to ensure the tunability of the coupling strength once the device has already been fabricated [60]. By changing the coupling voltage, electrostatic coupling force between resonators can be adjusted to leave the sensor with greater flexibility for various applications. Electrostatic coupling is a non-linear coupling approach. However, the non-linearity can be suppressed by implementing a compensation voltage and by carefully controlling the motion and gap distance [77].

3.3 Inverse Eigenvalue Sensing

As it has been discussed, eigenvalues and eigenvectors demonstrate unique characteristics in coupled sensing. These sensing metrics differ from each other by how the observations are processed, yet do not reveal their intrinsic connections. Inverse eigenvalue analysis can be used to provide further insight into the eigen-sensing mechanisms of coupled systems. With the knowledge of the two sets of eigenvalues provided by perturbation analysis, Gladwell's method described in Section 2.5.1 can be used to extract the eigenvectors and, hence, the full sensing parameters.

3.3.1 Full-parameter Extraction

For any two coupled resonators with a system matrix

$$\mathbf{S} = \begin{bmatrix} s_{11} & s_{12} \\ s_{21} & s_{22} \end{bmatrix} = \frac{1}{m} \begin{bmatrix} k_1 + k_c & -k_c \\ -k_c & k_2 + k_c \end{bmatrix} \tag{3.13}$$

a perturbation on the terminal element modifies the system matrix into

$$\mathbf{S}^* = \frac{1}{m} \begin{bmatrix} k_1 + k_c + \Delta k & -k_c \\ -k_c & k_2 + k_c \end{bmatrix} \tag{3.14}$$

By letting λ_1 and λ_2 be the two original eigenvalues, one can first calculate the difference between them:

$$\Delta\lambda = \lambda_2 - \lambda_1 \tag{3.15}$$

Let

$$\Delta\lambda_1 = \lambda_1^* - \lambda_1, \qquad \Delta\lambda_2 = \lambda_2^* - \lambda_2 \tag{3.16}$$

be the changes of the first and second eigenvalues before and after perturbation. Hence, using Gladwell's inverse problem theory [101], the two elements of the first scaled eigenvector $\mathbf{x_1}/\|\mathbf{x_1}\|$ are determined by

$$\begin{aligned} x_{1,1} =& \sqrt{\frac{\Delta\lambda_1}{\Delta\lambda_1 + \Delta\lambda_2}\left(1 + \frac{\Delta\lambda_2}{\Delta\lambda}\right)} \\ x_{2,1} =& \sqrt{\frac{\Delta\lambda_2}{\Delta\lambda_1 + \Delta\lambda_2}\left(1 - \frac{\Delta\lambda_1}{\Delta\lambda}\right)} \end{aligned} \tag{3.17}$$

Inverse Lanczos' algorithm can now be used with these eigenvectors and eigenvalues to obtain the terminal element s_{11} and off-diagonal element s_{12} (or s_{21}) of $\mathbf{S}$

$$s_{11} = \lambda_1 x_{1,1}^2 + \lambda_2 x_{2,1}^2 \tag{3.18}$$

$$s_{12} = s_{21} = -x_{1,1}x_{2,1}\Delta\lambda \tag{3.19}$$

One can then calculate the two elements of the second scaled eigenvector $\mathbf{x_2}/\|\mathbf{x_2}\|$ using

$$\begin{aligned} x_{1,2} &= (s_{11} - \lambda_1)x_{1,1}/s_{12} \\ x_{2,2} &= (s_{11} - \lambda_2)x_{2,1}/s_{12} \end{aligned} \tag{3.20}$$

Hence, all eigenvectors can be extracted by the knowledge of the eigenvalues of the systems before and after perturbation.

The second terminal element s_{22} is determined by

$$s_{22} = \lambda_1 x_{1,2}^2 + \lambda_2 x_{2,2}^2 \tag{3.21}$$

Therefore, all parameters of the systems can be extracted by simply using the frequency data, with the mass normalised stiffness and coupling strength being

$$\begin{aligned} k_1/m =& s_{11} + s_{12} \\ k_2/m =& s_{22} + s_{12} \\ k_c/m =& -s_{12} \end{aligned} \tag{3.22}$$

To calculate the stiffness change Δk, which is of particular interest for sensing, the trace property of $\mathbf{S}$ and $\mathbf{S}^*$ is used:

$$\begin{aligned} \lambda_1 + \lambda_2 &= (k_1 + k_2 + 2k_c)/m \\ \lambda_1^* + \lambda_2^* &= (k_1 + \Delta k + k_2 + 2k_c)/m \end{aligned} \tag{3.23}$$

which generate

$$\Delta k/m = (\lambda_1^* + \lambda_2^*) - (\lambda_1 + \lambda_2) = \Delta\lambda_1 + \Delta\lambda_2 \tag{3.24}$$

One can now find out the relative stiffness change $\Delta k/k$. To obtain the actual stiffness, one has to calibrate the sensor and find the effective mass.

3.3.2 Eigenvector Error

Having derived the deterministic expressions for inverse eigenvalue sensing in two coupled systems, it is now possible to explore the sensing accuracy through error analysis. This can be performed analytically or using Monte Carlo simulations. The first step of the proposed sensing method is to extract the eigenvectors. Hence, one may start by studying the eigenvector error.

Analytical Expressions

Gladwell's algorithm offers a robust solution for eigenvectors. To simplify the problem and explore eigenvector error, one can operate the sensor at the zero point, i.e. $k_1 = k_2 = k$. In this sense, the system matrix in Equation 3.13 has two eigenvalues $\lambda_1 = k/m$ and $\lambda_2 = (k + 2k_c)/m$, hence $\Delta\lambda = 2k_c/m$. Substituting this into Equation 3.17, the amplitude ratio of the first eigenvector has the form

$$v_1 = \left|\frac{x_{1,1}}{x_{2,1}}\right| = \sqrt{\frac{\Delta\lambda_1}{\Delta\lambda_2} \cdot \frac{2k_c/m + \Delta\lambda_2}{2k_c/m - \Delta\lambda_1}} \tag{3.25}$$

Since the two resonators are symmetrical, they oscillate with the same amplitude at first mode, i.e. $x_{1,1} = x_{2,1}$. Therefore

$$1/\Delta\lambda_1 - 1/\Delta\lambda_2 = m/k_c \tag{3.26}$$

which can be used together with Equation 3.24 to solve $\Delta\lambda_1$ and $\Delta\lambda_2$. When $\Delta k \ll k_c$, the solutions are

$$\Delta\lambda_1 \approx \Delta\lambda_2 = \Delta k/2m \tag{3.27}$$

Using error propagation analysis, the first eigenvector extracted from Equation 3.25 has a standard deviation error

$$\left.\frac{\delta v_1}{v_1}\right|_{v_1=1} \approx \frac{1}{2}\sqrt{\frac{\delta^2(\Delta\lambda_1)}{\Delta\lambda_1^2} + \frac{\delta^2(\Delta\lambda_2)}{\Delta\lambda_2^2}} \approx 2m\frac{\delta\lambda}{\Delta k} \tag{3.28}$$

where $\delta\lambda$ is the eigenvalue error, assuming $\delta\lambda = \delta\lambda_1 = \delta\lambda_2$. Since $\lambda \approx k/m$, the above equation can be written as

$$\left.\frac{\delta v_1}{v_1}\right|_{v_1=1} \approx \frac{2}{\Delta k/k}\cdot\frac{\delta\lambda}{\lambda} = \frac{4}{\Delta k/k}\cdot\frac{\delta f}{f} \tag{3.29}$$

Hence, for $\Delta k \ll k_c$ the accuracy of the extracted eigenvector rests on the perturbation amount as well as frequency noise. A larger perturbation increases both $\Delta\lambda_1$ and $\Delta\lambda_2$, which helps reduce sensing error.

For $\Delta k \gg k_c$, the solutions are different:

$$\Delta\lambda_1 \approx k_c/m, \quad \Delta\lambda_2 \approx \Delta k/m \tag{3.30}$$

The standard deviation of the extracted eigenvector is derived using a similar analysis, resulting in

$$\left.\frac{\delta v_1}{v_1}\right|_{v_1=1} \approx \frac{1}{k_c/k}\cdot\frac{\delta\lambda}{\lambda} = \frac{2}{\kappa}\cdot\frac{\delta f}{f} \tag{3.31}$$

Therefore, for a greater perturbation ($\Delta k \gg k_c$), a stronger coupling ratio is preferred. In this case, as $\Delta\lambda_1 \ll \Delta\lambda_2$, the error mainly relies on the first eigenvalue shift. By increasing the coupling ratio, $\Delta\lambda_1$ increases substantially and hence lowers the relative error. It is worth noting that, for a given amount of perturbation, the sum of $\Delta\lambda_1 + \Delta\lambda_2$ remains constant, which means an increase in $\Delta\lambda_1$ would reduce the eigenvalue shift of the second mode $\Delta\lambda_2$.

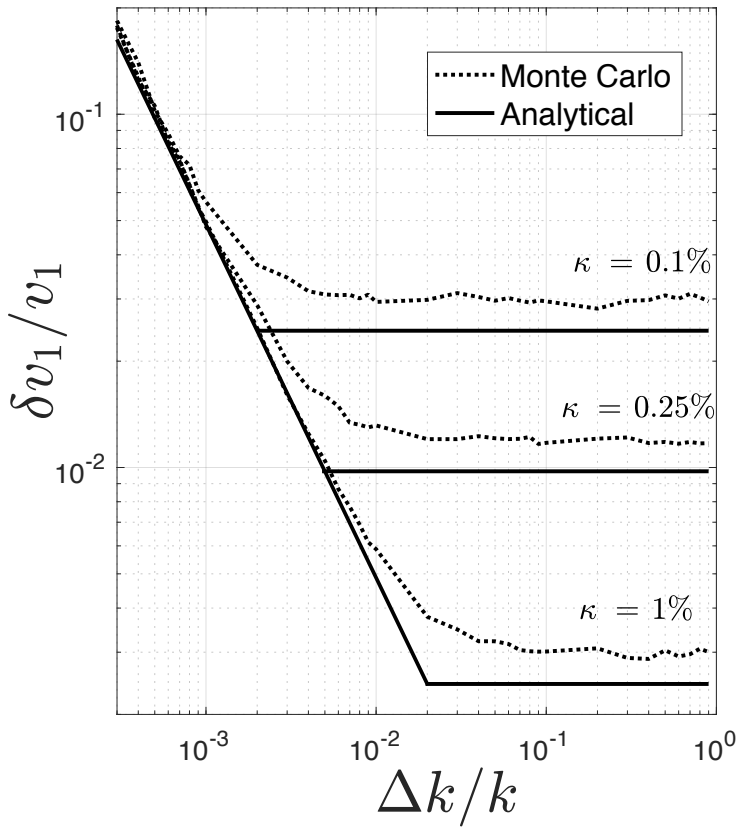


Figure 3.5: Using Monte Carlo analysis and analytical expressions to determine the relative errors of the first eigenvector ($v_1 = x_{1,1}/x_{2,1}$) under different perturbations and coupling ratios.

Simulations

These analytical results can be compared with Monte Carlo simulations to determine the accuracy of extracted eigenvectors under different perturbations. The results are depicted in Figure 3.5, assuming 15kHz resonance and $\delta f = 0.5$Hz. Analytical expressions presented in Equation 3.29 ($\Delta k/k \ll \kappa$) and Equation 3.31 ($\Delta k/k \gg \kappa$) provide a good match with these Monte Carlo results. Three different coupling ratios, 0.1%, 0,25% and 1%, are examined and compared. The results suggest that larger perturbations and stronger couplings reduce eigenvector errors.

3.3.3 Stiffness Error

Besides extracting eigenvector, IEA is capable of sensing stiffness. For stiffness extraction, a similar error analysis can be performed using analytical and simulation tools.

Analytical Expressions

Error propagation analysis for the spring constant is more complicated than for the eigenvector. To begin with, Equation 3.17 and 3.18 are used to determine s_{11}. Under the assumption of $k_1 = k_2 = k$, s_{11} is determined to be

$$s_{11} = \frac{k + k_c}{m} = \lambda_2 - \frac{\Delta\lambda_1(\lambda_2^* - \lambda_1)}{\Delta\lambda_1 + \Delta\lambda_2} \tag{3.32}$$

Since

$$\frac{k_c}{m} = \frac{\Delta\lambda}{2} \tag{3.33}$$

k is expressed as

$$\frac{k}{m} = \frac{\lambda_1 + \lambda_2}{2} - \frac{\lambda_2^* - \lambda_1}{1 + \Delta\lambda_2/\Delta\lambda_1} \tag{3.34}$$

For $\Delta k \ll k_c$, the error for k is dominated by the denominator $(1+\Delta\lambda_2/\Delta\lambda_1)$, hence

$$\delta\left(\frac{k}{m}\right) \approx \frac{\lambda_2^* - \lambda_1}{2} \cdot \frac{\delta(\Delta\lambda_2/\Delta\lambda_1)}{1 + \Delta\lambda_2/\Delta\lambda_1} \approx \frac{2k_c}{\Delta k} \cdot \delta\lambda \tag{3.35}$$

This leads to a relative stiffness error

$$\frac{\delta k}{k} \approx \frac{4\kappa}{\Delta k/k} \cdot \frac{\delta f}{f} \tag{3.36}$$

Similarly, the stiffness error when $\Delta k \gg k_c$ can be determined with

$$\frac{\delta k}{k} \approx \frac{3\delta f}{f} \tag{3.37}$$

To perform sensing, it is also important to know the tolerance of stiffness change Δk, which can be derived through the trace property in Equation 3.24:

$$\delta(\Delta k/m) = \sqrt{\delta^2(\Delta\lambda_1) + \delta^2(\Delta\lambda_2)} \approx 2\delta(\lambda) \tag{3.38}$$

Therefore, the relative error of stiffness change

$$\frac{\delta(\Delta k)}{\Delta k} \approx \frac{4}{\Delta k/k} \cdot \frac{\delta f}{f} \tag{3.39}$$

is irrelevant to coupling strength. By the same principle, the noise on the coupling strength can be determined by Equation 3.33, giving

$$\frac{\delta(k_c)}{k_c} = \frac{\sqrt{2}}{\kappa} \cdot \frac{\delta f}{f} \tag{3.40}$$

This indicates that the coupling strength deviation is decided by both the coupling ratio and the frequency variation.

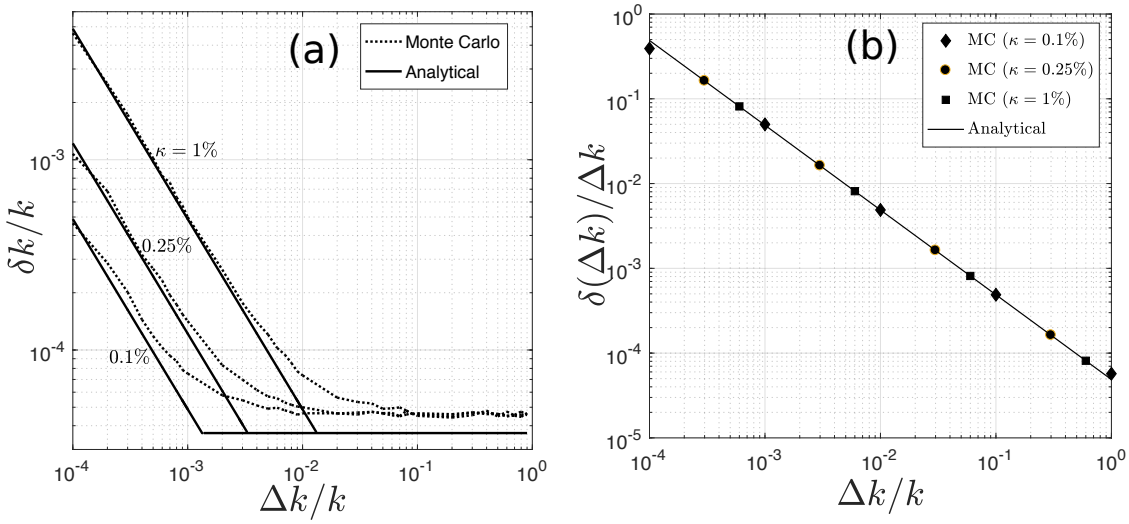


Figure 3.6: The relative errors of extracted (a) stiffness k and (b) stiffness change Δk under different perturbations and coupling ratios.

Simulations

In Figure 3.6, analytical results are verified using further Monte Carlo simulations. Figure 3.6(a) shows that stiffness error $\delta k/k$ can be mitigated through a weaker coupling for $\Delta k/k \ll \kappa$. For large perturbations $\Delta k/k \gg \kappa$, however, it is bound by frequency resolution only. These results agree with the observations in Figure 2.9 and explain the slow decay of stiffness error following an increase in the perturbation. Apart from the perturbation amount, the coupling ratio also plays an important role in eigenvector and stiffness sensing. The error on stiffness change $\delta(\Delta k)/\Delta k$, however, is independent of the coupling ratio, and is solely affected by the perturbation. This can be confirmed by both the analytical and simulated results in Figure 3.6(b). The relative error of measured stiffness change can be reduced by increasing the perturbation level.

Another way of reducing errors on all the parameters is to enhance the eigenfrequency resolution. To study how the frequency noise affects different spring constants, the relative errors of k_1, k_2 and k_c, under different frequency noises, are simulated in Figure 3.7, assuming $\kappa = 0.25\%$ and $\Delta k/k = 1\%$. The error of k_c is two orders of magnitude higher than that of the stiffness, while k_1 and k_2 have similar tolerances for noise.

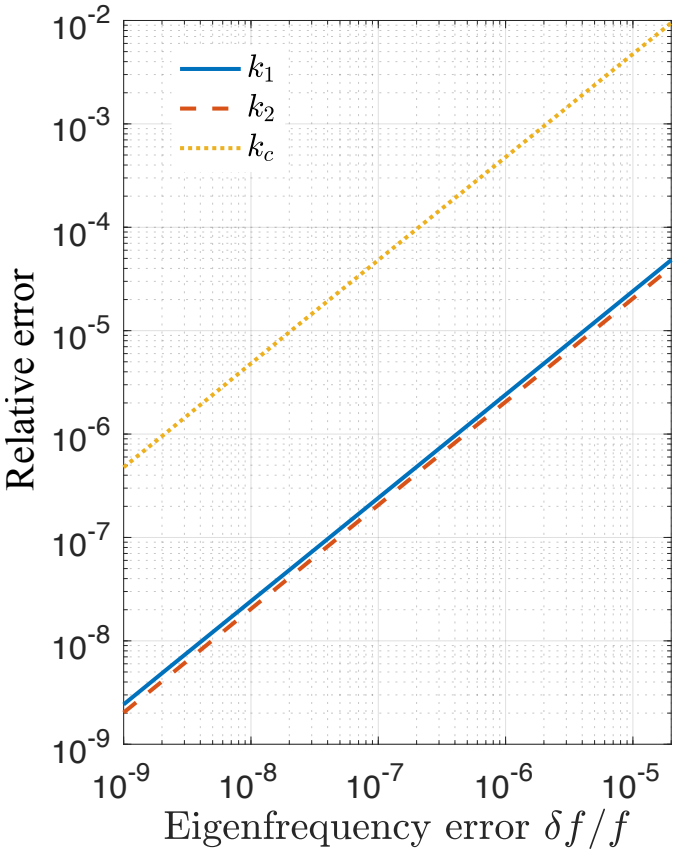


Figure 3.7: Monte Carlo analysis for the relative errors of k_1, k_2 and k_c under different eigenfrequency errors ($\kappa = 0.25\%$, $\Delta k/k = 1\%$).

Till now, the mechanisms of inverse eigenvalue sensing have been fully described for a two-element coupled array. Simple analytical models have been developed to identify the sensing errors. Simulation results have validated the feasibility of this method for highly accurate mass/stiffness sensing applications.

3.4 Summary

Before delving into more complex coupled systems, it is important to first understand the behaviour of a simple array of two coupled resonators, which is also the most widely used sensor structure in coupled sensing. This chapter has studied the eigen-sensing information of two coupled systems through mathematical modelling. With the eigenvalue approach, one can apply either single-resonance or multi-resonance sensing. The former is simple to use, but less linear and less sensitive. Multi-resonance sensing has emerged as an alternative method to provide enhanced

sensitivity and the potential of noise rejection. In addition, an amplitude-based eigenvector sensing approach has been suggested for weakly coupled resonators to further enhance the sensitivity by orders of magnitude, while rejecting common mode noises such as temperature or pressure drift.

To further investigate the nature of these different sensing metrics in two-element coupled systems, inverse eigenvalue analysis has been conducted, which is capable of extracting the eigenvector or stiffness. By developing various analytical models and performing numerical experiments, the accuracy of the method has been fully characterised. Moreover, the effects of perturbation amount as well as coupling ratio have been inspected. It is worth noting that the theories presented in this chapter have recently been verified by a MEMS sensor from the author's research collaborators [1].

In conclusion, the proposed inverse eigenvalue technique demonstrates robust and full-parameter sensing capabilities, and holds huge promise for ultra-sensitive mass/stiffness detection. In the next chapter, using a fabricated array of two coupled resonant sensors, IEA will be studied experimentally.

Little things are indeed little, but to be faithful in little things is a great thing.

— Mother Teresa

4 Sensor Characterisation

Contents

4.1 Introduction 69
4.2 Resonant Sensor 70
4.2.1 Sensor Architecture 70
4.2.2 Circuitry 72
4.2.3 Electrostatic Stiffness 75
4.2.4 Experimental Setup 76
4.3 Tow Thomas Biquad Resonator 78
4.3.1 Configuration 79
4.3.2 Coupling Mechanism 81
4.4 Experiment and Results 84
4.4.1 Frequency Response and System Matrix 84
4.4.2 Validation 85
4.5 Sensitivity Determination 86
4.5.1 Process Variability 87
4.5.2 Characterisation Results 89
4.5.3 Sensitivity Shift 90
4.5.4 Sensitivity Tuning 93
4.5.5 Scalability 95
4.6 Summary 96

A significant part of this chapter has been published as:

- Guowei Tao and Bhaskar Choubey. "Variability induced sensitivity degradation in coupled nano/micro resonant sensors". In: *IEEE Transactions on Nanotechnology* 17.4 (2018), pp. 709–713

- Guowei Tao and Bhaskar Choubey. "On measuring variability and its effect on sensitivity of coupled nano/micro resonators". In: *Nano/Micro Engineered and Molecular Systems (NEMS), 2017 IEEE 12th International Conference on.* IEEE. 2017, pp. 657–660

- Guowei Tao and Bhaskar Choubey. "A simple technique to readout and characterize coupled MEMS resonators". In: *Journal of Microelectromechanical Systems* 25.4 (2016), pp. 617–625

4.1 Introduction

IEA methods, such as Gladwell's approach or de Boor and Golub's algorithm, involve perturbing the terminal element or connecting/disconnecting another resonator. These can be challenging for many reasons. First, for mechanical arrays, physical perturbations such as substance deposition [73] or cutting off one section of the resonator [58] are difficult to implement and can potentially break down the device. Electrostatic perturbations, on the other hand, have a narrow perturbation range accompanied by the threat of non-linearity and pull-in. Connecting or disconnecting another mechanical resonant element to the terminal element is unrealistic once the sensor has been manufactured. To relieve these problems, a novel method is proposed herein by connecting MEMS array with an additional electrical resonator, which is capable of performing both the old and new IEA characterisation methods.

This chapter presents an array of two coupled MEMS resonators with linear output, and the coupling of such to an electrical resonator. All eigenvalues, before and after perturbation, are readout in a SISO fashion from the electrical resonator alone, and can be used with IEA to determine the system matrix and sensitivity of the microsystems. Process-induced variability has been identified as the ground for sensitivity degradation; however, can be compensated by tuning the electrical resonator.

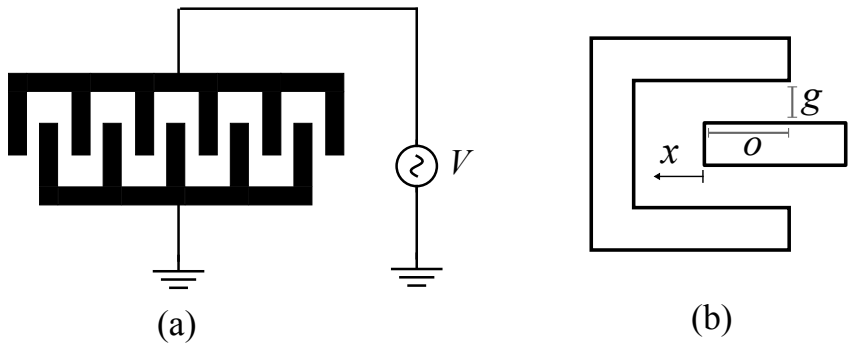


Figure 4.1: (a) A comb structure MEMS resonator and (b) the geometry of opposing fingers.

4.2 Resonant Sensor

To test the IEA algorithms, a previously fabricated capacitive resonant sensor based on interdigitated comb structure was used. Capacitive MEMS resonators are advantageous for sensing and actuation due to their simplicity, low cost, wide operating temperature range, reduced size and compatibility with integrated circuits such as pre-driver, preamplifier and signal processing [110]. The interdigitated comb structure resonator relies on an electrostatic actuation scheme that has been extensively applied in accelerometers and gyroscopes [111]. It also provides linear output, making it possible to couple to an external electrical resonator and implement de Boor and Golub's algorithm.

4.2.1 Sensor Architecture

Figure 4.1 shows a basic comb structure resonator together with its opposing finger geometry. If one comb is fixed, and the displacement of the opposing movable comb is x, then the capacitance between the fixed comb and the moving comb is

$$C = N_f \frac{\varepsilon S}{g} = N_f \frac{\varepsilon t_f (o + x)}{g} \tag{4.1}$$

where N_f is the number of fingers on the fixed comb, t_f is the finger thickness, o is the initial overlapping length for adjacent fingers, and g is the gap distance in between. One advantage of this configuration is that, ideally, the capacitance

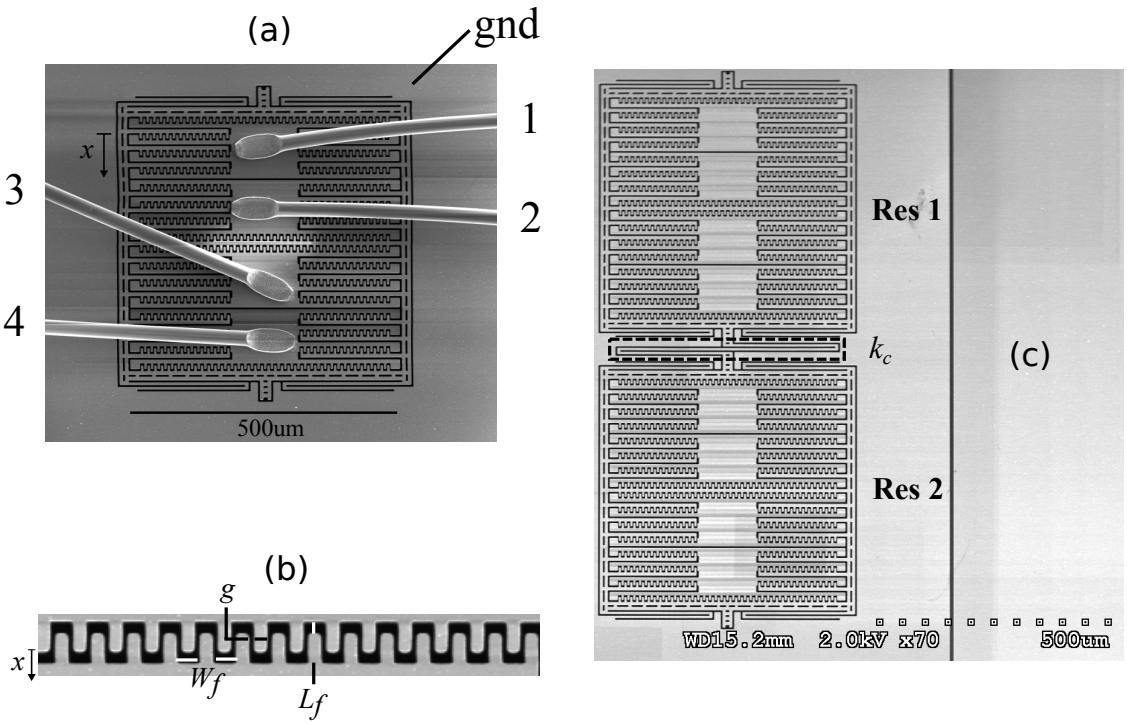


Figure 4.2: SEM images of the comb structure sensor: (a) single resonator, (b) two rows of opposing comb fingers and (c) an array of two coupled resonators.

change with regard to displacement change maintains a constant value:

$$\frac{dC}{dx} = \frac{N_f \varepsilon t_f}{g} \tag{4.2}$$

The energy stored in the capacitor is given by

$$E = \frac{1}{2} C V^2 \tag{4.3}$$

Therefore, the electrostatic force between the two combs

$$F_{capacitor} = -\frac{dE}{dx} = \frac{1}{2} V^2 \frac{dC}{dx} = \frac{N_f \varepsilon t_f V^2}{2g} \tag{4.4}$$

is not affected by higher order non-linear terms, and is quadratic in the voltage applied.

The sensor prototype was fabricated by research collaborators using an Integram silicon-on-insulator (SOI) high aspect ratio micro-machining (HARM) process, with 1μm resolution [112–114]. SEM images in Figure 4.2 show the architecture of the comb resonators, including (a) a single resonator, (b) a magnified view of opposing fingers and (c) the coupling of two such resonators. The SEM image of a single

resonator with the proposed comb architecture is depicted in Figure 4.2(a). The silicon resonator has a thickness of 20μm and the sensor takes up an area of 550μm $\times$ 550μm. The comb fingers are designed with a width (W_f) of 3μm, a length (L_f) of 10μm, a gap distance (g) of 3μm, and an initial overlapping distance (o) of 5μm, as shown in Figure 4.2(b). The direction of the finger displacement x is labelled in Figure 4.2(a)(b). Therefore, according to Equation 4.2, the value of dC/dx is estimated to be 13.4fF/μm, with the capacitance C being around 250fF.

The sensor comprises four fixed comb structures and one grounded moving shuttle with combs attached. The moving shuttle forms a push-pull configuration with those fixed comb structures. The moving shuttle is supported by four 178μm long and 3μm wide folded flexure springs at both ends. The designed mass is 3.6μg, with a spring constant 23.8N/m. With these parameters, the nominal frequency is calculated to be around 13kHz. There are four pads in the middle of the device, each having dimensions of 120μm $\times$ 100μm, to connect to the four fixed comb structures, through connections 1, 2, 3 and 4 in Figure 4.2(a). Wires are bonded between these pads and a 24-pin dual in-line (DIL) package, i.e. DIL24. The package is mounted on a socket that is integrated into a printed circuit board (PCB). A small stub structure located at both ends of the moving frame makes it possible to attach to another resonator using a coupling spring. Figure 4.2(c) shows two such resonators coupled via a mechanical spring in between, which has a 575μm length and a 3μm width.

4.2.2 Circuitry

On each resonator, the four sets of combs resonate at the same magnitude but can move in opposite directions. Hence, these opposing combs can be electrostatically actuated using differential drive and readout circuits.

Differential Drive

In Figure 4.2(a), comb 1 and comb 3 move in the same direction with identical displacement x, while comb 2 and 4 move in the reverse direction with each having displacement $-x$. The design makes it possible to use the differential drive by

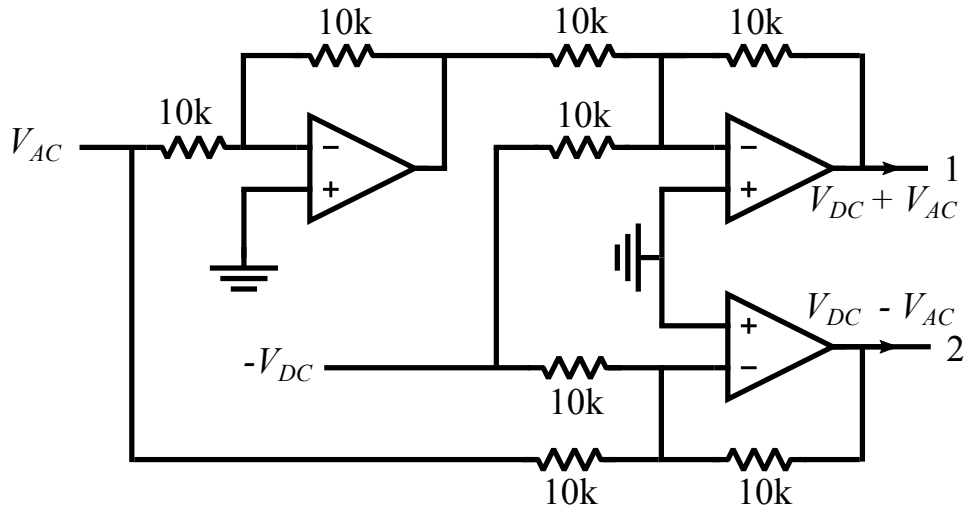


Figure 4.3: The circuit for generating a differential pair of driving signals.

applying $V_{DC} + V_{AC}\cos\omega t$ and $V_{DC} - V_{AC}\cos\omega t$ to comb 1 and 2 respectively, with the electrostatic force for each being

$$\begin{aligned} F_1 &= \frac{1}{2}\frac{dC}{dx}(V_{DC} + V_{AC}\cos\omega t)^2 \\ F_2 &= \frac{1}{2}\frac{dC}{dx}(V_{DC} - V_{AC}\cos\omega t)^2 \end{aligned} \tag{4.5}$$

The overall electrostatic force is the difference between these two forces:

$$F_{capacitor} = F_1 - F_2 = 2V_{DC}V_{AC}\cos\omega t\frac{dC}{dx} \tag{4.6}$$

which does not contain any static term or second harmonic. The circuit for generating such a differential pair of driving signals is depicted in Figure 4.3.

Differential Readout

Similarly, a separate readout scheme is employed for comb 3 and 4 using a constant voltage readout circuit shown in Figure 4.4. The circuit is essentially a transimpedance amplifier (TIA) with a static voltage V_S biased at the non-inverting input. The output current

$$i(t) = V_S\frac{dC}{dt} = V_S\frac{dC}{dx}\frac{dx}{dt} \tag{4.7}$$

transforms velocity, which is a mechanical quantity, into a current signal that can be electrically measured. The magnitude of the output current can be adjusted by

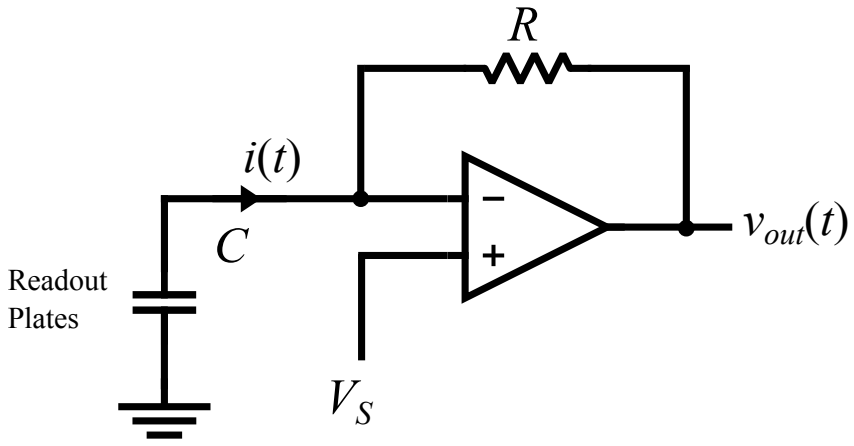


Figure 4.4: A constant voltage readout circuit using a transimpedance amplifier.

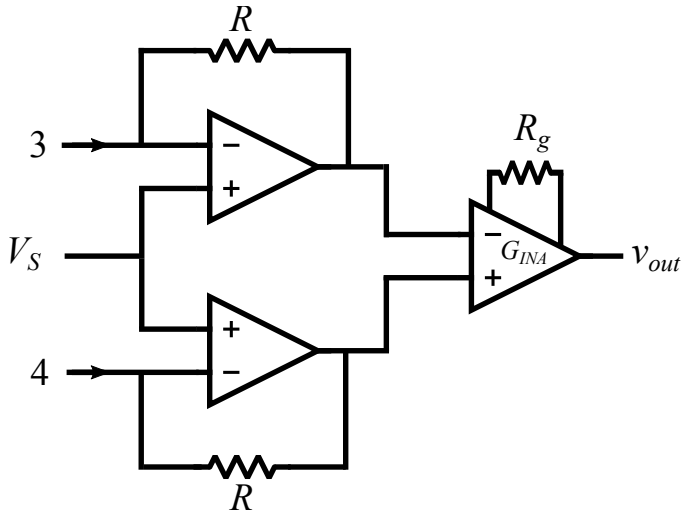


Figure 4.5: The full readout circuit using two transimpedance amplifiers and one instrumentation amplifier.

changing the DC voltage. The generated output voltage has a linear relationship with the velocity:

$$v_{out}(t) = V_S - i(t)R = V_S - V_S\frac{dC}{dx}\dot{x}R \tag{4.8}$$

Since comb 3 and 4 are anti-phase, their output voltages are

$$\begin{aligned} v_3(t) &= V_S - i(t)R = V_S - V_S\frac{dC}{dx}\dot{x}R \\ v_4(t) &= V_S + i(t)R = V_S + V_S\frac{dC}{dx}\dot{x}R \end{aligned} \tag{4.9}$$

An instrumentation amplifier can then be used to take the differential readout between them, giving an overall output that does not contain a constant term:

$$v_{out}(t) = G_{INA}(v_4(t) - v_3(t)) = 2G_{INA}V_S\frac{dC}{dx}\dot{x}R \tag{4.10}$$

where G_{INA} is the instrumentation amplifier gain. Figure 4.5 shows the two-stage readout circuit using two transimpedance amplifiers followed by an instrumentation amplifier.

4.2.3 Electrostatic Stiffness

Theoretically, the electrostatic force is independent of the displacement x. However, in the case of large displacement and non-ideal comb capacitor, it becomes a function of the location. This can be proven by modelling a classic capacitive resonator with an initial plate separation x_0 [69]. After applying Taylor expansion around $x = 0$ to the electrostatic force, the electrostatic force becomes a polynomial series

$$F_{capacitor} = \frac{CV^2}{2x_0}\left(1 + 2\frac{x}{x_0} + 3\frac{x^2}{x_0^2} + 4\frac{x^3}{x_0^3} + \cdots\right) \tag{4.11}$$

which contains higher order terms. These can be omitted for a small displacement $x \ll x_0$. Hence, the motion equation of the resonator is updated as

$$m\frac{d^2x}{dt^2} + \left(k - \frac{CV^2}{x_0^2}\right)x = \frac{CV^2}{2x_0} \tag{4.12}$$

of which the resonance frequency is associated with the coefficient of the x term divided by the coefficient of the d^2x/dt^2 term, i.e.

$$\omega_0 = \sqrt{\frac{k - CV^2/x_0^2}{m}} \tag{4.13}$$

As the magnitude of the bias voltage increases, the resonance frequency always drops. This phenomenon is called spring softening, which is attributed to the negative electrostatic stiffness

$$k_E = -\frac{C}{x_0^2}V^2 \tag{4.14}$$

The spring softening has been explored to offset spring hardening effects seen in MEMS resonators with mechanical hardening properties [115]. It also provides a simple way of tuning the stiffness once the device has been fabricated, and facilities perturbation analysis required by the IEA; however, it also brings in more non-linear terms as V_{DC} increases. Those non-linear terms, normally cubic and quadratic

nonlinearities [116], affect the prior state of the differential equations and hence there exists an unstable zone near the resonance where the response can be different depending on the direction of the frequency sweep. Chaotic behaviours such as bistability and Hopf bifurcation can be observed in such a non-linear system [117]. The design of non-linear MEMS resonators is an emerging field with potential applications in sensitivity enhancement [118] and secure communication [119].

For an unforced and undamped non-linear resonator, the resonance frequency will shift to a new value. This value is amplitude-dependent due to the cubic and quadratic spring constant terms. In this work, the eigenvalue is only related to the linear spring constant term. Hence, to accurately estimate it from the resonance, it is important to minimise non-linearity induced instability.

4.2.4 Experimental Setup

Figure 4.6 shows the typical experimental setup, using a vacuum pump, to provide the sensor with a high quality factor Q. A vacuum chamber, clamped by a support stand, enables a low pressure environment through a mechanical pump. The pressure is measured by a gauge and can be adjusted through the bleed valve. The sensor mounted on the PCB board is sealed underneath the chamber with the help of a rubber ring, which has a diameter of 70mm. The PCB integrates the afore-mentioned actuation circuits to access and control the sensor.

To experimentally control the motion of the resonant sensor, one can use the resonator transfer function in Equation 1.6 to determine the relationship between the displacement and drive force:

$$H(j\omega_0) = \frac{X(j\omega_0)}{F(j\omega_0)/m} = -j\frac{Q}{\omega_0^2} \tag{4.15}$$

The differential drive force is already given in Equation 4.6, therefore the displacement and velocity at ω_0 are derived as

$$\begin{aligned} x(t) &= \frac{2QV_{DC}}{k}\frac{dC}{dx}V_{AC}\sin\omega_0 t \\ \dot{x}(t) &= \frac{2QV_{DC}}{\sqrt{mk}}\frac{dC}{dx}V_{AC}\cos\omega_0 t \end{aligned} \tag{4.16}$$

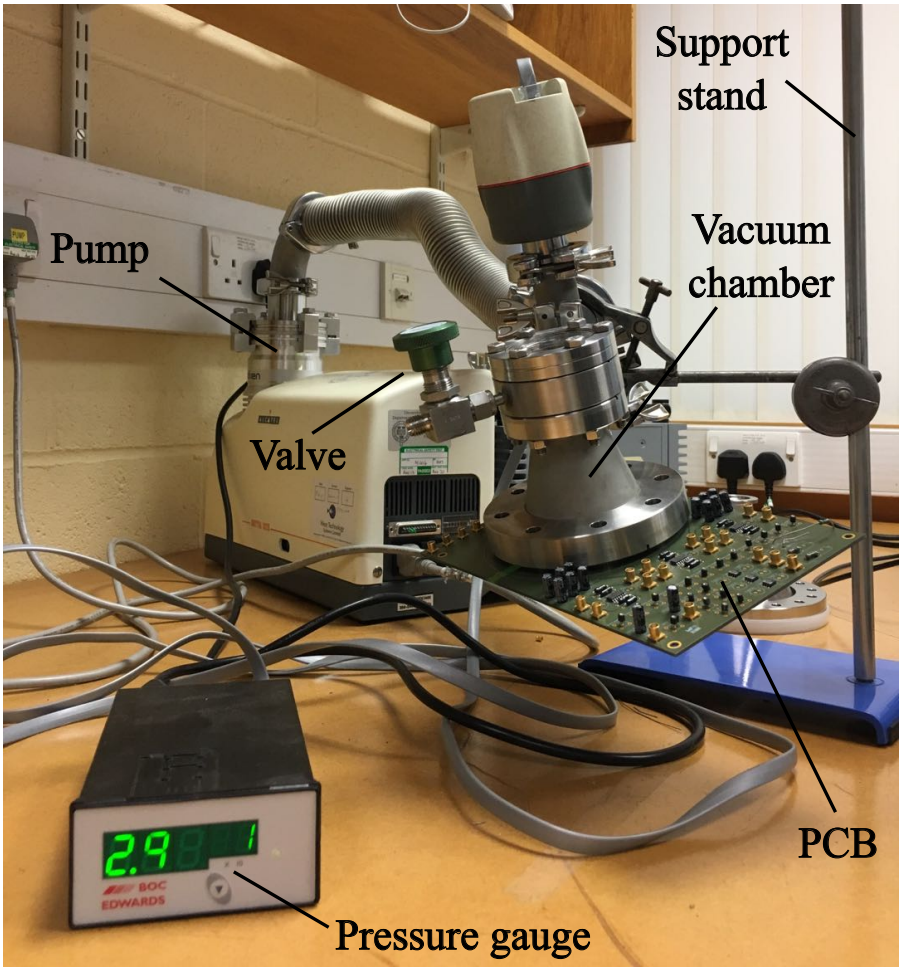


Figure 4.6: Test environment using a vacuum pump.

Table 4.1: Typical parameters for the drive and readout circuits.

Parameter	V_{DC}	V_S	R	G_{INA}
Value	5	8	1	10
Unit	V	V	MΩ	-

which can be translated into an output current or voltage using the proposed two-stage readout circuit:

$$\begin{aligned} i(t) &= \frac{2QV_{DC}V_S}{\sqrt{mk}}\left(\frac{dC}{dx}\right)^2 V_{AC}\cos\omega_0 t \\ v_{out}(t) &= \frac{4G_{INA}RQV_{DC}V_S}{\sqrt{mk}}\left(\frac{dC}{dx}\right)^2 V_{AC}\cos\omega_0 t \end{aligned} \tag{4.17}$$

Table 4.1 summarises the empirical parameters selected for the drive and readout circuits. Using these values, one can therefore estimate the displacement, output

current and voltage range:

$$\begin{aligned} x(t) &\approx QV_{AC} \sin \omega_0 t \times 5.6\text{nm/V} \\ i(t) &\approx QV_{AC} \cos \omega_0 t \times 0.05\text{nA/V} \\ v_{out}(t) &\approx QV_{AC} \cos \omega_0 t \times 0.001 \end{aligned} \tag{4.18}$$

For instance, with Q and V_{AC} being 1000 and 100mV, the comb displacement has a magnitude of around 560nm, generating a current amplitude of 5nA and a voltage amplitude of 100mV. Although increasing the driving voltage helps improve the SNR, the maximum displacement should be controlled to avoid the pull-in effect. The pull-in effect happens when the displacement exceeds a critical point, at which the restoring spring fails to counter the electrostatic force. This leads to the collapse of the capacitor. As suggested by prior research [112], the maximum allowed displacement of the device is suggested to be

$$|x(t)| < 1\mu\text{m} \tag{4.19}$$

which imposes a maximum driving voltage

$$V_{AC} < \frac{180\text{V}}{Q} \tag{4.20}$$

The quality factor in the air is close to 10, but increases sharply under a low pressure. The vacuum pump with an adjustable valve is used to bring down the pressure to as low as 10mPa, corresponding to a maximum quality factor of around 10000. Hence, the device provides a Q ranging from 10 to 10^4.

4.3 Tow Thomas Biquad Resonator

To characterise the fabricated two-element coupled MEMS array, de Boor and Golub's algorithm can be used, which requires attaching an additional resonant element to the array. An electrical resonator can be such a new element to electrically perturb or interact with the sensor. Coupling can be enabled/adjusted by simply activating/changing the feedback signals. Moreover, the electrical resonator provides flexible and wide range tuning of the centre frequency as well as quality factor. Hence, it allows the implementation of all existing IEA techniques.

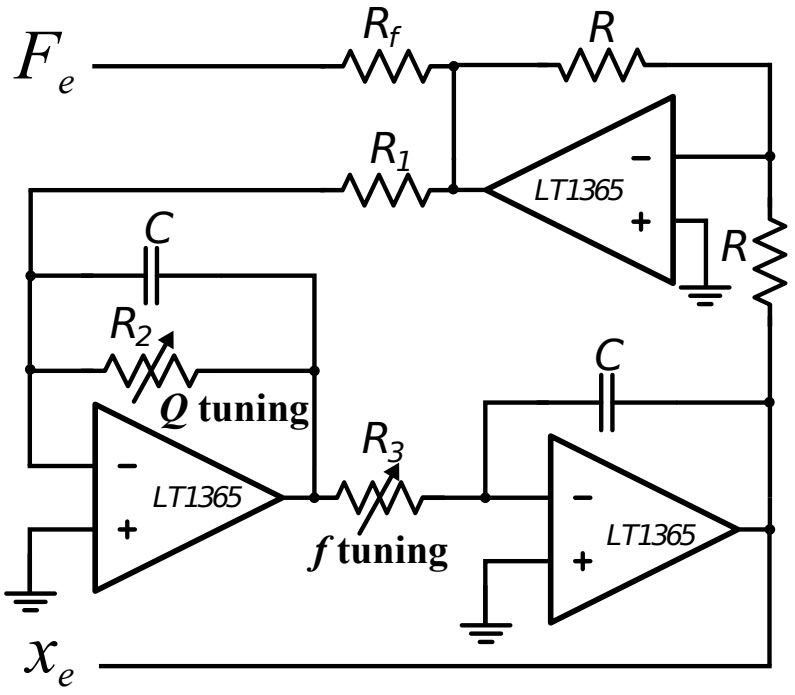


Figure 4.7: Schematic of the Tow-Thomas biquad filter used as an electrical resonator.

4.3.1 Configuration

The proposed electrical resonator to be coupled to the MEMS resonators can be a very simple Tow Thomas biquad filter operated in resonator mode [120]. The resonator is constructed with only three op-amps arranged in a loop, as shown in the schematic in Figure 4.7. Tow Thomas biquad is a classic building block to construct high order filters in different communication systems [121–123]. Compared with a passive-element resonator or other active filters, such a configuration has higher frequency, increased quality factor, enhanced stability, enlarged SNR and dynamic range, and is less sensitive to passive elements [124]. Most important of all, it allows non-interactive tuning, which means that the centre frequency and quality factor of this electrical resonator can be tuned independently.

The circuit is modelled by

$$\ddot{x}_e + \frac{1}{R_2 C}\dot{x}_e + \frac{1}{R_1 R_3 C^2} x_e = \frac{1}{R_3 R_f C^2} F_e \tag{4.21}$$

where F_e is the driving voltage and x_e is the output electrical voltage. The

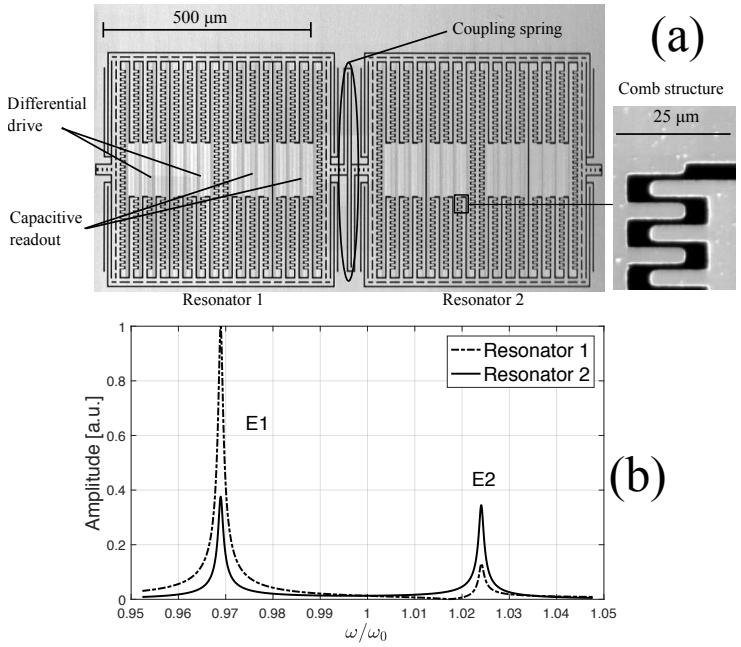


Figure 4.8: (a) SEM of two mechanically coupled MEMS resonators and (b) typical frequency responses of both resonators. E1 and E2 denote the first and second eigen-mode.

centre frequency

$$\omega_0 = \frac{1}{\sqrt{R_1 R_3} C} \tag{4.22}$$

and quality factor

$$Q = \frac{R_2}{\sqrt{R_1 R_3}} \tag{4.23}$$

can be easily adjusted by changing the resistance/capacitance values. Typical values of discrete components used are: $C = 10\text{nF}$, $R = 10\text{k}\Omega$ and $R_1 = R_f = 1\text{k}\Omega$. R_2 and R_3 are variable resistors set to $R_2 \approx 200\text{k}\Omega$ and $R_3 \approx 1\text{k}\Omega$ respectively, thereby providing a low damping ($Q > 200$) and a flexible frequency range between 10kHz to 20kHz.

Ideally, the quality factor of the electrical resonator should be similar to that of the mechanical resonators. However, as these MEMS devices operate under a low pressure, their mechanical quality factor Q_{MECH} can be one order of magnitude higher than the electrical quality factor Q_{ELEC}. This leads to a mismatch in damping. Figure 4.9 depicts the simulated frequency responses recorded from the electrical and mechanical resonators, assuming different practical values for

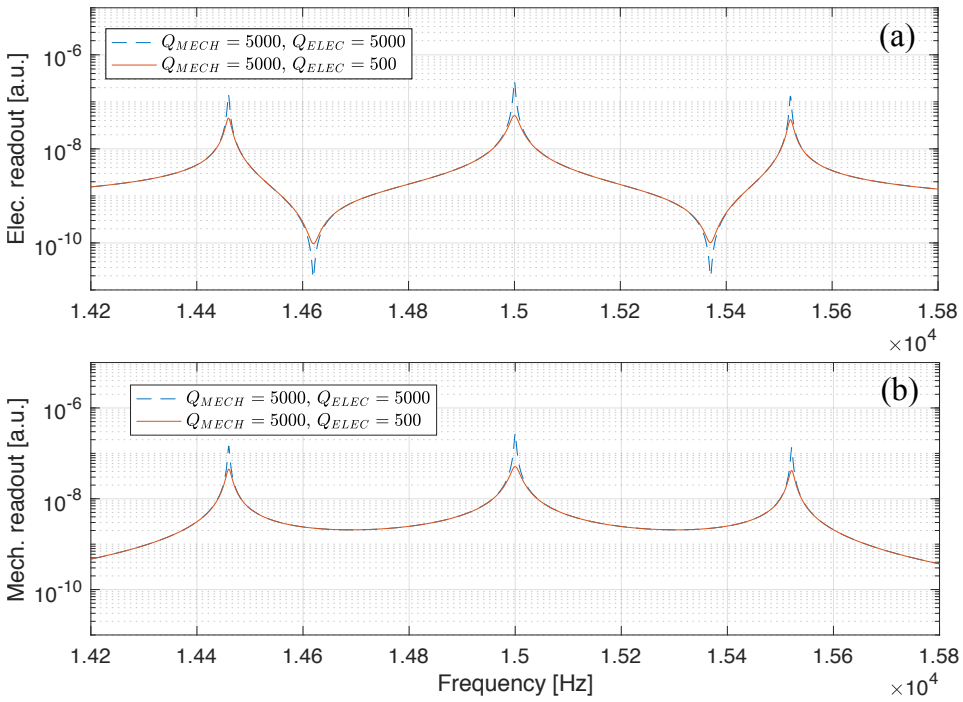


Figure 4.9: The effect of quality factor mismatch between the electrical and mechanical resonators.

Q_{MECH} and Q_{ELEC}. Interestingly, with the electrical quality factor ($Q_{ELEC} = 500$) being one order of magnitude below the mechanical resonator ($Q_{MECH} = 5000$), the average bandwidth for the three modes, observed from either the electrical or mechanical readout, increases by only two-fold. This leads to a high effective quality factor for the coupled systems at each mode, with an average value above 1500. Simulation results also suggest the average difference between the damped resonance frequencies and undamped eigenfrequencies is under 0.06Hz (or 4ppm). This is well below the noise floor and frequency resolution in the experiment. Hence, it is safe to assume that the quality factor mismatch and damping effect are insignificant. This also means the resonance frequency can be a very accurate approximation to the eigenfrequency.

4.3.2 Coupling Mechanism

The fabricated array of two coupled MEMS resonators has similar performance as the electrical resonator, with $Q > 1000$ and two eigenfrequencies around 15kHz. The SEM of the device and typical frequency responses of both resonators are

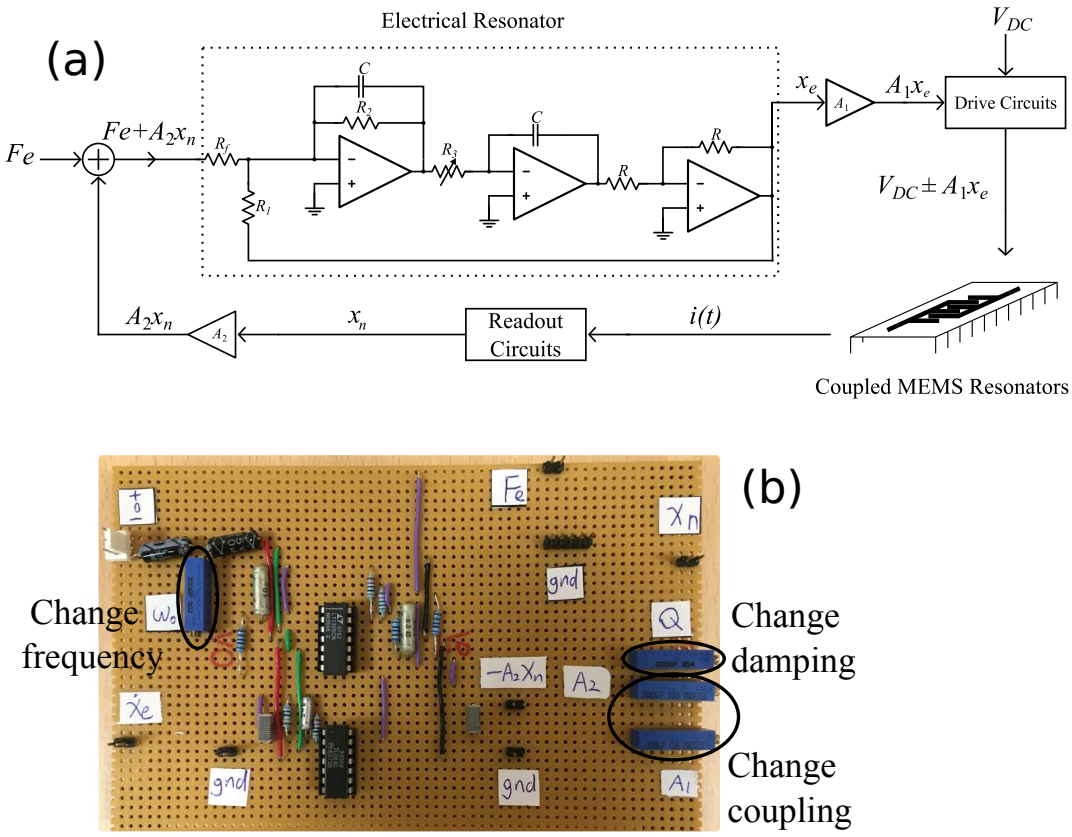


Figure 4.10: Coupling and actuation circuits for the new coupled systems: (a) schematic diagram and (b) electrical circuit board.

depicted in Figure 4.8, where E1 and E2 denote the first and second eigen-mode. The circuit is coupled to the array of MEMS resonators by converting its output to an electrostatic force to drive one of the MEMS resonators. Conversely, the mechanical output of the same MEMS resonator is converted to an electrical signal to feed back to the circuit. Once coupled, readouts from both the electrical circuit and the mechanical resonators contain $n+1$ resonant peaks. These can be measured from the response of the mechanical resonator or better still, the electrical resonator.

Figure 4.10 shows the coupling and actuation circuits for the new coupled systems. The electrical resonator output x_e is amplified and superimposed with a DC voltage to generate a pair of differential signals. The differential signals are subsequently applied to the opposing combs of one MEMS resonator to electrostatically drive it. The readout circuit for this resonator measures the change in capacitance and produces an output current, which is then converted into a voltage by the

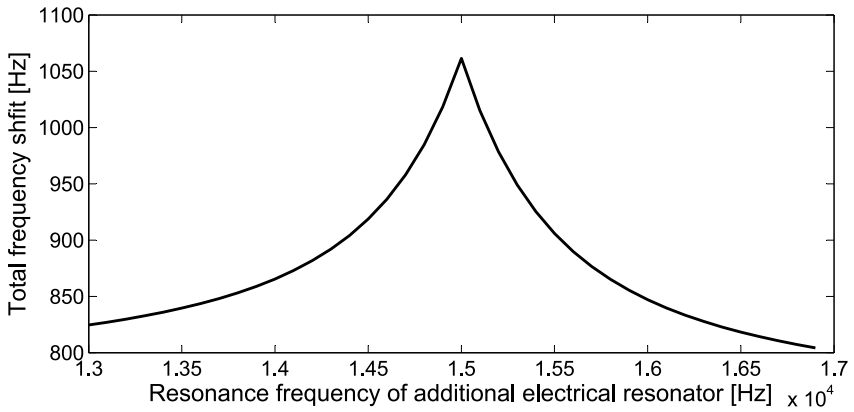


Figure 4.11: Total frequency shift after coupling an additional electrical resonator with different resonant frequencies to an array of two MEMS resonators.

transimpedance amplifier. The output is amplified and added to the driving voltage of the electrical circuit. The gains in the two signal paths, electrical to MEMS and MEMS to electrical, are carefully adjusted.

To capture the required resonant frequency of the electrical resonator, a simulation was undertaken by coupling a resonator with varying resonant frequencies to an array of two resonators with the same 15kHz resonance, assuming 5% coupling. The result in Figure 4.11 shows that a more prominent total frequency shift for all elements is achieved by matching the centre frequency of the resonant circuit to the natural frequency of the MEMS resonator at around 15kHz. This helps enhance the readout accuracy and model robustness, as suggested by the error analysis performed in Section 2.5.3.

Figure 4.12 shows the simulated responses of one MEMS resonator and the electrical resonator before and after coupling, assuming a same quality factor 1000 for each uncoupled resonator. Previous to coupling, the electrical resonator demonstrated one eigenvalue related to its centre frequency, while the MEMS array had two eigenvalues. After connecting them together, the readout from either the electrical or mechanical resonator contained the same three eigenvalues.

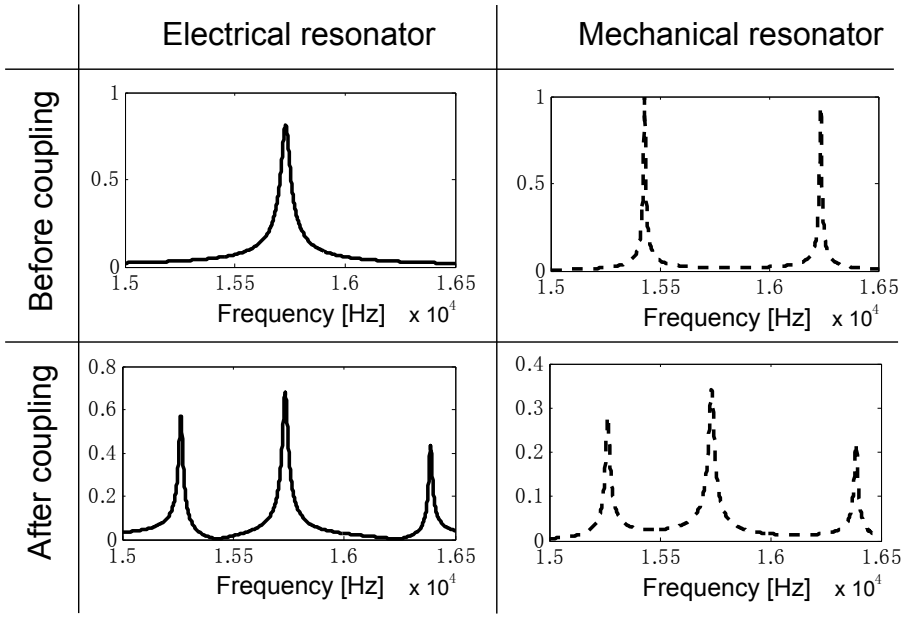


Figure 4.12: Simulated responses from electrical and mechanical resonators before and after coupling.

4.4 Experiment and Results

The last two sections have explained the dynamics of the mechanical and electrical resonators, and have proposed a mechanism to couple them. This section designs a set of experiments to verify the ideas and provide IEA characterisation results.

4.4.1 Frequency Response and System Matrix

Experimentally, with the electrical resonator coupled to the mechanical array, a driving voltage F_e was applied to the electrical resonator with a frequency sweep from 15kHz to 16.5kHz and a step of 1Hz. The measured responses of both the electrical and mechanical resonators are presented in Figure 4.13, showing three collective resonant frequencies at 15343Hz, 15745Hz and 16037Hz. With the damping effect ignored, these frequencies were used to represent the three eigenvalues of $\mathbf{S_3}$. The electrical resonator was then disconnected from the two mechanical resonators and the driving voltage was directly applied to one of the two coupled MEMS resonators. From the mechanical readout, two resonant peaks at 15371Hz and 16025Hz were observed. Using the new technique based on de Boor and Golub's algorithm, as

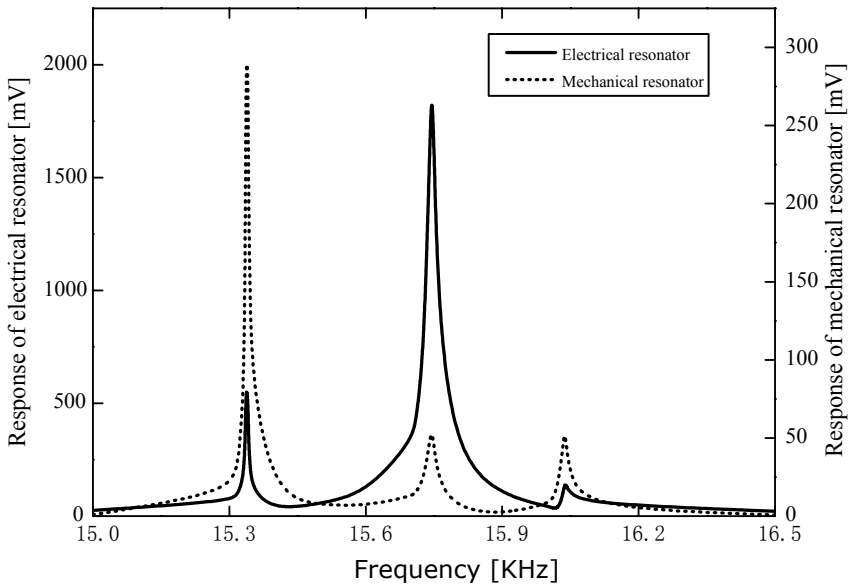


Figure 4.13: Experimentally measured responses from electrical and mechanical resonators after coupling.

discussed in Section 2.5.2, the system matrix $\mathbf{S_3}$ was extracted to be:

$$\mathbf{S_3} = 10^9 \times \begin{bmatrix} 9.9280 & -0.3552 & 0 \\ -0.3552 & 9.5375 & -0.1465 \\ 0 & -0.1465 & 9.7681 \end{bmatrix} \tag{4.24}$$

It is the diagonal elements of this matrix that contain the information about individual resonators, and are hence more relevant to sensing or characterisation. For example, the diagonal elements of $\mathbf{S_3}$ suggest that the centre frequency of the electrical resonator is 15730Hz. This can be verified by comparing with the actual resonant frequency of the electrical resonator (15723Hz). The relative error is as small as 0.04%. Similarly, the natural frequencies of the two MEMS resonators can be derived.

4.4.2 Validation

Two different approaches were used to further validate the results. For the first approach, perturbation analysis was performed in the conventional way using DC voltage based non-linearity in the spring. The electrical resonator was first disconnected, and then the MEMS array was perturbed by changing the applied DC voltage on one of the resonators. Ahead of the perturbation, resonant frequencies

were measured to be 15371Hz and 16024Hz. Following the perturbation, they shifted to 15388Hz and 16031Hz. These two sets of frequencies were converted into eigenvalues to extract the two-element system matrix:

$$\mathbf{S_2} = 10^9 \times \begin{bmatrix} 9.9000 & -0.3682 \\ -0.3682 & 9.5643 \end{bmatrix} \tag{4.25}$$

As $\mathbf{S_2}$ is the left principal submatrix of $\mathbf{S_3}$, the new technique produced comparable results. As mentioned formerly, the non-linear spring constant change introduced by the conventional method could affect the accuracy of measurement.

To further validate the results, a second approach using perturbation analysis on the complete electrical-mechanical array was also performed. When the electrical resonator was coupled to the MEMS array, perturbation was induced by simply changing the centre frequency of the electrical resonator. Frequency shifts for all three peaks were observed in Figure 4.14 to give another three eigenvalues. With these two sets of eigenvalues pre and post perturbation, the system matrix $\mathbf{S_3}$ was once again calculated:

$$\mathbf{S_3} = 10^9 \times \begin{bmatrix} 9.9195 & -0.3634 & 0 \\ -0.3634 & 9.5417 & -0.1334 \\ 0 & -0.1334 & 9.7726 \end{bmatrix} \tag{4.26}$$

The diagonal elements of the above system matrix show good agreement with the system matrix in Equation 4.24, indicating the feasibility and accuracy of the newly proposed technique.

4.5 Sensitivity Determination

The fabricated system matrix of the 2-resonator coupled systems, extracted by the inverse eigenvalue techniques in the previous section, provides a new way of understanding the sensitivity and process variability. This section studies the process-induced sensitivity shift of the device using forward analysis, and also reports an electronic trimming method with the help of the electrical circuit.

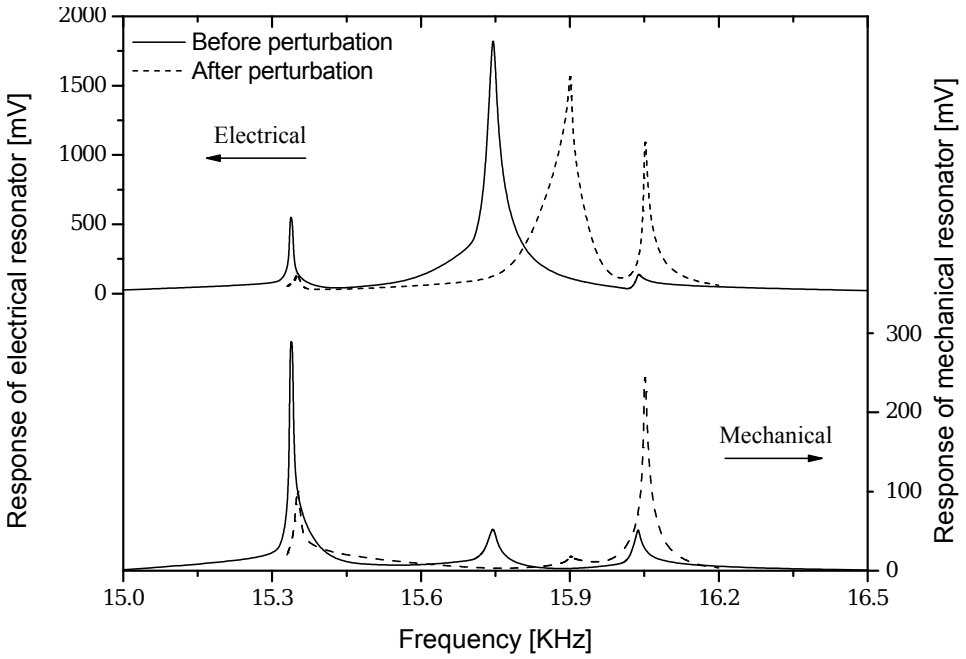


Figure 4.14: Measured responses of the electrical resonator and the mechanical resonator before and after a perturbation upon the centre frequency of the electrical resonator.

4.5.1 Process Variability

To understand how the manufacturing process affects the sensitivity in coupled systems, one can recall the forward perturbation analysis in Section 2.3.2:

$$\begin{aligned}
\frac{\partial \lambda_i}{\partial \mathbf{K}} =& x_{p,i} x_{q,i} (2 - \delta_{p,q}) \\
\frac{\partial \lambda_i}{\partial \mathbf{M}} =& \lambda_i x_{p,i} x_{q,i} (2 - \delta_{p,q}) \\
\frac{\partial \mathbf{x_i}}{\partial \mathbf{K}} =& \frac{x_{p,j} x_{q,i} (2 - \delta_{p,q})}{\lambda_i - \lambda_j} \mathbf{x_j} \Big|_{i \neq j} \\
\frac{\partial \mathbf{x_i}}{\partial \mathbf{M}} =& \frac{x_{p,i} x_{q,i} (\delta_{p,q} - 2) \mathbf{x_i}}{2} + \frac{\lambda_i x_{p,j} x_{q,i} (\delta_{p,q} - 2)}{\lambda_i - \lambda_j} \mathbf{x_j} \Big|_{i \neq j}
\end{aligned} \tag{4.27}$$

This analysis provides two different sensing mechanisms, one based on the eigenvalues and the other on the eigenvectors. The eigenvectors are more sensitive but they are, however, less linear and have limited dynamic range compared to the eigenvalues. A sensor designed using these equations will suffer from two different types of process irregularity. First, there will be absolute errors, which will shift the spring constants of the main and coupling springs as well as masses of the resonators by a fixed amount. Such absolute errors are generally unknown in advance, but are typically

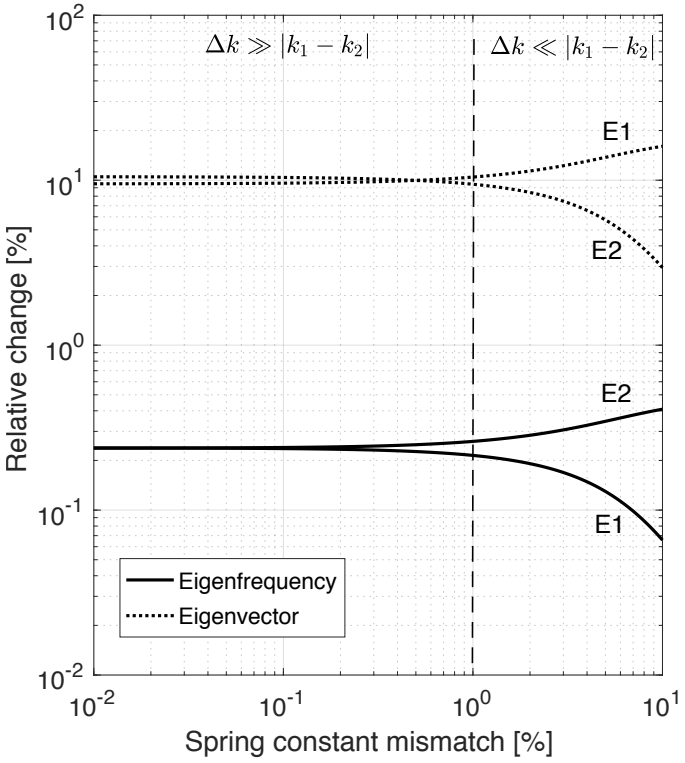


Figure 4.15: The effect of device mismatch on eigenfrequency and eigenvector sensitivities, assuming under 1% perturbation.

measurable. For example, if the stiffness of both resonators shifts by $\Delta k/k$, the mass shifts by $\Delta m/m$ and there are negligible errors in the coupling spring, the eigenvalues will shift by $(\Delta k/k - \Delta m/m)$. However, the eigenvectors will remain the same. This means that there will be a small shift in eigenvalue sensitivity, but negligible change in eigenvector sensitivity. In addition, there will be a second error due to manufacturing variations between the individual resonators.

Figure 4.15 simulates how eigenfrequency and eigenvector sensitivities at eigenmode 1 and 2 change when there is device mismatch, which has been defined as $|(k_1 - k_2)/(k_1 + k_2)|$. As one would expect, its impact on sensitivity can be ignored when the perturbation is larger than mismatch ($\Delta k \gg |k_1 - k_2|$). For a small perturbation ($\Delta k \ll |k_1 - k_2|$), however, the sensitivity of the eigenvector (E1) or eigenfrequency (E2) declines sharply. The second mode of the eigenvector and the first mode of the eigenfrequency, on the other hand, experience mild sensitivity improvement. These simulation results can be compared with the characterised

sensitivities of the sensor by performing forward perturbation analysis on the system matrix, which will be studied next.

4.5.2 Characterisation Results

The system matrix of the three-element array has been determined in Equation 4.24. The system matrix of the two MEMS resonators is its submatrix adjusted for coupling strength:

$$10^9 \times \begin{bmatrix} 9.39 & -0.36 \\ -0.36 & 9.93 \end{bmatrix} \tag{4.28}$$

which can be compared with the designed value

$$10^9 \times \begin{bmatrix} 6.69 & -0.08 \\ -0.08 & 6.69 \end{bmatrix} \tag{4.29}$$

Therefore, compared to the design, the diagonal and off-diagonal elements have deviated by 44.4% and 350% respectively. Despite the fact the two resonators were designed with the same geometry, there is 2.8% mismatch between diagonal elements.

Forward analysis can now be performed to determine the eigenfrequency or eigenvector sensitivity by perturbing a diagonal element of the system matrix. This can represent a certain mass/stiffness change. Figure 4.16 depicts the eigenfrequency and eigenvector changes at two sensing modes under different perturbation levels, and compares the designed and characterised values. Herein, the amplitude ratio of two resonators is used as the sensing metric for the eigenvector approach, which is equal to 1 when $k_1 = k_2$.

Ideally, for two identical resonators, the zero operating point (e.g. zero perturbation point) is the symmetric point of two response curves at mode 1 and mode 2. However, due to device mismatch, a zero drift of sensor operating point has been observed for both eigenfrequency and eigenvector methods. As a result, the behaviour of the two modes are no longer symmetrical and only one mode exhibits a linear response. As suggested by Section 3.2, this could limit the accuracy and sensing range, particularly for multi-mode sensing applications. One way of

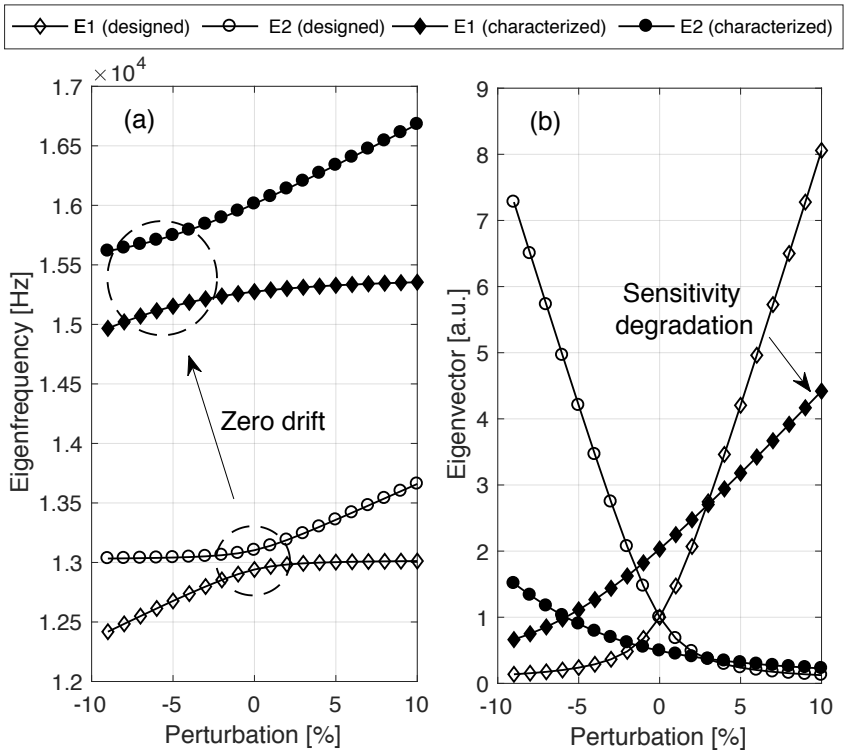


Figure 4.16: Designed and characterised sensitivities of (a) eigenfrequencies and (b) eigenvectors under different perturbations.

compensating for this effect is to apply an additional electrostatic stiffness with DC voltage. Maximum sensitivities can be achieved at mode 1 for the eigenvector method and at mode 2 for the eigenfrequency approach. Considering mass sensing as an example, the maximum eigenvector sensitivity has degraded by 54.2% compared with the original design. Eigenfrequency sensitivity, conversely, has increased from 77ppm/ng to 102ppm/ng at mode 2 and decreased from 53ppm/ng to 25ppm/ng at mode 1, matching with the trend in Figure 4.15. As indicated by previous simulations, this could be caused by the effect of device mismatch which moved the operating point away from the veering zone in Figure 4.16(a). This altered the gradient of eigenfrequency curves differently for two modes.

4.5.3 Sensitivity Shift

To better understand the effect of process variability, the resonant comb structure and coupling string were observed through SEM images in Figure 4.17(a)(b). Here W_f and L_f are the width and length of each finger structure, and g is the gap

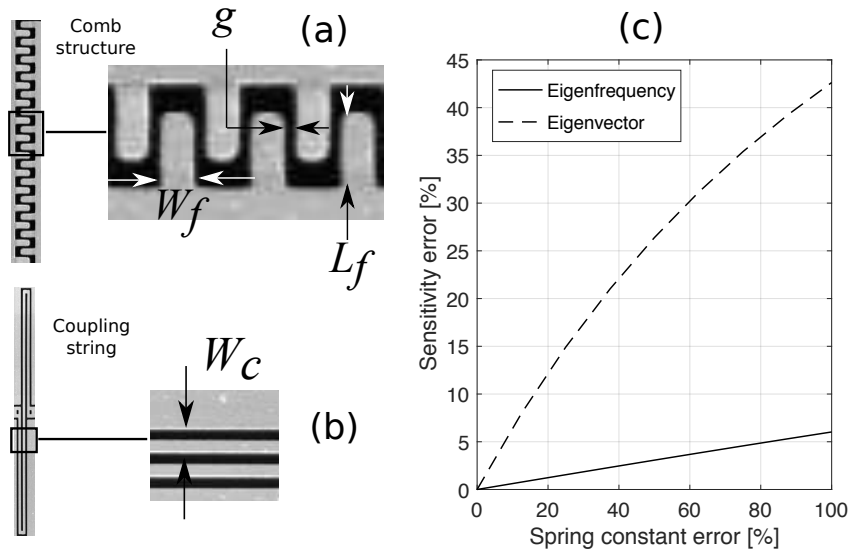


Figure 4.17: SEM images of (a) resonator comb structure and (b) coupling string. (c) Sensitivity errors of eigenfrequency and eigenvector methods caused by spring constant variations.

Table 4.2: Designed and characterised performance of the device.

Metric		**Designed**	**Characterised**
Sensor geometry	W_f	3μm	3.3μm
	L_f	10μm	10.2μm
	g	3μm	1.3μm
	W_c	3μm	4.5μm
Spring constant	k_1	23.8N/m	32.5N/m
	k_2	23.8N/m	34.5N/m
	k_c	0.3N/m	1.3N/m
Operating point	Eigen-frequency	E1: 12941Hz E2: 13103Hz	E1: 15371Hz E2: 16025Hz
	Eigen-vector	E1: 1 E2: 1	E1: 2.03 E2: 0.49
Mass sensitivity (1% change)	Eigen-frequency	E1: 53ppm/ng **E2: 77ppm/ng**	E1: 25ppm/ng **E2: 102ppm/ng**
	Eigen-vector	**E1: 12568ppm/ng** E2: 8368ppm/ng	**E1: 5751ppm/ng** E2: 1253ppm/ng

distance between adjacent fingers. The coupling string width is denoted by W_c. Table 4.2 compares the designed sensor performance against the characterised one. The width of the comb fingers and coupling string are oversized by 10% and 50% respectively, as a result of process variation during lithography. Therefore, an increase in the width from 3μm to 4.5μm has a potential of increasing the stiffness

by 2.4×, which agrees well with the observed coupling strength change. The increase in resonator mass can be ignored as it is less affected by geometry variation. A combination of these two factors leads to an 18.9% increase in resonant frequency.

The table also summarises the operating points of the eigenfrequency and eigenvector methods. Eigenfrequencies operate at higher frequencies of 15371Hz and 16025Hz, which can be compared with the designed 12941Hz and 13103Hz frequencies. The eigenvector shifts from (1,1) to (2.03,0.49), which means the first resonator has a larger amplitude at mode 1 and a smaller amplitude at mode 2 compared with the second resonator.

Contrary to the prediction in Figure 4.15, the eigenvector sensitivity shows a drastic decline in both modes. As the eigenvector sensitivity is associated with the gradient of the amplitude ratio at the zero perturbation point, the difference in the designed and characterised eigenvector sensitivity can also be visualised in Figure 4.16(b). To explain this, one can consider a coupled array of two identical resonators. The eigenvalue and eigenvector changes of this system, under small perturbations to the spring constant ($\Delta k \ll k_c$), can be approximated using Equation 4.27:

$$|\partial\lambda/\lambda| \approx |\Delta k/2k|\,, \quad |\partial\mathbf{x}/\mathbf{x}| \approx |\Delta k/4k_c| \tag{4.30}$$

For a given perturbation $\Delta k/k$, the eigenfrequency sensitivity remains relatively stable while the eigenvector sensitivity is highly susceptible to coupling strength. For the fabricated device, the coupling ratio has increased by more than twice due to the substantially over-sized coupling string, which has deteriorated the eigenvector sensitivity. The simulation results in Figure 4.17(c) have also confirmed this hypothesis by showing the sensitivity changes of eigenfrequency and eigenvector methods under different spring constant errors. It can be implied that coupling string design plays a crucial role in eigenvector sensing. For example, for the presented resonators, a wider and shorter coupling beam could be used to alleviate process-induced oversizing effect.

Table 4.3: Eigenvector and eigenvalue changes after 0.1% perturbation on the first MEMS resonator.

Sensing metric	Resonator	E1	E2	E3
Eigenvector	MEMS 1	-0.977%	-1.407%	0.508%
	MEMS 2	0.239%	4.967%	-0.881%
	Electrical	0.704%	0.064%	-2.642%
Eigenvalue	Any	0.024%	0.009%	0.067%

Table 4.4: Eigenvector and eigenvalue changes after 0.1% perturbation on the second MEMS resonator.

Sensing metric	Resonator	E1	E2	E3
Eigenvector	MEMS 1	0.733%	0.755%	-0.341%
	MEMS 2	-0.334%	0.656%	0.826%
	Electrical	1.093%	-0.089%	0.143%
Eigenvalue	Any	0.073%	0.001%	0.026%

4.5.4 Sensitivity Tuning

Once the microsystems are fabricated, the actual performance may represent a substantial departure from the original design due to process-induced variability. Tuning each resonator electrostatically to compensate for fabrication errors or device mismatches can be one solution, but this requires access to each element and introduces non-linearity. The attached electrical resonator, however, provides an effective way of tuning the sensitivity of the coupled systems by simply changing its centre frequency within a desired range. One can therefore improve the sensitivity of a particular resonator or eigen-mode. To manifest how this works, consider the constructed three-element coupled array, including two MEMS resonators and one electrical resonator, which has a system matrix derived in Equation 4.24. The eigenvector or eigenvalue sensitivity of the array, when 0.1% perturbation happens on the first or second MEMS resonator, can be determined using the forward perturbation analysis in Equation 4.27. The results are shown in Table 4.3 and 4.4, where MEMS 1 and MEMS 2 denote the first and second mechanical resonators.

In Table 4.3, when the stiffness or mass of the first MEMS resonator changes, the second resonator at the second eigen-mode experiences the largest amplitude shift at 5%. Using the amplitude ratio of MEMS 2 and MEMS 1 at E2 provides an

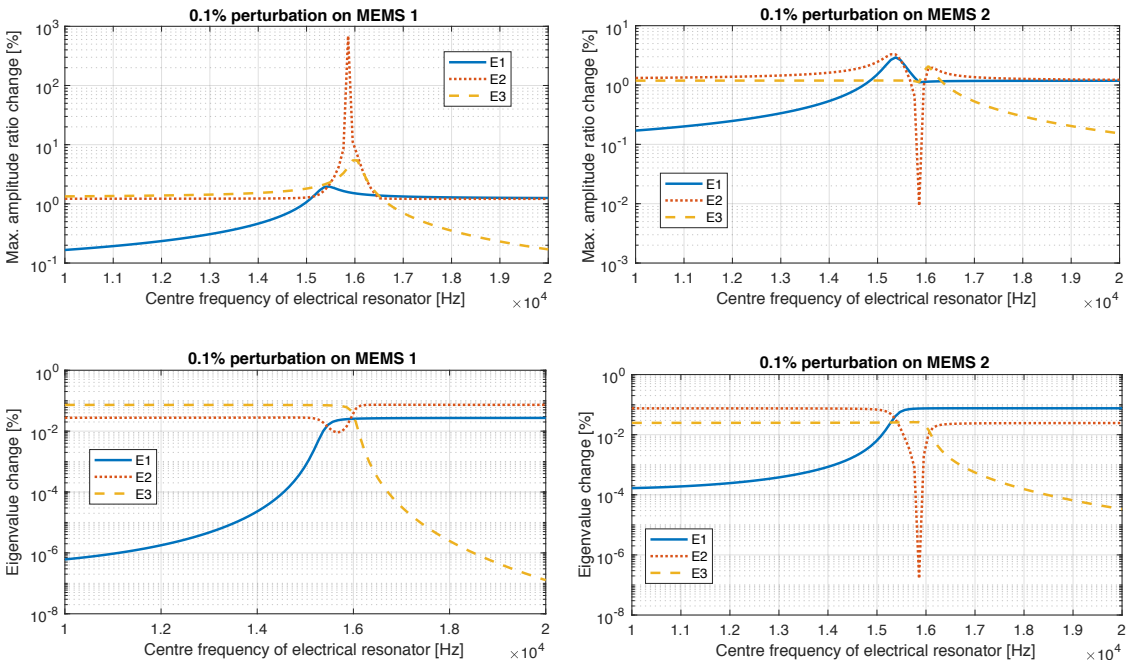


Figure 4.18: Sensitivity tuning by changing the centre frequency of the electrical resonator.

optimal sensitivity at around 6.4%. Similarly, the maximum eigenvector sensitivity at E1 is 1.7% by sensing the amplitude ratio of the electrical resonator and MEMS 1. At E3, a peak sensitivity at 3.1% can be achieved using the ratio of MEMS 1 and electrical resonator. For eigenvalue sensing, the readout from any resonator gives a maximum sensitivity at E3 (0.067%).

Based on the same analysis, the sensitivity of the systems by perturbing the second MEMS resonator can be derived from Table 4.4, which provides a maximum eigenvector sensitivity at 1.4% by using the amplitude ratio of the electrical resonator and MEMS 2 at the first eigen-mode, and a maximum eigenvalue sensitivity at 0.073% using the first eigen-mode. The overall maximum eigenvector and eigenvalue sensitivity can therefore be determined and compared with the two coupled MEMS systems in Table 4.2. For mass sensing, the maximum sensitivity after connecting the electrical resonator is 17778ppm/ng for the eigenvector and 87ppm/ng for the eigenvalue.

Figure 4.18 shows the sensitivity tuning capabilities of the electrical resonator by changing its centre frequency between 10kHz to 20kHz. At each centre frequency, one

can compare the eigenvalue and maximum amplitude ratio changes after perturbing the first/second MEMS resonator by 0.1%. While eigenvalue sensitivity does not benefit from the electrical resonator, eigenvector sensitivity can be substantially enhanced. Two orders of magnitude higher sensitivity for perturbing the first resonator can be achieved at E2 by tuning the electrical resonator frequency to around 15859Hz. When perturbing the second resonator, the sensitivity enhancement is not as prominent, but still increases the maximum amplitude ratio change from 1.4% to 3.3% after setting the centre frequency of the electrical resonator to 15275Hz. These results have proved the concept of an electronic trimming scheme by using the peripheral circuit. To experimentally implement such a technique, the centre frequency of the electrical resonator needs to be precisely controlled to stabilise the sensitivity enhancement factor. This will serve as a topic for the future work.

4.5.5 Scalability

Coupled sensing in nano electromechanical resonators has recently gained tremendous attention [125]. Hence, it is important to analyse the scalability of the technique used in this chapter. The shrinking of fabricated devices enables smaller sensors with enhanced resolution and the ability to form a large array. Nanofabrication technology also makes it possible to manufacture weaker and more robust coupling springs to heighten the sensitivity.

Since the device in this work was fabricated by an external foundry with one photoresist mask and on a multiple-project wafer (MPW) run, the dimensions are constrained to μm, and vary considerably for smaller beams. However, mode localisation is also widely seen in the nano scale. Essentially, coupled nano-systems share the same principle, hence the characterisation technique is still valid. While the sensitivity analysis has been undertaken on micro-scale devices, the results are equally effective for nano-scale dimensions due to similarity in manufacturing process. In order to study manufacturing variations, one needs to a have a more mature manufacturing process. This is so as any analysis from a novel fab could be attributed to quality control rather than inherent variability. Hence, the simple

approach used in this work is to analyse manufacturing variations at micro-scale dimensions from a commercial or very stable manufacturing line and then extrapolate the analysis to nano-scale.

4.6 Summary

Inverse eigenvalue analysis has been used to actuate and characterise coupled MEMS resonators. For an array of n coupled resonators, the coupling effect makes it possible to monitor n resonant frequencies by driving and measuring from only one member. These n resonant frequencies correspond to n eigenvalues of the system matrix of the coupled resonators. To inversely reconstruct the system matrix, another set of eigenvalues needs to be measured by exerting a change to the system. De Boor and Golub's algorithm, which involves the coupling of an additional electrical resonator, has been proposed to facilitate such a change and obtain the required eigenvalues. Rather than perturbing the spring constant of the MEMS array, this technique measures a second set of eigenvalues by coupling an external electrical resonator. Not only is such a coupling mechanism easy to implement, it also avoids non-linear change or even damage to the mechanical systems. In addition, the technique benefits from minimal bond pads and wire connections required, hence reducing the bandwidth and cost.

This new technique has been validated by characterising the system matrix and eigen-sensing information of two mechanically coupled MEMS resonators. Forward perturbation analysis shows a zero shift of the eigenfrequency and eigenvector as a result of device mismatch. Since eigenvectors are very sensitive to coupling ratio change, the oversized coupling string caused by lithography error has deteriorated the maximum sensitivity substantially (by 54.2%,). The eigenfrequency sensitivity, on the other hand, is only affected slightly due to device mismatch. To overcome process-induced sensitivity degradation, the centre frequency of the electrical resonator can be tuned to enhance the sensitivity of eigenvector sensing. The results provide valuable insight for coupled sensors designers and the new characterisation method offers a simple and low-cost solution for sensor testing and process monitoring. It

also provides a benchmarking strategy for future arrays of coupled nano-systems in light of process variations.

There is nothing, Sir, too little for so little a creature as man. It is by studying little things that we attain the great art of having as little misery and as much happiness as possible.

— Samuel Johnson

5

Corner Coupled Square Plate Resonators

Contents

5.1 Introduction 99
5.2 Resonant Square Plate 100
5.2.1 Resonance 100
5.2.2 Direct Drive and Readout 102
5.2.3 DC Bias 104
5.3 Corner Coupling 106
5.4 Design and Fabrication 108
5.4.1 PolyMUMPs 109
5.4.2 Parameters 110
5.5 Performance 111
5.5.1 Electromechanical Properties 111
5.5.2 Over-sizing 114
5.6 Array Perturbation 115
5.6.1 Electrostatic Perturbation 115
5.6.2 Terminal Decoupling 117
5.7 Summary 118

A significant part of this chapter has been published as:

- Guowei Tao and Bhaskar Choubey. "Inverse eigenvalue sensing with corner coupled square plate MEMS resonators array". In: *Analog Integrated Circuits and Signal Processing* 95.3 (2018), pp. 447–455

- Guowei Tao and Bhaskar Choubey. "IEA sensing for corner coupled square

plate MEMS resonators arrays". In: *Oxford Circuits and Systems Conference (OXCAS)*. 2017

5.1 Introduction

In the previous chapter, an array of two coupled micro resonators based on interdigitated combs has been characterised. Despite the high linearity of these comb structure resonators, their large mass (3.6μg) and low frequency (13kHz) are restricting the sensing resolution and potential applications. The numerous finger structures are prone to parasitic capacitance due to the undesired capacitors formed between the other sides of the comb arms [126]. Hence, complicated differential actuation circuits are required. Coupling dozens of those can be difficult for two reasons. First, as these resonators are large in size, arranging them in arrays would take up a substantial fabrication area. Second, for large coupled systems, some resonances can be too weak to capture through one resonator readout due to mode diminishing and noise effects.

To circumvent these problems and further extend to unique applications, an alternative MEMS design is desired. Square plate MEMS resonators can be a potential substitute to achieve large-scale multi-sensing. They offer several advantages. First of all, due to the simplicity and robustness of such a design, its vibration modes have been well studied. In addition, with a compact double-plate architecture, the resonant plate may serve as a basic building block to form massive arrays. The structure also employs a simultaneous capacitive actuation, making it feasible to test the array as a full sensor using discrete electronics within a single package. Most importantly, it is possible to couple scores of these resonators on the same substrate. Demirci and Nguyen reported a low-impedance resonant array by connecting more than ten square plate resonators using a corner coupling mechanism [66]. These corner coupled square plate MEMS resonators, having symmetric mode shapes and flexible phasing capabilities, can be explored for sensing applications.

This chapter aims to design, fabricate and test coupled arrays of such square plate resonators. The chapter starts by modelling a single vibratory unit, based

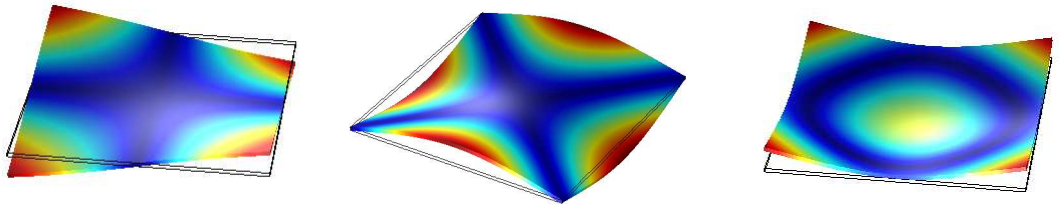


Figure 5.1: The three lowest modes of a resonant plate under free flexural vibration.

on which large systems can be constructed using corner coupling. Arrays of coupled devices are then designed and fabricated through foundry facilities. In the end, the chapter characterises the fabricated prototype sensors and evaluates different perturbation mechanisms.

5.2 Resonant Square Plate

Square plate resonator is a simple structure that utilises the flexural or bulk mode vibration of a square plate, and has been extensively applied in the fields of radio frequency and communication [127, 128]. Recently, square plate resonators have also attracted attention in mass sensing [129]. Agache *et al.* reported a square plate MEMS resonator with an embedded microfluidic channel to achieve a mass responsitivity superior to clamped-clamped beam or cantilever sensors [25].

In this section, the flexural vibration of a resonant square plate, which provides a large surface-to-volume ratio and differential capacitive actuation, will be explored. It is capable of providing a sufficiently high quality factor (e.g. $Q > 10000$ under vacuum [66]). This can substantially enhance the accuracy of inverse eigenvalue sensing. This section models such a resonant square plate by providing analysis on its resonance, actuation and DC bias.

5.2.1 Resonance

A flexural-mode resonator provides transverse standing waves, with the displacement of the structure orthogonal to the bending stress. During the deformation, the accumulated potential energy and kinetic energy of the plate can be derived. By

applying particular boundary conditions, these will finally lead to the differential equation of vibrations of the plate. For an ideal square plate with clamped edges, the solution is in a simple format [130]. However, as suggested by Ritz [131], plates with free edges have more complicated solutions. In addition, the fabrication requirement often leads to a non-perfect shape, which can be difficult to model mathematically. However, they can be solved accurately using finite element method (FEM) tools. FEM provides numerical solutions to boundary value problems in partial differential equations. In this work, COMSOL Multiphysics is being used to undertake FEM analysis of the MEMS vibratory structures. Solid mechanics interface is used for eigenfrequency analysis. To perform stationary study, MEMS module and electromechanics interface are included. Linear elastic material is assigned to a polysilicon plate.

Figure 5.1 simulates an example of the three lowest modes of such a resonant plate under free flexural vibration. The dark colour marks the nodal lines of the plate, where the amplitude is zero. These nodal lines can be used to anchor the device or weakly couple it to another plate while preserving the mode shape. In this work, the second mode in Figure 5.1(b) is exploited. The eigenfrequency of such a mode is slightly (about 14%) less than the third mode, but is substantially (about 46%) higher than the first mode [130]. However, compared with the third mode, it allows the device to be anchored using either centre or corner stem and provides a flexible corner coupling mechanism. In addition, the unique mode shape facilitates the electrode design underneath to intelligently control the phase and suppress other modes [132]. When actuated at the second mode, the two diagonal lines of the plate remain stationary. Meanwhile, the adjacent sides resonate at the same magnitude, but with 180° phase difference. Hence, by measuring from different locations, one can achieve flexible phasing and control the direction of the output current. The design also offers electrical benefits such as low impedance. In view of the above, the second transverse mode is an ideal candidate to build a large coupled array for sensing and transducing.

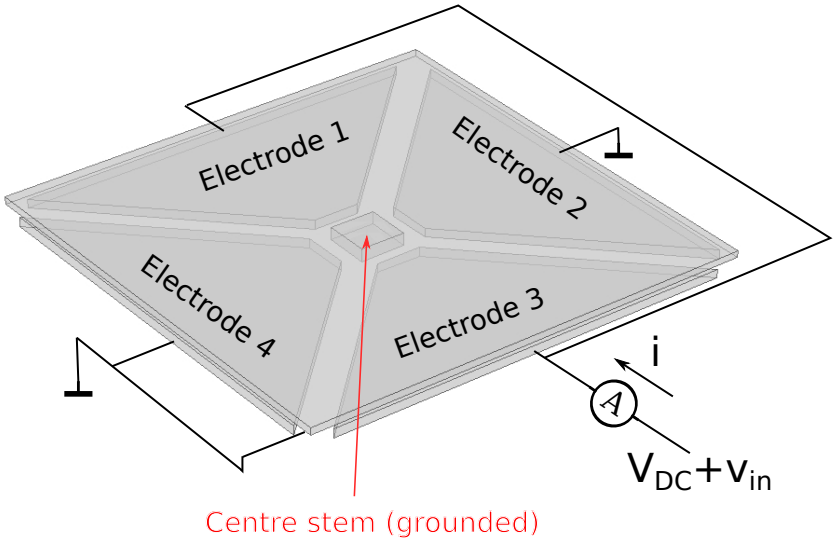


Figure 5.2: Electrical connections for one centre-stemmed plate resonator.

Using the proposed mode, the natural frequency f_0 of such a square plate with Young's modulus E, density ρ, side length L, and plate thickness d_p takes the form [130]

$$f_0 \approx \sqrt{\frac{E}{\rho}}\frac{d_p}{L^2} \tag{5.1}$$

The mass and stiffness of the resonator are calculated by

$$m = \rho d_p L^2 \tag{5.2}$$

and

$$k = E\left(\frac{2\pi}{L}\right)^2 d_p^3 \tag{5.3}$$

To achieve the transverse mode resonance, a dedicated actuation scheme is desired, which will be studied next.

5.2.2 Direct Drive and Readout

The simple structure benefits from simultaneous drive and readout. Figure 5.2 depicts a centre-stemmed square plate with driving electrodes at the bottom. The electrical connections are also demonstrated. A DC bias V_{DC} superimposed with a small AC signal v_{in} is applied to bottom electrodes 1 and 3. Electrodes 2, 4 and the top plate are grounded. Any change in the resonant magnitude results

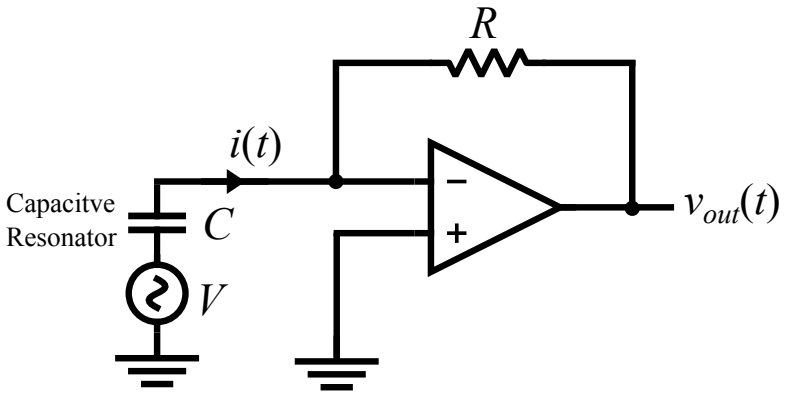


Figure 5.3: Actuating the capacitive resonator with a transimpedance amplifier.

in an AC current i which is linearly dependent on the vibration velocity, with the conductance being [66, 133]

$$|Y| = \left|\frac{i}{v_{in}}\right| = \frac{Q\varepsilon^2 S^2 V_{DC}^2}{\sqrt{km}d_0^4} \tag{5.4}$$

where d_0 is the initial gap distance between the top plate and bottom electrodes. S is the effective area where top plate and driving electrodes overlap.

The implementation of the direct drive and readout can be realised by a transimpedance amplifier designed in Figure 5.3. This allows simultaneous excitation of the device by applying a drive voltage V to one plate, with the transimpedance amplifier connected to the other plate to turn the time-dependent current

$$i(t) = V\frac{dC}{dt} + C\frac{dV}{dt} \tag{5.5}$$

into an output voltage signal

$$v_{out}(t) = -i(t)R \tag{5.6}$$

For a small signal ($v_{in} \ll V_{DC}$), the current is given by

$$\begin{aligned} i(t) =& V_{DC}\frac{dC}{dx}\frac{dx}{dt} + C\frac{d(v_{in}\cos\omega t)}{dt} \\ =& V_{DC}\frac{d(\varepsilon S/(d_0 - x))}{dx}\frac{dx}{dt} - \frac{\varepsilon S\omega v_{in}}{d_0}\sin\omega t \\ =& \frac{\varepsilon S V_{DC}}{d_0^2}\left(1 + 2\frac{x}{d_0} + 3\frac{x^2}{d_0^2} + \cdots\right)\frac{dx}{dt} - \frac{\varepsilon S\omega v_{in}}{d_0}\sin\omega t \end{aligned} \tag{5.7}$$

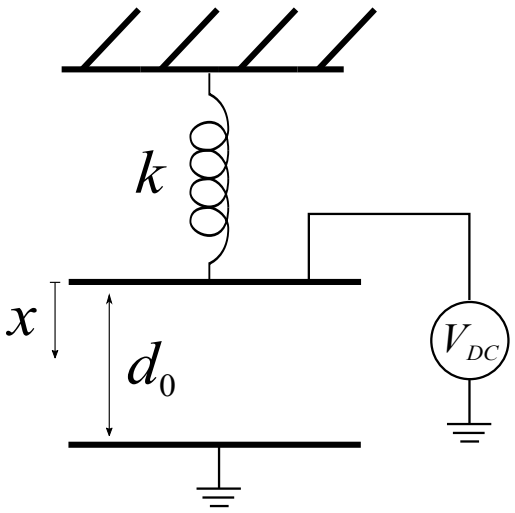


Figure 5.4: A simplified pull-in model using two parallel plates.

Ignoring higher order terms and letting $\dot{x} = dx/dt$ be the velocity of the vibration, the current can be approximated as

$$i(t) = \frac{\varepsilon S V_{DC}}{d_0^2}\dot{x} - \frac{\varepsilon S \omega v_{in}}{d_0}\sin\omega t \tag{5.8}$$

Such an expression contains a frequency-dependent AC component, which is not linked to mechanical motion. This is the drawback of applying the direct drive and readout scheme, but can be alleviated by using a small AC input.

5.2.3 DC Bias

The resonance of the proposed design is highly affected by the DC bias. The spring constant of the resonator can be tuned by tweaking the DC voltage, hence introducing a negative electrostatic stiffness

$$k_E = -\frac{\varepsilon S}{d_0^3}V_{DC}^2 \tag{5.9}$$

This reduces the resonant frequency. The spring softening effect provides a flexible way of perturbing the resonator as required by the IEA. In addition, an increase in the DC voltage strengthens the signal amplitude and hence the measured conductance. This, on the other hand, may cause non-linear and even pull-in effects that can potentially destroy the device.

To provide an insight into the pull-in effect for the MEMS structure, a simplified lumped model using two parallel conductive plates was proposed by Nathanson *et al.* [21], see Figure 5.4. The two plates, with each having an area S, are separated by an initial gap distance d_0. The bottom plate is fixed and grounded. Biased at a DC voltage V_{DC}, the top plate moves in the vertical direction with a static displacement x. Ignoring the mass, the top plate is only affected by a downward electrostatic force and an upward restoring spring force kx. In the equilibrium status, the electrostatic force equals the restoring force, hence

$$\frac{\varepsilon S V_{DC}^2}{2(d_0 - x)^2} = kx \tag{5.10}$$

For $0 < x < d_0$, the above equation is solvable only if the applied voltage is below a collapse voltage, which is calculated to be

$$V_{collapes} = \sqrt{\frac{8kd_0^3}{27\varepsilon S}} \tag{5.11}$$

Otherwise, the top plate would be pulled in towards the bottom plate thereby causing short circuit. The maximum displacement before the pull-in effect can also be calculated as

$$x_{\max} = \frac{d_0}{3} \tag{5.12}$$

The above one-third rule can be used to estimate the maximum allowed resonant magnitude.

One way of preventing the pull-in phenomenon from happening is to deposit a thin insulation layer, with a thickness of $d_{insulator}$ ($d_{insulator} \ll d_0$) and an electric permittivity of $\varepsilon_{insulator}$, on one of the electrodes. After the plate has collapsed, it can be restored by reducing the applied voltage to a snap-back value $V_{snap-back}$, which satisfies

$$\frac{\varepsilon_{insulator} S V_{snap-back}^2}{2d_{insulator}^2} = k(d_0 - d_{insulator}) \tag{5.13}$$

The snap-back voltage is derived as

$$V_{snap-back} = \sqrt{\frac{2kd_{insulator}^2(d_0 - d_{insulator})}{\varepsilon_{insulator} S}} \tag{5.14}$$

The snap-back or pull-in effect can be potentially used as a non-linear perturbation mechanism to activate or deactivate a particular resonant block.

The double-plate model provides a rough estimation of the collapse voltage. To analytically derive the pull-in voltage of the actual MEMS structure, more complicated calculations are required since the element is elastic, continuous and regulated by boundary conditions. In this scenario, the flexural stiffness at the maximum deflection location ($x = x_{\max}$), which is the edge of the plate, governs the instability. Hence, an effective stiffness k_{eff}, defined as

$$k_{\text{eff}} = \frac{q_0 l_c}{x_{\max}} \tag{5.15}$$

has been suggested to replace the stiffness in Equation 5.11 [134]. q_0 is a distributed transverse load over a partial length l_c that starts from the edge of the plate. In addition, the area in Equation 5.11 needs to be replaced with the effective area S_{eff} to factor in the fringing field effects and charge-redistribution effects [135]. The problem can also be addressed using COMSOL simulations, which will be presented later in Section 5.4.2.

In conclusion, the DC bias provides different degrees of perturbation depending on the magnitude. A small voltage reduces the spring constant linearly. However, when the magnitude increases, so does the non-linearity, which ultimately leads to the pull-in effect. So far, the characteristics of a single resonant plate have been explained. The next section will explore how resonator arrays may be formed by using the proposed square plate unit.

5.3 Corner Coupling

Arrays of square plate resonators can be coupled by arranging them in the same diagonal orientation and connecting two opposing corners using a mechanical beam. This coupling mechanism ensures that all the corner beams are stationary and in the same plane, without altering the mode shapes of the resonators. Figure 5.5 exhibits the in-phase and anti-phase vibration modes of two coupled square plate resonators.

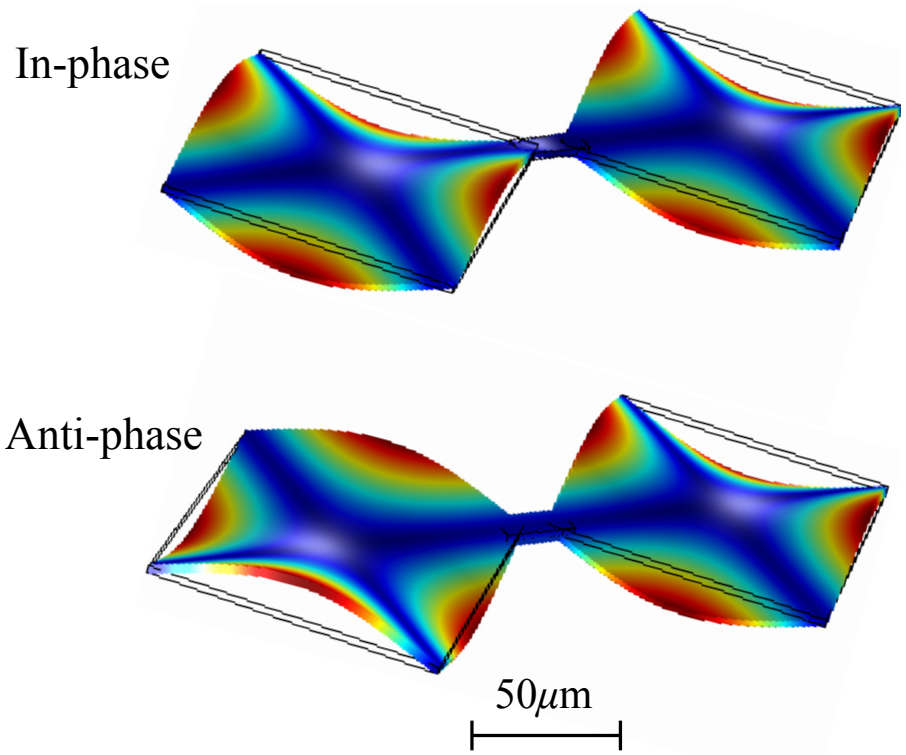


Figure 5.5: In-phase and anti-phase resonant modes of two coupled square plate resonators.

To understand how the geometry of the beam affects coupling, resonators with different beam lengths and widths were simulated in COMSOL. Figure 5.6(a) shows the geometry of two coupled square plate resonators with the same dimensions. W_c and L_c are the width and length of the coupling beam. By simulating combinations of these and recording the corresponding eigenfrequencies ω_1 and ω_2 at two modes, one may determine the coupling ratio using Equation 3.5:

$$\kappa \approx \frac{2(\omega_2 - \omega_1)}{\omega_2 + \omega_1} \tag{5.16}$$

Figure 5.6(b) presents the calculated coupling ratios for various beam geometries simulated through COMSOL solid mechanics interface, using a mesh size of 63052 elements and a minimum element quality of 0.03778. It can be observed that the coupling strength is three orders of magnitude more sensitive to W_c than L_c. By changing the width alone, the coupling ratio is tunable between 0.003% to 20%. Using such a corner coupling mechanism, it is now possible to establish

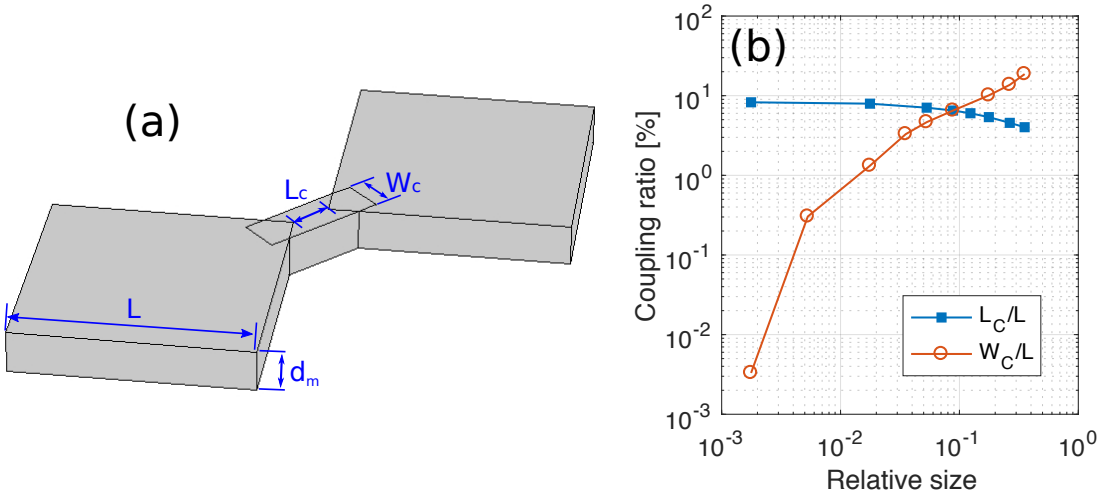


Figure 5.6: (a) The geometry of coupled square plate resonators and (b) simulated coupling ratios for different beam lengths and widths.

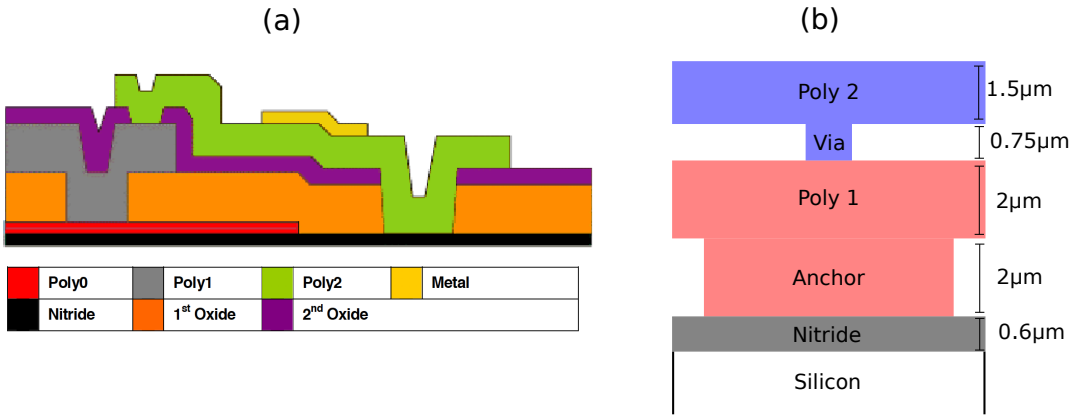


Figure 5.7: (a) Cross-sectional view of all layers of PolyMUMPs (courtesy of MEMSCAP). (b) Layers used for the proposed design and their dimensions.

large arrays of weakly coupled systems. These will be designed, fabricated and tested in future sections.

5.4 Design and Fabrication

Based on the theoretical foundations and simulation results, arrays of plate resonators can be designed and fabricated by accessing external manufacturing facilities. Foundries normally require additional design rules; therefore, it is important to understand the fabrication process and adjust the sensor parameters accordingly.

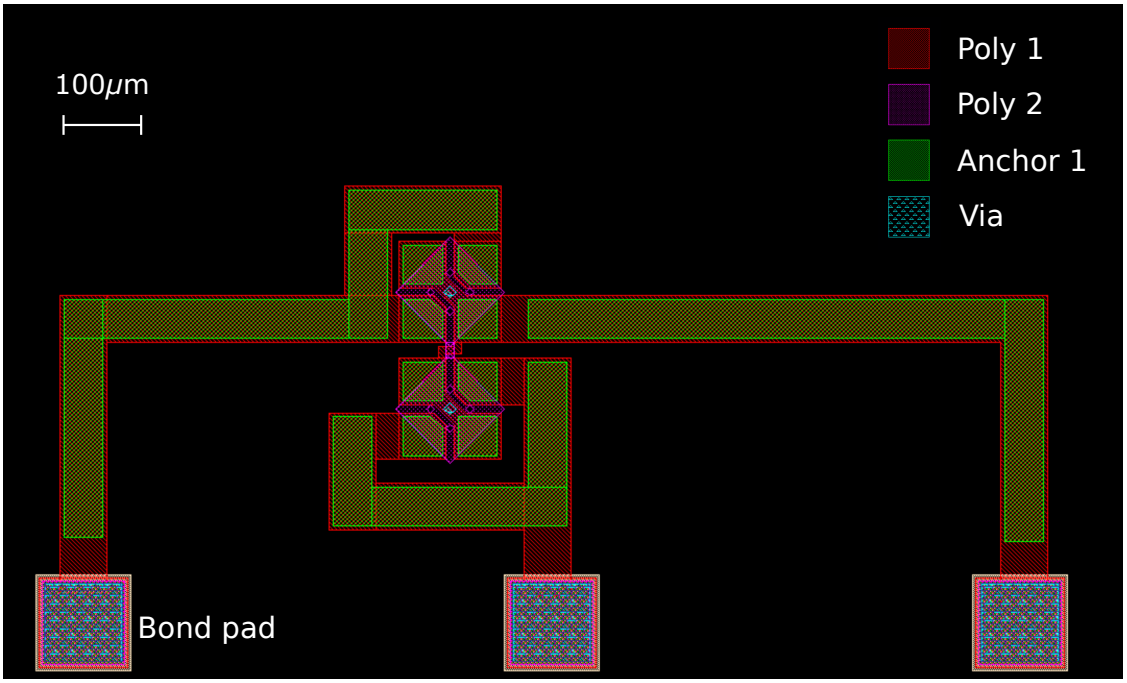


Figure 5.8: Layout of an example of two corner coupled square plate resonators.

5.4.1 PolyMUMPs

For fast prototyping of the designed square plate resonant sensors, one can use an established foundry. The Multi-user MEMS processes (MUMPs) programme offers standardised and low cost manufacturing easily approachable by users, without concerning about post processing and packaging [136]. The PolyMUMPs provided by the MEMSCAP Inc. was used for device fabrication.

The fabrication process was based on three-layer polysilicon surface micromachining, with its cross-sectional view illustrated in Figure 5.7(a) [137]. Specifically, two layers of polysilicon, i.e. Poly 1 and Poly 2, were incorporated in the layout. Since the polysilicon layers are conductive with 10Ω to 20Ω sheet resistance, the driving and readout electrodes as well as interconnections at the bottom were shaped by Poly 1. The interconnection wires were designed to be 60μm wide. Poly 2 acted as the centre-stemmed square plate. A 20μm × 10μm mechanical beam with the same Poly 2 material was used to couple the corners of two neighbouring square plates. The thickness of the square plate ($d_p = 1.5\mu$m) and the gap distance between the top plate and bottom electrode ($d_0 = 0.75\mu$m) were strictly defined

Table 5.1: Designed parameters of the proposed corner coupled square plate MEMS resonator array.

Parameter	Value	Unit
Plate side length, L	100	μm
Plate thickness, d_p	1.5	μm
Coupling beam length, L_c	20	μm
Coupling beam width, W_c	10	μm
Gap distance, d_0	0.75	μm
Young's modulus, E	158	GPa
Density, ρ	2330	kg/m^3
Stiffness, k	2020	N/M
Coupling strength, k_c	100	N/M
Mass, m	34	ng
Resonance, f_0	1.2	MHz
Conductance, $\|Y\|$	$\sim$14.5	μS
Pull-in voltage, $V_{collapse}$	50	V

by the process. As Poly 0 layer was not utilised, the device had to be anchored to the Nitride substrate by filling an anchor hole with Poly 1, thereby preventing the structure from falling off during HF release. The hole was formed by patterning silicon dioxide with a mask layer and reactive ion etching (RIE). 7μm $\times$ 7μm release holes with a maximum distance of 30μm in between were opened. Figure 5.7(b) shows all the layers used along with their thickness.

The layout was designed using the Cadence Virtuoso Analogue Design Environment. Figure 5.8 shows the layout of an example of two corner coupled square plate resonators based on the aforementioned principles. In addition, the bond pad design was based on a template provided by the MEMSCAP. Additional details about the layout, wire bonding and packaging for the test chips are described in Appendix C.

5.4.2 Parameters

The choice of parameters for the design is mainly dependent on the manufacturer, including the plate thickness, gap distance and material properties. The coupling beam width, which is the smallest part of the structure, is recommended to be no less than 5μm. Hence, it is designed to be 10μm to ensure robustness when forming large

arrays. After confirming the coupling beam width, the coupling beam length and plate side length can be calculated accordingly to provide around MHz resonance and 5% weak coupling, as suggested by the analysis in the previous section.

Table 5.1 details the designed parameters of the prototype MEMS resonator array. It is worth noting that the conductance $|Y|$ is an estimated value by assuming $Q = 10^4$ and $V_{DC} = 10$V. In practice, it is alterable depending on the experimental conditions. The DC bias is important since a higher value would augment the output signal strength. However, as V_{DC} rises, so does the risk of pull-in, which is detrimental to the device since the plates are not protected from any insulation layer. Therefore, further COMSOL simulations have been performed in Figure 5.9 to determine the static displacement of the plate by biasing electrodes 1 and 3 with different voltages. MEMS module and Electromechanics interface are used in the simulation. Fixed constraint is applied to the stem to anchor the plate at the centre. Electromechanical interface is assigned to the lower surface of the plate. Stationary electrical potential (bias voltage) is applied to electrode 1,3 to bend the plate, while the square plate, the centre stem and electrode 2,4 are grounded. The results suggest a pull-in voltage at around 50V based on the one-third rule specified in Equation 5.12. These simulation results will be verified in the subsequent experiments.

5.5 Performance

To evaluate the performance of the fabricated prototype sensors, a number of experiments were first conducted to characterise the properties of a single resonator.

5.5.1 Electromechanical Properties

Figure 5.10 presents the experimental setup for device testing. Operating at MHz range, the sensor is likely to pick up more noises (e.g. radio frequency noises). Hence, a two layered PCB with proper ground shielding on the bottom layer was designed to connect the resonator to an external impedance analyser. In the experiment, the sensor was attached to a DIL24 package, which was then mounted

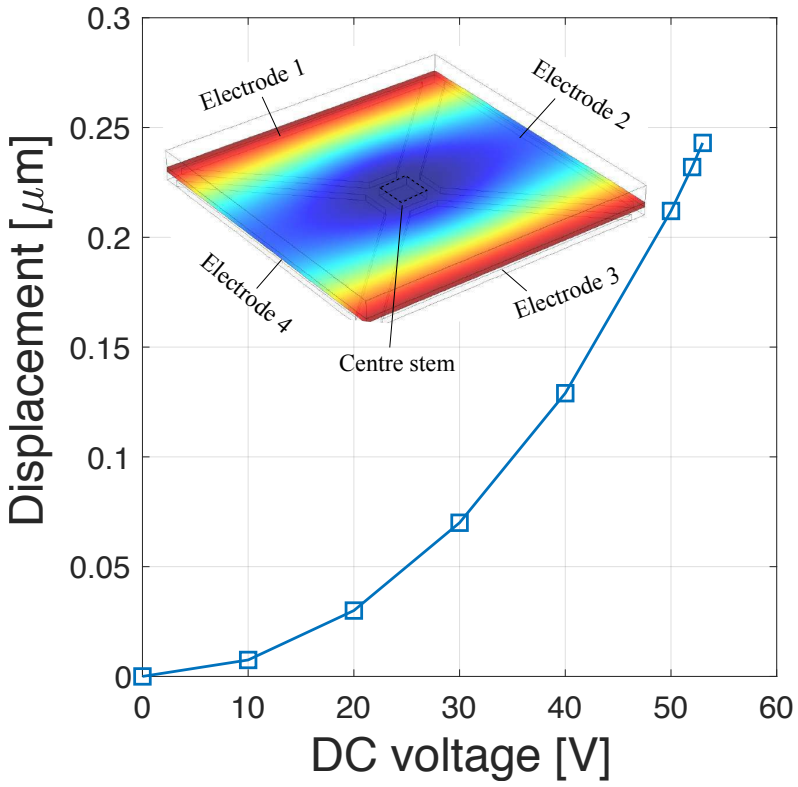


Figure 5.9: FEM simulation of the static displacement under various DC voltages.

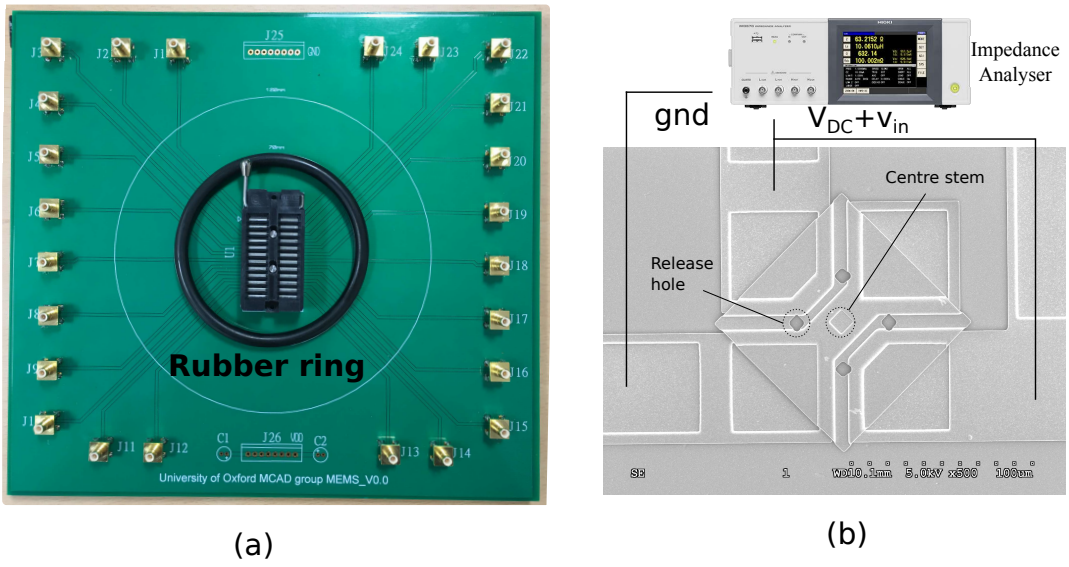


Figure 5.10: Experimental setup: (a) drive and readout PCB with rubber ring to seal the device under a vacuum pump; (b) SEM image of a single square plate resonator and test arrangement for the impedance analyser.

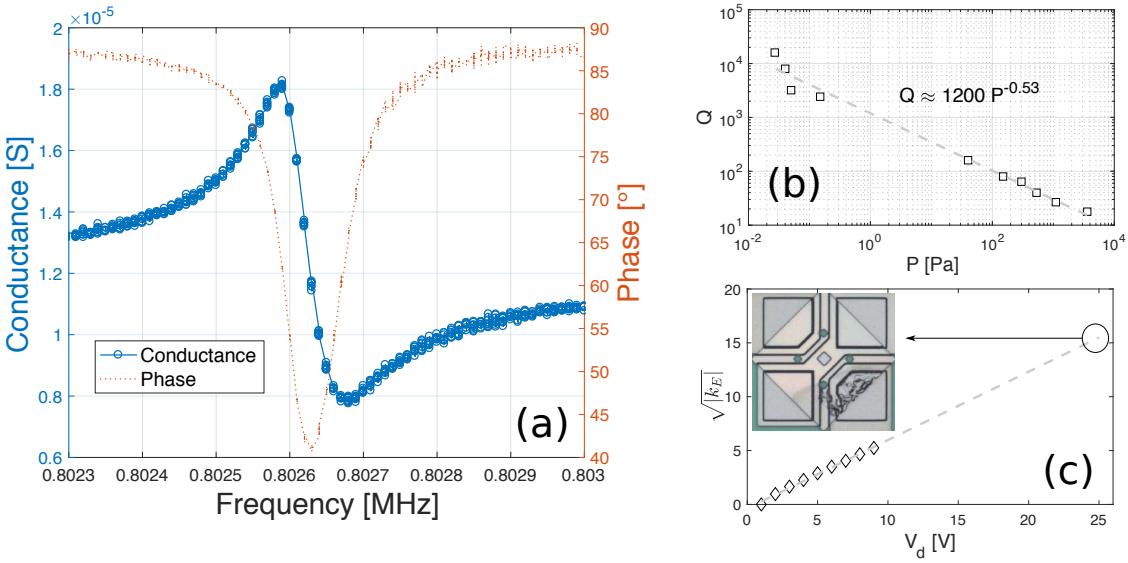


Figure 5.11: Experimental characterisation of a single resonator: (a) conductance and phase responses of a single resonator, (b) quality factor under different pressures and (c) square root of the electrostatic stiffness as a linear function of DC bias voltage. The inset shows the breakdown of a resonator due to pull-in.

on a socket in the middle of the board. A centre rubber ring was used to seal and fixate the device under a vacuum pump.

The SEM image of a single resonator is illustrated in Figure 5.10(b). An impedance analyser (Hioki IM3570) supplied the required test voltages and measured the impedance or conductance with below 0.08% error [138].

Figure 5.11(a) shows the conductance and phase responses of a prototype resonator by applying $V_{DC} = 10\text{V}$ and $v_{in} = 50\text{mV}$ under a low pressure level $P < 100\text{mPa}$. The conductance at resonance, compensated for parasitic capacitance, was measured to have a maximum value of $18\mu\text{S}$, which was close to the simulated value $14.5\mu\text{S}$. The 90° phase at non-resonance frequencies was attributed to the second component in Equation 5.8, which has a constant 90° lead. This also explains why the phase did not flip by 180° after the resonance as expected in Figure 1.2(b), but returned to 90° instead.

From the frequency spectrum, damping was characterised for a single resonator by measuring the bandwidth using the two -3dB corner frequency points. The quality factor Q varied between 10 and 1.6×10^4 when the pressure P dropped from 3.6kPa to 27mPa. The relationship between Q and P is plotted in Figure

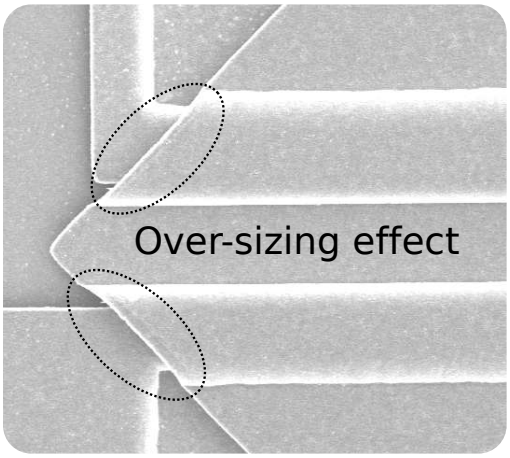


Figure 5.12: Over-sizing effect of the plate side length.

5.11(b), which can be fitted by the following function:

$$Q \approx 1200P^{-0.53} \tag{5.17}$$

Figure 5.11(c) shows the square root of the electrostatic stiffness as a linear function of V_{DC}. The resonator collapsed at a pull-in voltage of about 25V, which led to short circuit between the top plate and bottom electrodes, therefore burning the device. To prevent this irreversible process from happening and ensure good linearity, the recommended DC operating range is within 10V.

5.5.2 Over-sizing

In general, the fabricated resonators demonstrate a natural frequency between 0.8 and 0.85MHz, which is approximately 30% less than the designed value 1.2MHz due to fabrication tolerance. This was likely to be caused by the extra side length when depositing Poly 2 layer onto the uneven silicon dioxide, which was formed during the patterning process. In consequence, the effective length increased by approximately 15%. This is observable under the SEM in Figure 5.12, where a staircase or bump structure was formed when Poly 2 layer started to overlap a different layer, therefore causing an increase in the side length and effective area. This also explains the lower-than-expected pull-in voltage seen in the experiment.

The actual mass and stiffness adjusted for the over-sizing are estimated to be 45ng and 1530N/m. For the proposed MEMS plate resonator, the noise due to thermal

excitation, i.e. continuous exchange between thermal and mechanical energy, places the ultimate theoretical limit to the frequency stability as well as the mass sensitivity [139]. The theoretical sensing resolution can therefore be calculated using Equation 2.40. The maximum SNR observed is around 60dB, hence the minimum detectable mass is 2.8fg (2.8×10^{-15}g). Compared with the previously used comb structure resonator which has a theoretical limit of 0.36pg, this marks 128× improvement.

5.6 Array Perturbation

The previous section has characterised a single resonant unit. However, to understand the sensing behaviour in larger arrays, one needs to perform perturbation analysis. In addition, coupled systems require a different actuation scheme to monitor the collective output and a unique perturbation mechanism to implement the IEA characterisation techniques. These can be achieved by using a novel array configuration presented in this section, which allows both electrostatic perturbation and terminal decoupling.

5.6.1 Electrostatic Perturbation

By changing the bias voltage of a resonator, electrostatic perturbation can be introduced to represent a particular mass/stiffness shift and study its sensitivity. As implied from the experimental results, a DC operating range within 10V would provide a maximum 2.1% stiffness change on the resonant plate, which is a sufficient perturbation level for the IEA algorithms. Figure 5.13 presents two fabricated arrays using five corner coupled square plate MEMS resonators, but with distinct perturbation channels. The first design fully accesses all members to determine individual sensitivity information, such as the measurement of mode-specific eigenvectors. Flexible as it is, the design requires complex routing and in total nine bond pads.

This can be avoided by using an updated design in Figure 5.13(b). The first four elements (resonator 1-4) share the same DC supply, while the last element (resonator 5) is connected to an independent bias voltage V_P to enable terminal perturbation.

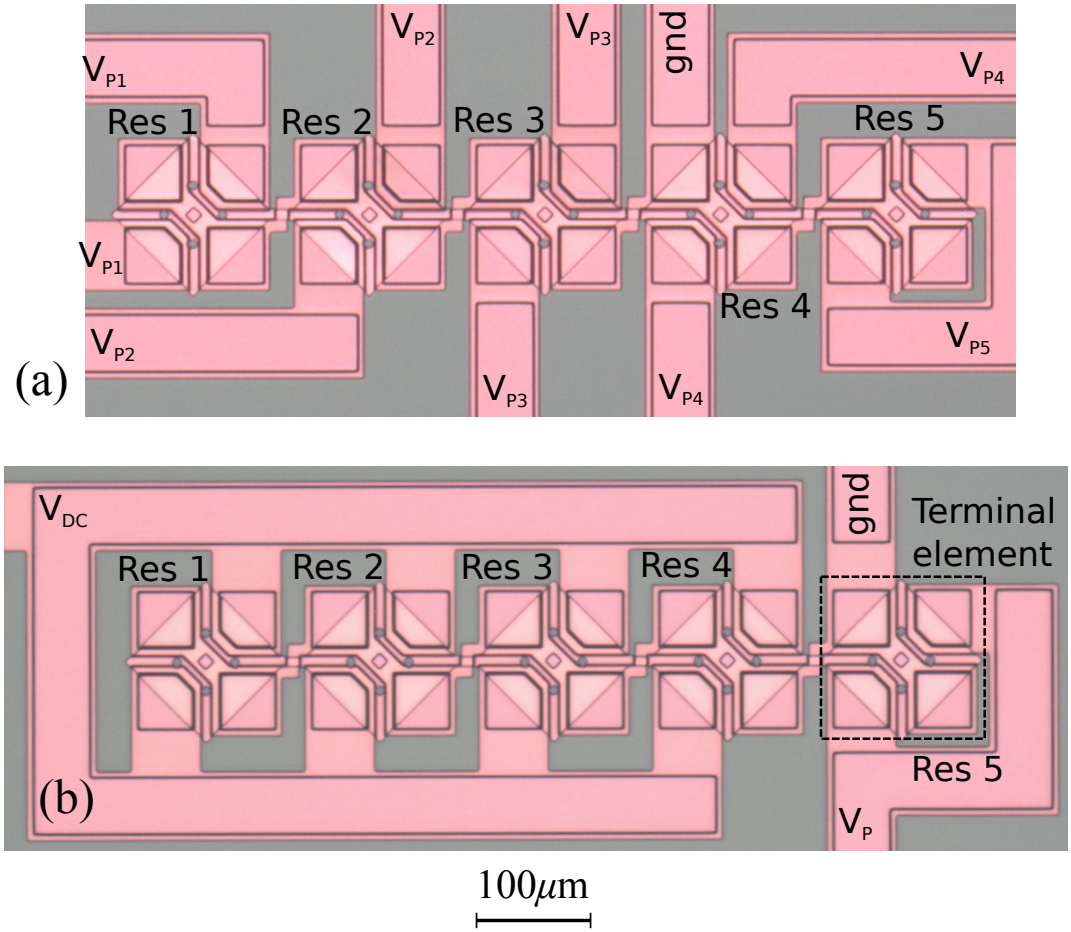


Figure 5.13: Two coupled micro mechanical systems based on different perturbation channels: design (a) has full DC voltage control and readout for all elements, while (b) connects the first four resonators and perturbs the terminal element only. Each five-element array takes up a total size of approximately 920μm $\times$ 330 μm excluding the bond pads.

This array configuration has reduced the number of bond pads to three and has simplified the connections without compromising the functionality, as all eigenvalues are measurable from the terminal element or through the shunt readout from the first four capacitive resonators. According to inverse problem theory, one only needs to perturb and readout from the terminal element to fully reconstruct the system matrix, indicating that the second design is equally competent to perform all possible IEA techniques. Hence, the majority of the manufactured sensors are based on the principle of the second design, i.e. the array depicted in Figure 5.13(b). The frequency responses of such an array, measured from the shunt conductance of the first four elements, are shown in Figure 5.14. Two unique sets of eigen-

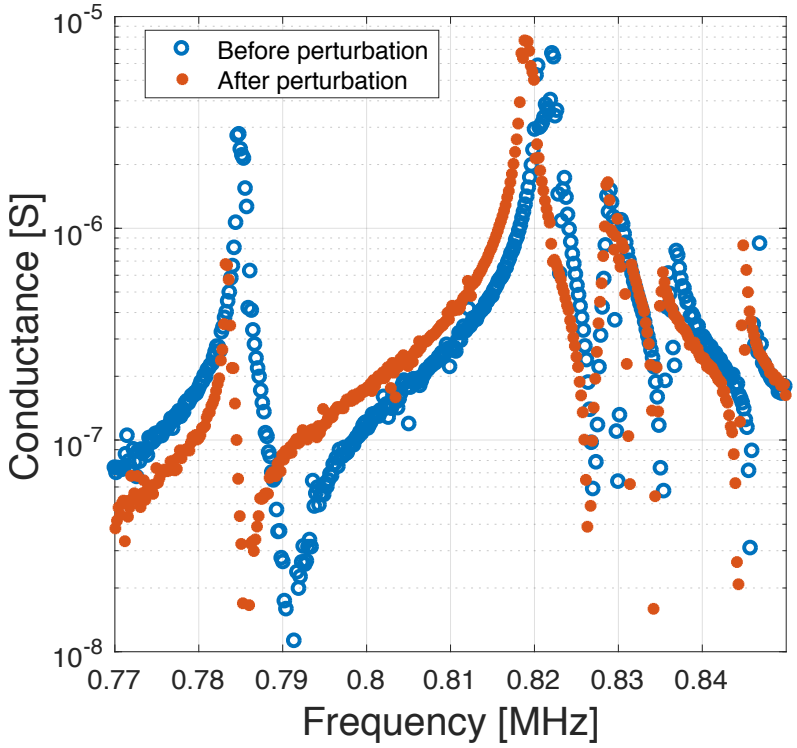


Figure 5.14: Frequency responses of the shunt conductance measured from the first four elements using the second design before and after terminal perturbation.

modes, each having five collective resonances, were clearly observed before and after perturbing the terminal element electrostatically.

5.6.2 Terminal Decoupling

The array is also suited for the new IEA method based on de Boor and Golub's algorithm, which requires connecting/disconnecting the terminal element. For the designed array, the last resonator can be mechanically disconnected by exerting a large pull-in voltage to the terminal electrode, hence preventing it from moving. Array size is then reduced to $n-1$ to derive a second set of eigenvalues.

Figure 5.15 shows this perturbation mechanism using five coupled resonators. The fifth element collapsed and burned out by the heavy instantaneous current. After the breakdown, four eigenvalues of the submatrix could be measured from the intact resonators. This terminal decoupling approach, however, is not the most ideal perturbation mechanism due to its irreversible and destructive characteristic.

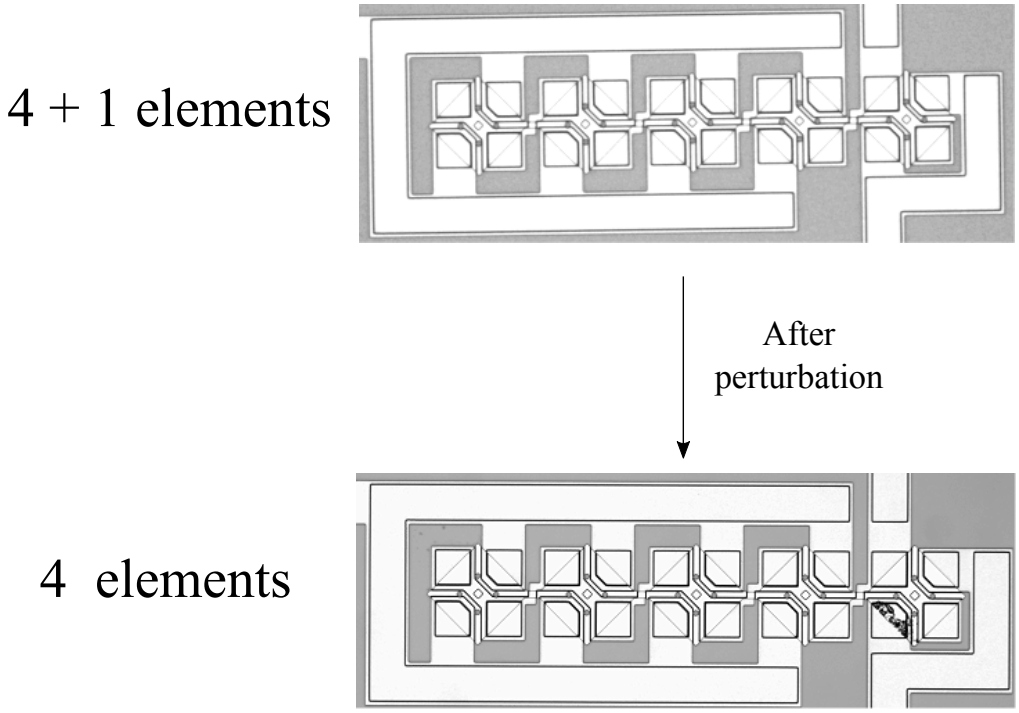


Figure 5.15: Decoupling the terminal resonator by applying a pull-in voltage to the terminal unit.

To make such a perturbation mechanism reversible, it is possible to deposit a thin insulation layer on the bottom electrode, hence getting around short circuit. The array can be recovered to n elements by reducing the pull-in voltage to the snap-back voltage specified in Equation 5.13. During the PolyMUMPs fabrication, this can be done by utilising the Nitride layer as a natural insulator and breaching it to access the substrate, which may serve as the new bottom electrode. Another solution, as already discussed in Chapter 4, is to couple an electrical resonator to the array as the new terminal element, which can be simply coupled/decoupled by connecting/disconnecting it.

5.7 Summary

A sensor structure based on corner coupled square plate MEMS resonators has been designed and fabricated to reduce sensor size and generate MHz vibration, which opens a new perspective for large array and ultra-sensitive applications. After modelling the device with mathematical analysis and FEM simulations, arrays of

coupled structures were designed and fabricated using the shared PolyMUMPs wafer run. A series of experiments were conducted to test the device using an impedance analyser and a designed PCB. Each resonator demonstrates around 0.85MHz resonance, with a $Q > 10^4$ and a maximum 18μS conductance. The miniature architecture permits a theoretical mass resolution of 2.8fg. An over-sizing effect has been observed for the plate side length thereby reducing the effective frequency and pull-in voltage. To achieve multi-sensing in coupled systems, a new array configuration has been proposed and tested for sensing using a five-element array. This configuration allows collective eigenvalue readout as well as different IEA perturbation mechanisms to be implemented. More simulation and experimental results of large coupled systems will be presented and discussed in the following chapter.

There are many things that seem impossible only so long as one does not attempt them.

— André Gide

6 Inverse Eigenvalue Sensing in Large Coupled Systems

Contents

6.1 Introduction 120
6.2 Damping 121
6.2.1 Error Analysis 122
6.2.2 Maximum Number of Resonators 124
6.3 Mode Attenuation 125
6.3.1 Eigen-mode Analysis 126
6.3.2 Multiple Actuation 127
6.4 Eigenvalue Readout 129
6.4.1 Interweaving Condition 129
6.4.2 Eigenvalue Change 130
6.4.3 Device Failure 132
6.5 Sensing Complexity 133
6.5.1 Linearisation 134
6.5.2 Accuracy 135
6.5.3 An Example of Twenty Coupled Resonators 136
6.6 Summary 137

6.1 Introduction

Before providing experimental results, one would analyse experimental conditions and their effects on the systems. However, unlike normal arrays where thousands of

micro/nano resonators can be fabricated on the same die [44], the study of coupled arrays is typically limited to few resonators [84]. The robustness, sensing complexity and connectivity issues are not fully addressed in large coupled systems. Although coupled arrays with around ten elements have been made possible, these are based on cantilevers only and require complicated optical readout [51, 83]. Hence, to achieve large-scale multi-dimensional sensing, it is crucial to find a new way of characterising and actuating these massive resonator arrays.

This chapter aims to expand the IEA techniques to enlarged coupled arrays and identify their pragmatic sensing constraints and potential solutions, using the fabricated corner coupled square plate MEMS resonators. Four principal constraints for scaling, namely damping effect, mode attenuation, eigenvalue selection and sensing complexity, will be studied through theoretical analysis and experiments.

6.2 Damping

In this work, the analysis of coupled resonators normally assumes zero damping and uses the values of resonance frequency and eigenfrequency interchangeably. This is due to the fact that each resonator was tested under a low pressure ($Q > 1000$). However, for real-word sensing, the air/liquid media may lower the quality factor and hence the damping $\mathbf{C}$ in Equation 2.2 needs to be considered. In multi DOF systems, the damping force applied to the ith resonator is determined by

$$F_d(i) = -\sum_{j=1}^{n} c_{ij}\dot{x}_j \tag{6.1}$$

To model the elements c_{ij} in the matrix $\mathbf{C}$, one may use a basic viscous damping model and assume the damping matrix to be linearly proportional to the stiffness matrix [140, 141]:

$$\mathbf{C} = 2\zeta\mathbf{K} \tag{6.2}$$

where ζ is the damping ratio, which is assumed to be constant here.

By taking damping into account, this section provides error analysis and explores the maximum number of resonators allowed in large coupled systems.

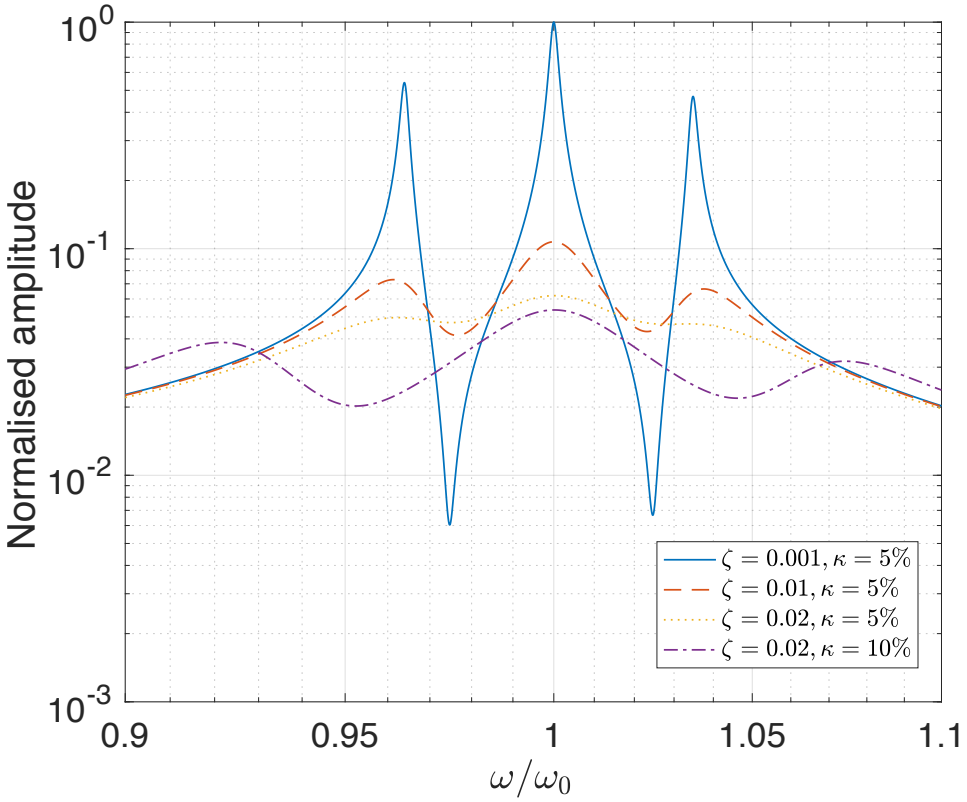


Figure 6.1: Amplitude responses of an array of three coupled resonators under different damping ratios and coupling strengths.

6.2.1 Error Analysis

Damping is the source of two errors: one is the shift between the measured resonance and actual eigenfrequency, another is the mode liaison, making it difficult to accurately pinpoint the centre frequency. Figure 6.1 simulates the frequency responses of a coupled array consisting of three same resonators, in different damping and coupling situations. The uncoupled natural frequency for reach resonator is ω_0. As ζ increases from 0.001 to 0.01, the resonant frequencies decrease slightly. The frequency deviation can be observed in Figure 6.1, giving an error of 0.3%, which is negligible. The second error, mode liaison effect, is of more detrimental impact. When ζ further increases to 0.02, the three peaks broaden widely and start overlapping, making the resonant frequencies unrecognisable. One solution to overcome such is to increase the coupling strength. Increasing the coupling ratio κ from 5% to 10% avoids overlapping, therefore enabling more precise peak location.

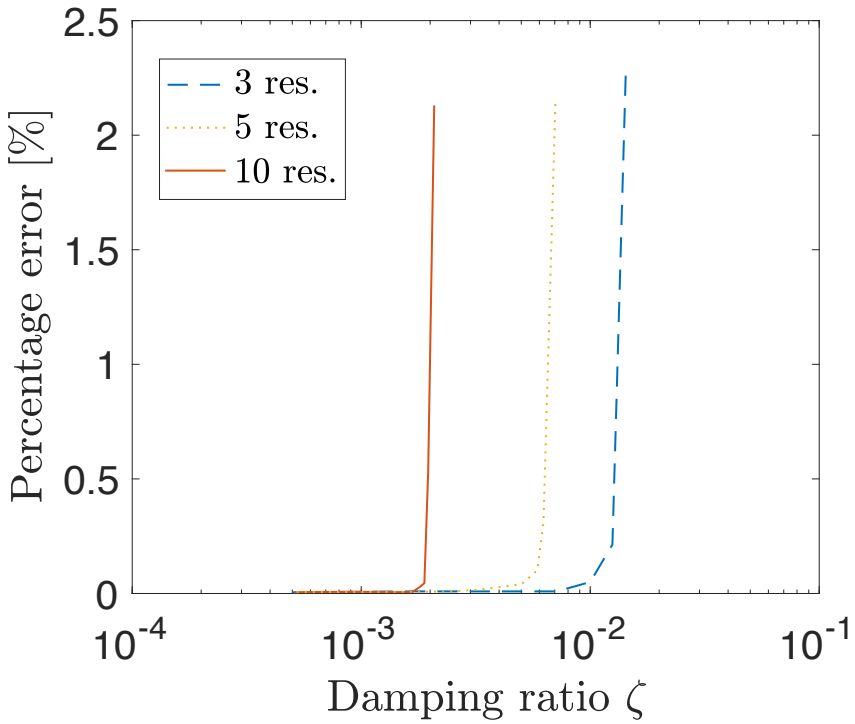


Figure 6.2: Percentage errors of the diagonal elements in the system matrix under different damping ratios for coupled arrays of three, five and ten resonators ($\kappa = 5\%$).

To understand how damping affects the precision of inverse eigenvalue analysis, an array of three, five and ten coupled resonators ($\kappa = 5\%$) were simulated respectively to characterise the accuracy of de Boor and Golub's algorithm under different damping ratios. The damped resonant peaks were found in the frequency domain by MATLAB `findpeaks()` function. Using inverse eigenvalue analysis, these damped resonant frequencies would lead to a different system matrix $\hat{\mathbf{S}}_\mathbf{n}$, hence introducing errors. The damping error could be represented by the root mean square deviation of the relative error between the diagonal elements of $\hat{\mathbf{S}}_\mathbf{n}$ and the actual system matrix $\mathbf{S}_\mathbf{n}$:

$$D_r = \frac{\sqrt{\sum_{i=1}^{n} (|\frac{\hat{S}_n(i,i) - S_n(i,i)}{S_n(i,i)}| \times 100\%)^2}}{n} \tag{6.3}$$

The results are shown in Figure 6.2. To keep the variation comparable to the numerical error, a maximum ζ of around 0.01, 0.006 and 0.002 is allowed for three, five and ten resonators respectively. Hence, systems with more elements require a lower damping. If ζ exceeds a threshold, the percentage error would sharply increase.

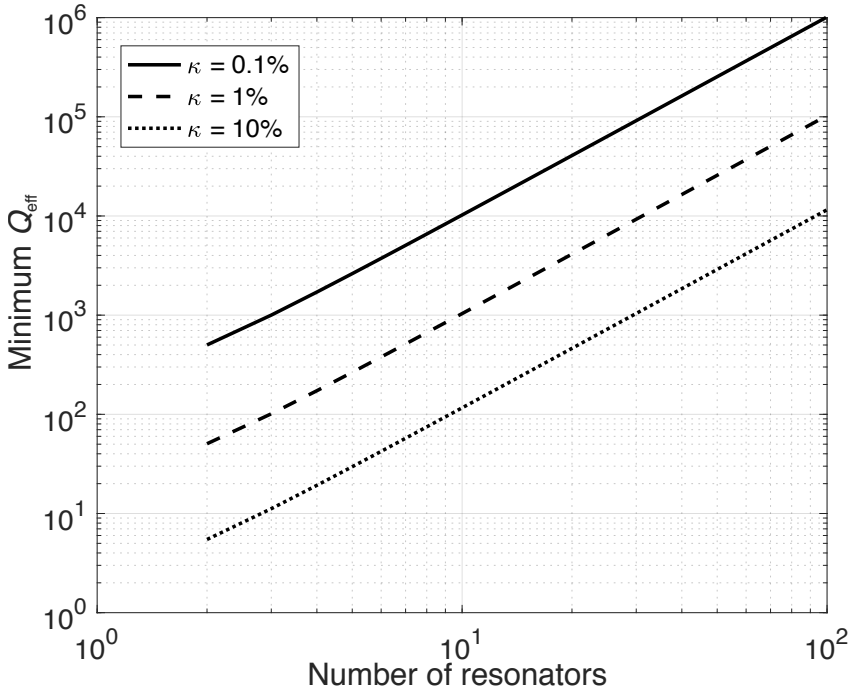


Figure 6.3: Percentage errors of the diagonal elements in the system matrix under different effective quality factors for coupled arrays of three, five and ten resonators ($\kappa = 5\%$).

As the damping ratio increases further, the damping effect makes it unrealistic to record the resonant frequencies due to flattening or overlapping peaks.

6.2.2 Maximum Number of Resonators

Mode liaison with lack of resolution between adjoining eigenvalues is restraining the growth of the size for coupled systems. Previous analysis has shown such can be improved by reducing the damping ratio and increasing the coupling ratio. Hence, to increase the maximum number of coupled resonators allowed, one has to take these two factors into consideration.

For an array of n coupled resonators, the frequency separation between any two peaks should be broader than half the bandwidth, hence

$$|\omega_i - \omega_j|_{\min} < \frac{\omega_0}{2Q_{\text{eff}}} \tag{6.4}$$

where Q_{eff} is the effective quality factor of the coupled systems, implied from the

bandwidth. This leads to a minimum effective quality factor required

$$Q_{\text{eff}} > \frac{\omega_0}{2|\omega_i - \omega_j|_{\min}} \tag{6.5}$$

An increase in the number of resonators would tighten the minimum eigenfrequency separation, which can be extracted from the system matrix of a simulated array of n coupled resonators, with each resonator having the same spring constant. Figure 6.3 shows the minimum Q_{eff} required for different n and κ. As a rule of thumb, the following equation has to be satisfied:

$$Q_{\text{eff}} > \frac{n}{\kappa} \tag{6.6}$$

which leads to a maximum n

$$n_{\max} = \kappa Q_{\text{eff}} \tag{6.7}$$

For the fabricated square plate coupled devices, the effective quality factor and coupling ratio are around 10^4 and 5% respectively, therefore the ultimate size of the array is calculated to be 500 elements. However, this is a very optimistic estimation, as there are other limiting factors from a practical point of view. These include noises, mode attenuation, spurious eigenvalues, device failure and signal processing constraints, which will be assessed in the sections to follow.

6.3 Mode Attenuation

For a single-actuation coupled array, not all resonators vibrate at the same magnitude, and their values can be substantially different for each mode. In the presence of noise, a decrease in the resonant amplitude would deteriorate the SNR and add complexity to the subsequent signal processing, which is undesired for multi-resonance sensing.

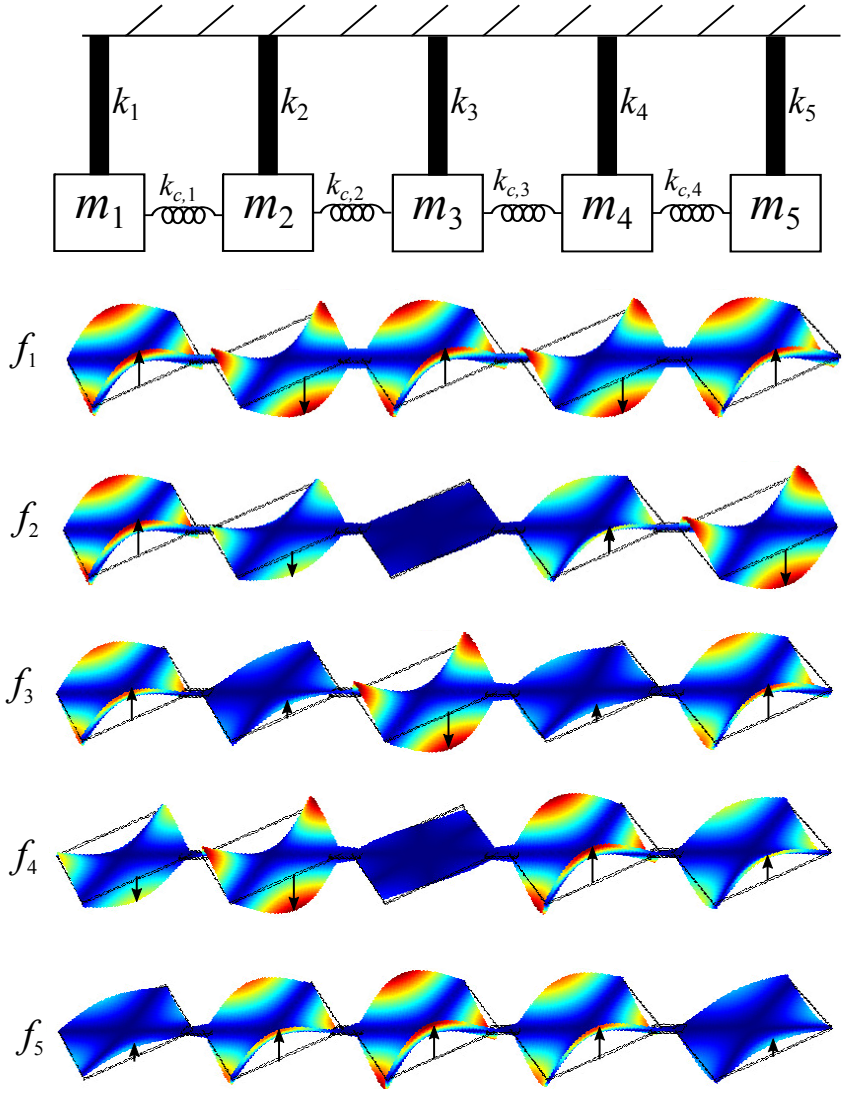


Figure 6.4: Eigen-modes of five corner coupled square plate resonators and the spring-mass model.

6.3.1 Eigen-mode Analysis

To analyse vibrations at different eigen-modes, Figure 6.4 simulates five corner coupled square plate resonators using COMSOL eigenfrequency analysis, along with their lumped-parameter spring-mass model. Even if all the resonators are designed to be identical, their collective resonances behave differently at each mode.

Normalised resonant magnitudes of the five corner coupled resonators are recorded in Table 6.1, suggesting that their amplitudes vary substantially at different modes, such as the third resonator at the second and fourth mode, where only three eigenvalues could be measured from that resonator. One can imagine for larger

Table 6.1: Normalised resonant magnitudes of five coupled resonators at five modes.

	Res 1	Res 2	Res 3	Res 4	Res 5
Mode 1	0.4472	0.4472	0.4472	0.4472	0.4472
Mode 2	0.6015	0.3717	0	0.3717	0.6015
Mode 3	0.5117	0.1954	0.6325	0.1954	0.5117
Mode 4	0.3717	0.6015	0	0.6015	0.3717
Mode 5	0.1954	0.5117	0.6325	0.5117	0.1954

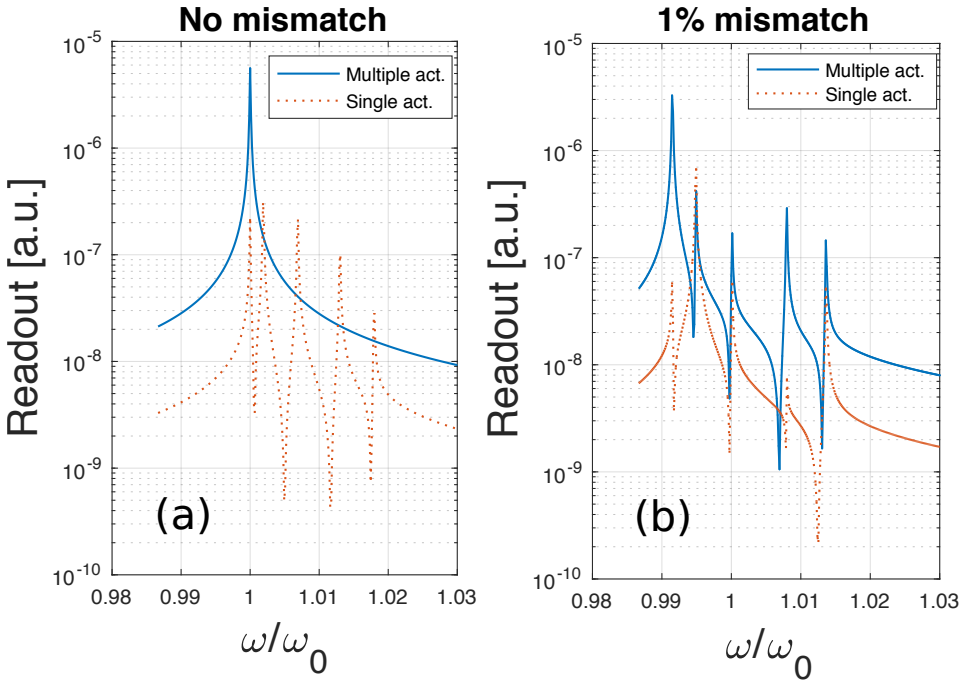


Figure 6.5: Simulated frequency responses of five coupled resonators when there is (a) no mismatch and (b) 1% frequency variation, under both the single and multiple actuation schemes.

arrays, the conventional IEA method based on the SISO scheme, i.e. driving and reading out from one resonator, may fail to properly identify all the eigenvalues. Widening the dynamic range and SNR may improve the resolution, yet it is still impossible to capture any resonance that is stationary.

6.3.2 Multiple Actuation

To combat the readout issues in larger arrays, a multiple actuation scheme can be used. Such a new actuation scheme drives multiple resonators with the same AC signal and reads out their current summation. This enhances the power handling

while avoiding an extremely low output. For an array of n resonators, this would on average increase the output signal strength by n-fold without altering the eigenvalues. However, one may notice from the mode shapes in Figure 6.4 that when there is no device mismatch, the output currents of particular resonators are anti-phase and would hence cancel each other out when reading out simultaneously. For MEMS bandpass filter applications, this is desired because it produces a clean and sharp resonant peak while suppressing higher modes [66]. This can be demonstrated in Figure 6.5(a), where the frequency responses of five identical resonators have been simulated under both the single and multiple actuations, assuming $\zeta = 5 \times 10^{-5}$ and a weak coupling at 1%. In the case of multi-mode sensing when these higher-mode peaks are desired, the proposed multiple actuation scheme becomes counterproductive due to the eigen-mode cancellation effect.

One solution is to introduce device mismatch. For better illustration, Figure 6.5(b) shows the frequency responses of five coupled resonators with the existence of only 1% frequency variation. All the five modes, using the multiple actuation scheme, have been clearly separated with enhanced signal strength compared with the single actuation scheme. The implication is that one may design each resonator differently, or simply take advantage of the inherent process-induced variability, to facilitate the eigenvalue readout under the multiple actuation.

The fabricated corner coupled square plate MEMS resonators in Figure 5.13 allow either the single actuation or multiple actuation scheme to be implemented. The former actuates the terminal unit by just adding v_{in} to V_P, while the latter provides AC signals to all elements and senses the collective current flowing through V_{DC} of the first $n-1$ elements and V_P of the terminal. The frequency responses of a fabricated array of five corner coupled square plate MEMS resonators were experimentally measured using both schemes, with results shown in Figure 6.6. The results are in line with the simulations presented in Figure 6.5(b), showing substantial enhancement in signal strength due to the multiple actuation scheme and frequency variation. In the experiment, under the multiple actuation scheme, the SNR of the five eigen-modes was improved by 12.5dB, 19.8dB, 20.2dB, 19.2dB and 15.8dB

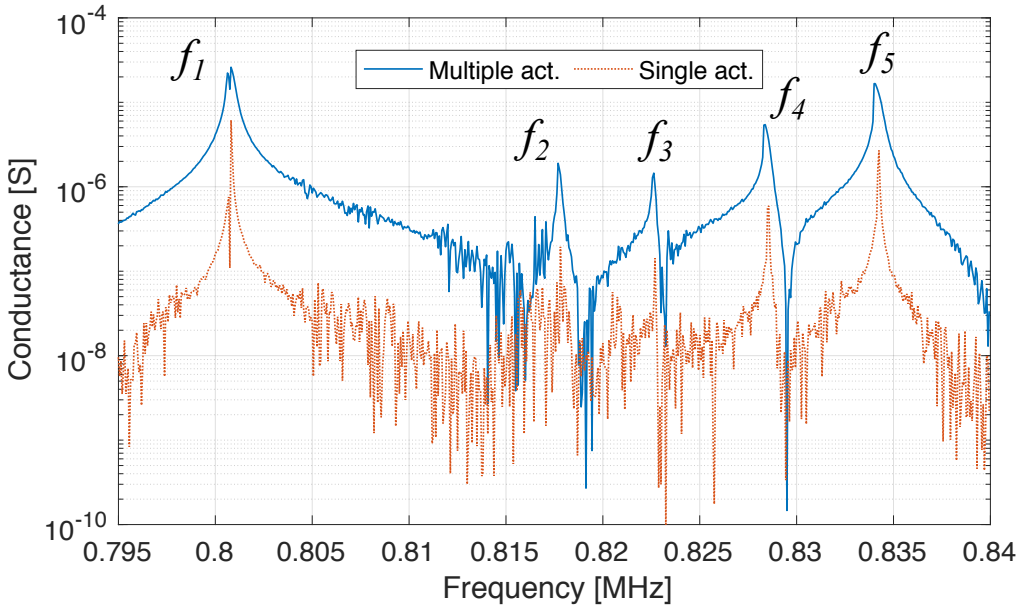


Figure 6.6: Measured frequency responses of a fabricated array of five corner coupled square plate MEMS resonators using both actuation schemes.

respectively, compared with that under the single actuation scheme. The second mode experienced the most prominent sensitivity enhancement (20.2dB), which was hardly distinguishable by the previous single actuation scheme. The results provide a good example of utilising process induced variability to enhance eigenvalue readout in coupled systems. Having obtained these eigenvalues, one needs to analyse them and provide correct eigen-sensing results, which will be discussed next.

6.4 Eigenvalue Readout

The number of eigenvalues recorded from n coupled systems can be greater or less than n due to spurious modes or resonator breakdown. Hence, in large systems, the eigenvalues need to be carefully selected before applying the IEA algorithms.

6.4.1 Interweaving Condition

In order to identify appropriate eigenvalues, it is important to resort to the error analysis results from Section 2.5.3, which manifest that the desired eigenfrequencies should move towards the same direction after perturbation, and satisfy an interweaving condition. The breach of such a rule is the major source of error.

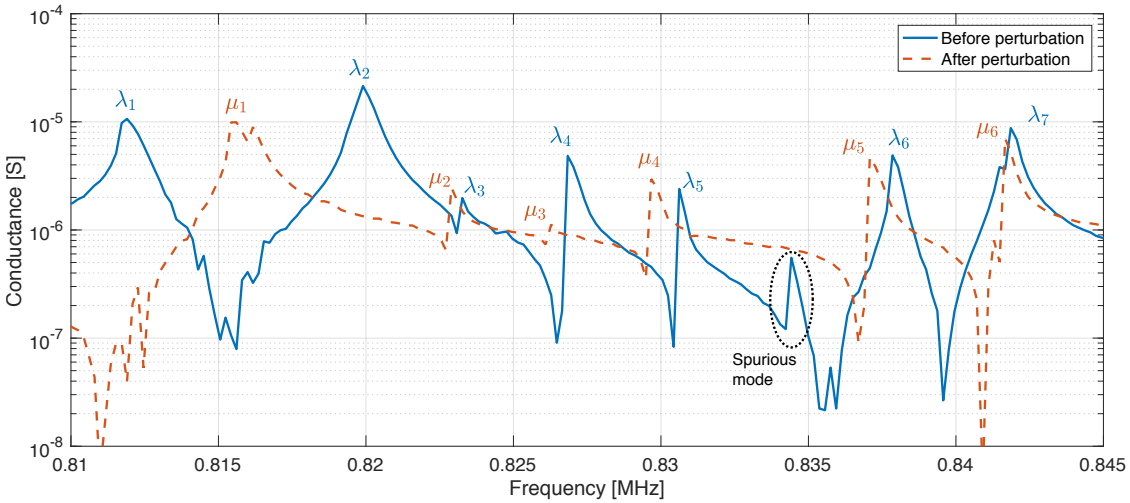


Figure 6.7: The interweaving condition for de Boor and Golub's algorithm, observed from the frequency responses of seven coupled resonators before and after pull-in of the terminal element.

Hence, the interweaving rule provides one way of excluding incorrect eigenvalues and minimising the error tremendously. To demonstrate how the interweaving condition works, an array of seven corner coupled square plate MEMS resonators was fabricated to experimentally perform inverse eigenvalue sensing.

Taking the new IEA method as an example, de Boor and Golub's algorithm was implemented by applying a pull-in voltage towards the terminal element. This reduced the resonator count from seven to six and led to a change in the frequency response of the systems, as shown in Figure 6.7. The desired eigenvalues before perturbation λ_i and after perturbation μ_i should abide by the interweaving condition set by Equation 2.63. The spurious mode at near 0.835MHz, which did not meet the requirement, was therefore identified as an outlier.

6.4.2 Eigenvalue Change

The implementation of de Boor and Golub's algorithm on the square plate resonators is an irreversible process that destructs the terminal element, hence only one perturbation is permitted. To better exemplify the rule of eigenvalue change, Gladwell's method, which shares a similar interlacing formalism for λ_i and λ_i^*, is

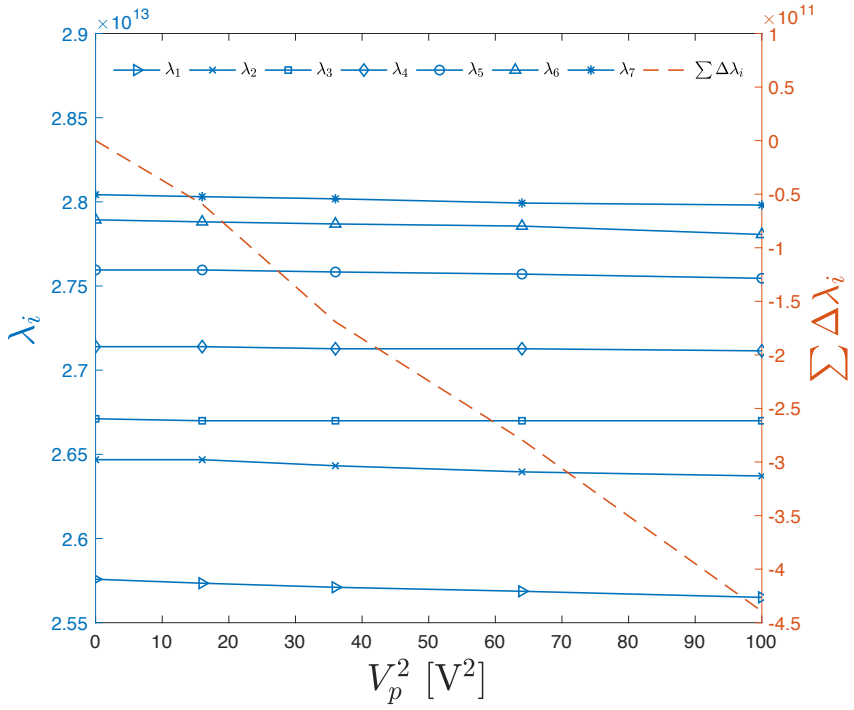


Figure 6.8: The shifts of eigenvalues after changing the perturbation voltage of the terminal resonator.

further investigated using a similar seven-element coupled array. Here λ_i and λ_i^* are the two sets of eigenvalues before and after a terminal perturbation.

Figure 6.8 shows how the changes of seven eigenvalues met the interweaving condition when increasing the perturbation voltage V_P of the last element gradually from 0V to 10V. The total eigenvalue shift, $\sum \Delta\lambda_i$, has a linear relationship with the voltage squared. This can be explained by Equation 2.35, where the total perturbation induced by the electrostatic stiffness Δk is linearly proportional to the square of the voltage. Hence, by measuring $\sum \Delta\lambda_i$, it is possible to solve the exact amount of stiffness change.

To test the efficacy of these results, one can select two sets of eigenvalues at any two perturbation levels, and compute their corresponding system matrices. System matrices at the same perturbation level can therefore be extracted and compared. For instance, to characterise the system matrix at zero perturbation level, i.e. $V_P = 0$V, one may take the seven eigenvalues at $V_P = 0$V as λ_i, and

those at $V_P = 6\text{V}$ as λ_i^*. This generates a system matrix:

$$\mathbf{S} = 10^{13} \times \begin{bmatrix} 2.716 & -0.043 & 0 & 0 & 0 & 0 & 0 \\ -0.043 & 2.731 & -0.035 & 0 & 0 & 0 & 0 \\ 0 & -0.035 & 2.732 & -0.037 & 0 & 0 & 0 \\ 0 & 0 & -0.037 & 2.725 & -0.055 & 0 & 0 \\ 0 & 0 & 0 & -0.055 & 2.664 & -0.055 & 0 \\ 0 & 0 & 0 & 0 & -0.055 & 2.678 & -0.089 \\ 0 & 0 & 0 & 0 & 0 & -0.089 & 2.715 \end{bmatrix} \tag{6.8}$$

The result can be compared with that extracted from the two sets of eigenvalues at $V_P = 0\text{V}$ and $V_P = 10\text{V}$, yielding a similar system matrix at the same perturbation:

$$\mathbf{S} = 10^{13} \times \begin{bmatrix} 2.733 & -0.043 & 0 & 0 & 0 & 0 & 0 \\ -0.043 & 2.721 & -0.038 & 0 & 0 & 0 & 0 \\ 0 & -0.038 & 2.731 & -0.041 & 0 & 0 & 0 \\ 0 & 0 & -0.041 & 2.722 & -0.048 & 0 & 0 \\ 0 & 0 & 0 & -0.048 & 2.670 & -0.060 & 0 \\ 0 & 0 & 0 & 0 & -0.060 & 2.691 & -0.089 \\ 0 & 0 & 0 & 0 & 0 & -0.089 & 2.692 \end{bmatrix} \tag{6.9}$$

On average, there is only 0.4% difference in diagonal elements and 6.5% difference in off-diagonal elements. In a nutshell, it is important to monitor how eigenvalues change to decide whether IEA techniques should be implemented or not.

6.4.3 Device Failure

An additional threat to the eigenvalue readout is device failure. Coupled resonators are usually more sophisticated with respect to geometry, as they are connected through delicate beams that are prone to fabrication errors. Another vexing challenge is that if any coupling beam or element breaks down, the collective behaviour of the entire array would be jeopardised. This is very likely to happen in large systems, as can be seen from the SEM image of fifty coupled resonators depicted in Figure 6.9. Owing to photoresist residue, one resonator was destructed, hence giving rise to the malfunction of the whole sensor. As a result, the perturbation would terminate at the break point without propagating to the rest of the elements.

Assuming the yield for each one resonator is y and the failure of each element is independent, since they are coupled in series, the failure rate of the whole device

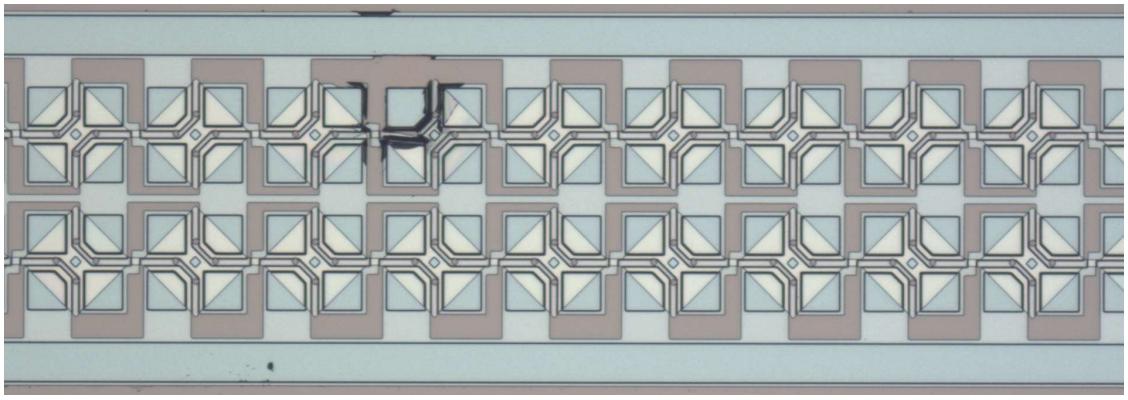


Figure 6.9: Failure of an array of fifty coupled square plate MEMS resonators caused by fabrication error in one resonant unit.

made up of n resonators can be calculated as

$$1 - y^n \tag{6.10}$$

which would increase exponentially if n grows larger. Assuming $y = 90\%$, for 7 resonators the failure rate would exceed 50% and for 20 resonators, the sensor is almost 90% likely to fail. To increase the overall throughput, a robust resonant unit with high success rate is desired.

Fortunately, by combining the multiple actuation scheme and the interweaving condition, it is possible to diagnose faulty elements. For example, when a chain of resonators is split into two segments as a result of foundry error or resonator breakdown, IEA can still be used to derive the system matrix of one chain by choosing the eigenvalues that satisfy the interweaving condition. Hence, the location of the broken resonator, or coupling beam, can be identified.

6.5 Sensing Complexity

In addition to the sophistication of sensor configuration, sensing from a large number of coupled resonators is complicated as n resonators would each render n unique eigen-modes with accelerated growth in non-linearity and irregularity. These changes are further unforeseeable when considering device mismatches and process variabilities. Hence, complex sensing models using extensive signal processing techniques and hardware are often required. One strategy to expedite

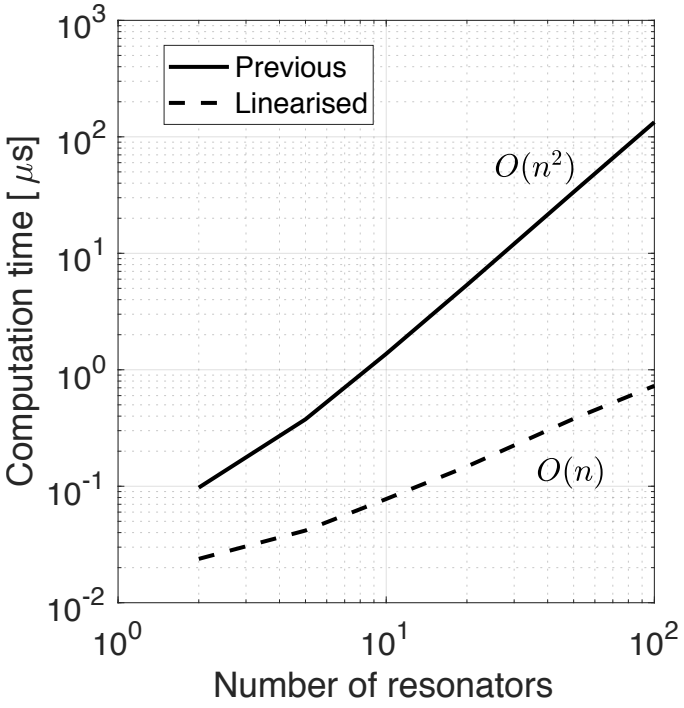


Figure 6.10: Complexity of the previous eigenvector extraction algorithm and the new linearised algorithm for different numbers of coupled resonators.

the sensing process without compromising the accuracy is to linearise these models for small perturbations.

6.5.1 Linearisation

To exemplify this, one can consider Gladwell's eigenvector extraction algorithm in Equation 2.60, which is computationally expensive and impractical for real-world sensing when the array size becomes massive. Nonetheless, by ignoring higher order terms, the perturbed eigenvalue problem

$$(\mathbf{S_n} + \Delta\mathbf{S_n})(\mathbf{x_i} + \Delta\mathbf{x_i}) = (\lambda_i + \Delta\lambda_i)(\mathbf{x_i} + \Delta\mathbf{x_i}) \tag{6.11}$$

can be linearised as

$$\mathbf{x_i}^\mathbf{T}\Delta\mathbf{S_n}\mathbf{x_i} = \Delta\lambda_i \tag{6.12}$$

given that $\mathbf{x_i}^\mathbf{T}\mathbf{x_i} = 1$ and $\mathbf{x_i}^\mathbf{T}\mathbf{S_n} = \mathbf{x_i}^\mathbf{T}\lambda_i$. This yields a new eigenvector solution

$$x_{p,i}^2 = \frac{\lambda_i^* - \lambda_i}{\sum_{i=1}^{n}(\lambda_i^* - \lambda_i)} \tag{6.13}$$

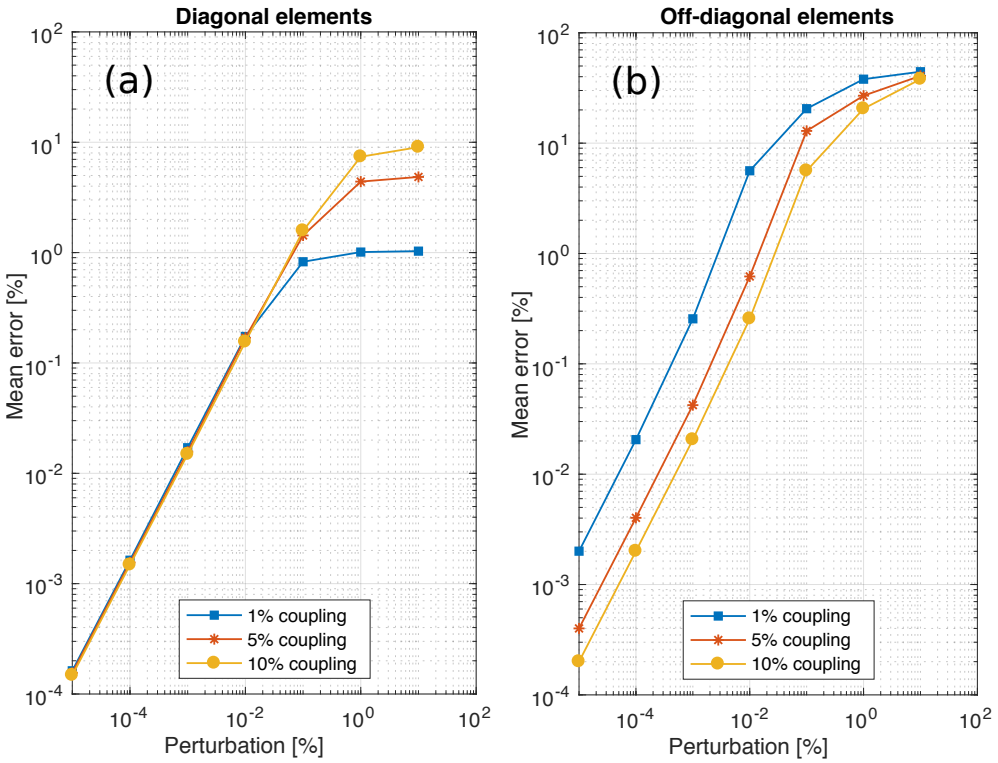


Figure 6.11: Sensing errors of the linearised algorithm for extracting (a) diagonal elements and (b) off-diagonal elements.

with significantly reduced complexity compared with the previous algorithm in Equation 2.60.

Figure 6.10 simulates the algorithmic complexity of the linearised algorithm in conjunction with the previous algorithm for different numbers of resonators using MATLAB computation time analysis. It can be seen that the previous algorithm has $O(n^2)$ computational complexity while the new algorithm has cut down the complexity to $O(n)$.

6.5.2 Accuracy

To understand the accuracy of the linearised algorithm with regard to system matrix determination, the mean absolute errors of the extracted diagonal elements as well as off-diagonal elements were simulated using an example of five coupled resonators, see Figure 6.11. Different perturbation levels and coupling strengths were considered. Perturbations were applied to the terminal element, hence inverse Lanczos' algorithm

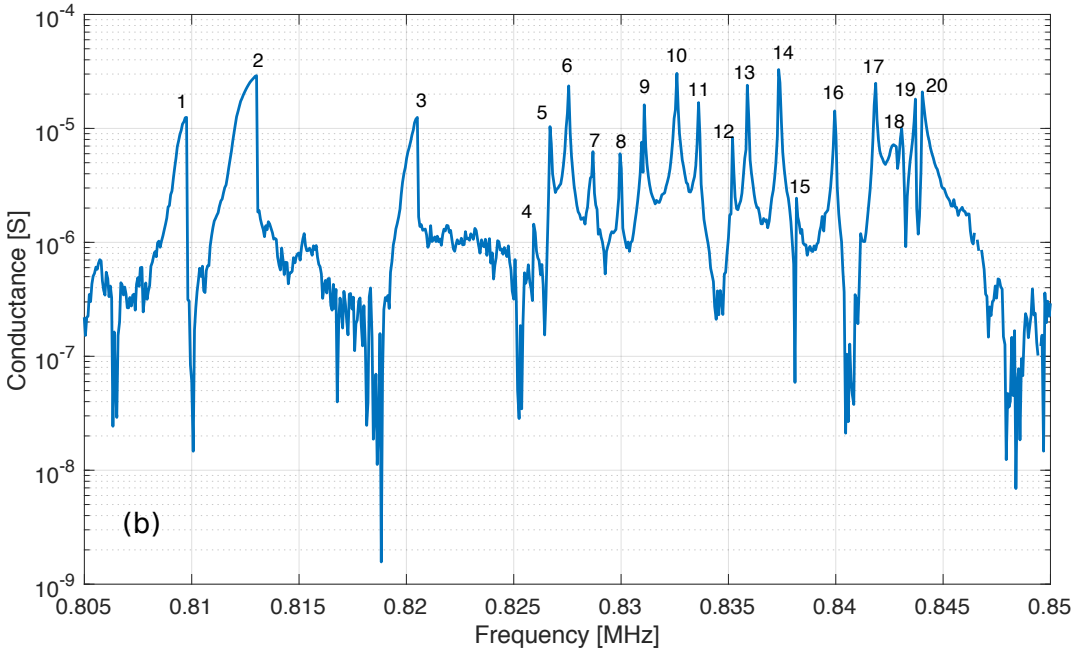


Figure 6.12: The frequency response of twenty corner coupled square plate MEMS resonators.

was used to determine the full system matrix. Results suggest that for a small perturbation, i.e. $\Delta k/k \ll \kappa$, the relative error is well controlled below 1%.

6.5.3 An Example of Twenty Coupled Resonators

The linearised algorithm paves the way for rapid and real time detection of various chemical or physical quantities. For an example of twenty resonators, this has the potential of speeding up the sensing by 23×.

To illustrate how useful the simplified sensing approach is for large coupled arrays, twenty corner coupled square plate MEMS resonators were fabricated and tested. Figure 6.12 depicts the frequency response of the array, which contains twenty eigen-modes marked by numbers. Through perturbation analysis, the attained system matrix from the linearised method could be compared with the previous IEA approach. The characterisation results, including *uncoupled* natural frequency, stiffness and mass for each resonator are presented in Figure 6.13. The horizontal axis denotes the resonator number counted from the perturbation terminal to the opposite end. The relative error between the new algorithm and the previous Gladwell's approach is as low as 0.08%. The results also provide information about

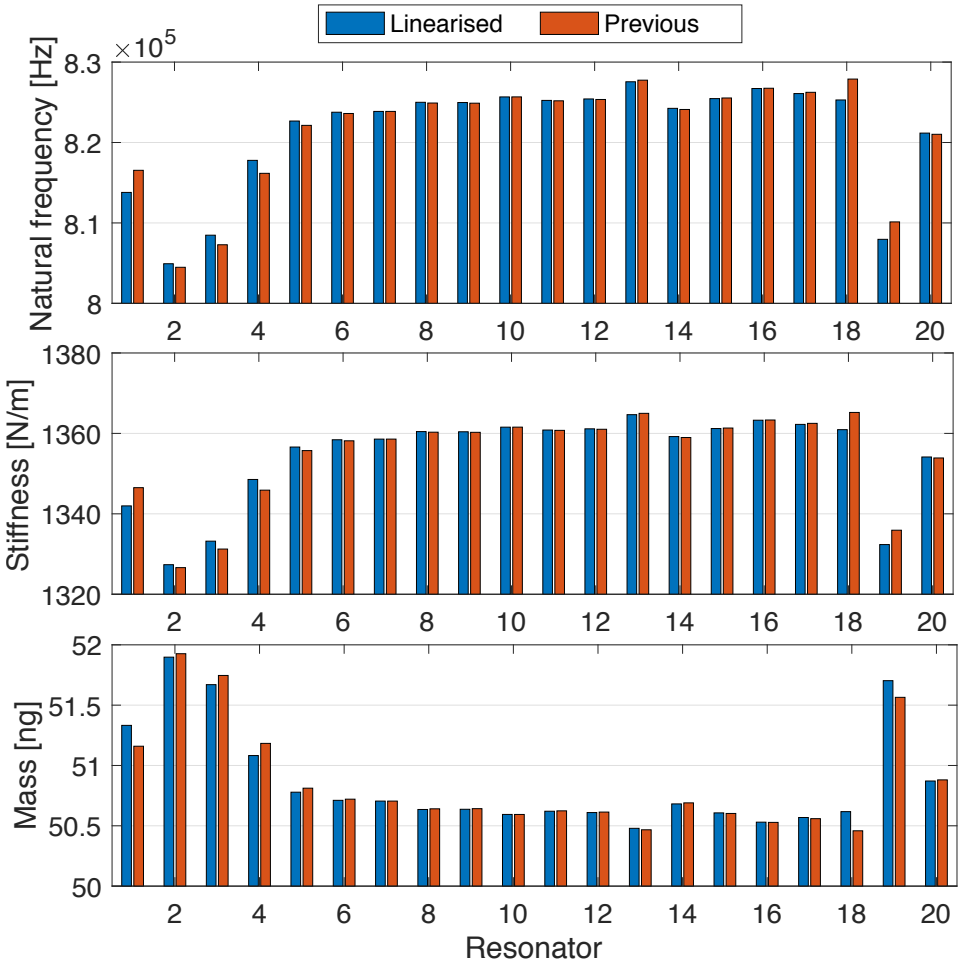


Figure 6.13: Extracted *uncoupled* natural frequency, stiffness and mass of all twenty resonators using the linearised eigen-sensing method and the previous algorithm.

fabrication tolerance. The mean frequency is characterised to be 0.821MHz, with a standard deviation of 6.9kHz. Hence, the frequency variation is around 0.8%. The average mass and stiffness for each resonator are determined to be 51ng and 1355N/m respectively. These can be compared with the designed values 34ng and 2020N/m.

6.6 Summary

This chapter has explored the capabilities of massive coupled sensors using arrays of corner coupled square plate MEMS resonators. The increase in array size triggers issues such as damping, mode attenuation, eigenvalue readout, device failure and sensing complexity.

Damping causes two sensing errors: one is a reduction in the resonant frequency,

and another is the mode liaison effect. While the frequency deviation is normally negligible, the second error is particularly critical as it places an ultimate limit to the mode resolution and hence the maximum number of resonators in any coupled array.

Besides damping, large systems are experiencing attenuated or diminished resonant peaks that are responsible for a low SNR. Hence, a multiple actuation scheme has been proposed to increase the eigenvalue resolution and signal power by turning the inherent process variation into an advantage.

Sensing performance can be further enhanced by applying an interweaving condition, thereby discounting eigenvalue outliers that may introduce serious errors. The eigenvalue selection criterion enables a more robust measurement and is capable of detecting faulty resonant cells.

In the end, with the aim of reducing sensing complexity, a linearised IEA method with below 1% error has been reported and applied to an array of twenty coupled resonators. Such a massive array was successfully characterised and actuated as a sensor by determining the mass and stiffness of individual resonant units.

If you know both yourself and your enemy, you can win a hundred battles without jeopardy.

— Sun Tzu

7 Conclusions and Future Work

Contents

7.1 Conclusions 139
7.2 Future Outlook 141
7.2.1 Sensor Design and Fabrication 141
7.2.2 Simultaneous Eigenvalue Readout 143
7.2.3 Damping and Non-linearity Compensation 145
7.2.4 System Integration 146

7.1 Conclusions

There have been great strides made to enhance the applications of micro/nano machines. Among these, micro/nano resonators have become key to enabling technology in the field of MEMS thanks to their versatility. MEMS resonators have found a host of real-world applications including mass sensor, force sensor, accelerometer, gyroscope, RF filter, ultrasound transducers and energy harvesting. Following the advances in nanotechnology, the dimensions of these resonators are constantly shrinking to enhance their sensitivity. Resonators can be arranged in arrays to provide new functionalities such as multi-sensing. Despite these achievements, the reduction in feature size is confronted with new challenges. First of all, with several sensors fabricated on the same substrate, connectivity issues are

problematic as one requires more interconnects and bond pads. Second, nonidealities such as process error, non-linearity and coupling become conspicuous. To handle these challenges, the collective behaviour of coupled systems has been exploited to achieve multi-dimensional eigen-sensing with ultra-high sensitivity. By delving into fundamental theories and developing real-world micro electromechanical sensors, this thesis has accomplished a number of objectives.

The thesis provided a literature survey on resonator-based micro/nano sensors in Chapter 1, focusing on three important aspects: characterisation, process variation and sensitivity. Coupled systems were introduced to address their associated challenges.

Second, by analysing both the forward and backward problems in coupled eigen-sensing, Chapter 2 evaluated eigen-sensing approaches including the use of eigenvalues and eigenvectors. The advantages and disadvantages of different sensing methods as well as their physical limitations were discussed. Furthermore, a comprehensive review on IEA was presented. Inspired by perturbation analysis and inverse problem theory, a new IEA characterisation method with enhanced robustness and accuracy was devised. The theories were put into practice by modelling a simple array of two coupled resonators, as presented in Chapter 3.

Followed by the theoretical analysis, a novel perturbation approach was then proposed in Chapter 4, which attaches an electrical resonator to a MEMS array. This approach provides a simple way of perturbing the terminal element, and hence permits the implementation of the new IEA method as well as the previous ones. It also reduces the adverse impact of traditional perturbation mechanisms and further brings down the number of interconnections. The electrical resonator has a simple structure, providing complete control of the array through a single actuation scheme. The electrical resonator was experimentally used to characterise fabricated sensors, hence providing sensitivity information in light of process variabilities. Since process-induced sensitivity degradation in coupled MEMS resonators has received limited attention, these findings can be of potential interest to the sensor community. The electrical resonator offers an enhanced tuning range which can be

used to compensate for device mismatch and elevate the sensitivity of the array, with the potential of two orders of magnitude enhancement.

The thesis also presented new sensors based on corner coupled square plate micro/nano resonators. These were designed and fabricated through the PolyMUMPs in Chapter 5. The device manifests a sensitivity superior to previously used sensors by offering MHz resonance and femtogram mass resolution. These resonators have miniaturised size and can form large arrays, with up to fifty elements fabricated experimentally. In Chapter 6, different numbers of coupled square plate resonators were tested to understand the limiting factors of scaling, including damping effect, eigenvalue readout, device robustness and sensing complexity. To address these challenges, measures including the use of a multiple actuation scheme, a linearised inverse eigenvalue sensing algorithm, and an eigenvalue selection approach were recommended and confirmed experimentally to reduce errors in large systems.

By building and investigating coupled arrays, this thesis has explored a range of new paths for coupled sensing applications. Notwithstanding, there are intrinsic limitations associated with the methodologies and some of the observations diverge from the initial plan due to unexpected reasons. The next section provides a summary of these limitations as well as potential countermeasures that can be explored in the future.

7.2 Future Outlook

To address the current limitations, there are four possible directions for future researches. These include an enhanced sensor design, a simultaneous eigenvalue readout method, a damping and non-linearity compensation scheme and an integrated system solution.

7.2.1 Sensor Design and Fabrication

One limitation of comb structure resonators is their high failure rate. There are more than 800 minuscule fingers on each resonator that are vulnerable to process

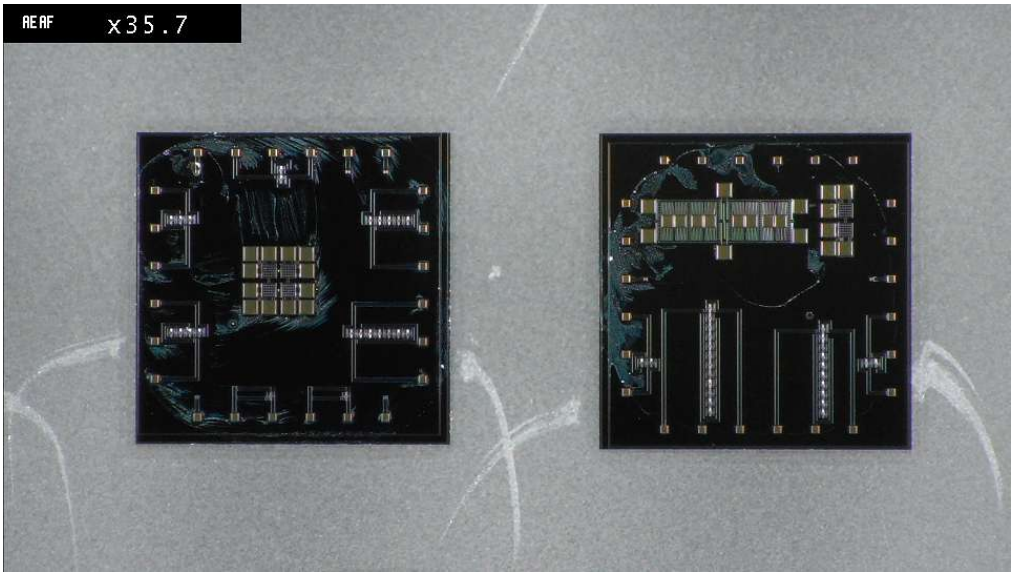


Figure 7.1: Contaminations of fabricated chips resulting from photoresist residue.

errors. The large surface area and close distance between opposing combs can provoke frequent pull-in. In fact, only 10% of these devices are working.

Although the second batch of sensors based on a new design has mitigated these issues and works reasonably well, they are not ideal in many senses. First, they demonstrate a lower resonant frequency and collapse voltage than COMSOL simulation results due to the unexpected oversizing effect. Second, the centre stem that supports the square plate is at the risk of misalignment, which has deteriorated the quality factor, making the resonator heavily damped under the ambient environment. Furthermore, the sensor is based on a conservative design without breaching the Nitride to provide an additional insulation layer. As a result, the short circuit after pull in damages the terminal resonator, making the characterisation process with de Boor and Golub's algorithm irreversible.

The research progress has also been hindered by foundry delay. A large scale of contaminations were spotted on the fabricated sensors when performing dicing and wire bonding. Figure 7.1 shows a microscopic image of contaminated chips resulting from photoresist residue. Fortunately, the foundry was able to offer backup wafers; however, these led to further delays. In addition, on these backup chips there still exists signs of residues, which are particularly detrimental to large arrays

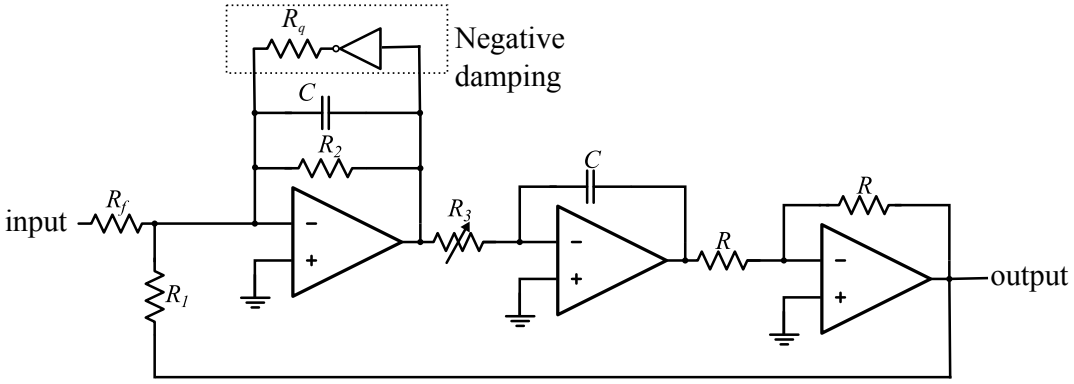


Figure 7.2: Schematic of a Tow Thomas oscillator.

where resonators are coupled in series.

On the positive side, a wealth of process-related experience and technical know-how have been accumulated, which provide valuable guidance for subsequent wafer runs. Future improvements encompass the optimisation of the resonator structure, such as the adoption of four corner stems to anchor the resonator. This would help reduce the damping and suppress redundant eigen-modes, making the sensor usable under an atmospheric pressure to perform real-world sensing of multiple chemical or biomedical substances. New coupled systems will be designed with known eigenvalue or eigenvector profiles. These profiles can help determine the coupling constants.

7.2.2 Simultaneous Eigenvalue Readout

Multi-resonance sensing, at its core, requires eigenvalue readout at multiple resonant modes. In the time domain, a driving signal with mode-switching capability is desirable. This can be a potential obstacle to inverse eigenvalue sensing. Moreover, the coupled systems need an external drive to maintain vibration. One possible remedy for these problems is to couple an oscillating circuit to the MEMS array, rather than an electrical resonator. Not only does the oscillator provide driving energy, it also enables collective oscillation at all eigen-modes that can be observed simultaneously in the time domain.

A damping compensation scheme is hence required to make up for energy losses of the whole coupled systems, including heat dissipation in the electrical circuit as well as mechanical loss in the MEMS resonators. Negative damping is impossible

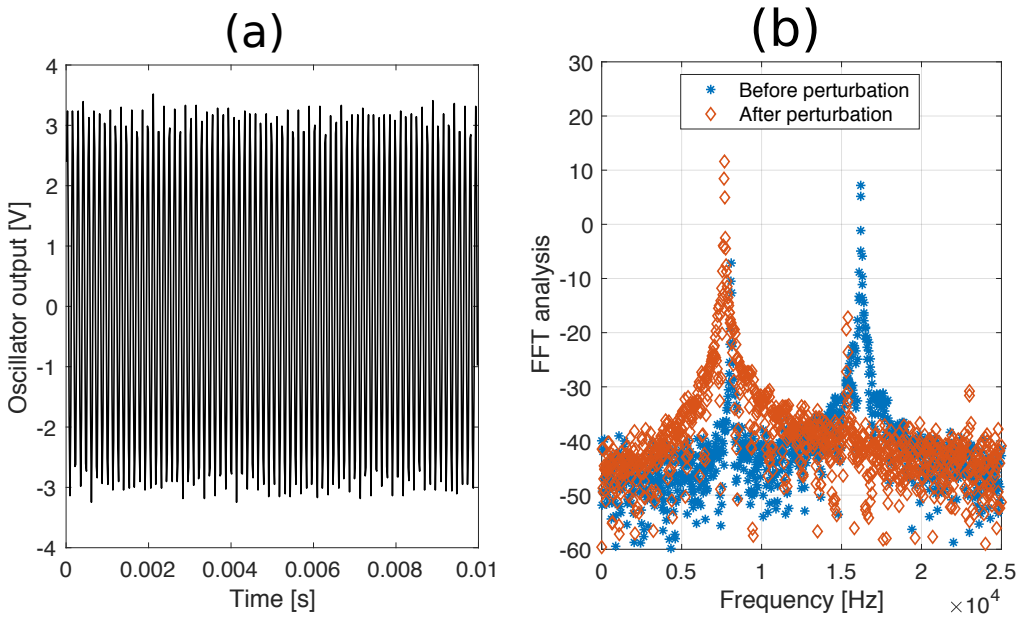


Figure 7.3: (a) Output from the oscillator in the time domain and (b) FFT analysis of the time domain signal.

using passive electrical elements; however, can be realised with the help of active components. A minor modification to the Tow Thomas electrical resonator can translate itself into an oscillator using a negative damping feedback [142]. The feedback is made up of an inverter and a resistor R_q, see Figure 7.2. The Tow Thomas oscillator is modelled by the equation

$$\ddot{x}_e + \left(\frac{1}{R_2 C} - \frac{1}{R_q C}\right)\dot{x}_e + \frac{1}{R_1 R_3 C^2} x_e = \frac{1}{R_3 R_f C^2} F_e \tag{7.1}$$

where F_e is the input driving voltage and x_e is the electrical output. By providing a $R_q < R_2$, the circuit is able to sustain a self-oscillation.

To show preliminary evidence for this approach, the proposed oscillator with around 15kHz resonance was experimentally constructed and coupled to the Tow Thomas electrical resonator used in Chapter 4. The output of the oscillator provided the electrical resonator with a driving signal, and the output of the electrical resonator was fed back to the input of the oscillator to establish coupling. Figure 7.3(a) shows the concurrent oscillations at two coupled resonant modes recorded experimentally from the oscillator. To find out the eigenvalues, fast Fourier transform (FFT) was performed to convert time domain signals into the frequency domain.

By changing the centre frequency of the oscillator, terminal perturbation became handy. Clearly, the two eigenvalues before and after perturbation, as depicted in the frequency spectrum in Figure 7.3(b), comply with the interweaving condition. Hence, IEA can be used subsequently to solve the system matrix. Future work will be dedicated to the implementation of this new coupling scheme in MEMS resonators, therefore achieving simultaneous eigenvalue readout from numerous sensors.

7.2.3 Damping and Non-linearity Compensation

The analysis presented in this thesis is primarily based on the assumption of undamped systems. The damping and non-linearity effects, although not pronounced in the experiments due to the vacuum environment and small signals used, should be considered in future work to meet extreme or changing sensing conditions.

Damping would drift the resonance frequencies, flatten the resonance peaks and deteriorate the minimum detectable mass or stiffness, hence limiting the accuracy of the inverse eigenvalue techniques and their scaling capabilities in large arrays. The damping is highly sensitive to multiple factors, such as the ambient and sensor design, which are difficult to adjust individually in a precise and real-time fashion. Another non-ideality seen in mechanical resonators is the duffing effect caused by non-linear elasticity, meaning that the resorting force, as a function of the displacement x, contains x^3 or higher order odd terms [143]. An additional source of non-linearity can be the electrostatic stiffness of the DC bias voltage, which is also dependent on the displacement. As the resonant amplitude increases, so does the impact of these non-linear terms, hence destabilising the eigenvalues or eigenvectors. As a result, the signal strength and sensing resolution are largely affected.

Given the above, a reliable and integrated solution is desired to compensate for these effects. Considering the damping and the x^3 duffing term with a coefficient k_d, a more realistic motion equation is given by

$$m\ddot{x} + c\dot{x} + kx + k_d x^3 = F + c_f\dot{x} + k_f x^3 \tag{7.2}$$

Both the damping and duffing terms, at the left hand side of this equation, can be cancelled out by superimposing the force, at the right hand side, with a $\dot{x}$

term having a coefficient c_f and a x^3 term with a coefficient k_f. These can be realised through a feedback circuit by sampling the velocity, which is linked to the output current of the transducer. Integrator and multiplier circuits can then be used to provide the corresponding feedback terms, which need to be cautiously adjusted. By incorporating this intelligent feedback, an enhanced electronic trimming scheme with post-fabrication and real-time compensation capabilities will be explored in the future.

7.2.4 System Integration

The ultimate goal is to create a fully integrated and miniaturised multi-sensor. Thus far, this research has heavily depended on off-the-shelf test equipment including bulky impedance analyser, signal generator and power source. The actuation, electrical resonator and coupling circuits were built on separate boards, making it inconvenient for realistic sensing. Therefore, it is crucial to mount the MEMS resonators and all these electrical circuits in a self-contained PCB, which will eventually lead to a compact and battery-powered sensing device. In addition, a customised perturbation and feedback circuitry will be designed and integrated to periodically calibrate the sensor. Future efforts will also be dedicated to the utilisation of the CMOS-MEMS technology to combine mechanical and electrical components, thereby providing a multitude of functional micro/nano systems on a single chip.

Appendices

With engineering, I view this year's failure as next year's opportunity to try it again. Failures are not something to be avoided. You want to have them happen as quickly as you can so you can make progress rapidly.

— Gordon Moore

A MATLAB Code

Contents

A.1 Eigenvector Extraction 148
A.1.1 Traditional Method 148
A.1.2 Linearised Method 149
A.2 Inverse Lanczos' Algorithm 149
A.3 De Boor and Golub's Algorithm 150

A.1 Eigenvector Extraction

A.1.1 Traditional Method

```
function x_p = extractEigenvector_oldMethod(f,f_star)
% x_p: displacement vector of the perturbed element at all modes
% f: eigenfrequencies before perturbation
% f_star: eigenfrequencies after perturbation

% Convert eigenfrequencies to eigenvalues
l = (2 * pi * f).^2;
l_star = (2 * pi * f_star).^2;

% Total amount of perturbation
totalPerturbation = sum(l_star - l);

% Initialise the output
n = numel(f);
x_p = zeros(1,n);
```

```
16
17 % Determine the amplitude iteratively
18 for i = 1:1:n
19     tmp = (l_star(i) - l(i)) ./ totalPerturbation;
20     for j = 1:1:n
21         if i ~= j
22             tmp = tmp * (l(i) - l_star(j)) ./ (l(i) - l(j));
23         end
24     end
25     x_p(i) = sqrt(tmp);
26 end
27
28 end
```

A.1.2 Linearised Method

```
1  function x_p = extractEigenvector_newMethod(f,f_star)
2  % x_p: displacement vector of the perturbed element at all modes
3  % f: eigenfrequencies before perturbation
4  % f_star: eigenfrequencies after perturbation
5
6  % Convert eigenfrequencies to eigenvalues
7  l = (2 * pi * f).^2;
8  l_star = (2 * pi * f_star).^2;
9
10 % Total amount of perturbation
11 totalPerturbation = sum(l_star - l);
12
13 % Initialise the output
14 n = numel(f);
15 x_p = zeros(1,n);
16
17 % Determine the amplitude iteratively
18 for i = 1:1:n
19     tmp = abs((l_star(i) - l(i))/totalPerturbation);
20     x_p(i) = sqrt(tmp);
21 end
22
23 end
```

A.2 Inverse Lanczos' Algorithm

```
1 function S = Lanczos(f,f_star)
2 % S: system matrix before perturbation
3 % f: eigenfrequencies before perturbation
4 % f_star: eigenfrequencies after perturbation
```

```
5
6  % Construct the Lambda matrix
7  l = (2 * pi * f).^2;
8  L = diag(l);
9
10 % Initialise the output
11 n = numel(f);
12 S = zeros(n,n);
13
14 % Initialise the displacement matrix
15 X = zeros(n,n);
16
17 % Extract the motion of the terminal element using the new method
18 X(1,:) = extractEigenvector_newMethod(f,f_star);
19
20 % Uncomment this to use the old method
21 % x(1,:) = extractEigenvector_oldMethod(f,f_star);
22
23 % Apply Lanczos' algorithm
24 for i = 1:1:(n-1)
25     if i == 1
26         S(1,1) = X(1,:) * L * X(1,:)';
27         S(1,2) = -norm(S(1,1) * X(1,:)' - L * X(1,:)');
28         S(2,1) = S(1,2);
29         X(2,:) = (L * X(1,:)' - S(1,1) * X(1,:)') / S(1,2);
30     else
31         S(i,i+1) = -norm(S(i,i) * X(i,:)' + S(i-1,i) * ...
               X(i-1,:)' - L * X(i,:)');
32         S(i+1,i) = S(i,i+1);
33         X(i+1,:) = (L * X(i,:)' - S(i,i) * X(i,:)' - S(i-1,i) * ...
               X(i-1,:)') / S(i,i+1);
34     end
35     S(i+1,i+1) = X(i+1,:) * L * X(i+1,:)';
36 end
37
38 end
```

A.3 De Boor and Golub's Algorithm

```
1  function S = deBoor(f,f_star)
2  % S: system matrix of n coupled resonators
3  % f: eigenfrequencies of n coupled resonators
4  % f_star: eigenfrequencies of n-1 resonators by removing the ...
       terminal element
5
6  % Calculate lambda and mu
7  l = (2 * pi * f).^2;
8  mu = (2 * pi * f_star).^2;
9
10 % Initialise the output
```

```
n = numel(f);
S = zeros(n,n);

% Initialise a series of weights (w)
w = zeros(1,n);

% Initialise diagonal elements (d)
d = zeros(1,n);

% Initialise the square of off-diagonal elements (o_squared)
o_squared = zeros(1,n-1);

% Initialise a series of polynomials
pkml = zeros(1,n);
pk = zeros(1,n);

% Step 1: compute the weights from lambda and mu
tmp = zeros(1,n);
for i = 2:1:n
    tmp(i-1) = l(i);
end
for i = 1:1:n
    w(i) = (l(i) - mu(1)) / (l(i) - tmp(1));
    for j = 2:1:(n-1)
        w(i) = w(i) * (l(i) - mu(j)) / (l(i) - tmp(j));
    end
    tmp(i) = l(i);
end

% Step 2: generate the values at lambda of the first two ...
   orthogonal polynomials
s = sum(w);
d(1) = sum(w * l') / s;
for i = 1:1:n
    pkml(i) = 1;
    pk(i) = l(i) - d(1);
end

% Step 3: compute pk, d and o_squared, then generate the values ...
   at lambda of subsequent pk using three-term recurrence:
for k = 2:1:n
    s_prime = s;
    t = 0;
    s = 0;
    for i = 1:1:n
        p = w(i) * (pk(i).^2);
        s = s + p;
        t = t + l(i) * p;
    end
    o_squared(k-1) = s / s_prime;
    d(k) = t / s;
    for i=1:1:n
        p = pk(i);
        pk(i) = (l(i) - d(k)) * p - o_squared(k-1) * pkml(i);
        pkml(i) = p;
```

```
64      end
65  end
66
67  % Step 4: compute o from o_squared, then reorder the diagonal ...
        and off-diagonal elements
68  o = sqrt(o_squared);
69  S(1,1) = d(1);
70  for i = 2:1:n
71      S(i,i) = d(i);
72      S(i,i-1) = -o(i-1);
73      S(i-1,i) = S(i,i-1);
74  end
75  end
```

Two roads diverged in a wood, and I—I took the one less traveled by, And that has made all the difference.

— Robert Frost

B

Mathematical Proof for Inverse Eigenvalue Analysis

Contents

B.1 Inverse Lanczos' Algorithm 153
B.2 Gladwell's Inverse Problem 154

B.1 Inverse Lanczos' Algorithm

The eigenvalue problem governed by the equation

$$\mathbf{S_n X} = \mathbf{X}\Lambda \tag{B.1}$$

can be turned into the form

$$\mathbf{U S_n} = \Lambda \mathbf{U} \tag{B.2}$$

where $\mathbf{U}$ is the transpose of $\mathbf{X}$. Letting d_i and o_i be the ith diagonal and off-diagonal elements of the system matrix respectively, then taking this equation column by column, the first column satisfies

$$d_1\mathbf{u_1} - o_1\mathbf{u_2} = \Lambda\mathbf{u_1} \tag{B.3}$$

Premultiplying $\mathbf{u_1}^\mathbf{T}$, the equation becomes

$$d_1\mathbf{u_1}^\mathbf{T}\mathbf{u_1} = d_1 = \mathbf{u_1}^\mathbf{T}\Lambda\mathbf{u_1} \tag{B.4}$$

Equation B.3 can be rewritten as

$$o_1\mathbf{u_2} = d_1\mathbf{u_1} - \Lambda\mathbf{u_1} = \mathbf{z_2} \tag{B.5}$$

Hence

$$o_1 \parallel \mathbf{u_2} \parallel = o_1 = \parallel \mathbf{z_2} \parallel \tag{B.6}$$

$$\mathbf{u_2} = \mathbf{z_2}/o_1 \tag{B.7}$$

With d_1, o_1 and $\mathbf{u_2}$ known, one can proceed to the next column:

$$-o_1\mathbf{u_1} + d_2\mathbf{u_2} - o_2\mathbf{u_3} = \Lambda\mathbf{u_2} \tag{B.8}$$

Similarly, by premultiplying $\mathbf{u_2}^\mathbf{T}$, one can derive:

$$d_2 = \mathbf{u_2}^\mathbf{T}\Lambda\mathbf{u_2} \tag{B.9}$$

$$o_2\mathbf{u_3} = d_2\mathbf{u_2} - o_1\mathbf{u_1} - \Lambda\mathbf{u_2} = \mathbf{z_3} \tag{B.10}$$

Therefore

$$o_2 \parallel \mathbf{u_3} \parallel = o_2 = \parallel \mathbf{z_3} \parallel \tag{B.11}$$

$$\mathbf{u_3} = \mathbf{z_3}/o_2 \tag{B.12}$$

By the same logic, the rest of the diagonal and off-diagonal elements can be extracted iteratively.

B.2 Gladwell's Inverse Problem

The eigenvalue equation for a perturbed system matrix $\mathbf{S_n^*}$ is

$$\mathbf{S_n}^*\mathbf{x} = \lambda\mathbf{x} \tag{B.13}$$

Thus

$$\mathbf{S_n}\mathbf{x} + (d_p^* - d_p)x_p\mathbf{e_p} = \lambda\mathbf{x} \tag{B.14}$$

where $\mathbf{x}$ can be written as

$$\mathbf{x} = \sum_{i=1}^{n} \alpha_i \mathbf{x_i} \tag{B.15}$$

Equation B.13 now becomes

$$\sum_{i=1}^{n} \lambda_i \alpha_i \mathbf{x_i} + (d_p^* - d_p) x_p \mathbf{e_p} = \lambda \sum_{i=1}^{n} \alpha_i \mathbf{x_i} \tag{B.16}$$

Therefore

$$(\lambda - \lambda_i)\alpha_i = (d_p^* - d_p) x_p x_{p,i} \tag{B.17}$$

Substituting this into Equation B.15 yields

$$\mathbf{x} = (d_p^* - d_p) x_p \sum_{i=1}^{n} \frac{x_{p,i} \mathbf{x_i}}{\lambda - \lambda_i} \tag{B.18}$$

Equating the first component on each side of the equation gives

$$1 = (d_p^* - d_p) \sum_{i=1}^{n} \frac{x_{p,i}^2}{\lambda - \lambda_i} \tag{B.19}$$

The roots of this equation are λ_i^*:

$$1 - (d_p^* - d_p) \sum_{i=1}^{n} \frac{x_{p,i}^2}{\lambda - \lambda_i} = \prod_{i=1}^{n} \frac{\lambda - \lambda_i^*}{\lambda - \lambda_i} \tag{B.20}$$

Therefore

$$x_{p,i}^2 = \frac{\lambda_i^* - \lambda_i}{d_p^* - d_p} \prod_{j=1, j \neq i}^{n} \frac{\lambda_i - \lambda_j^*}{\lambda_i - \lambda_j} \tag{B.21}$$

Using the trace property:

$$d_p^* - d_p = \sum_{i=1}^{n} (\lambda_i^* - \lambda_i) \tag{B.22}$$

The amplitudes of the pth resonator at all resonant modes are hence determined:

$$x_{p,i}^2 = \frac{\lambda_i^* - \lambda_i}{\sum_{i=1}^{n} (\lambda_i^* - \lambda_i)} \prod_{j=1, j \neq i}^{n} \frac{\lambda_i - \lambda_j^*}{\lambda_i - \lambda_j} \tag{B.23}$$

A man provided with paper, pencil, and eraser, and subject to strict discipline, is in effect a universal machine.

— Alan Turing

C Test Chips

Contents

C.1 Layout and Packaging 156
C.2 Test Chip I 158
C.3 Test Chip II 158
C.4 Test Chip III 159
C.5 Test Chip IV 160

C.1 Layout and Packaging

Figure C.1 pictures the full layout for different designs of single as well as coupled square plate resonators, which is drawn in the Cadence Virtuoso software. The PolyMUMPs tapeout provided an allocated space of 10000μm $\times$ 10000μm and delivered a batch of 15 dies. To fit in with the DIL24 packages required by the designed PCB board, each die was then subdiced into four different pieces (i.e. test chip I, II, III and IV) through vertical and horizontal laser cuts. Hence, each test chip takes up an area of 5000μm $\times$ 5000μm. By breaching the Nitride, several windows (50μm $\times$ 50μm) were opened in each chip to access the silicon underneath and provide more ground connections to the substrate, therefore minimising the

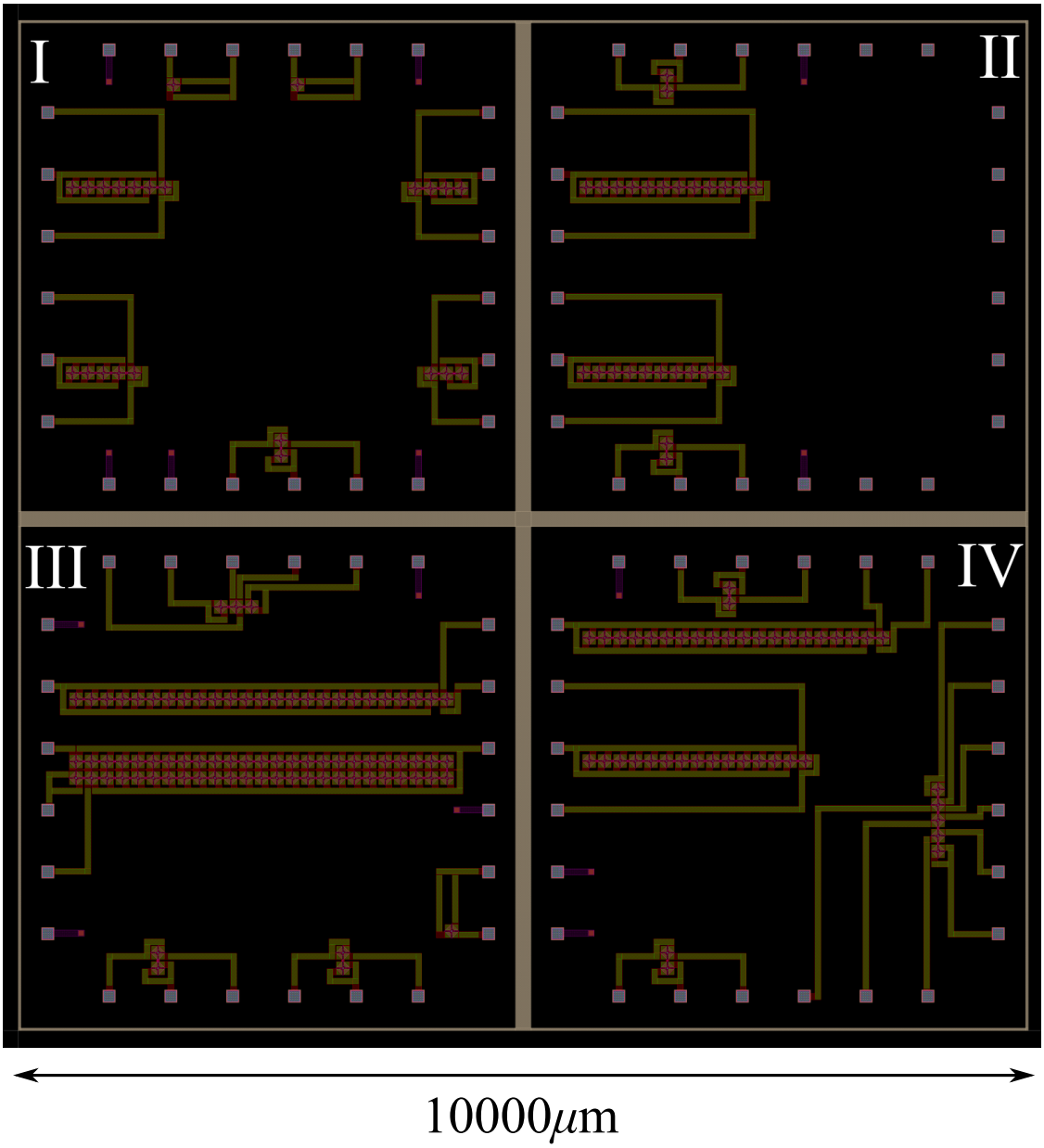


Figure C.1: Full layout for the square plate MEMS resonators.

effect of noise. One test chip contains 24 standardised bond pads that are arranged uniformly around the edges, with each having a size of 120μm $\times$ 120μm.

The bonding diagrams of the four test chips are depicted in Figure C.2. All post process steps including subdicing, wire bonding and packaging were outsourced to the Europractice.

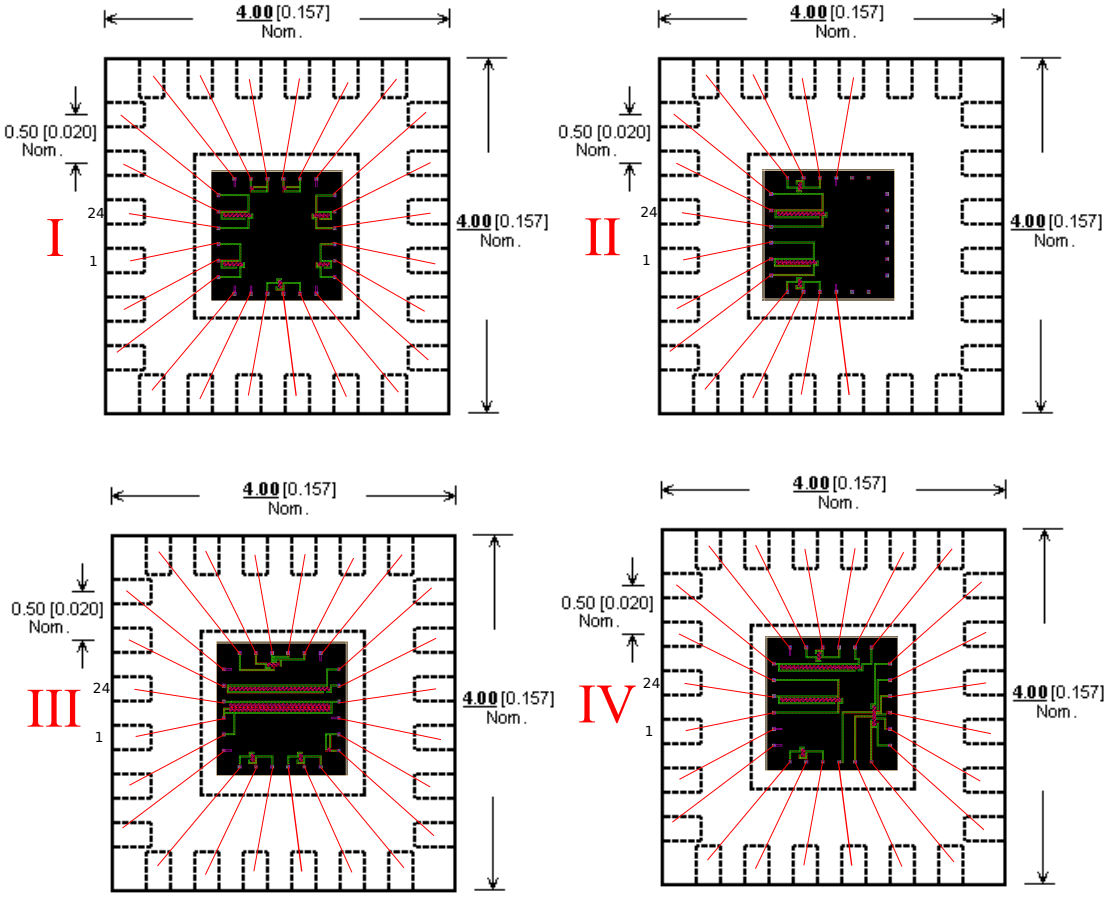


Figure C.2: Bonding diagrams for the four test chips.

C.2 Test Chip I

The electrical connections for test chip I, including the number of resonators and pin functionality, are presented in Table C.1. There are 7 sensors available in the same chip, including coupled arrays of two, three, four, five and seven resonators. The two-element array is driven by the single actuation, while the rest adopt the new multiple actuation scheme. In addition to coupled resonators, there are 2 single resonators. 5 dedicated pins (4,5,9,16,21) are used to connect to the silicon substrate.

C.3 Test Chip II

As summarised in Table C.2, test chip II has only 4 coupled resonant sensors since half of the space was reserved for a research partner. These 4 sensors include 1

Table C.1: Electrical connections for test chip I.

Package pin	PCB pin	Number of resonators	Function
1	J1	5	gnd
2	J2	5	V_{DC}
3	J3	5	V_P
4	J4	-	substrate
5	J5	-	substrate
6	J6	2	V_P
7	J7	2	V_{DC}
8	J8	2	gnd
9	J9	-	substrate
10	J10	3	V_P
11	J11	3	V_{DC}
12	J12	3	gnd
13	J13	4	V_P
14	J14	4	V_{DC}
15	J15	4	gnd
16	J16	-	substrate
17	J17	1	V_{DC}
18	J18	1	gnd
19	J19	1	V_{DC}
20	J20	1	gnd
21	J21	-	substrate
22	J22	7	gnd
23	J23	7	V_{DC}
24	J24	7	V_P

ten-element coupled array (multiple actuation), 1 twelve-element coupled array (multiple actuation) and 2 two-element coupled arrays (single actuation). Pin 7 and 18 are linked to the substrate.

C.4 Test Chip III

The summary for test chip III is presented in Table C.3. The chip accommodates 3 two-element arrays and 1 three-element array, both utilising the single actuation scheme. The three-element array, in particular, allows perturbation on any resonator besides the terminal one. Additionally, there are two large coupled arrays consisting of twenty-five resonators and fifty resonators respectively. Test chip III also includes a single resonator and 4 substrate connections.

Table C.2: Electrical connections for test chip II.

Package pin	PCB pin	Number of resonators	Function
1	J1	10	gnd
2	J2	10	V_{DC}
3	J3	10	V_P
4	J4	2	V_P
5	J5	2	V_{DC}
6	J6	2	gnd
7	J7	-	substrate
8	J8	-	-
9	J9	-	-
10	J10	-	-
11	J11	-	-
12	J12	-	-
13	J13	-	-
14	J14	-	-
15	J15	-	-
16	J16	-	-
17	J17	-	-
18	J18	-	substrate
19	J19	2	gnd
20	J20	2	V_{DC}
21	J21	2	V_P
22	J22	12	gnd
23	J23	12	V_{DC}
24	J24	12	V_P

C.5 Test Chip IV

Test chip IV is summarised in Table C.4. The chip has 2 two-element arrays, 1 five-element array, 1 fifteen-element array and 1 twenty-element array. The five-element array provides perturbation access to all resonators. Four pins are provided to contact the substrate.

Table C.3: Electrical connections for test chip III.

Package pin	**PCB pin**	**Number of resonators**	**Function**
1	J1	50	V_P
2	J2	50	gnd
3	J3	-	substrate
4	J4	2	V_P
5	J5	2	V_{DC}
6	J6	2	gnd
7	J7	2	V_P
8	J8	2	V_{DC}
9	J9	2	gnd
10	J10	1	gnd
11	J11	1	V_{DC}
12	J12	-	substrate
13	J13	50	V_{DC}
14	J14	25	V_P
15	J15	25	gnd
16	J16	-	substrate
17	J17	3	V_{P1}
18	J18	3	gnd
19	J19	3	V_{P2}
20	J20	3	V_{P3}
21	J21	3	V_{P2}
22	J22	-	substrate
23	J23	25	V_{DC}
24	J24	50	gnd

Table C.4: Electrical connections for test chip IV.

Package pin	**PCB pin**	**Number of resonators**	**Function**
1	J1	15	V_P
2	J2	-	substrate
3	J3	-	substrate
4	J4	2	V_P
5	J5	2	V_{DC}
6	J6	2	gnd
7	J7	5	V_{P2}
8	J8	5	V_{P3}
9	J9	5	V_{P4}
10	J10	5	V_{P5}
11	J11	5	V_{P4}
12	J12	5	V_{P4}
13	J13	5	gnd
14	J14	5	V_{P2}
15	J15	5	V_{P1}
16	J16	20	V_P
17	J17	20	gnd
18	J18	2	gnd
19	J19	2	V_{DC}
20	J20	2	V_P
21	J21	-	substrate
22	J22	20	V_{DC}
23	J23	15	gnd
24	J24	15	V_{DC}

Rich in knowledge and tenacious of purposes, inquiring with earnestness and reflecting with self-practice.

— Bu Shang

References

[1] Guowei Tao, Hemin Zhang, Honglong Chang, and Bhaskar Choubey. "Inverse eigenvalue sensing in coupled micro/nano system". In: *Journal of Microelectromechanical Systems* 27.5 (2018), pp. 886–895.

[2] Guowei Tao and Bhaskar Choubey. "Variability induced sensitivity degradation in coupled nano/micro resonant sensors". In: *IEEE Transactions on Nanotechnology* 17.4 (2018), pp. 709–713.

[3] Guowei Tao and Bhaskar Choubey. "Inverse eigenvalue sensing with corner coupled square plate MEMS resonators array". In: *Analog Integrated Circuits and Signal Processing* 95.3 (2018), pp. 447–455.

[4] Guowei Tao and Bhaskar Choubey. "A simple technique to readout and characterize coupled MEMS resonators". In: *Journal of Microelectromechanical Systems* 25.4 (2016), pp. 617–625.

[5] Guowei Tao and Bhaskar Choubey. "IEA sensing for corner coupled square plate MEMS resonators arrays". In: *Oxford Circuits and Systems Conference (OXCAS)*. 2017.

[6] Guowei Tao and Bhaskar Choubey. "On measuring variability and its effect on sensitivity of coupled nano/micro resonators". In: *Nano/Micro Engineered and Molecular Systems (NEMS), 2017 IEEE 12th International Conference on*. IEEE. 2017, pp. 657–660.

[7] Guowei Tao and Bhaskar Choubey. "Inverse eigenvalue analysis techniques for coupled M/NEMS resonators". In: *Nano/Micro Engineered and Molecular Systems (NEMS), 2016 IEEE 11th Annual International Conference on*. IEEE. 2016, pp. 217–220.

[8] Guowei Tao and Bhaskar Choubey. "Characterizing coupled MEMS resonators with an electrical resonator". In: *Journal of Physics: Conference Series*. Vol. 757. 1. IOP Publishing. 2016, p. 012017.

[9] Vojislav Z Lukic, Aleksej Makarov, Guowei Tao, and Bhaskar Choubey. "Vehicle speed estimation from tracking license plates". In: *Telecommunications Forum Telfor (TELFOR), 2015 23rd*. IEEE. 2015, pp. 429–432.

[10] Aleksej Makarov, Vojislav Lukic, Guowei Tao, and Bhaskar Choubey. "Vehicle speed estimation from partially calibrated monocular images". In: *International Conference on Sensors Engineering and Electronics Instrumental Advances (SEIA' 2015)*. 2015.

[11] Richard P Feynman. "There's plenty of room at the bottom". In: *Journal of Microelectromechanical Systems* 1.1 (1992), pp. 60–66.

[12] Vincenzo Balzani, Alberto Credi, Françisco M Raymo, and J Fraser Stoddart. "Artificial molecular machines". In: *Angewandte Chemie International Edition* 39.19 (2000), pp. 3348–3391.

[13] Sense Jan van der Molen, Jianhui Liao, Tibor Kudernac, Jon S Agustsson, Laetitia Bernard, Michel Calame, Bart J van Wees, Ben L Feringa, and Christian Schönenberger. "Light-controlled conductance switching of ordered metal- molecule- metal devices". In: *Nano Letters* 9.1 (2008), pp. 76–80.

[14] Jean-Pierre Sauvage. "From chemical topology to molecular machines (nobel lecture)". In: *Angewandte Chemie International Edition* (2017).

[15] Chih-Ming Ho and Yu-Chong Tai. "Micro-electro-mechanical-systems (MEMS) and fluid flows". In: *Annual Review of Fluid Mechanics* 30.1 (1998), pp. 579–612.

[16] Julian W Gardner, Vijay K Varadan, and Osama O Awadelkarim. *Microsensors, MEMS, and smart devices*. Vol. 1. Wiley Online Library, 2001.

[17] Xiangyu Zeng, Kaidi Zhang, Guowei Tao, Zhi Zeng, Shih-Kang Fan, and Jia Zhou. "Recoverable electrowetting-on-dielectric device in chemiluminescence enzymatic detector". In: *Japanese Journal of Applied Physics* 53.6 (2014), p. 060304.

[18] Munehisa Takeda. "Applications of MEMS to industrial inspection". In: *Micro Electro Mechanical Systems, 2001. MEMS 2001. The 14th IEEE International Conference on*. IEEE. 2001, pp. 182–191.

[19] Masako Tanaka. "An industrial and applied review of new MEMS devices features". In: *Microelectronic Engineering* 84.5 (2007), pp. 1341–1344.

[20] Yole Développement. *2015-2021 MEMS market forecast in US$B*. 2017. URL: `http://www.yole.fr/iso_album/illus_mis2017_marketrevenue_yole_june2017.jpg`.

[21] Harvey C Nathanson, William E Newell, Robert A Wickstrom, and J Ransford Davis. "The resonant gate transistor". In: *IEEE Transactions on Electron Devices* 14.3 (1967), pp. 117–133.

[22] Kurt E Petersen. "Silicon as a mechanical material". In: *Proceedings of the IEEE* 70.5 (1982), pp. 420–457.

[23] Gregory N Nielson, Dilan Seneviratne, Francisco Lopez-Royo, Peter T Rakich, Ytshak Avrahami, Michael R Watts, Hermann A Haus, Harry L Tuller, and George Barbastathis. "Integrated wavelength-selective optical MEMS switching using ring resonator filters". In: *IEEE Photonics Technology Letters* 17.6 (2005), pp. 1190–1192.

[24] J Jason Yao. "RF MEMS from a device perspective". In: *Journal of Micromechanics and Microengineering* 10.4 (2000), R9.

[25] V Agache, G Blanco-Gomez, F Baleras, and P Caillat. "An embedded microchannel in a MEMS plate resonator for ultrasensitive mass sensing in liquid". In: *Lab on a Chip* 11.15 (2011), pp. 2598–2603.

[26] Stephen D Senturia. *Microsystem design*. Springer Science & Business Media, 2007.

[27] Jan Korvink and Oliver Paul. *MEMS: A practical guide of design, analysis, and applications*. Springer Science & Business Media, 2010.

[28] Roger G Jackson. *Novel sensors and sensing*. CRC Press, 2004.

[29] MA Hopcroft et al. "Using the temperature dependence of resonator quality factor as a thermometer". In: *Applied Physics Letters* 91.1 (2007), p. 013505.

[30] Julien Chaste, A Eichler, J Moser, G Ceballos, R Rurali, and A Bachtold. "A nanomechanical mass sensor with yoctogram resolution". In: *Nature Nanotechnology* 7.5 (2012), pp. 301–304.

[31] S. A. Zotov, B. R. Simon, A. A. Trusov, and A. M. Shkel. "High quality factor resonant MEMS accelerometer with continuous thermal compensation". In: *IEEE Sensors Journal* 15.9 (Sept. 2015), pp. 5045–5052.

[32] S P Beeby, M J Tudor, and N M White. "Energy harvesting vibration sources for microsystems applications". In: *Measurement Science and Technology* 17.12 (2006), R175.

[33] Osamu Takahashi, Yasuharu Hashimoto, Eiichi Nagasaka, Hajime Miyazaki, and Tsukasa Funasaka. *Piezoelectric power generator for a portable power supply unit and portable electronic device equipped with same*. US Patent 5,751,091. May 1998.

[34] Kamran Entesari and Gabriel M Rebeiz. "A 12-18-GHz three-pole RF MEMS tunable filter". In: *IEEE Transactions on Microwave Theory and Techniques* 53.8 (2005), pp. 2566–2571.

[35] I. J. Oppenheim, A. Jain, and D. W. Greve. "Electrical characterization of coupled and uncoupled MEMS ultrasonic transducers". In: *IEEE Transactions on Ultrasonics, Ferroelectrics, and Frequency Control* 50.3 (Mar. 2003), pp. 297–304.

[36] S. A. Chandorkar, M. Agarwal, R. Melamud, R. N. Candler, K. E. Goodson, and T. W. Kenny. "Limits of quality factor in bulk-mode micromechanical resonators". In: *2008 IEEE 21st International Conference on Micro Electro Mechanical Systems*. Jan. 2008, pp. 74–77.

[37] J Mertz, O Marti, and J Mlynek. "Regulation of a microcantilever response by force feedback". In: *Applied Physics Letters* 62.19 (1993), pp. 2344–2346.

[38] Javier Tamayo, Mar Alvarez, and Laura M Lechuga. "Digital tuning of the quality factor of micromechanical resonant biological detectors". In: *Sensors and Actuators B: Chemical* 89.1 (2003), pp. 33–39.

[39] Robert Bogue. "MEMS sensors: past, present and future". In: *Sensor Review* 27.1 (2007), pp. 7–13.

[40] Ram Datar, Seonghwan Kim, Sangmin Jeon, Peter Hesketh, Scott Manalis, Anja Boisen, and Thomas Thundat. "Cantilever sensors: nanomechanical tools for diagnostics". In: *Mrs Bulletin* 34.6 (2009), pp. 449–454.

[41] P Alex Greaney and Jeffrey C Grossman. "Nanomechanical resonance spectroscopy: a novel route to ultrasensitive label-free detection". In: *Nano Letters* 8.9 (2008), pp. 2648–2652.

[42] Alexander Bietsch, Jiayun Zhang, Martin Hegner, Hans Peter Lang, and Christoph Gerber. "Rapid functionalization of cantilever array sensors by inkjet printing". In: *Nanotechnology* 15.8 (2004), p. 873.

[43] S Guillon et al. "Biological functionalization of massively parallel arrays of nanocantilevers using microcontact printing". In: *Sensors and Actuators B: Chemical* 161.1 (2012), pp. 1135–1138.

[44] I Bargatin et al. “Large-scale integration of nanoelectromechanical systems for gas sensing applications”. In: *Nano Letters* 12.3 (2012), pp. 1269–1274.

[45] Ira O Wygant, Nafis S Jamal, Hyunjoo J Lee, Amin Nikoozadeh, Ömer Oralkan, Mustafa Karaman, and Butrus T Khuri-Yakub. “An integrated circuit with transmit beamforming flip-chip bonded to a 2-D CMUT array for 3-D ultrasound imaging”. In: *IEEE Transactions on Ultrasonics, Ferroelectrics, and Frequency Control* 56.10 (2009), pp. 2145–2156.

[46] Jing-Quan Liu, Hua-Bin Fang, Zheng-Yi Xu, Xin-Hui Mao, Xiu-Cheng Shen, Di Chen, Hang Liao, and Bing-Chu Cai. “A MEMS-based piezoelectric power generator array for vibration energy harvesting”. In: *Microelectronics Journal* 39.5 (2008), pp. 802–806.

[47] Insu Jeon. “The study on failure mechanisms of bond pad metal peeling: Part B—Numerical analysis”. In: *Microelectronics Reliability* 43.12 (2003), pp. 2055–2064.

[48] Madhav Kumar and Harish Bhaskaran. “Ultrasensitive room-temperature piezoresistive transduction in graphene-based nanoelectromechanical systems”. In: *Nano Letters* 15.4 (2015), pp. 2562–2567.

[49] Ryan KW Chee, Alexander Sampaleanu, Deepak Rishi, and Roger J Zemp. “Top orthogonal to bottom electrode (TOBE) 2-D CMUT arrays for 3-D photoacoustic imaging”. In: *IEEE Transactions on Ultrasonics, Ferroelectrics, and Frequency Control* 61.8 (2014), pp. 1393–1395.

[50] Patrick A Truitt, Jared B Hertzberg, CC Huang, Kamil L Ekinci, and Keith C Schwab. “Efficient and sensitive capacitive readout of nanomechanical resonator arrays”. In: *Nano Letters* 7.1 (2007), pp. 120–126.

[51] Matthew Spletzer, Arvind Raman, Hartono Sumali, and John P Sullivan. “Highly sensitive mass detection and identification using vibration localization in coupled microcantilever arrays”. In: *Applied Physics Letters* 92.11 (2008), p. 114102.

[52] Marcel W Pruessner, Todd H Stievater, and William S Rabinovich. *Optical MEMS chemical sensor array.* US Patent 8,542,365. Sept. 2013.

[53] Peter M Osterberg and Stephen D Senturia. “M-TEST: a test chip for MEMS material property measurement using electrostatically actuated test structures”. In: *Journal of Microelectromechanical Systems* 6.2 (1997), pp. 107–118.

[54] Jinghui Xu and Julius Minglin Tsai. “A process-induced-frequency-drift resilient 32 kHz MEMS resonator”. In: *Journal of Micromechanics and Microengineering* 22.10 (2012), p. 105029.

[55] Masayuki Sato, BE Hubbard, AJ Sievers, B Ilic, DA Czaplewski, and HG Craighead. “Observation of locked intrinsic localized vibrational modes in a micromechanical oscillator array”. In: *Physical Review Letters* 90.4 (2003), p. 044102.

[56] Seung-Bo Shim, Matthias Imboden, and Pritiraj Mohanty. “Synchronized oscillation in coupled nanomechanical oscillators”. In: *Science* 316.5821 (2007), pp. 95–99.

[57] Samuel Jackson, Stefanie Gutschmidt, Dennis Roeser, and Thomas Sattel. "Development of a mathematical model and analytical solution of a coupled two-beam array with nonlinear tip forces for application to AFM". In: *Nonlinear Dynamics* 87.2 (2017), pp. 775–787.

[58] Bhaskar Choubey, Euan James Boyd, Ian Armstrong, and Deepak Uttamchandani. "Determination of the anisotropy of Young's modulus using a coupled microcantilever array". In: *Journal of Microelectromechanical Systems* 21.5 (2012), pp. 1252–1260.

[59] A Qazi, D Nonis, A Pozzato, M Tormen, M Lazzarino, S Carrato, and G Scoles. "Asymmetrical twin cantilevers for single molecule detection". In: *Applied Physics Letters* 90.17 (2007), p. 173118.

[60] Pradyumna Thiruvenkatanathan, Jize Yan, Jim Woodhouse, and Ashwin A Seshia. "Enhancing parametric sensitivity in electrically coupled MEMS resonators". In: *Journal of Microelectromechanical Systems* 18.5 (2009), pp. 1077–1086.

[61] Pradeep Pai, Hoorad Pourzand, and Massood Tabib-Azar. "Magnetically coupled resonators for rate integrating gyroscopes". In: *SENSORS, 2014 IEEE*. IEEE. 2014, pp. 1173–1176.

[62] Hemin Zhang, Boyang Li, Weizheng Yuan, Michael Kraft, and Honglong Chang. "An acceleration sensing method based on the mode localization of weakly coupled resonators". In: *Journal of Microelectromechanical Systems* 25.2 (2016), pp. 286–296.

[63] Mohamad Sadegh Hajhashemi, Amin Rasouli, and Behraad Bahreyni. "Improving sensitivity of resonant sensor systems through strong mechanical coupling". In: *Journal of Microelectromechanical Systems* 25.1 (2016), pp. 52–59.

[64] Mohamad Sadegh Hajhashemi and Behraad Bahreyni. "Characterization of disturbances in systems of coupled micro-resonator arrays". In: *IEEE Sensors Journal* 12.7 (2012), pp. 2510–2516.

[65] Barry E DeMartini, Jeffrey F Rhoads, Mark A Zielke, Kyle G Owen, Steven W Shaw, and Kimberly L Turner. "A single input-single output coupled microresonator array for the detection and identification of multiple analytes". In: *Applied Physics Letters* 93.5 (2008), p. 054102.

[66] Mustafa U Demirci and Clark T-C Nguyen. "Mechanically corner-coupled square microresonator array for reduced series motional resistance". In: *Journal of Microelectromechanical Systems* 15.6 (2006), pp. 1419–1436.

[67] Shanshan Li, Zhuoteng Peng, Ai Zhang, and Fei Wang. "Dual resonant structure for energy harvesting from random vibration sources at low frequency". In: *AIP Advances* 6.1 (2016), p. 015019.

[68] Crist Lu, Erno Klaassen, and Sathi Perumal. *Dynamic temperature compensation for a digitally controlled oscillator using dual MEMS resonators*. US Patent 7,545,228. June 2009.

[69] Bhaskar Choubey, Carl Anthony, Nor Hayati Saad, Mike Ward, Ross Turnbull, and Steve Collins. "Characterization of coupled micro/nanoresonators using inverse eigenvalue analysis". In: *Applied Physics Letters* 97.13 (2010), p. 133114.

[70] Bhaskar Choubey, Steve Collins, and Mike Ward. "On characterizing microelectromechanical processes using coupled resonators". In: *Journal of Microelectromechanical Systems* 21.4 (2012), pp. 791–800.

[71] Bhaskar Choubey. "Going fabless with MEMS". In: *Sensors & Transducers* 127.4 (2011), p. 1.

[72] Dazhong Jin, Xinxin Li, Jian Liu, Guomin Zuo, Yuelin Wang, Min Liu, and Haitao Yu. "High-mode resonant piezoresistive cantilever sensors for tens-femtogram resoluble mass sensing in air". In: *Journal of Micromechanics and Microengineering* 16.5 (2006), p. 1017.

[73] Matthew Spletzer, Arvind Raman, Alexander Q Wu, Xianfan Xu, and Ron Reifenberger. "Ultrasensitive mass sensing using mode localization in coupled microcantilevers". In: *Applied Physics Letters* 88.25 (2006), p. 254102.

[74] Pradyumna Thiruvenkatanathan, Jize Yan, and Ashwin A Seshia. "Differential amplification of structural perturbations in weakly coupled MEMS resonators". In: *IEEE Transactions on Ultrasonics, Ferroelectrics, and Frequency Control* 57.3 (2010).

[75] Eduardo Gil-Santos, Daniel Ramos, Anirban Jana, Montserrat Calleja, Arvind Raman, and Javier Tamayo. "Mass sensing based on deterministic and stochastic responses of elastically coupled nanocantilevers". In: *Nano Letters* 9.12 (2009), pp. 4122–4127.

[76] Hemin Zhang, Jie Huang, Weizheng Yuan, and Honglong Chang. "A high-sensitivity micromechanical electrometer based on mode localization of two degree-of-freedom weakly coupled resonators". In: *Journal of Microelectromechanical Systems* 25.5 (2016), pp. 937–946.

[77] Chun Zhao, Graham S Wood, Jianbing Xie, Honglong Chang, Suan Hui Pu, and Michael Kraft. "A force sensor based on three weakly coupled resonators with ultrahigh sensitivity". In: *Sensors and Actuators A: Physical* 232 (2015), pp. 151–162.

[78] Laure Mercier de Lépinay, Benjamin Pigeau, Benjamin Besga, Pascal Vincent, Philippe Poncharal, and Olivier Arcizet. "A universal and ultrasensitive vectorial nanomechanical sensor for imaging 2D force fields". In: *Nature Nanotechnology* (2016).

[79] Chun Zhao, Graham S Wood, Jianbing Xie, Honglong Chang, Suan Hui Pu, and Michael Kraft. "A comparative study of output metrics for an MEMS resonant sensor consisting of three weakly coupled resonators". In: *Journal of Microelectromechanical Systems* 25.4 (2016), pp. 626–636.

[80] Ali Mohammadi and Bhaskar Choubey. "Ultra high sensitivity in differential coupled micro/nano-resonator sensors". In: *Nano/Micro Engineered and Molecular Systems (NEMS), 2017 IEEE 12th International Conference on*. IEEE. 2017, pp. 652–656.

[81] Hemin Zhang, Jiming Zhong, Jing Yang, Weizheng Yuan, Hao Kang, and Honglong Chang. "Algebraic summation of eigenstates as a novel output metric to extend the linear sensing range of mode-localized sensors". In: *SENSORS, 2017 IEEE*. IEEE. 2017, pp. 1–3.

[82] Pierre Prache, Arantxa Uranga, Nuria Barniol, and Jérôme Juillard. "Temperature-drift rejection and sensitivity to mismatch of synchronized strongly-coupled M/NEMS resonators". In: *Micro Electro Mechanical Systems (MEMS), 2016 IEEE 29th International Conference on*. IEEE. 2016, pp. 1054–1057.

[83] Stefano Stassi, Alessandro Chiadò, Giuseppe Calafiore, Gianluca Palmara, Stefano Cabrini, and Carlo Ricciardi. "Experimental evidence of Fano resonances in nanomechanical resonators". In: *Scientific Reports* 7.1 (2017), p. 1065.

[84] Chun Zhao, Mohammad H Montaseri, Graham S Wood, Suan Hui Pu, Ashwin A Seshia, and Michael Kraft. "A review on coupled MEMS resonators for sensing applications utilizing mode localization". In: *Sensors and Actuators A: Physical* 249 (2016), pp. 93–111.

[85] Yong S Joe, Arkady M Satanin, and Chang Sub Kim. "Classical analogy of Fano resonances". In: *Physica Scripta* 74.2 (2006), p. 259.

[86] Chun Zhao, Graham S Wood, Jianbing Xie, Honglong Chang, Suan Hui Pu, and Michael Kraft. "A three degree-of-freedom weakly coupled resonator sensor with enhanced stiffness sensitivity". In: *Journal of Microelectromechanical Systems* 25.1 (2016), pp. 38–51.

[87] Mehmet Bulent Ozer and Thomas J Royston. "Application of Sherman–Morrison matrix inversion formula to damped vibration absorbers attached to multi-degree of freedom systems". In: *Journal of Sound and Vibration* 283.3-5 (2005), pp. 1235–1249.

[88] CT Sun and JM Bai. "Vibration of multi-degree-of-freedom systems with non-proportional viscous damping". In: *International Journal of Mechanical Sciences* 37.4 (1995), pp. 441–455.

[89] Zhongxu Hu and Barry J Gallacher. "Precision mode tuning towards a low angle drift MEMS rate integrating gyroscope". In: *Mechatronics* (2017).

[90] A Elka and I Bucher. "On the synthesis of micro-electromechanical filters using structural dynamics". In: *Journal of Micromechanics and Microengineering* 18.12 (2008), p. 125018.

[91] John William Strutt Baron Rayleigh. *The theory of sound*. Vol. 2. Macmillan, 1896.

[92] Carl D Meyer. *Matrix analysis and applied linear algebra*. Vol. 71. Siam, 2000.

[93] Leslie Hogben. *Handbook of linear algebra*. CRC Press, 2016.

[94] Teresa J Ryan, John A Judge, Joseph F Vignola, and Aldo A Glean. "Noise sensitivity of a mass detection method using vibration modes of coupled microcantilever arrays". In: *Applied Physics Letters* 101.4 (2012), p. 043104.

[95] Ankush Goel and Hossein Hashemi. "Concurrent dual-frequency oscillators and phase-locked loops". In: *IEEE Transactions on Microwave Theory and Techniques* 56.8 (2008), pp. 1846–1860.

[96] KL Ekinci, YT Yang, and ML Roukes. "Ultimate limits to inertial mass sensing based upon nanoelectromechanical systems". In: *Journal of Applied Physics* 95.5 (2004), pp. 2682–2689.

[97] Pradyumna Thiruvenkatanathan, Jim Woodhouse, Jize Yan, and Ashwin A Seshia. "Limits to mode-localized sensing using micro-and nanomechanical resonator arrays". In: *Journal of Applied Physics* 109.10 (2011), p. 104903.

[98] Hemin Zhang, Weizheng Yuan, Yongcun Hao, and Honglong Chang. "Influences of the feedthrough capacitance on the frequency synchronization of the weakly coupled resonators". In: *IEEE Sensors Journal* 15.11 (2015), pp. 6081–6088.

[99] Nor Hayati Saad, Carl J Anthony, Raya Al-Dadah, and Michael CL Ward. "Exploitation of multiple sensor arrays in electronic nose". In: *SENSORS, 2009 IEEE*. IEEE. 2009, pp. 1575–1579.

[100] Cornelius Lanczos. "An iteration method for the solution of the eigenvalue problem of linear differential and integral operators". In: *Journal of Research of the National Bureau Standards* 45.4 (1950).

[101] Graham ML Gladwell. *Inverse problems in vibration*. 2nd. Kluwer Academic, 2004.

[102] Carl De Boor and Gene Howard Golub. "The numerically stable reconstruction of a Jacobi matrix from spectral data". In: *Linear Algebra and Its Applications* 21.3 (1978), pp. 245–260.

[103] Carlo Jacoboni and Paolo Lugli. *The Monte Carlo method for semiconductor device simulation*. Springer Science & Business Media, 2012.

[104] Samuel Jackson and Stefanie Gutschmidt. "Utilisation of a two beam cantilever array for enhanced AFM sensitivity". In: *Journal of Vibration and Acoustics* (2017).

[105] Animesh Chatterjee. "Sensitivity and error analysis of a coupled micro-resonator array for ultra-sensitive mass detection using matrix perturbation theory". In: *IEEE Sensors Journal* 16.5 (2016), pp. 1304–1309.

[106] Barry J Gallacher, John Hedley, James S Burdess, Alun James Harris, Alexandria Rickard, and David O King. "Electrostatic correction of structural imperfections present in a microring gyroscope". In: *Journal of Microelectromechanical Systems* 14.2 (2005), pp. 221–234.

[107] Barry J Gallacher. "Principles of a micro-rate integrating ring gyroscope". In: *IEEE Transactions on Aerospace and Electronic Systems* 48.1 (2012), pp. 658–672.

[108] BR Mace and E Manconi. "Mode veering in weakly coupled systems". In: *Proceedings of the ISMA conference*. 2012.

[109] Barry E DeMartini, Jeffrey F Rhoads, Steven W Shaw, and Kimberly L Turner. "A single input–single output mass sensor based on a coupled array of microresonators". In: *Sensors and Actuators A: Physical* 137.1 (2007), pp. 147–156.

[110] Cheng-Syun Li, Li-Jen Hou, and Sheng-Shian Li. "Advanced CMOS–MEMS resonator platform". In: *IEEE Electron Device Letters* 33.2 (2012), pp. 272–274.

[111] Huikai Xie and Gary K Fedder. "Fabrication, characterization, and analysis of a DRIE CMOS-MEMS gyroscope". In: *IEEE Sensors Journal* 3.5 (2003), pp. 622–631.

[112] Ross G Turnbull, Mike CL Ward, Steve Collins, and Carl J Anthony. "A simple technique to increase the quality factor of micro-mechanical resonators". In: *Micro-and Nanotechnology Sensors, Systems, and Applications* 7318.1 (2009), 73181G.

[113] Nor Hayati Saad. "Modelling and performance evaluation of coupled micro resonator array for artificial nose". PhD thesis. University of Birmingham, 2010.

[114] Chenchen Deng. "Exploitation of nonlinear effects in micro-electromechanical resonators". PhD thesis. Oxford University, 2011.

[115] LC Shao, M Palaniapan, and WW Tan. "The nonlinearity cancellation phenomenon in micromechanical resonators". In: *Journal of Micromechanics and Microengineering* 18.6 (2008), p. 065014.

[116] Farid Tajaddodianfar, Mohammad Reza Hairi Yazdi, and Hossein Nejat Pishkenari. "Nonlinear dynamics of MEMS/NEMS resonators: analytical solution by the homotopy analysis method". In: *Microsystem Technologies* 23.6 (2017), pp. 1913–1926.

[117] S Liu, A Davidson, and Q Lin. "Simulation studies on nonlinear dynamics and chaos in a MEMS cantilever control system". In: *Journal of Micromechanics and Microengineering* 14.7 (2004), p. 1064.

[118] Ronen Almog, Stav Zaitsev, Oleg Shtempluck, and Eyal Buks. "Noise squeezing in a nanomechanical duffing resonator". In: *Physical Review Letters* 98.7 (2007), p. 078103.

[119] Ehsan Maani Miandoab, Hossein Nejat Pishkenari, Aghil Yousefi-Koma, and Farid Tajaddodianfar. "Chaos prediction in MEMS-NEMS resonators". In: *International Journal of Engineering Science* 82 (2014), pp. 74–83.

[120] J Tow. "Active RC filters—A state-space realization". In: *Proceedings of the IEEE* 56.6 (1968), pp. 1137–1139.

[121] S Celma, PA Martinez, and J Sabadell. "A transformation method for equivalent infinite-gain op amp to unity-gain CCII networks". In: *IEEE Transactions on Circuits and Systems I: Fundamental Theory and Applications* 43.1 (1996), pp. 61–63.

[122] Maria Cristina Piccirilli. "A fully integrated Tow-Thomas biquad using current feedback amplifiers". In: *Electronics, Circuits and Systems, 1999. Proceedings of ICECS'99. The 6th IEEE International Conference on.* Vol. 3. IEEE. 1999, pp. 1325–1328.

[123] Ahmed M Soliman. "Voltage mode and current mode Tow Thomas bi-quadratic filters using inverting CCII". In: *International Journal of Circuit Theory and Applications* 35.4 (2007), pp. 463–467.

[124] L Thomas. "The Biquad: Part I-Some practical design considerations". In: *IEEE Transactions on Circuit Theory* 18.3 (1971), pp. 350–357.

[125] Sungwan Cho, Sung Un Cho, Myunglae Jo, Junho Suh, Hee Chul Park, Sang Goon Kim, Seung-Bo Shim, and Yun Daniel Park. "Strong two-mode parametric interaction and amplification in a nanomechanical resonator". In: *Physical Review Applied* 9.6 (2018), p. 064023.

[126] Ross Turnbull. "Sensitivity enhancement in micro-electromechanical systems for sensor applications". PhD thesis. University of Oxford, 2010.

[127] Reza Abdolvand, Behraad Bahreyni, Joshua E-Y Lee, and Frederic Nabki. "Micromachined resonators: A review". In: *Micromachines* 7.9 (2016), p. 160.

[128] Chin-Yu Chou, Ming-Huang Li, Chao-Yu Chen, Chun-You Liu, and Sheng-Shian Li. "An innovative 3-D mechanically-coupled array design for MEMS resonator and oscillators". In: *Solid-State Sensors, Actuators and Microsystems (TRANSDUCERS), 2017 19th International Conference on*. IEEE. 2017, pp. 90–93.

[129] Gerald Blanco-Gomez and Vincent Agache. "Experimental study of energy dissipation in high quality factor hollow square plate MEMS resonators for liquid mass sensing". In: *Journal of Microelectromechanical Systems* 21.1 (2012), pp. 224–234.

[130] William Weaver Jr, Stephen P Timoshenko, and Donovan Harold Young. *Vibration problems in engineering*. John Wiley & Sons, 1990.

[131] Walter Ritz. "Theorie der transversalschwingungen einer quadratischen platte mit freien Rändern". In: *Annalen der Physik* 333.4 (1909), pp. 737–786.

[132] Ming-Huang Li, Wen-Chien Chen, and Sheng-Shian Li. "CMOS-MEMS transverse-mode square plate resonator with high Q and low motional impedance". In: *Solid-State Sensors, Actuators and Microsystems Conference (TRANSDUCERS), 2011 16th International*. IEEE. 2011, pp. 1500–1503.

[133] Igal Ladabaum, Xuecheng Jin, Hyongsok T Soh, Abdullah Atalar, and BT Khuri-Yakub. "Surface micromachined capacitive ultrasonic transducers". In: *IEEE Transactions on Ultrasonics, Ferroelectrics, and Frequency Control* 45.3 (1998), pp. 678–690.

[134] Raymond Jefferson Roark and Warren C Young. *Formulas for stress and strain*. McGraw-Hill, 1975.

[135] Sayanu Pamidighantam, Robert Puers, Kris Baert, and Harrie AC Tilmans. "Pull-in voltage analysis of electrostatically actuated beam structures with fixed–fixed and fixed–free end conditions". In: *Journal of Micromechanics and Microengineering* 12.4 (2002), p. 458.

[136] Jessica Liu, Clyde Oakley, and Robin Shandas. "Capacitive micromachined ultrasonic transducers using commercial multi-user MUMPs process: Capability and limitations". In: *Ultrasonics* 49.8 (2009), pp. 765–773.

[137] Allen Cowen, Busbee Hardy, Ramaswamy Mahadevan, and Steve Wilcenski. "PolyMUMPs design handbook". In: *Memscap Inc* 13 (2011).

[138] Hioki. *Single device solution for high speed testing and frequency sweeping*. 2017. URL: `https://www.hioki.com/file/cmw/hdCatalog/4765/pdf/?action=browser&log=1&lang=en`.

[139] Nickolay V Lavrik and Panos G Datskos. "Femtogram mass detection using photothermally actuated nanomechanical resonators". In: *Applied Physics Letters* 82.16 (2003), pp. 2697–2699.

[140] Alfred Brian Pippard. *The physics of vibration*. Cambridge University Press, 2007.

[141] Pierre Jehel, Pierre Léger, and Adnan Ibrahimbegovic. "Initial versus tangent stiffness-based Rayleigh damping in inelastic time history seismic analyses". In: *Earthquake Engineering & Structural Dynamics* 43.3 (2014), pp. 467–484.

[142] Angelo Brambilla, Giambattista Gruosso, and Giancarlo Storti Gajani. "Determination of Floquet exponents for small-signal analysis of nonlinear periodic circuits". In: *IEEE Transactions on Computer-Aided Design of Integrated Circuits and Systems* 28.3 (2009), pp. 447–451.

[143] Ronen Almog, Stav Zaitsev, Oleg Shtempluck, and Eyal Buks. "Signal amplification in a nanomechanical Duffing resonator via stochastic resonance". In: *Applied Physics Letters* 90.1 (2007), p. 013508.